

Universidade de São Paulo  
Instituto de Astronomia, Geofísica e Ciências Atmosféricas  
Departamento de Astronomia

Heitor Ernandes

**Abundances in field and globular cluster  
stars of the Galactic bulge: spectroscopy  
from the near-ultraviolet to the near-infrared**  
Abundâncias de estrelas do campo e em aglomerados globulares do bojo galáctico:  
espectroscopia do ultravioleta ao infra-vermelho próximo

São Paulo

2022



Heitor Ernandes

**Abundances in field and globular cluster  
stars of the Galactic bulge: spectroscopy  
from the near-ultraviolet to the near-infrared**

**Abundâncias de estrelas do campo e em aglomerados globulares do bojo galáctico:  
espectroscopia do ultravioleta ao infra-vermelho próximo**

Thesis presented to Departamento de Astronomia of Instituto de Astronomia, Geofísica e Ciências Atmosféricas, Universidade de São Paulo, as partial requirement to get the title of PhD in Science.

”Versão Corrigida. O original encontra-se disponível na Unidade.”

Area: Astronomy

Advisor: Profa. Dra. Beatriz L. S. Barbuy

São Paulo

2022



*To my grandfather*



# Acknowledgements

This endeavor would not have been possible without Beatriz Barbuy. I am very grateful for all the support, motivation, and discussions that made me a professional astrophysicist;

To Vinicius Placco for the fantastic discussions and suggestions on my thesis, and career as an astronomer;

To Bruno Dias for our many discussions on my thesis, papers, and career; for receiving me at ESO/Santiago;

To Chris Evans for receiving me at University of Edinburgh in the Royal Observatory, for his support beyond his duties in the very difficult year of 2020 ;

To Ruben Sanchez for our discussions on data handling, analysis, and to make me feel welcome in Edinburgh;

To professor Jorge Melendez for teaching me observational astronomy and present me the Paranal observatory;

To professor Silvia Rossi for all support and motivation;

To professor Walter Maciel for presenting me Galactic archaeology;

To professor Amâncio Friaça for the discussions and the calculations of chemical evolution model;

To astronomers, Cristina Chiappini and Vanessa Hill for the discussions and suggestions that improved my papers;

To my dear colleagues Antonio, Christiano, Larissa, Livia, and Julian for the excellent discussions and support;

To CAPES for the financial support;



*“Once you eliminate the impossible, whatever remains, no matter how improbable, must be the truth.”*

Sherlock Holmes on “The Sign of Four”. Sir Arthur Conan Doyle (1890)

*“Considerate la vostra semenza: fatti non foste viver come bruti, ma per seguir virtute e canoscenza. ”*

The Divine Comedy, Inferno 26, Dante Alighiere (1307)

*“My desire and wish is that the things I start with should be so obvious that you wonder why I spend my time stating them. This is what I aim at because the point of philosophy is to start with something so simple as not to seem worth stating, and to end with something so paradoxical that no one will believe it.”*

The Philosophy of Logical Atomism, Bertrand Russell (1918)



# Resumo

Os principais objetivos deste trabalho são a melhor compreensão da formação e evolução do bojo Galáctico, e da nucleossíntese ocorrida nas primeiras supernovas que enriqueceram o bojo em elementos químicos.

O bojo galáctico está sob intensa discussão quanto a sua origem e populações estelares. Este contém estrelas muito antigas pobres em metais que estão espacialmente distribuídas em uma forma esferoidal que se formaram durante o processo inicial de formação de bojo. O bojo tem uma barra que se formou provavelmente a partir do disco espesso. Esta componente contém principalmente estrelas ricas em metais.

O principal objetivo deste trabalho é expandir os estudos de abundâncias químicas em diferentes populações estelares do bojo Galáctico, associado com o estudo de processos de nucleossíntese. As características de abundâncias químicas de diferentes grupos de elementos como elementos- $\alpha$ , elementos do pico do ferro e elementos pesados, vem sendo considerado como discriminadores chave de populações estelares e processos de nucleossíntese. Este trabalho também visa relacionar as perspectivas dos futuros instrumentos VLT-MOONS, VLT-CUBES e ELT-MOSAIC no estudo dessas populações estelares.



# Abstract

The aim of this work is a better understanding of the formation and evolution of the Galactic bulge, and the nucleosynthesis that took place in the first stars that enriched the early bulge.

The Galactic bulge is under intense discussion as concerns its origin and stellar populations. It contains very old metal-poor stars spatially distributed in a spheroidal shape that should have been formed at early times in an early process of bulge formation. The bulge has also a bar that formed from a thick disk probably. This component contains mostly metal-rich stars.

The main aim of this work is to expand the studies of chemical abundances in different stellar populations in the Galactic bulge associated with the study of the nucleosynthesis processes. Chemical tagging of different groups of elements such as  $\alpha$ -, iron-peak, and heavy elements are considered presently as the key discriminator of stellar populations and nucleosynthesis processes. This work also relates to the prospects of the forthcoming instruments VLT-MOONS, VLT-CUBES, and ELT-MOSAIC in the studies of these stellar populations.



## List of Figures

2.1	Terzan 9: composed image in B, V and R, from 5 different pointings of Terzan 9 obtained with MUSE on Yepun in 2016. Size is $1.1 \times 1.1$ arcmin <sup>2</sup> , exposures with seeing from 0.51" to 1.01". . . . .	48
2.2	AL 3: 3 min. B image, with the three sample stars identified. Extraction of $3' \times 3'$ . North is up and East is left. . . . .	52
3.1	Comparison of the spectra for each globular cluster in the sample. Features of interest are indicated for Mn I ( <i>top</i> ), Cu I ( <i>middle</i> ), and Zn I lines ( <i>bottom</i> ). . . . .	55
3.2	Fittings on solar, Arcturus, and $\mu$ Leo spectra for the Cu I lines at 5105 Å and 5218 Å (yellow lines). Observations (black crosses) are compared with synthetic spectra computed using the adopted abundances (dashed blue lines). . . . .	57
3.3	Fits of best lines of Sc I, Sc I 6604.601 Å for some sample stars. . . . .	62
3.4	Fits of best lines of V I, V I 5703.560 Å, and, Mn I 6013.513 Å for some sample stars. . . . .	62
3.5	Fits of best lines of Cu I, Cu I 5105.537 Å, and Zn I, Zn I 4810.529 Å for some sample stars. . . . .	63
3.6	Excitation and ionization equilibria of Fe I and Fe II lines for the star 2939 in LTE. . . . .	64
3.7	Upper left panel: LTE. Upper right panel: NLTE abundance corrected. Lower panel: NLTE gravity corrected. Excitation and ionization equilibria of Fe I and Fe II lines for star 2939. Upper left panel: applying NLTE abundance correction; upper right panel: applying NLTE gravity correction. . . . .	65

3.8	[Sc/Fe] vs. [Fe/H]. Symbols: present work (filled red circles), Bensby et al. (2017) (black filled circles), Nissen et al. (2000) (filled blue diamonds), Howes et al. (2015) (open green circles), Howes et al. (2016) (green crosses); Battistini & Bensby (2015) (grey filled circles). Error bars on [Sc/Fe] are indicated. Errors in [Fe/H] can be assumed to be constant, of the order of $\Delta[\text{Fe}/\text{H}]=\pm 0.17\text{dex}$ . . . . .	68
3.9	[V/Fe] vs. [Fe/H]. Symbols: present work (filled red circles); Reddy et al. (2003) (green filled triangles), Reddy et al. (2006) (navyblue filled triangles) Battistini & Bensby (2015) (grey filled circles). Errors are assumed as in Fig. 3.8. . . . .	69
3.10	[Mn/Fe] vs. [Fe/H] for the sample stars and literature data: the present sample (red filled circles), Nissen et al. (2000) (blue filled diamonds), Sobeck et al. (2006) (black filled circles), McWilliam et al. (2003) (deep sky blue filled circles), Barbuy et al. (2013) (green filled triangles), Schultheis et al. (2017) (blue filled circles), and Battistini & Bensby (2015) (grey filled circles). Chemical evolution models by Cescutti et al. (2008) (blue dashed line); are overplotted. Errors are assumed as in Fig. 3.8. . . . .	71
3.11	[Mn/O] vs. [Fe/H]. Symbols: present work (red filled circles), Barbuy et al. (2013) (green filled triangles), Feltzing et al. (2007) thin disk (violet open squares), Feltzing et al. (2007) thick disk (violet filled circles). Errors are assumed as in Fig. 3.8. . . . .	72
3.12	[Cu/Fe] vs. [Fe/H] for the present sample (red filled circles), Johnson et al. (2014) (green filled circles), and Ishigaki et al. (2013) (blue filled circles). Chemical evolution models by and Kobayashi et al. (2006) (red dotted lines) are overplotted. Errors are assumed as in Fig. 3.8. . . . .	73
3.13	[Cu/O] vs. [Fe/H]. Data from the present work (red filled circles), and from Johnson et al. (2014) (green filled circles) are plotted. . . . .	73

3.14	[Zn/Fe] vs. [Fe/H]. Symbols: present work (filled red circles), Barbuy et al. (2015) (green filled triangles), Ishigaki et al. (2013) (blue filled circles), Howes et al. (2015) (green open circles), Howes et al. (2016) (green crosses), Casey & Schlafman (2016) (grey filled circles), Koch et al. (2016) (black open squares), Bensby et al. (2017) (black filled circles). Chemical evolution models by Kobayashi et al. (2006) (red dotted line). The Barbuy et al. (2015) models are shown for enrichment timescales of 2 (black) and 3 (blue) Gyr. In each case, the models for radius with respect to the Galactic centre of $r < 0.5$ kpc (dashed lines), $0.5 < r < 1$ kpc (dotted lines), $1 < r < 2$ kpc (dash-dotted lines), $2 < r < 3$ kpc (long-dashed lines) are overplotted. Errors are assumed as in Fig. 3.8. . . . . .	74
4.1	Fits of synthetic spectra to the eight observed lines of Co I in star BWc-4. The dotted line is the observed spectrum. The green lines correspond to the value adopted, and with [Co/Fe]=+0.09 and -0.09. . . . .	90
4.2	Fits of synthetic spectra to the two observed lines of Cu I in star BL-7. The dotted line is the observed spectrum. The green lines correspond to the value adopted, and with [Cu/Fe]=+0.12 and -0.12. . . . .	90
4.3	Upper panel: [Co/Fe] vs. [Fe/H] with the present results in LTE and corrected for NLTE, together with literature data. Lower panel: [Cu/Fe] vs. [Fe/H] with the present results and literature data. Shown are: the present results in LTE (open green circles); present results in NLTE (open magenta circles); Johnson et al. (2014) (filled blue circles); Lomaeva et al. (2019) for the SW field (open cyan circles); Xu et al. (2019) in LTE (open Indian red triangles); Xu et al. (2019) in NLTE (filled Indian red triangles); Ernandes et al. (2018) for bulge globular clusters (open dark orange squares) and chemodynamical evolution models are overplotted; specific star formation rates of $3 \text{ Gyr}^{-1}$ , with SNII yields from WW95 (black lines); specific star formation rates of $1 \text{ Gyr}^{-1}$ , with SNII yields from WW95 and from Kobayashi et al. (2006) for [Fe/H] < -4.0 (green lines). Models are for distances to the Galactic center of: $r < 0.5$ kpc (solid lines), $0.5 < r < 1$ kpc (dotted lines), $1 < r < 2$ kpc (dashed lines), and $2 < r < 3$ kpc (dash-dotted lines).	93

4.4	[Co/Fe] vs. [Fe/H]: present results in LTE and corrected for NLTE, compared with data from Hasselquist et al. (2017) for the Sagittarius dwarf galaxy. Symbols: open green circles represent present results in LTE; red circles represent present results in NLTE; filled blue dots represent Hasselquist et al. (2017). . . . .	96
4.5	[Cu/O] vs. [Fe/H] for the present results in NLTE and literature data. Symbols: open magenta circles represent present results in NLTE; filled blue dots represent Jonhson et al. (2014); open orange squares represent Ernandes et al. (2018). . . . .	96
5.1	Terzan 9: I image of Terzan 9 obtained at NTT in 2012, with seeing of 0.5 arcsec. Size is 2.2x2.2 arcmin <sup>2</sup> . . . . .	101
5.2	Emission line subtraction from spectrum of star 2582. . . . .	103
5.3	Spectra of Terzan 9 star id 0072 from different data cubes obtained with PampelMUSE. . . . .	104
5.4	Fit obtained with ETOILE for star 0072 with a good S/N =129.80. Upper panel: region 6000- 6800 Å where the strongest lines (telluric feature at 6282 Å, BaII 6496.9 Å and H $\alpha$ ) are indicated; lower panel: calcium triplet region. . . . .	105
5.5	Histograms of radial velocities obtained in the cases: green distribution: MILES library in the range 4860 - 5600 Å; blue distribution: Coelho05 library in the range 4860 - 9000 Å; and yellow distribution: Coelho05 library in the CaT region at 8400 - 8750 Å. . . . .	107
5.6	Smoothed histogram of radial velocities obtained with the Coelho05 library in the CaT region at 8400 - 8750 Å. A kernel density estimation (KDE) gaussian fitting the main peak of radial velocity distribution is overplotted. . . . .	108
5.7	Proper motions from Gaia. Symbols: gray dots: Gaia stars contained within a radius of 15 arcmin from the cluster center; Green dots: Gaia stars in a density representation enclosed in the MUSE field (1.1'x1.1'). The clustering of stars from Terzan 9 can be seen in red and blue, where blue is the densest part. . . . .	108

5.8	Metallicity distribution of sample stars based on the optical analysis. The black curve represents a gaussian fit centered at a mean value of $[\text{Fe}/\text{H}]=-1.12\pm 0.12$ . The blue curve is a KDE gaussian bandwidth estimated using Scott's rule .	110
5.9	Fit to CaT lines A: 8498 Å; B: 8542 Å, and C: 8662 Å for star 1378 as example. The shaded gray areas show the local continuum regions and the shaded orange areas show the line region defined by (269). The black lines and dots trace the observed spectrum in the rest frame and the blue lines are the best model fit to the data, using a sum of Gaussian and Lorentzian functions. The spectrum has been locally normalized using the highlighted local continuum regions before the fitting. In this analysis we only use the sum of the equivalent widths of the two strongest lines (B+C) following the recipe of (269; 270).	112
5.10	Metallicity distribution of sample stars based on CaT analysis.	112
5.11	Metallicity distribution based on optical analysis vs. radial velocity distribution, for identified member stars.	113
5.12	Corner plot: metallicity, proper motion and radial velocities.	114
5.13	I vs. V-I color-magnitude diagram showing all stars (gray) and member stars (red) (left panel), compared with the $\log g$ vs. $T_{\text{eff}}$ diagram (middle panel), and CMD in Gaia magnitudes and colors G vs. BP-RP for the stars in common (right panel). Dartmouth isochrones of 13 Gyr, and $[\text{Fe}/\text{H}]=-1.0$ are overplotted in black and isochrones of 13 Gyr, and $[\text{Fe}/\text{H}]=-2.0$ are overplotted in gray.	115
5.14	Distribution in $[\text{Mg}/\text{Fe}]$ . A KDE plot indicates a mean value of $[\text{Mg}/\text{Fe}]=+0.27$ .	116
6.1	AL 3-3: radial velocity derivation. The solid black line is the observed spectrum, the solid grey line is the noise spectrum, the solid red line is the synthetic spectrum, the dashed red lines are those used to derive the radial velocity, and the dashed black lines are the OH sky lines.	124

6.2	AL 3-6: radial velocity derivation. The solid black line is the observed spectrum, the solid grey line is the spectrum of star AL3-7, the dashed red lines are those used to derive the radial velocity, and the dashed black lines are the OH sky lines. . . . .	124
6.3	AL 3-7: radial velocity derivation. The solid black line is the observed spectrum, the solid grey line is the noise spectrum, the solid red line is the synthetic spectrum, the dashed red lines are those used to derive the radial velocity, and the dashed black lines are the OH sky lines. . . . .	124
6.4	AL 3-3 and AL 3-7: Hydrogen Brackett 16 line computed for $T_{eff} = 4250, 4500, 4750, 5000$ K (upper panels) and adopted values of 4250 K and 4750 K, respectively (lower panels). The dashed line is the observed spectrum .	128
6.5	AL 3-6: Tentative fit to this low S/N spectrum, showing that it is compatible with a high CNO abundance. Blue and black lines: Same observed spectrum normalized in two different ways. Red and cyan lines: Synthetic spectra computed with $[C/Fe]=0.7$ (red), $0.8$ (cyan), $[N/Fe]=+1.0$ , $[O/Fe]=+0.8$ . .	129
6.6	NGC 6558-42: Line identification in the range 15527-15555 Å. Dashed line: Observed spectrum. Solid red line: Synthetic spectrum. Synthetic spectrum computed with $[C/Fe]=-0.5$ , $[N/Fe]=0.8$ , $[O/Fe]=+0.5$ . . . . .	130
6.7	NGC 6558-42: Same as Fig. 6.6, in the range 15555-15587 Å. . . . .	131
6.8	HP 1-5, AL 3-3, and AL 3-7: Spectrum in selected wavelength regions containing CN, OH lines and the CO bandhead. Synthetic spectra are computed for the CNO abundances given in Table 6.6.2. . . . .	133
7.1	Fits to the Be II 3130.42 and 3131.07 Å doublet. Blue, magenta, yellow and green model spectra correspond to $A(Be) = -2.5, -2.4, -2.1$ and $-2.0$ , respectively. The grey line is the model spectrum without Be. . . . .	142
7.2	$\log(Be/H)$ vs. $[Fe/H]$ for CS 31082-001 (red circle) compared with literature data as follows: solid blue circles, Smiljanic et al. (2021); solid black circles, Smiljanic et al. (2009); solid green pentagons, Spite et al. (2019); solid yellow pentagons, Placco et al. (2014); solid cyan circles, Boesgaard et al. (2011). The solid line is a fit to the data by Smiljanic et al. (2009). The dashed line is the locus of dwarf metal-poor stars (Spite et al. 2019). . . .	143

7.3	Best-fit abundance for the Cr I 3578.68 Å line, computed with $[\text{Cr}/\text{Fe}] = -0.31$ , without NLTE correction (see Sect. 7.4.0.2). . . . .	148
7.4	Best fit abundance for V II 3517.299, 3545.196, 3715.464 and 3951.96 Å lines, computed with $[\text{V}/\text{Fe}] = +0.22$ . HFS was not applied to the V II 3715.464 Å line. . . . .	148
7.5	Best fit for the Cu I 3247.537 and 3273.954 Å lines, computed with $[\text{Cu}/\text{Fe}] = -0.79$ (including hyperfine structure). . . . .	149
7.6	Best fit to the Cu I 5105.5 and 5218.2 Å lines, computed with $[\text{Cu}/\text{Fe}] = -0.80$ .	149

7.7	<p><i>Upper panel:</i> Relation of [V II/Fe] vs. [Fe/H]. Symbols: red dots: present work; green dots: Ou et al. (2020), blue pentagons: Ishigaki et al. (2013). Our chemical evolution model for the halo/disk (LF03) is shown for several Galactocentric radii and for the halo (thick solid lines). Our fiducial model includes neutrino processes with <math>E_\nu = 3 \times 10^{53}</math> erg. The various curves for the halo correspond to different assumptions for the neutrino process. From bottom to top: 1) no neutrino process; 2) the fiducial model (<math>E_\nu = 3 \times 10^{53}</math> erg); 3) <math>E_\nu = 3 \times 10^{53}</math> erg and <math>T_\nu = 8</math> Mev; 4) <math>E_\nu = 9 \times 10^{53}</math> erg. As we can see from the comparison of the LF03 model with the data, inclusion of the neutrino process could account for the high [V/Fe] ratios of extremely metal-poor and very metal-poor stars. The solid long-dashed line refers to the predictions of the fiducial model of Kobayashi et al. (2020), while the K15 model from Kobayashi et al. (2020), which includes an 0.3 dex enhancement of the V yields, is also shown (dotted-dashed line). <i>Lower panel:</i> Relation of [Cu I/Fe] vs. [Fe/H]. Symbols: red dots: present work; yellow dots: Mishenina et al. (2002); blue pentagons: Ishigaki et al. (2013); gray pentagons: Cohen et al. (2013). The thick solid line refers to the halo in the LF03 model and the thin lines to the disk in the model at the radii <math>r= 4, 8</math> and <math>12</math> kpc. The neutrino process follows the fiducial case (<math>E_\nu = 3 \times 10^{53}</math> erg). The LF03 model not only reproduces the CS 31082-001 data point but also predicts the wave shape of the [Cu/Fe] versus [Fe/H] curve. The resulting evolution of Cu abundance predicted by the model of Kobayashi et al. (2020) for the solar neighborhood is given by the black long-dashed line, and the dotted-dashed line refers to the model without production of Cu by the s-process in AGB stars. . . . .</p>	154
7.8	<p>Elemental abundances of CS 31082-001, with the symbol colours showing the source of the result, as indicated in the legend. The red shaded region highlights the iron-peak elements, with the blue regions highlighting the first, second and third peaks of s-process elements . . . . .</p>	155

7.9	<i>Upper panel:</i> Elemental abundances of CS 31082-001. Symbols: red circles are from the present work; blue circles, Hill et al. (2002); gray circles, Siqueira-Mello et al. (2013). The orange diamonds are the elemental abundances of CS 22892-052 from Sneden et al. (2003). <i>Lower panel:</i> Iron-peak abundances of CS 31082-001 with the same symbol colours as the upper panel. The predicted abundance yields from for Nomoto et al. (2013) for faint supernovae and hypernovae are shown by the green and black dashed lines, respectively. . . . .	156
8.1	Abundances of elements in the Solar System vs. atomic number ( $Z$ ) normalised by the abundance of $^{28}\text{Si}$ to $10^6$ (Lodders, 2003). Iron-peak elements and the three peaks of the s-process are highlighted by the pink and blue panels, respectively. Elements with near-UV (3020-4000Å) spectral lines and observable with CUBES (at $R=20000$ ) are indicated in red. . . . .	162
8.2	<i>Red:</i> Synthetic spectrum of a metal-poor star generated using the TURBOSPECTRUM radiative transfer code (Plez, 2012), adopting physical parameters as for CS31082-001 (Cayrel et al. 2001; Hill et al. 2002) including $[\text{Fe}/\text{H}]=-2.9$ . <i>Grey:</i> Synthetic spectrum of the same star, but now N-rich ( $\Delta[\text{N}/\text{H}]=+2.0\text{dex}$ ). . . . .	166
8.3	Example section of metal-poor ( $[\text{Fe}/\text{H}]=-3.0$ ) giant spectrum at $R=20000$ , prior to introduction of noise. . . . .	167
8.4	Simulated giant spectra ( $[\text{Fe}/\text{H}]= -3.0$ ) for example diagnostic lines, $\text{GeI } \lambda 3039.07$ , $\text{CoI } \lambda 3529.03$ , $\text{NiI } \lambda 3597.71$ , $\text{YII } \lambda 3600.74$ at $R = 20000$ and $40000$ (with $\text{S}/\text{N}=100$ ). Abundance variations of $-0.5$ , $0.0$ , $+0.5$ and $+1.0\text{dex}$ (in $[\text{X}/\text{H}]$ ) for the elements in Table C.1 are shown in purple, black, blue and grey, respectively. . . . .	168
8.5	Illustrative comparison of $\text{BeII}$ (upper panel) and $\text{CoI } \lambda 3412$ (lower panel) diagnostic lines at $R=10000$ and $20000$ (at $\text{S}/\text{N}=100$ , for the $[\text{Fe}/\text{H}]=-3.0$ giant model). Abundance variations of $-0.5$ , $0.0$ , $+0.5$ and $+1.0\text{dex}$ (in $[\text{X}/\text{H}]$ ) for the elements in Table C.1 are shown in purple, black, blue and grey, respectively. . . . .	171

8.6	Equivalent widths of Ge I 3039 Å (upper panels) and Hf II 3400 Å (lower panels) for an input stellar model in the left-hand panels. The centre and right-hand panels show the output spectra from the end-to-end (E2E) simulator for $U = 16$ mag. for 30 and 240 min, respectively. Differences between the measured width from the simulations compared to the models are given by $\Delta EW$ . The regions considered for the estimates are shown in grey. . . . .	173
8.7	Abundance uncertainties ( $\Delta A$ ) compared to the input values for the $U_{E2E} = 16$ mag. CS31082-001 simulations. <i>Left:</i> Ge I 3039 Å, <i>Right:</i> Hf II 3400. . . . .	176
8.8	Abundance uncertainties ( $\Delta A$ ) compared to the input values for the $U_{E2E} = 18$ mag. CS31082-001 simulations for Hf II 3400. . . . .	176
8.9	Simulated 2 hr CUBES spectrum of CS 31082-001 (with $U_{E2E} \sim 16$ mag.) for the Ge I 3039 Å region. The reference model ( $A(\text{Ge}) = +0.10$ ) is plotted in black, with the best fit model ( $A(\text{Ge}) = +0.1$ ) in red. The red shaded area indicates $\pm 0.1$ dex in Ge abundance. . . . .	177
8.10	Simulated 2 hr CUBES spectrum of CS 31082-001 (with $U_{E2E} = 16$ mag.) for the Hf II 3400 Å region. The reference model ( $A(\text{Hf}) = -0.30$ ) is plotted in black, with the best fit model ( $A(\text{Hf}) = -0.25$ ) in red. The red shaded area indicates $\pm 0.1$ dex in Hf abundance. . . . .	178
8.11	Simulated 2 hr CUBES spectrum of CS 31082-001 (with $U_{E2E} = 16$ mag.) for the Hf II 3719 Å region. The reference model ( $A(\text{Hf}) = -0.30$ ) is plotted in black, with the best fit model ( $A(\text{Hf}) = -0.19$ ) in red. The red shaded area indicates $\pm 0.1$ dex in Hf abundance. . . . .	178
8.12	Simulated 4 hr CUBES observation of the Bi I 3024.64 Å line for $U_{E2E} = 16$ mag. and models with $A(\text{Bi}) = -0.6, -0.2,$ and $0.0$ . The pink shaded regions are to highlight the differences between the models (where both abundance and S/N contribute). . . . .	179
8.13	<i>Upper panel:</i> Model spectra in the region of U II 3859.57 Å for $U_{E2E} = 16$ mag. and with $A(\text{U})$ as indicated in the legend. The spectra have been convolved to $R = 22,000$ but are left oversampled to better highlight the other contributing lines. <i>Lower panel:</i> Simulated 4 hr CUBES observation of the same region. As in Fig. 8.12, the shaded regions highlight the differences between the models. . . . .	179

8.14	Simulated RGB spectra with diferent magnitudes in I band showing the impact in S/N in a MOSAIC observation. . . . .	184
8.15	Simulated main-sequence-turn-off spectra with diferent magnitudes in I band showing the impact in S/N in a MOSAIC observation. . . . .	184
8.16	Simulated RGB spectra with diferent magnitudes in H band showing the impact in S/N in a MOSAIC observation. . . . .	185
8.17	Cramér-Rao Lower Bound for the two considered designs for MOSAIC, Baseline in yellow and Blue-extension in blue showing the precision in the determination of the stellar parameters and elemental abundances. . . . .	186
8.18	The Cramér-Rao Lower Bound for the bands in the blue extension (columns 1-3), the bands in the baseline (columns 4 and 5), and in the columns 6 and 7 the whole wavelength coverage of the two designs. The colour bar represented the spectated precision in elemental abundances for each element found in each band for the same S/N ratio of 50. . . . .	188
8.19	MOONlight code diagram. . . . .	189
8.20	XSWITCH Mode. . . . .	190
8.21	Fitting factor of STARE and XSWITCH modes. . . . .	192
8.22	Example of a fiber set in a GC case. . . . .	193
8.23	Fitting factor over Kingsmodel (c factor). . . . .	194
8.24	Fitting factor over number of targets in the catalogue, the size of the dots is the core radius. . . . .	195
8.25	Fitting factor over radius of the core, the size of the dots is the number of targets ind the catalogue. . . . .	196
8.26	Fitting factor over half light radius, the size of the dots is the core radius. . . . .	197
8.27	Fitting factor over number of targets in the catalogue, running multiples times and removing the targets that have already been obtained for NGC6401. . . . .	198
B.1	CoI 5212.537, 5280.629 Å fitted to the Sun, Arcturus, and $\mu$ Leo. . . . .	229
B.2	Co I 5301.039, 5342.695 Å fitted to the Sun, Arcturus, and $\mu$ Leo. . . . .	229
B.3	Co I 5454.572, 5647.234 Å fitted to the Sun, Arcturus, and $\mu$ Leo. . . . .	229
B.4	Co I 6117.0, 6188.996 Å fitted to the Sun, Arcturus, and $\mu$ Leo. . . . .	229

B.5	Copper lines Cu I 5105.537 and 5218.197 Å, as fitted to the Sun, Arcturus, and $\mu$ Leo. . . . .	231
E.1	Arcturus: Fits to the six selected lines of Co I. . . . .	249
E.2	Arcturus: Fits to Cu I 3247.537 and 3273.954 Å lines. . . . .	250
E.3	Best-fit abundances for the Sc II lines computed with $[\text{Sc}/\text{Fe}] = +0.03$ for the Sc II 3576.34 Å line and $[\text{Sc}/\text{Fe}] = +0.52$ for the Sc II 3590.47 Å line (without hyperfine structure). . . . .	250
E.4	Best-fit abundances for the Ti I lines, computed with $[\text{Ti}/\text{Fe}] = +0.35$ , whereas for the Ti I 3998.64 Å line a best fit is found for $[\text{Ti}/\text{Fe}] = +0.02$ . . . .	251
E.5	Best-fit abundance for the Ti II lines, computed with $[\text{Ti}/\text{Fe}] = +0.35$ . . . .	251
E.6	Best-fit abundance for the Mn II lines, computed with $[\text{Mn}/\text{Fe}] = -0.39$ (without hyperfine structure). . . . .	252
E.7	Best-fit abundance for the Co I lines, computed with $[\text{Co}/\text{Fe}] = +0.19$ (including hyperfine structure). . . . .	252
E.8	Best-fit abundance for the Ni I lines, computed with $[\text{Ni}/\text{Fe}] = +0.05$ . . . .	253
E.9	Best-fit abundance for the Zn I lines, computed with $[\text{Zn}/\text{Fe}] = +0.22$ . . . .	253

# List of Tables

2.1	Log of spectroscopic observations of globular clusters, 47 Tucanae, NGC 6553, NGC 6528, HP 1, and NGC 6558. . . . .	45
2.2	MUSE observation log. . . . .	47
2.3	2 . . . . .	51
2.4	Adopted abundances for the Sun, Arcturus, and $\mu$ Leo. References: [1]: Grevesse et al. (1996); Grevesse & Sauval (1998); Asplund et al. (2009); Lodders (2009); [2]: Allende Prieto et al. (2001); [3]: Ramírez & Allende Prieto (2011); [4]: Meléndez et al. (2003) [5]: Ernandes et al. 2018; [6]: Barbuy et al. (2015); Friaça & Barbuy (2017); [7]: Fulbright et al. (2007); [8]: Smith et al. (2013); [9]: Gratton & Sneden (1990); [10]: Steffen et al. (2015); [11]: Lecureur et al. (2007); [12]: Barbuy et al. (2014); [13]: Smith & Ruck (2000); [14]: Scott et al. (2015a,b); [15]: McWilliam et al. (2013).	52
3.1	Reddening and distance moduli adopted. References: 1 Harris (1996); 2 Zoccali et al. (2001a); 3 Zoccali et al. (2004); 4 Barbuy et al. (1998); 5 Guarnieri et al. (1998); 6 Barbuy et al. (2006); 7 Ortolani et al. (2007, 2011); 8 Barbuy et al. (2009); 9 Terndrup (1988); 10 Rossi et al. (2015). .	59
3.2	Central wavelengths from NIST or Kurucz line lists and total oscillator strengths from line lists by Kurucz, NIST and VALD, literature, and adopted values. In column 7, literature oscillator strength values are from the following references: 1 Ramírez & Allende Prieto 2011; 2 Lawler et al. (2014).	60
3.3	Atmospheric parameters adopted. . . . .	61

3.4	Sensitivity of abundances to changes of $\Delta T_{\text{eff}} = 100$ K, $\Delta \log g = +0.20$ , and $\Delta v_t = 0.20$ km s <sup>-1</sup> . Error estimation usually take into account only these three stellar parameters, $[X/\text{Fe}]_{sp}$ , as given in column (5). The error in $\Delta[\text{Fe}/\text{H}] = 0.1$ dex is added in the last column, warning that this is an overestimation. . . . .	66
3.5	Line-by-line abundance ratios of Sc, V, Mn, Cu, and Zn for the sample. . .	77
3.6	Mean abundances of Sc, V, Mn, Cu, and Zn for the sample. . . . .	78
4.1	Central wavelengths and total oscillator strengths. . . . .	86
4.2	LTE abundances of Co and Cu derived in the present work. . . . .	88
4.3	Atmospheric parameters and radial velocities adopted from Zoccali et al. (2006) and Lecureur et al. (2007), and resulting Co and Cu abundances. .	89
4.4	Abundance uncertainties for the metal-rich star B6-f8 and the metal-poor star BW-f8 for uncertainties of $\Delta T_{\text{eff}} = 100$ K, $\Delta \log g = 0.2$ , and $\Delta v_t = 0.2$ km s <sup>-1</sup> , and corresponding total error. The errors are to be added to reach the reported abundances. . . . .	91
4.5	Comparison of stellar parameters and Co and Cu abundances of the present work with Johnson et al. (2014) and Lomaeva et al. (2019). . . . .	97
5.1	Terzan 9: data from literature. References: (1) Rossi et al. (2015), (2) Bica et al. (2006), (3) Ortolani et al. (1999), (4) Harris (1996, 2010 Edition). . .	100
5.2	Comparison of radial velocity and metallicity for two stars in common with Vásquez et al. (2018, V+18). The metallicity from V+18 adopts the metallicity scale by Dias et al. (2016). . . . .	106
6.1	2 . . . . .	123
6.2	3 . . . . .	127
6.3	4 . . . . .	127
7.1	Stellar parameters adopted for CS 31082-001 (Hill et al. 2002), HD 122563 (Cayrel et al. 2004), and the reference star Arcturus (Meléndez et al. 2003).	139
7.2	Published light-element abundances for CS 31082-001. Refs: 1) Hill et al. (2002); 2) Cayrel et al. (2004); 3) Spite et al. (2005); 4) NLTE calculations from Spite et al. (2011), 5) present work. . . . .	140

7.3	Published heavy-element abundances for CS 31082-001. Refs: 1) Hill et al. (2002); 2) Plez et al. (2004); 3) Barbuy et al. (2011); 4) Siqueira-Mello et al. (2013). . . . .	141
7.4	List of near-UV absorption lines considered. Refs: 1) Wood et al. (2014); 2) Den Hartog et al. (2011); 3) Li et al. (1999); 4) Lawler et al. (2013); 5) VALD3; 6) Ou et al. (2020). Adopted log gf values are indicated in bold face. . . . .	145
7.5	Comparison of our derived abundances with results from Hill et al. (2002). Solar abundances are from Grevesse & Sauval (1998). . . . .	147
8.1	Summary of models used to investigate the diagnostic lines. . . . .	166
8.2	Differential equivalent widths ( $\Delta EW$ ) for simulated CUBES observations of the Ge I 3039.07 Å and Hf II 3399.79, 3719.28 Å lines compared to the published values for CS 31082-001 (used here as the input model abundances).	172
8.3	Predicted continuum signal-to-noise (S/N) per pixel from the end-to-end (E2E) CUBES simulations near the Ge I 3039 Å line and the redder Hf II line (3719 Å). The adopted magnitudes for the E2E simulations were $U_{E2E} = 16$ and 18 mag. For simulations of CS 31082-001 these values are a good approximation to the real flux at 3730 Å, but given the use of continuum-normalised model spectra, the effective observed magnitudes ( $U_{\text{eff}}$ ) for the Ge I 3039 Å line are $\sim 1.75$ mag brighter (see Section 8.1.6.3 for discussion).	175
8.4	Number of our selected lines that are detectable for each ion in the CUBES wavelength range for both a G-type dwarf and a K-type giant with $[Fe/H] = -3.0$ and $[Fe/H] = -1.0$ with $R \sim 20\,000$ . Those flagged with an asterisk are ions for which no lines are feasible for quantitative analysis in our simulated spectra.	
	182	
8.5	Pristini’s spectral library models from Starkenburg et al. 2017. . . . .	184
8.6	Bulge globular clusters data from Bica et al. 2016. . . . .	191
A.1	Extracted stars from the MUSE datacubes with S/N selection. . . . .	221
A.1	continued. . . . .	222
A.1	continued. . . . .	223

A.1	continued. . . . .	224
A.2	Identified member stars from MUSE datacubes selected with S/N>85. Columns correspond to: ID from NTT 2012 data, coordinates (RA,DEC-J2000), proper motions from Gaia, NTT pixels x, y, NTT V, NTT V-I, and S/N. . . . .	225
A.3	Identified members stars from MUSE datacubes selected with S/N>85. Columns correspond to: ID and results from the present work: $v_r^h$ (km s <sup>-1</sup> ), T <sub>eff</sub> (K), log g, [Fe/H], [Mg/Fe], and [Fe/H] <sub>CaT</sub> . . . . .	226
B.1	NLTE corrections to the derived LTE abundances of Co. . . . .	228
B.2	Metallicity [Fe/H] and abundances of C, N, O, Na, Mg, Al, Mn, Co, Cu for the 56 sample red giants. . . . .	230
C.2	Line list of prominent lines in the wavelength region 15520-16000 Å, with species, their wavelengths, excitation potential (eV), and oscillator strengths from Meléndez & Barbuy (1999, MB99), APOGEE, and VALD. . . . .	233
C.2	continued. . . . .	234
C.2	continued. . . . .	235
C.2	continued. . . . .	236
C.2	continued. . . . .	237
C.2	continued. . . . .	238
C.1	List of near-UV absorption lines considered. . . . .	239
C.3	4 . . . . .	240
C.4	4 . . . . .	241

D.1	Atomic constants for ScI and ScII used to compute hyperfine structure: A and B constants from Mansour, N. B., Dinneen, T. P., Young, L. 1989, NIMPB, 40-252M , Villemoes et al. 1992, PhRvA, 45-6241V for ScII and Biehl (1976) for ScI. For VI the A and B constants are from 1 UBDE Unkel, P., Buch, P., Dembczynski, J., Ertmer, W.. and Johan, U. 1989, Z. Phys. D 11, 259-271. 2 CPGC Childs, W.J., Poulsen, O., Goodman, L.S., and Crosswhite, H. 1979, Phys. Rev. A 19, 168-176. 3 PBAG Palmeri, P., Biemont, E., Aboussaid, A., and Godefroid, M. 1995, J.Phys.B 28, 3741-3752. 4 CBFGB Cochrane, E.C.A., Benton, D.M., Foreset, D.H., and Griffith, J.A.R. 1998, J.Phys.B 31, 2203-2213. 5 LGB Lefebvre, P-H, Garnir, H-P, Biemont, E 2002, Physica Scripta 66, 363-366. B constants not available in the literature are assumed as null. . . . .	244
D.2	Atomic constants for CoI and CuI used to compute hyperfine structure: A and B constants from Pickering (1996) for CoI. For CuI, the A and B constants are from Kurucz (1993) and Biehl (1976), and they are reported in Ernandes et al. (2018). . . . .	244
D.3	Hyperfine constants A and B for Sc II (Villemoes et al. 1992; Kurucz, 1993); V II (Wood et al. 2014); Mn II (Den Hartog et al. 2011); Co I (Pickering 1996); Cu I (Biehl, 1976; Kurucz, 1993). For transitions where the electric quadrupole constants were not available we adopted the B-factor as zero. .	245
D.4	Calculated hyperfine structure for the Co I 3412.34, 3412.63, and 3449.16 Å lines. . . . .	245
D.5	Calculated hyperfine structure for the Co I 3529.03, 3842.05, and 3845.47 Å lines. . . . .	246
D.6	Hyperfine structure for CoI lines. . . . .	246
D.7	Hyperfine structure for CoI lines. . . . .	247
D.8	Hyperfine structure for CoI lines. . . . .	247
D.9	Calculated hyperfine structure for the Cu I 3247.53 and 3273.95 Å lines. . .	248
D.10	Hyperfine structure for CuI lines. . . . .	248



# Contents

1. <i>Introduction</i> . . . . .	37
1.1 Galactic Archaeology . . . . .	37
2. <i>Spectroscopic Data</i> . . . . .	43
2.1 FLAMES-UVES . . . . .	44
2.1.1 Iron-peak elements Sc, V, Mn, Cu and Zn in bulge globular clusters	44
2.1.2 Iron-peak elements Co and Cu in bulge field stars . . . . .	44
2.1.3 CS 31082-001, Near-UV spectroscopy . . . . .	46
2.2 MUSE . . . . .	47
2.2.1 Terzan 9 data . . . . .	47
2.2.2 Datacube combination . . . . .	49
2.3 Infrared spectroscopy . . . . .	50
2.3.1 AL3 observations . . . . .	50
2.4 Adopted solar abundances . . . . .	51
3. <i>Iron-peak elements in bulge globular clusters</i> . . . . .	53
3.1 Introduction: Iron-peak elements . . . . .	53
3.2 Line parameters: Hyperfine structure, oscillator strengths . . . . .	55
3.2.1 Scandium and vanadium . . . . .	56
3.2.2 Copper . . . . .	56
3.2.3 Manganese and zinc . . . . .	58
3.3 Abundance analysis . . . . .	58
3.3.1 Atmospheric parameters and abundance derivation . . . . .	58
3.3.2 Uncertainties . . . . .	60

3.4	Results and discussion . . . . .	66
3.4.1	Scandium, vanadium and manganese . . . . .	67
3.4.2	Copper . . . . .	70
3.4.3	Zinc . . . . .	72
3.5	Summary . . . . .	78
4.	<i>Cobalt and Copper in bulge field stars</i> . . . . .	81
4.1	Introduction: Iron-peak elements Cobalt and Copper in bulge field stars . .	81
4.2	Abundance analysis . . . . .	84
4.2.1	Line parameters: hyperfine structure, oscillator strengths . . . . .	84
4.2.2	Non-local thermodynamic equilibrium corrections . . . . .	85
4.2.3	Uncertainties . . . . .	86
4.3	Chemical evolution models . . . . .	87
4.4	Discussion of results . . . . .	92
4.4.1	Comments on results for cobalt . . . . .	94
4.4.2	Comments on results for copper . . . . .	95
4.5	Summary of Co and Cu abundances in the bulge . . . . .	95
5.	<i>The faint old bulge globular cluster Terzan 9</i> . . . . .	99
5.1	Introduction: Terzan 9 . . . . .	99
5.1.1	Extraction of Stellar Spectra . . . . .	102
5.2	Analysis . . . . .	103
5.2.1	Sample extraction and radial velocities . . . . .	105
5.2.2	Coordinates and proper motions . . . . .	106
5.2.3	Stellar parameters . . . . .	108
5.2.4	Uncertainties . . . . .	110
5.2.5	Metallicities from CaT . . . . .	111
5.2.6	Color-magnitude diagrams of member stars . . . . .	113
5.3	Discussion . . . . .	114
5.4	Summary of Terzan 9 . . . . .	116
6.	<i>The globular cluster AL 3</i> . . . . .	119
6.1	Introduction: Globular cluster AL 3 . . . . .	119

6.2	The spectra of the AL 3 observed stars . . . . .	120
6.3	Spectroscopy in the H-band: atomic and molecular lines . . . . .	120
6.4	Gaia cross-check . . . . .	122
6.5	Radial velocity of AL 3 . . . . .	123
6.6	Stellar parameters . . . . .	125
6.6.1	NGC 6558 and HP 1 . . . . .	125
6.6.2	AL 3 . . . . .	125
6.7	CNO abundances . . . . .	126
6.7.1	The cool red giant N6558-42 . . . . .	130
6.7.2	AL-3 and HP 1 . . . . .	132
6.7.3	Uncertainties . . . . .	132
6.8	Summary of AL 3 . . . . .	134
7.	<i>Near-UV study of the halo star CS 31082-001</i> . . . . .	137
7.1	Introduction of the metal-poor halo star CS 31082-001 . . . . .	137
7.2	The halo star CS 31082-001 . . . . .	139
7.3	Beryllium abundance in CS 31082-001 . . . . .	140
7.4	Iron-peak elements in CS-31082-001 . . . . .	143
7.4.0.1	Hyperfine structure . . . . .	144
7.4.0.2	Non-LTE abundance corrections . . . . .	146
7.4.1	Abundances: Sc, Ti, Cr, Mn, Co, Ni and Zn . . . . .	146
7.4.2	Abundances: V and Cu . . . . .	147
7.5	Chemical evolution models . . . . .	150
7.5.1	Abundances and chemical-evolution models for V . . . . .	151
7.5.2	Abundances and chemical evolution models for Cu . . . . .	152
7.5.3	Abundances: Summary . . . . .	155
7.6	Summary of CS 31082-001 . . . . .	157
8.	<i>Simulations on upcoming instruments</i> . . . . .	159
8.1	The CUBES spectrograph . . . . .	159
8.1.1	Introduction . . . . .	159
8.1.2	Science motivation: stellar nucleosynthesis . . . . .	160
8.1.2.1	Beryllium . . . . .	162

8.1.2.2	Iron-peak elements . . . . .	163
8.1.2.3	Heavy elements . . . . .	163
8.1.2.4	CNO abundances . . . . .	164
8.1.3	Spectral Analysis . . . . .	165
8.1.3.1	Simulated spectra . . . . .	165
8.1.4	Quantitative analysis . . . . .	167
8.1.5	Abundance estimates . . . . .	169
8.1.6	Results . . . . .	170
8.1.6.1	Performance comparison . . . . .	170
8.1.6.2	Expected uncertainties on measured equivalent widths . . . . .	171
8.1.6.3	Results: Ge & Hf . . . . .	172
8.1.6.4	Results: Bi & U . . . . .	175
8.1.7	Summary of CUBES analysis . . . . .	177
8.2	MOSAIC . . . . .	181
8.2.1	COMPASS . . . . .	183
8.2.2	Stellar spectral library . . . . .	183
8.2.3	Chemcalc . . . . .	183
8.2.4	Summary of MOSAIC analysis . . . . .	187
8.3	Observations of bulge globular cluster stars with MOONS . . . . .	187
8.3.1	MOONlight code . . . . .	189
8.3.1.1	STARE . . . . .	189
8.3.1.2	XSWITCH . . . . .	190
8.3.2	Catalogues . . . . .	190
8.3.3	Results of the simulations . . . . .	190
9.	<i>Conclusions</i> . . . . .	199
9.1	Galactic bulge and Iron-peak elements . . . . .	199
9.2	Globular Clusters . . . . .	200
9.3	The halo star CS 31082-001 . . . . .	200
9.4	Upcoming instruments . . . . .	200
9.4.1	MOSAIC . . . . .	200
9.4.2	CUBES . . . . .	201

9.4.3	MOONS . . . . .	201
9.5	Perspectives . . . . .	201
<i>Bibliography</i> . . . . .		203
 <i>Appendix</i>		219
A.	<i>MUSE datacubes and selections</i> . . . . .	221
A.1	Extracted stars from the MUSE datacubes with S/N selection. . . . .	221
A.2	Extracted stars from the MUSE datacubes . . . . .	224
B.	<i>Abundances</i> . . . . .	227
B.1	NLTE corrections to cobalt abundances . . . . .	227
B.2	Fits of studied lines to the spectra of the Sun, Arcturus, and $\mu$ Leo . . . . .	227
B.3	Abundances of C, N, O, Na, Mg, Al, Mn, Co, and Cu for the 56 sampled red giants . . . . .	227
C.	<i>Line lists</i> . . . . .	233
C.0.1	Near-UV line list . . . . .	233
C.0.2	Near-Infrared line list . . . . .	233
C.1	Molecular line lists: CO, OH and CN . . . . .	238
D.	<i>Atomic data</i> . . . . .	243
D.1	Hyperfine structure constants . . . . .	243
E.	<i>Line fits to Arcturus and CS 31082-001</i> . . . . .	249



## Introduction

### *1.1 Galactic Archaeology*

The formation and evolution of our Galaxy and galaxies in general is under debate in the literature. How galaxies are formed in cosmological context? How a galaxy evolves, physically and chemically? Most of our understanding in the formation of the Milky Way (MW) are from stellar population observations regarding their chemical abundances. The extended research on stellar nucleosynthesis models help us to interpret those chemical abundances in a galactic archaeology sense.

In order to better understand these topics we study some of the oldest objects in the MW. In this work we analysed field and globular cluster stars in the Galactic bulge, and a metal-poor halo star in terms of their chemical characteristics. These objects carry imprinted in their atmospheres the elements synthesised in stars and supernovae explosions in the early Galaxy.

To better understand the observed chemical abundances in stars, the elements were grouped according to their main nucleosynthesis channel. The Big Bang nucleosynthesis produced the H, He, Li, and Be. However the He, Li, and Be are also produced in main-sequence stars during the proton-proton chain. While the He endures and is further produced in the p-p chain, the Li and Be are consumed in the process, depleting their observed abundances.

The  $\alpha$ -elements are synthesised using He as a the seed used to create elements heavier than carbon, which is produced by the triple-alpha process.

The iron is a key element to interpret the enrichment in the Galaxy because the [Fe/H] ratio is used as a timescale of the chemical evolution in the Galaxy. This is mostly due

to atomic reasons, i.e. Fe has a large number of spectral lines. In general, the plot of  $[\alpha\text{-element}/\text{Fe}]$  versus  $[\text{Fe}/\text{H}]$  indicates the time delay between the supernovae type Ia (SNe Ia) and type II (SNe II). The iron is mainly produced by SN Ia and the oxygen is produced in SNe II. The turnover when Fe starts to be produced by SNIa indicates therefore the star formation rate in a stellar population.

The iron-peak elements ( $21 \leq Z \leq 30$ ) are synthesised through many nucleosynthesis channels. The lower iron-group Sc, Ti, V, Cr, Mn and Fe they are synthesised during the explosive oxygen burning and in explosive Si burning (Umeda & Nomoto 2002). While the upper iron-group Co, Ni, Cu, Zn, Ga, and Ge are synthesised mostly by two processes, neutron capture in weak s-component and the  $\alpha$ -rich freezeout during the complete Si burning (Umeda & Nomoto 2002). This characteristic of the iron-peak element abundances can be used to distinguish the astrophysical site and process that created each of them. It helps evaluating which is the predominant process or event that enriched the analysed stellar population in these elements.

The  $\alpha$ -freezeout mechanism occurs in core-collapse SNe when the shock wave passes through the Si shell making the nuclei within this shell to heat reaching the point of breaking into alpha particles and nucleons that further recombine forming heavier elements (Woosley & Weaver 1995). The weak s-process on the other hand occurs in massive stars where the  $^{22}\text{Ne}(\alpha, n)^{25}\text{Mg}$  reaction injects neutrons triggering this process at the border of the convective He-burning core and the convective C-burning shell (Pignatari et al. 2010).

The  $\alpha$ -elements and iron-peak elements show their spectral lines in near-UV, visible and infrared. The elements beyond the  $Z=30$  have most of their diagnostic lines within the UV wavelength range (Snedden et al. 2003).

The heavy elements are synthesised through neutron-capture nucleosynthesis by two mechanisms, the r-process and s-process. The slow neutron capture (s-process) occurs when the timescale of neutron capture is much lower than that for  $\beta$ -decay. Consequently there are abundance peaks for the isotopes that have the magical number of neutrons. It is due the  $\beta$ -decay stability for those isotopes. The s-process requires less energy than the r-process, making it viable to occur inside AGB stars (weak s-process). The rapid neutron capture (r-process) takes place when the neutron-capture is faster than the  $\beta$ -decay, and for this reason it is present in explosive astrophysical sites.

As described in Watson et al (2019), a neutron-star merger (kilonova) produce r-process

elements as well as in magnetohydrodynamically-driven jets from core-collapse SNe (Nishimura, Takiwaki & Thielemann, 2015). Identify the sites and processes that create certain r-process elements are an important aim in current astrophysics. The Pb, Th, Bi and U abundances can be very useful for tracing the time of their formation, since they are radioactive elements. These elements have formed by the same r-process mechanism but Pb and Bi decay directly from U and Th. For this reason the ratios U/Bi and U/Th are good cosmochronometers. The clear difference between the astrophysical sites where the two neutron-capture mechanisms take place is useful to distinguish which process enriched the environment in the early Galaxy.

To better study the formation of the Galaxy in terms of chemical abundances, including most of the elements, it can be useful to cover the stellar spectrum from ultra-violet, visible, to the near-infrared.

The Galactic bulge can be a useful region to study and develop galactic archaeology in the MW. The stellar populations within the Galactic bulge can inform about its complex formation and appraise the many possible formation scenarios.

It was confirmed that this region is formed by a relatively metal-poor spheroidal that contributed with half of the stellar mass in the bulge (Zoccali et al. 2018) and a metal-rich bar along with debris from past accretion events. The metal-poor component is alpha enhanced suggesting that this stellar population was formed during a higher star formation rate when compared with the thick disc (Queiroz et al. 2021). This fact associated with old metal-poor globular clusters in the bulge as HP 1, AL 3, and Terzan 9 suggests a formation scenario based on violent mergers of substructures, compatible with the cosmological  $\Lambda$ CDM model. However simulations are also able to mimic this behavior through a secular formation scenario (Fragkoudi et al. 2018).

A concentration of globular clusters with  $[\text{Fe}/\text{H}] \sim -1.0$  in the Galactic bulge was identified by Rossi et al. (2015). A density peak in bulge globular cluster distribution in  $[\text{Fe}/\text{H}] \sim -1.0$  was further confirmed in Bica et al. (2016) and Pérez-Villegas et al. (2020). Some of these clusters with a blue horizontal branch should be very old objects. These objects, located within 3 kpc from the Galactic center are probably formed in situ, suggesting that they are relics in the Galaxy, and therefore bulge studies sites that inform on the early Galaxy formation.

Therefore the Galactic bulge is under intense discussion as concerns its origin and stellar

populations. To discriminate these stellar populations and their nucleosynthesis processes the chemical tagging are the key aspect that help us understanding the bulge formation and evolution.

In this thesis we carry out analyses of spectra of individual red giants in the field and in globular clusters of the Galactic bulge associated with iron-peak element abundances; We characterise two bulge globular clusters, Terzan 9 and AL 3; We analysed the iron-peak elements in the halo star CS 31082-001.

- Iron-peak element abundances in UVES high-resolution spectra of 28 red giants in the disk reference cluster 47 Tucanae and the bulge globular clusters NGC 6528, NGC 6553, NGC 6522, NGC 6558, and HP 1, resulting in a paper on the iron-peak elements Sc, V, Mn, Cu, and Zn in these clusters (Ernandes et al. 2018) (Chapter 3).
- The following work consisted in the analysis of the iron-peak elements Cobalt and Copper in bulge field stars, also using UVES spectra of resolution  $R = 45,000$  of 56 red giants of the Galactic bulge, observed in Zoccali et al. (2006) and Hill et al. (2011). These stars were already analysed for O, Mg (Lecureur et al. 2007), Mn (Barbuy et al. 2013), and Zn (Barbuy et al. 2015) (see Chapter 4).
- The analysis of mid-resolution spectra of faint globular cluster stars using the instrument MUSE at the Very Large Telescope (VLT) is presented in Chapter 5. MUSE@VLT data on the bulge globular cluster Terzan 9 were obtained by our group in 2016. The data reductions were carried out in collaboration with Sebastian Kamman (John Moores university) and Bruno Dias (Universidad de Tarapacá).
- Using the Near-infrared spectroscopy obtained with Gemini-Phoenix we analysed the AL 3 Globular cluster. This cluster was previously characterised in Ortolani et al. 2006 as an old bulge globular cluster, using photometry.
- The near-UV analyse of the metal-poor halo star CS 31082-001 was motivated by the necessity of comparison between the iron-peak element abundances derivation from optical lines and near-UV lines since Lawler et al. 2013 observed a discrepancy between the Ti I abundances derived in the near-UV line and the lines above  $3700\text{\AA}$ . It led us to derive abundances for Be, V, and Cu that was not derived in the previous

work for this star. Giving us the opportunity to build chemical-evolutionary models for V and Cu with neutrino process and hypernovae, respectively.

Related to the main topic we carry out studies of upcoming instruments CUBES-VLT, MOONS-VLT, and MOSAIC-ELT under the optics of the Galactic archaeology studies (see Chapter 8).

CUBES-VLT is focused on achieving high efficiency in the ground-UV, observing in the 300nm-400nm window with mid-resolution. This new instrument will provide more efficient observations of metal-poor stars characterising their CNO abundances using CN, NH, and OH features in the UV and measuring abundances of key elements as Be and heavy elements as described in (Ernandes et al. 2020b). In Ernandes et al. 2022a and Ernandes et al. 2022b in preparation we used the halo star CS31082-001 as model to develop and test a line list in the ground-UV.

MOSAIC is a multi-object spectrograph with MOSAIC that will observe in the visible and near-infrared. In the present work we evaluated the High multiplex mode, HMM-VIS and HMM-NIR. With these modes it is possible to observe beyond the current limits of observations, for example, the spectra of dwarf stars of the Galactic bulge.

The Multi-Object and Near-IR Spectrograph (MOONS) is a near-infrared spectrograph with a Field of View of 25 arcmin of diameter, covering the wavelength range of 0.65 to 1.80  $\mu\text{m}$ . The outstanding aspect of MOONS is the high multiplex. It will be capable to allocate  $\sim 1000$  fibers to objects and sky targets. In this work we tested its performance simulating bulge globular clusters observations.

As a more general objective, we intend to get prepared for the efficient use of data from the gigantic telescopes, in particular the E-ELT. Spectroscopy of stars in dense fields, in particular in globular clusters and Galactic bulge field, requires knowledge of techniques such as astrometric precision of coordinates, use of software to prepare the observations, comparison of old charts with new images with different scales, as well as techniques and knowledge on data acquiring and reduction on multi-object spectroscopy with other instruments now and in the future. In the next chapters follow more detailed descriptions of the present work.



## Spectroscopic Data

We use near-UV, optical, and near-infrared data, from different instruments and telescopes to develop the analysis in this work. In the near-UV and optical we had access to data from UVES (Ultraviolet and Visual Echelle Spectrograph) in single mode and FLAMES-UVES mode. This spectrograph is installed at the 8.2m Kueyen Very Large Telescope(VLT) (UT2): these data include high resolution ( $R\sim 45,000$ ) spectra collected with the UVES spectrograph, and mid/high-resolution ( $R\sim 22,000$ ) spectra collected with the GIRAFFE spectrograph. We also had access to data from the MUSE spectrograph at the 8.2m Yepun VLT (UT4), to gather mid-resolution spectra ( $R\sim 4,000$ ) of fainter stars in the globular cluster Terzan 9.

In the near-infrared we had access to spectra of red giant stars of the bulge globular clusters NGC 6558, AL 3, and HP 1, observed with the Phoenix spectrograph installed on the 8m Gemini-South telescope. The program was tri-national from Brazil (PI: B. Barbuy), Chile (PI: M. Zoccali) and Australia (PI: J. Meléndez). The suitable spectral data includes three stars of AL 3, two stars of NGC 6558, and one star of HP 1, centered at  $1.555\ \mu\text{m}$  in the H band. Another 3 stars in NGC 6558, and 3 stars in HP 1 were also observed.

Also in the near-infrared (NIR) we selected spectra taken with high resolution spectra with the APOGEE/SDSS data. These data are collected at the APOGEE North (N) 2.5m Sloan Foundation Telescope at Apache Point Observatory; and APOGEE South (S), 2.5m du Pont Telescope at Las Campanas Observatory. Discussion of the paper "Abundance analysis of 58 APOGEE spectra of metal-poor bulge stars" by Roberta Razera, Beatriz Barbuy et al. (2022, submitted), is given in the master thesis of Roberta Razera. Therefore the target selection and abundance analysis of this work is not include in the present thesis.

## 2.1 FLAMES-UVES

The Ultraviolet and Visual Echelle Spectrograph (UVES) is a high-resolution optical spectrograph installed at Kueyen (UT2). It was designed to operate with high efficiency from the atmospheric cut-off at 3000 Å. The light beam from the telescope is split in two arms, The Blue- and the Red-arm, the Blue-arm, UV to blue and the Red-arm, Visible to red. These two arms can be operated separately, or in parallel using a dichroic. The resolving power (R) is about 40,000 when a 1 arcsec slit is used. The maximum resolution is 80,000 or 110,000 in the Blue- and the Red Arm, respectively. UVES also could operate with Fibre Large Array Multi-Element Spectrograph (FLAMES).

### 2.1.1 Iron-peak elements Sc, V, Mn, Cu and Zn in bulge globular clusters

Ernandes et al. (2018) analysed iron-peak element abundances in 28 red giant stars, including five in the reference cluster 47 Tucanae (Alves-Brito et al. 2005), and 23 in 5 bulge globular clusters, with four in NGC 6553 (Alves-Brito et al. 2006), three in NGC 6528 (Zoccali et al. 2004), eight in HP 1 (Barbuy et al. 2006, 2016), four in NGC 6522 (Barbuy et al. 2009, 2014), and four in NGC 6558 (Barbuy et al. 2017). These stars were observed with UVES in the wavelength range of 4800-6800 Å. The red portion of the spectra (5800-6800 Å) was obtained with the ESO CCD # 20, an MIT backside illuminated, of 4096x2048 pixels, and pixel size 15x15µm. The blue portion of the spectra (4800-5800 Å) used ESO Marlene EEV CCD-44, backside illuminated, 4102x2048 pixels, and pixel size 15x15µm. With the UVES standard setup 580, the UVES resolution is  $R \sim 45\,000$  for a 1 arcsec slit width, while  $R \sim 55\,000$  for a slit of 0.8 arcsec. The pixel scale is 0.0147 Å/pix. The log of observations is given in Table 2.1.

Reductions are described in the references given above, in all cases including bias and inter-order background subtraction, flatfield correction, extraction, and wavelength calibration (Ballester et al. 2000).

### 2.1.2 Iron-peak elements Co and Cu in bulge field stars

The analysis of the Co and Cu in the Galactic bulge field stars included high-resolution spectra of 43 bulge red giants, chosen to have one magnitude brighter than the red clump, from ESO programmes 71.B-0617A and 73.B0074A (PI: A. Renzini) obtained with the

Table 2.1 - Log of spectroscopic observations of globular clusters, 47 Tucanae, NGC 6553, NGC 6528, HP 1, and NGC 6558.

Star	Slit width	(S/N)/px
47 Tucanae		
M8	0.8arcsec	280
M11	0.8arcsec	241
M12	0.8arcsec	247
M21	0.8arcsec	213
M25	0.8arcsec	258
NGC 6553		
II-64	0.8arcsec	110
II-85	0.8arcsec	200
III-8	0.8arcsec	170
267092	0.8arcsec	110
NGC 6528		
I-18	1.0arcsec	40
I-36	1.0arcsec	40
II-42	0.8arcsec	30
HP 1		
2	0.8arcsec	70
3	0.8arcsec	45
2115	0.8arcsec	> 200
2461	0.8arcsec	> 200
2939	0.8arcsec	> 200
3514	0.8arcsec	> 200
5037	0.8arcsec	> 200
5485	0.8arcsec	> 200
NGC 6522		
B-107	0.9arcsec	180
B-122	0.9arcsec	170
B-128	0.9arcsec	180
B-130	0.9arcsec	210
NGC 6558		
283	1.0arcsec	130
364	1.0arcsec	150
1072	1.0arcsec	190
1160	1.0arcsec	170

FLAMES-UVES spectrograph (Dekker et al. 2000) at the 8.2 m Kueyen Very Large Telescope at the Paranal Observatory of the European Southern Observatory (ESO). The stars were observed in four fields, namely Baade’s Window (BW) ( $l=1.14^\circ$ ,  $b=-4.2^\circ$ ), a field at  $b = -6^\circ$  ( $l=0.2^\circ$ ,  $b=-6^\circ$ ), the Blanco field ( $l=0^\circ$ ,  $b=-12^\circ$ ), and a field near NGC 6553 ( $l=5.2^\circ$ ,  $b=-3^\circ$ ). Thirteen additional red clump bulge giants were observed in programme GTO 71.B-0196 (PI: V. Hill), as described in Hill et al. (2011).

The mean wavelength coverage is 4800-6800 Å. With the UVES standard setup 580, the resolution is  $R \sim 45\,000$  for a 1 arcsec slit width, given that the fibres are 1.0'' wide. Typical signal-to-noise ratios obtained by considering average values at different wavelengths vary in the range  $30 \leq S/N \leq 280$  per pixel in the programme stars. Here the analysis is based uniquely on the UVES spectra, but it is noteworthy that the same sample of stars was also observed with the GIRAFFE spectrograph, as part of a larger sample (Zoccali et al. 2008), with the purpose of validating their abundance analysis at the lower resolution ( $R \sim 22,000$ ) of GIRAFFE.

As described in Zoccali et al. (2006), Lecureur et al. (2007), and Hill et al. (2011), the spectra were reduced using the FLAMES-UVES pipeline, including bias and inter-order background subtraction, flat-field correction, extraction, and wavelength calibration (Ballester et al. 2000).

### 2.1.3 CS 31082-001, Near-UV spectroscopy

In our new analysis of CS 31082-001, we use the mean combined spectrum of the three 1 hr exposures obtained by the First Stars programme (ID 165.N-0276, PI: Cayrel) on 2001 October 19-21, using the bluest setting of UVES (with a central wavelength of 346 nm). These observations were obtained with a relatively narrow slit of  $0''45$ , giving  $R \sim 77,000$  (see Hill et al. 2002), and are the same reduced data analysed by Siqueira-Mello et al. (2013).

The combined UVES data were the primary source spectrum used in our analysis, supported by comparisons with *HST* data. The latter were obtained with the E230M mode of STIS, giving  $R \sim 30,000$  over the 1575-3100 Å range, with a S/N of  $\sim 40$  from a 45-orbit programme (see Barbuy et al. 2011, Siqueira-Mello et al. 2013).

These observations used the blue ESO Marlene EEV CCD#44 chip, backside illuminated, of 4102 x 2048 pixels, and pixel size  $15 \times 15 \mu\text{m}$  was used. and  $R \sim 55\,000$  for a slit

Table 2.2 - MUSE observation log.

cube name	date	exp. time	airm. start	airm. end	seeing start	seeing end	relative humidity
WFM_Ter9_OB1 exp1	2016-05-28T06:37:58	948	1.003	1.01	0.51	0.51	17.5
WFM_Ter9_OB1 exp2	2016-05-28T06:55:37	948	1.011	1.023	0.56	0.62	17.5
WFM_Ter9_OB1 exp3	2016-05-28T07:13:16	948	1.024	1.041	0.57	0.80	15.0
WFM_Ter9_OB2 exp1	2016-05-28T07:39:44	948	1.053	1.078	0.72	0.53	17.0
WFM_Ter9_OB2 exp2	2016-05-28T07:57:35	948	1.08	1.112	0.53	0.59	17.0
WFM_Ter9_OB2 exp3	2016-05-28T08:15:43	948	1.115	1.155	0.59	0.87	15.5
WFM_Ter9_OB3 exp1	2016-06-05T06:58:55	948	1.041	1.063	1.01	0.89	35.0
WFM_Ter9_OB3 exp2	2016-06-05T07:16:45	948	1.065	1.093	0.97	0.91	35.0
WFM_Ter9_OB3 exp3	2016-06-05T07:34:40	948	1.095	1.131	0.95	0.86	35.0
WFM_Ter9_OB4 exp1	2016-06-09T03:35:40	948	1.116	1.083	0.77	0.63	4.5
WFM_Ter9_OB4 exp2	2016-06-09T03:53:47	948	1.081	1.055	0.63	0.72	4.0
WFM_Ter9_OB4 exp3	2016-06-09T04:12:05	948	1.053	1.033	0.73	0.67	4.0
WFM_Ter9_OB5 exp1	2016-06-11T02:20:22	948	1.332	1.263	0.74	0.70	16.0
WFM_Ter9_OB5 exp2	2016-06-11T02:38:13	948	1.259	1.201	0.70	0.71	16.0
WFM_Ter9_OB5 exp3	2016-06-11T02:56:06	948	1.198	1.151	0.71	0.76	16.0

of 0.8 arcsec. The pixel scale is  $0.0147 \text{ \AA}/\text{pix}$ , with  $\sim 7.5$  pixels per resolution element at  $6000 \text{ \AA}$ .

## 2.2 MUSE

### 2.2.1 Terzan 9 data

The observations of the Terzan 9 field were conducted with the The Multi Unit Spectroscopic Explorer (MUSE) with the Wide Field Mode (WFM), standard coverage (nominal mode WFM-NOAO-E). MUSE is an Integral Field Unit (IFU) instrument, installed at the 8.2m Yepun VLT (UT4). It gives a panoramic integral-field spectra in the visible wavelength range. Which a field of view of  $1.1 \times 1.1 \text{ arcmin}^2$  combined with an adaptive optics of VLT we have an excellent spatial resolution.

The WFM has a spatial resolution of 0.3 to 0.4 arcsec and simultaneously a large spectral range ( $4650\text{-}9300 \text{ \AA}$ ) with a resolving power of 2000 at  $4600 \text{ \AA}$ , and 4000 at  $9300 \text{ \AA}$  in the WFM mode.

The total observing time was 5 hours including overheads, that were distributed along 5 observation blocks with 3 exposures each (one in the central field and 2 offsets) of 948 seconds. Detailed information about each exposure is given in Table 2.2. A composed slice of the data cube is shown in fig. 2.1.

The input list of stars was created from a combination of the photometric observations of Ortolani et al. (1999) with the Danish telescope in 1998 and more recent observations with the NTT@ESO in 2012, see fig. 5.1. The absolute calibration of the NTT 2012 data has been performed using our previous 1998 Danish data (Ortolani et al. 1999). About

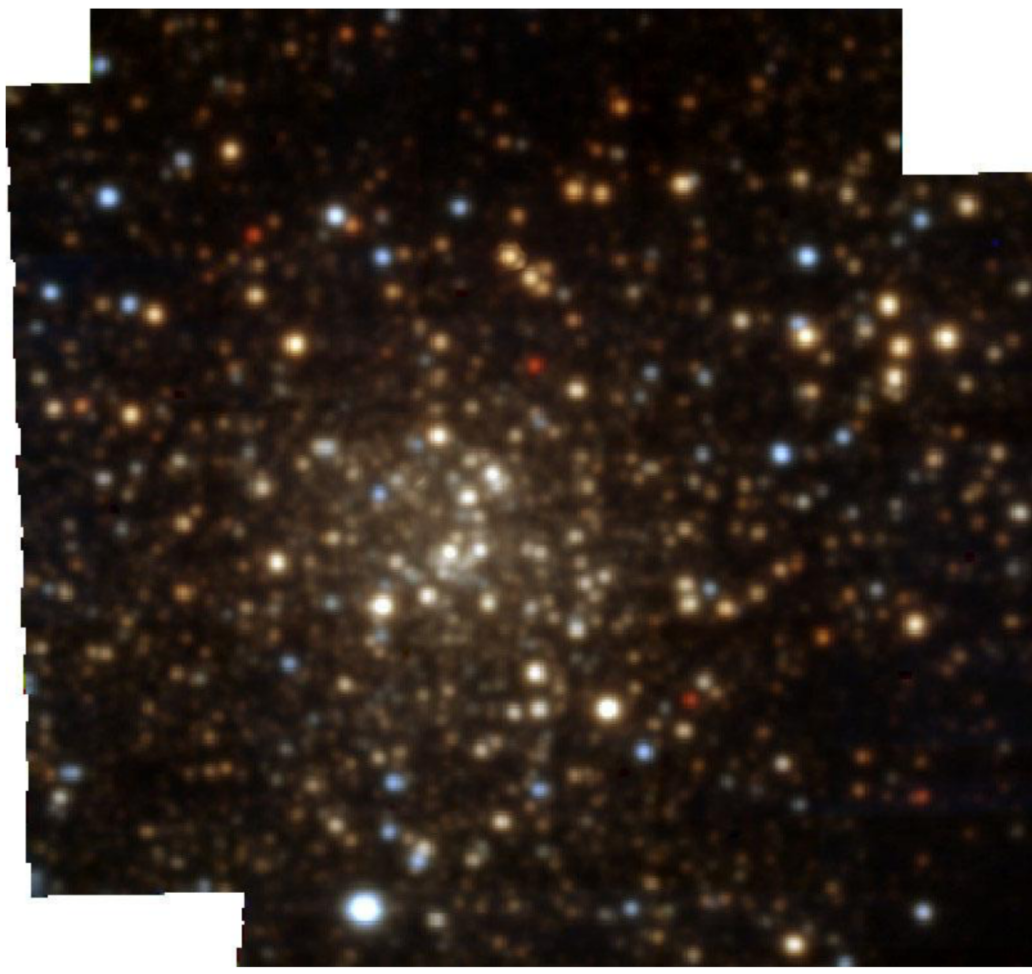


*Figure 2.1:* Terzan 9: composed image in B, V and R, from 5 different pointings of Terzan 9 obtained with MUSE on Yepun in 2016. Size is  $1.1 \times 1.1$  arcmin<sup>2</sup>, exposures with seeing from 0.51" to 1.01".

800 stars in common between the Danish 1998 data and NTT 2012 have been matched and checked in order to transform the instrumental NTT magnitudes into the calibrated ones. Two almost linear relations in magnitude and colors have been found, with a residual slope, in a range within 0.01 mag, possibly due to minor linearity deviations mostly at magnitudes brighter than  $V < 16$ . A simple offset has been applied then to the instrumental magnitudes and colors. The formal error of the transformation in V and V-I is of about 0.025 magnitudes for both. The photometric error is dominated by linearity deviations at faint magnitudes. The V and I data were calibrated with the following conversion coefficients:

$$V_{calibrated} = V_{NTT2012} + 6.798 \pm 0.015$$

$$(V - I)_{calibrated} = (V - I)_{NTT2012} + 1.77 \pm 0.02$$

These two sets of data were combined in Rossi et al. (2015) and used for proper-motion decontamination, making use of the 14 yr time difference between the 1998 and 2012 observations to have an optimized selection of member stars. We transformed the original data given in pixels in X,Y into right ascension and declination (RA,DEC) based on the NTT 2012 image. The final coordinates are established by matching stars in common with the Gaia Data Release 2 (Gaia Collaboration 2018). The list of stars with their coordinates, along with their V and V-I, are reported in Table A.2.

### 2.2.2 Datacube combination

The combination of the exposures was done by observation block (OB) using the most recent version (v2.1.1) of the MUSE instrument pipeline available only in the Gasgano environment, at the time. Gasgano's interface allows for a quick assignment of frames to specific recipes and easy parameter manipulation, together with a processing request pool, so it is convenient for doing tests and requesting different datasets. We combined the three exposures of each OB to end up with five final cubes. The combination of all OBs was not done in the same way because they were observed in different conditions. The final stellar spectra correspond to the combination of the extracted 1D spectra of each star from the five cubes.

During the combination, several tests were carried out. The most influential para-

meter was the resampling method in building the combined cube. The MUSE pipeline default method is "drizzle" and comparisons between this method, along with other complex methods "renka" and "lanczos," were performed. The renka method showed the best spatial resolution and image coverage among the three. We performed some tests with the renka resample method to find the critical radius  $cr$  value that optimizes the S/N of the extracted spectra, starting with the default value  $cr = 1.25$ . We noticed that the S/N increases for  $cr < 0.1$  and that the line spread function (LSF) starts to degrade if we adopt  $cr < 0.03$ , therefore we chose  $cr = 0.03$  to optimize the S/N of the extracted spectra without degrading the LSF. We also note that the reconstructed images using  $cr = 0.03$  reveal fainter stars with a stable PSF and higher S/N, delivering a better result than with the default parameters.

In addition, there were three other, simpler resampling methods: nearest, quadratic, and linear. A comparison between these three and the more complex methods discussed above showed that the linear method achieved even better results than 'renka' both in terms of the S/N ratio, and the spectral and spatial resolution. Our final resampling was done using the linear method. All of the comparisons were made visually with different source brightness in the regions of the Mg I triplet, H $\alpha$  and Ca II triplet, as well as the spatial resolution and PSF quality, using DS9.

For each of the final cubes, 2D images were created by convolving the cube by filters transmission curves available in the pipeline: Johnson B, V, Cousins R, I, and a few HST-ACS filters. These images were used to generate color-magnitude diagrams (CMDs) and select Red Giant Branch (RGB) stars to be cross-matched with our previous catalogue.

## 2.3 Infrared spectroscopy

### 2.3.1 AL3 observations

With the tri-national program involving Brazil (PI: B. Barbuy), Chile (PI: M. Zoccali) and Australia (PI: J. Meléndez) we had access to red giant stars of the bulge globular cluster AL 3 from Phoenix spectrograph.

This is the first spectroscopic work on AL 3, except for Gaia data (Gaia Collaboration 2020). In Fig. 2.2 is shown a 3 min  $B$  exposure of AL 3 for a field extraction of  $3.3' \times 3.3'$  ( $510 \times 510$  pixels).

Table 2.3 - Log-book of observations. Proposals GS-2006A-C9 on 15-16/07/2006, and GS-2008A-Q-23 on 10/04/2008 and 22/05/2008

Object	Date	LST h:m	Exp. (m)	seeing (")
NGC 6558-11	15-07-2006	22:00	2x25	0.6
NGC 6558-64	16-07-2006	14:48	3x30	0.7
NGC 6558-11	16-07-2006	16:33	2x20	0.5
NGC 6558-42	16-07-2006	19:13	2x30	0.7
NGC 6558-97	16-07-2006	20:25	3x20	0.6
NGC 6558-73	16-07-2006	21:38	2x30	0.9
HP 1-4	15-07-2006	13:42	3x30	0.6
HP 1-6	15-07-2006	20:12	3x30	0.6
HP 1-5	16-07-2006	13:03	3x30	0.8
HP 1-3	16-07-2006	18:02	2x30	0.6
AL 3-3	10-04-2008	15:58	4x15	—
AL 3-6	22-05-2008	15:09	4x15	—
AL 3-7	22-05-2008	16:21	4x15	—

The final suitable spectra include three stars of AL 3, two stars of NGC 6558, and one star of HP 1, centered at  $1.555 \mu\text{m}$  in the H band. Another 3 stars in NGC 6558, and 3 stars in HP 1 were also observed, however with a low S/N, due to clouds or high airmass. The log of observations is provided in Table 2.3.

The sample stars of AL 3 are identified in the chart. Charts and identifications of the observed stars in NGC 6558 and HP 1 are given in Barbuy et al. (2009, 2018) and Barbuy et al. (2006, 2016) respectively.

## 2.4 Adopted solar abundances

In Table 2.4, we present the adopted abundances for the Sun, Arcturus and  $\mu$  Leo adopted in chapters 3, 4 and 6.

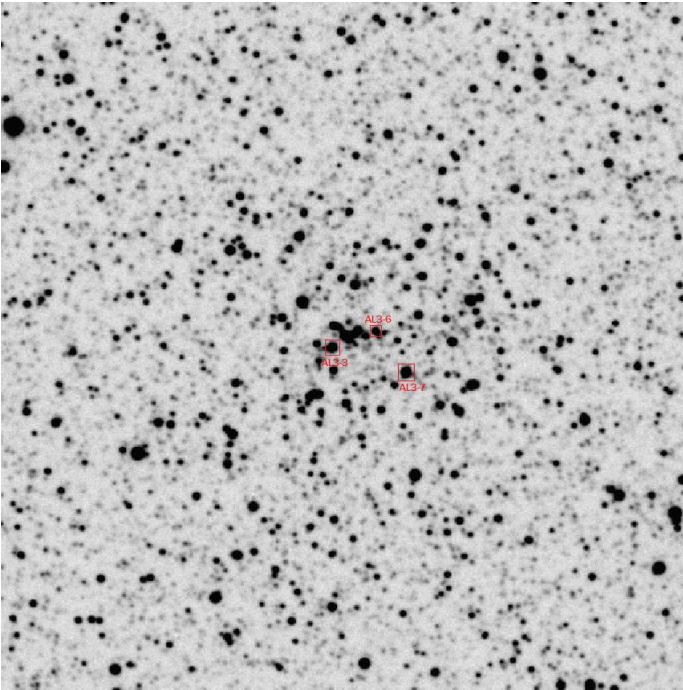


Figure 2.2: AL 3: 3 min. B image, with the three sample stars identified. Extraction of  $3' \times 3'$ . North is up and East is left.

Table 2.4 - Adopted abundances for the Sun, Arcturus, and  $\mu$ Leo. References: [1]: Grevesse et al. (1996); Grevesse & Sauval (1998); Asplund et al. (2009); Lodders (2009); [2]: Allende Prieto et al. (2001); [3]: Ramírez & Allende Prieto (2011); [4]: Meléndez et al. (2003) [5]: Ernandes et al. 2018; [6]: Barbuy et al. (2015); Friaça & Barbuy (2017); [7]: Fulbright et al. (2007); [8]: Smith et al. (2013); [9]: Gratton & Sneden (1990); [10]: Steffen et al. (2015); [11]: Lecureur et al. (2007); [12]: Barbuy et al. (2014); [13]: Smith & Ruck (2000); [14]: Scott et al. (2015a,b); [15]: McWilliam et al. (2013).

El.	Z	$A(X)_{\odot}$	$A(X)_{Arcturus}$	$A(X)_{\mu Leo}$	$A(X)_{\odot}$	$A(X)_{Arcturus}$	$A(X)_{\mu Leo}$
Chapter 3				Chapter 4, 6			
Fe	26	7.50 <sup>1</sup>	6.96 <sup>4</sup>	7.80 <sup>6</sup>	7.50 <sup>1</sup>	6.96 <sup>4</sup>	7.80 <sup>6</sup>
C	6	8.55 <sup>1</sup>	8.32 <sup>3</sup>	8.55 <sup>6</sup>	8.55 <sup>1</sup>	7.79 <sup>11</sup>	8.55 <sup>6</sup>
N	7	7.97 <sup>1</sup>	7.68 <sup>4</sup>	8.83 <sup>6</sup>	7.97 <sup>1</sup>	7.65 <sup>11</sup>	8.83 <sup>6</sup>
O	8	8.76 <sup>10</sup>	8.66 <sup>4</sup>	8.97 <sup>6</sup>	8.77 <sup>10</sup>	8.62 <sup>12</sup>	8.97 <sup>5</sup>
Na	11	6.33 <sup>1</sup>	5.82 <sup>3</sup>	7.06 <sup>7</sup>	6.33 <sup>1</sup>	5.90 <sup>3</sup>	7.07 <sup>13</sup>
Mg	12	7.58 <sup>1</sup>	7.47 <sup>3</sup>	7.85 <sup>8</sup>	7.58 <sup>1</sup>	7.41 <sup>3</sup>	7.91 <sup>13</sup>
Al	13	6.47 <sup>1</sup>	6.26 <sup>3</sup>	6.90 <sup>8</sup>	6.47 <sup>1</sup>	6.26 <sup>3</sup>	6.90 <sup>8</sup>
Si	14	7.55 <sup>1</sup>	7.30 <sup>3</sup>	7.76 <sup>8</sup>	7.55 <sup>1</sup>	7.34 <sup>14</sup>	8.02 <sup>9</sup>
K	19	5.12 <sup>1</sup>	4.99 <sup>3</sup>	5.63 <sup>8</sup>	5.12 <sup>1</sup>	4.99 <sup>3</sup>	5.63 <sup>8</sup>
Ca	20	6.36 <sup>1</sup>	5.94 <sup>3</sup>	6.62 <sup>8</sup>	6.36 <sup>1</sup>	5.94 <sup>3</sup>	6.62 <sup>8</sup>
Sc	21	3.17 <sup>1</sup>	2.81 <sup>3</sup>	3.34 <sup>9</sup>	3.17 <sup>1</sup>	2.86 <sup>6</sup>	3.34 <sup>9</sup>
Ti	22	5.02 <sup>1</sup>	4.66 <sup>3</sup>	5.40 <sup>8</sup>	5.02 <sup>1</sup>	4.74 <sup>3</sup>	5.39 <sup>13</sup>
V	23	4.00 <sup>1</sup>	3.58 <sup>3</sup>	4.18 <sup>8</sup>	4.00 <sup>1</sup>	3.58 <sup>3</sup>	4.34 <sup>9</sup>
Cr	24	5.67 <sup>1</sup>	4.99 <sup>3</sup>	6.14 <sup>8</sup>	5.67 <sup>1</sup>	5.08 <sup>3</sup>	5.97 <sup>9</sup>
Mn	25	5.39 <sup>1</sup>	4.74 <sup>3</sup>	5.79 <sup>8</sup>	5.39 <sup>1</sup>	4.71 <sup>15</sup>	5.70 <sup>9</sup>
Co	27	4.92 <sup>1</sup>	4.71 <sup>3</sup>	5.23 <sup>8</sup>	4.92 <sup>1</sup>	5.11 <sup>3</sup>	4.93 <sup>9</sup>
Ni	28	6.25 <sup>1</sup>	5.73 <sup>4</sup>	6.60 <sup>8</sup>	6.25 <sup>1</sup>	5.77 <sup>3</sup>	6.60 <sup>13</sup>
Cu	29	4.21 <sup>1</sup>	3.67 <sup>5</sup>	4.46 <sup>5</sup>	4.21 <sup>1</sup>	4.09 <sup>3</sup>	4.46 <sup>13</sup>
Zn	30	4.60 <sup>1</sup>	4.06 <sup>6</sup>	4.80 <sup>6</sup>	4.60 <sup>1</sup>	4.06 <sup>6</sup>	4.80 <sup>6</sup>

## Iron-peak elements in bulge globular clusters

### 3.1 Introduction: Iron-peak elements

A useful discriminator for stellar populations is the abundance of the elements, given that each group of chemical elements can provide a different understanding of the nucleosynthesis that took place in the formation of the environment that formed a stellar population. Alpha-elements, light odd-Z elements and heavy elements are more often studied when compared with iron-peak elements.

The iron-peak elements ( $21 \leq Z \leq 32$ ) are subdivided in two groups, the lower and the upper (Woosley & Weaver 1995, hereafter WW95). The Sc with  $Z=21$  is a transition element between the so-called alpha-elements and the iron-peak elements. They are produced in complex nucleosynthesis processes, leading to a division of the iron-peak elements in two groups, the lower iron group:  $21 \leq Z \leq 26$  including Scandium (Sc), Titanium (Ti), Vanadium (V), Chromium (Cr), Manganese (Mn), Iron (Fe), and the upper iron group:  $27 \leq Z \leq 32$  which includes Cobalt (Co), Nickel (Ni), Copper (Cu), Zinc (Zn), Gallium (Ga), and Germanium (Ge). The lower iron group elements are produced in explosive oxygen burning at temperatures  $3 \times 10^9 < T < 4 \times 10^9$  K, explosive Si burning at  $4 \times 10^9 < T < 5 \times 10^9$  K, or nuclear statistical equilibrium for  $T > 5 \times 10^9$  (WW95, Nomoto et al. 2013). The upper iron group elements are produced in two processes: neutron capture on iron group nuclei during helium burning and later burning stages, and the alpha-rich freezeout from material heated to  $> 5 \times 10^9$  K in the deepest layers. The quantity of each element ejected at the supernova event depends on the mass that falls back.

Most of the iron-peak elements have solar abundance ratios for bulge stars in the metallicity range ( $[\text{Fe}/\text{H}] \gtrsim -1.5$ ). A different behaviour is observed in the Large Magellanic

Cloud (LMC) for Ni, Co, Cr that vary in lockstep with Fe, but they are deficient relative to Fe  $[\text{Ni,Co,Cr/Fe}] \sim -0.15$  (Pompéia et al. 2008). The elements Sc, Mn, Cu, and Zn however show different trends relative to Fe (e.g. Nissen et al. 2000; Ishigaki et al. 2013). In particular, Zn is found to be enhanced in metal-poor halo and thick disk stars in the Milky Way (e.g. Cayrel et al. 2004, Ishigaki et al. 2013), and in dwarf spheroidal galaxies (Skúladóttir et al. 2017). Mn is deficient in metal-poor stars, and increases with metallicity for  $[\text{Fe/H}] \gtrsim -1.0$  (e.g. Cayrel et al. 2004; Ishigaki et al. 2013) for halo and thick disk stars and McWilliam et al. 2003; Sobeck et al. 2006; Barbuy et al. 2013, Schultheis et al. 2017) for bulge stars. The same applies to Cu in field halo, thick disk, and bulge stars (Ishigaki et al. 2013; Johnson et al. 2014).

There are very few analyses of the odd-Z iron-peak elements Sc, V, Mn, Co, and Cu in bulge field and globular cluster stars. Star clusters are tracers of the formation history of different components of galaxies. Globular clusters are probably the earliest objects to have formed, and they trace the formation of the halo and bulge of our Galaxy (Hansen et al. 2013; Kruijssen 2015; Renzini 2017).

As to whether the field stars and globular clusters can be identified as having a similar origin, has been a matter of debate in the literature. The detection of abundance anomalies in field stars similar to the anomalies found in globular cluster stars (Gratton et al. 2012) has been used to conclude that at least a fraction of the field stars have their origin in the clusters (Kraft 1983; Martell et al. 2011; Schiavon et al. 2017).

McWilliam et al. (2003) derived Mn abundances in eight bulge field stars. Barbuy et al. (2013, 2015) have derived abundances of Mn, and Zn, for 56 bulge field stars, based on FLAMES-UVES spectra from the Zoccali et al. (2006) sample. Johnson et al. (2014) have derived abundances of the iron-peak elements Cr, Co, Ni, and Cu in stars located in bulge field stars using FLAMES-GIRAFFE data by Zoccali et al. (2008), comprising 205 stars in the  $(+ 5^{\circ}25, -3^{\circ}02)$  field near the globular cluster NGC 6553, and 109 stars in the  $(0, -12^{\circ})$  field.

The iron-peak group became the focus of more studies in metal-poor stars because these elements can be directly associated with prediction models of the massive stars yields. Cobalt specially has a distinguished role in the study of metal-poor stars (Cowan et al. 2020), although the iron-peak elements are not easily detected for many metal-poor stars. In the Galactic bulge Howes et al. (2014, 2015, 2016), Casey & Schlafman (2015),

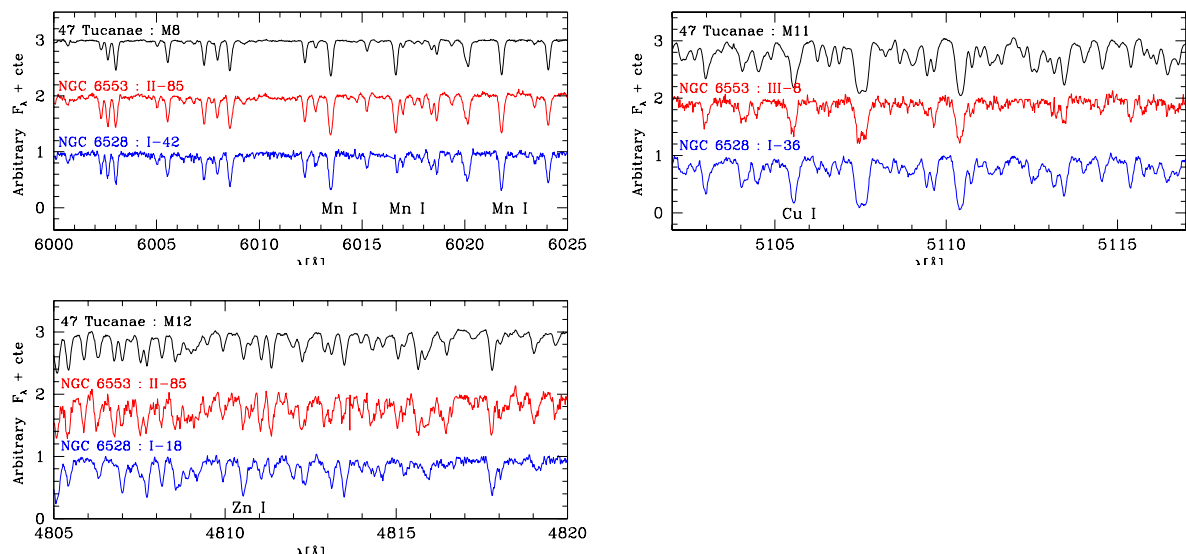


Figure 3.1: Comparison of the spectra for each globular cluster in the sample. Features of interest are indicated for Mn I (*top*), Cu I (*middle*), and Zn I lines (*bottom*).

and Koch et al. (2016) presented abundances of iron-peak elements for metal-poor stars.

In this chapter we present the analysis of individual stars in the 47 Tucanae ( $[\text{Fe}/\text{H}]^1 = -0.67$ , Alves-Brito et al. 2005), and the bulge globular clusters NGC 6553 ( $[\text{Fe}/\text{H}] = -0.20$ , Alves-Brito et al. 2006), NGC 6528 ( $[\text{Fe}/\text{H}] = -0.11$ , Zoccali et al. 2004), NGC 6522 ( $[\text{Fe}/\text{H}] = -0.95$ , Barbuy et al. 2014, 2021), HP 1 ( $[\text{Fe}/\text{H}] = -1.00$ , Barbuy et al. 2006, 2016), and NGC 6558 ( $[\text{Fe}/\text{H}] = -1.00$ , Barbuy et al. 2018c).

The sample reported in table 2.1 consists of 28 red giant stars, including five in 47 Tucanae, four in NGC 6553, three in NGC 6528, eight in HP 1, four in NGC 6522, and four in NGC 6558, all observed with UVES. The wavelength coverage is 4800-6800 Å, including the red (5800-6800 Å), and the blue (4800-5800 Å) portions of the spectrum. The log of observations is given in Table 2.1. Figure 3.1 shows the spectra for some of the programme stars around the features studied.

### 3.2 Line parameters: Hyperfine structure, oscillator strengths

To settle suitable values of oscillator strengths and central wavelengths, the studied lines were checked by using high-resolution spectra of the Sun (using the same instrument

<sup>1</sup> We adopted here the usual spectroscopic notation that  $[A/B] = \log(N_A/N_B)_\star - \log(N_A/N_B)_\odot$  and  $\epsilon(A) = \log(N_A/N_B) + 12$  for each elements A and B.

settings as the present sample of spectra<sup>2</sup>), Arcturus (Hinkle et al. 2000) and the metal-rich giant star  $\mu$  Leo (Lecureur et al. 2007). We adopted the stellar parameters effective temperature ( $T_{\text{eff}}$ ), surface gravity ( $\log g$ ), metallicity ( $[\text{Fe}/\text{H}]$ ) and microturbulent velocity ( $v_t$ ) of (4275 K, 1.55, -0.54, 1.65 km.s<sup>-1</sup>) for Arcturus from Meléndez et al. (2003), and (4540 K, 2.3, +0.30, 1.3 km.s<sup>-1</sup>) for  $\mu$  Leo from Lecureur et al. (2007).

Oscillator strengths for Sc I, Sc II, V I, and Cu I reported in table 3.2 are from Kurucz (1993)<sup>3</sup>, NIST (Martin et al. 2002)<sup>4</sup>, VALD3 (Piskunov et al. 1995)<sup>5</sup>, literature values, and adopted final values.

### 3.2.1 Scandium and vanadium

The only species of Sc is <sup>45</sup>Sc, and the V abundance corresponds to 99.75% of <sup>51</sup>V and 0.25% of <sup>50</sup>V (Asplund et al. 2009), therefore we adopted <sup>51</sup>V as unique isotope. We selected Sc I, Sc II, and V I lines that were shown to be strong enough to be detected in red giants. Hyperfine structure (HFS) was taken into account, by applying the code made available by McWilliam et al. (2013), together with the A and B constants. V and Sc have a nuclear spin  $I = 7/2$ . Some lines that were blended in the sample stars, or affected by telluric lines, were discarded. This applies to the lines V I 4831.640, 4851.480, 4875.480, 4932.030, 5627.640, 5670.850, 6216.370, and 6285.160 Å.

### 3.2.2 Copper

The isotopic fractions of 0.6894 for <sup>63</sup>Cu and 0.3106 for <sup>65</sup>Cu (Asplund et al. 2009) are considered. Copper abundances were derived from the Cu I lines at 5105.50 Å and 5218.20 Å. The 5782 Å line is not available in the UVES spectra analysed, which cover the wavelengths 4780-5775 Å and 5817-6821 Å, therefore with a gap of about 40 Å in the range 5775-5817 Å. Oscillator strengths of the Cu I lines were selected in the literature from Kurucz (1993), Bielski (1975), NIST or VALD.

<sup>2</sup> [http://www.eso.org/observing/dfo/quality/UVES/pipeline/solar\\_spectrum.html](http://www.eso.org/observing/dfo/quality/UVES/pipeline/solar_spectrum.html)

<sup>3</sup> <http://kurucz.harvard.edu/atoms.html>

<sup>4</sup> [http://physics.nist.gov/PhysRefData/ASD/lines\\_form.html](http://physics.nist.gov/PhysRefData/ASD/lines_form.html)

<sup>5</sup> <http://vald.astro.univie.ac.at>

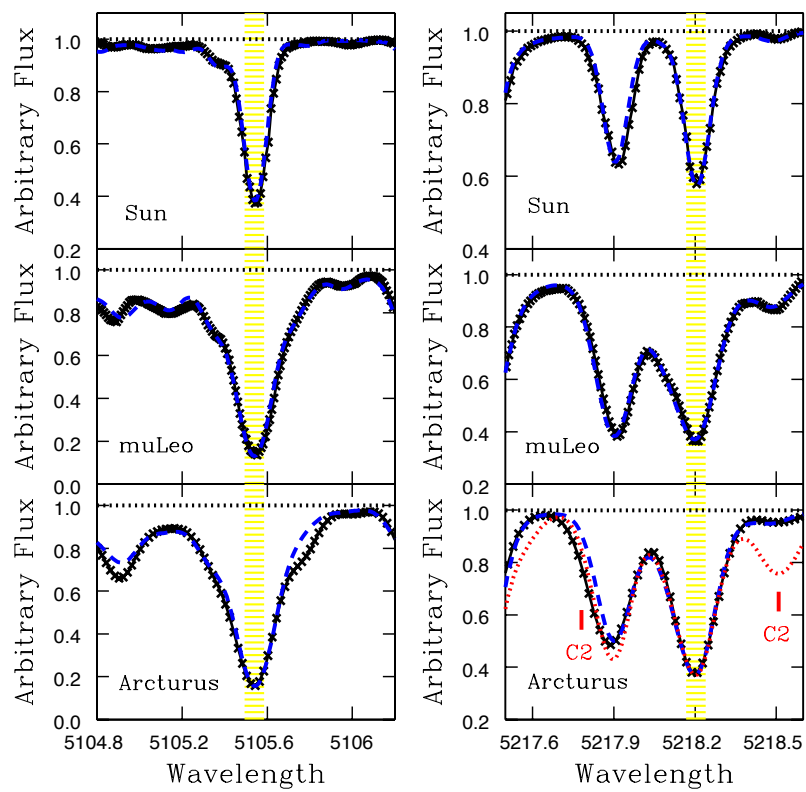


Figure 3.2: Fittings on solar, Arcturus, and  $\mu$ Leo spectra for the Cu I lines at 5105 Å and 5218 Å (yellow lines). Observations (black crosses) are compared with synthetic spectra computed using the adopted abundances (dashed blue lines).

The magnetic dipole A-factor and the electric quadrupole B-factor constants were adopted from Kurucz (1993), and Biehl (1976), in order to compute HFS. For the 5218 Å line the constants for the 4d 2D level are not available. According to R. Kurucz (private communication), the upper level should have much smaller HFS than the lower, because its wavefunction is further away from the nucleus, and setting its splitting to 0.0 is acceptable.

The Cu I 5105 Å and Cu I 5218 Å lines in the solar spectrum were fitted adopting  $A(\text{Cu})_{\odot} = 4.21$  (Grevesse et al. 1996) cf. Table 2.4. The adopted or derived abundances for each of the reference stars are also presented in Table 2.4, corresponding to  $[\text{Cu}/\text{Fe}] = 0.0$  and  $+0.05$  in Arcturus and  $\mu\text{Leo}$ , respectively.

Figure 3.2 shows the fits to the solar, Arcturus, and  $\mu\text{Leo}$  spectra for the Cu lines. For the Cu I 5218 Å in Arcturus, an asymmetry remained in the blue wing of the Fe profile close to the Cu I line. Consequently, the Cu I 5218 Å line was used in the sample stars with caution.

### 3.2.3 Manganese and zinc

Manganese has one isotope  $^{55}\text{Mn}$  and, for zinc,  $^{64,66,68}\text{Zn}$  are the dominant species, present in fractions of 48.63, 27.90, and 18.75% respectively (Asplund et al. 2009). For these elements a splitting in isotopes was not considered. Manganese abundances were derived from the Mn I triplet lines at 6013.513, 6016.640, 6021.800 Å. The line list of HFS components are given in Barbuy et al. (2013). For zinc we used the Zn I 4810.529 and 6362.339 Å lines as detailed in Barbuy et al. (2015).

## 3.3 Abundance analysis

### 3.3.1 Atmospheric parameters and abundance derivation

The adopted effective stellar atmospheric parameters for all programme stars were derived in previous work (Zoccali et al. 2004; Alves-Brito et al. 2005; Alves-Brito et al. 2006; Barbuy et al. 2006, 2014, 2016, 2018c).

The method adopted in this analysis consists in firstly analyse the colours V-I, V-K, and J-K, corrected by the reddening values reported in Table 3.1, used together with colour-temperature calibrations by Alonso et al. (1999, 2001), and/or Houdashelt et al.

Table 3.1 - Reddening and distance moduli adopted. References: 1 Harris (1996); 2 Zoccali et al. (2001a); 3 Zoccali et al. (2004); 4 Barbuy et al. (1998); 5 Guarnieri et al. (1998); 6 Barbuy et al. (2006); 7 Ortolani et al. (2007, 2011); 8 Barbuy et al. (2009); 9 Terndrup (1988); 10 Rossi et al. (2015).

Cluster	E(B-V)	Ref.	$(m - M)_0$	Ref.
47 Tucanae	0.04	1	13.09	2
NGC 6528	0.46	3	14.45	4
NGC 6553	0.70	5	13.54	4
HP 1	1.12	6	14.15	7
NGC 6522	0.45	8	13.91	4
NGC 6558	0.38	9	14.43	10

(2000).

Then secondly, gravities of the sample stars were obtained adopting the classical relation below, and final  $\log g$  values were obtained from ionization equilibrium of Fe I and Fe II lines.

$$\log g_* = 4.44 + 4 \log \frac{T_*}{T_\odot} + 0.4(M_{\text{bol}*} - M_{\text{bol}\odot}) + \log \frac{M_*}{M_\odot} \quad (3.1)$$

We adopted  $T_\odot = 5770$  K and  $M_{\text{bol}\odot} = 4.75$  for the Sun and  $M_* = 0.80$  to  $0.88 M_\odot$  for the red giant branch (RGB) stars.

In Table 3.1 are reported the distance moduli assumed for each sample cluster and corresponding references.

And thirdly, the initial photometric temperatures and gravities were used to compute the excitation and ionization equilibrium. Effective temperatures were then checked by imposing excitation equilibrium for FeI and FeII lines of different excitation potential, and gravities were checked against ionization equilibrium. Microturbulent velocity  $v_t$  was determined by cancelling any trend in a FeI abundance versus equivalent width diagram.

Finally, the metallicities for the sample were derived using a set of equivalent widths of FeI and Fe II lines.

Table 3.3 summarizes the final atmospheric parameters obtained for the programme stars. In this Table we also present carbon, nitrogen and oxygen abundance ratios, derived from the  $C_2(0,1)$   $A^3\Pi-X^3\Pi$  bandhead at  $5635.3 \text{ \AA}$ ,  $CN(5,1)$   $A^2\Pi-X^2\Sigma$   $6332.18$  and the forbidden  $[OI]$   $6300.311 \text{ \AA}$  lines.

Elemental abundances were obtained through line-by-line spectrum synthesis calculations. The calculations of synthetic spectra were carried out using the code PFANT described in Barbuy et al. (2003), Coelho et al. (2005), and Barbuy et al. (2018b).

Table 3.2 - Central wavelengths from NIST or Kurucz line lists and total oscillator strengths from line lists by Kurucz, NIST and VALD, literature, and adopted values. In column 7, literature oscillator strength values are from the following references: 1 Ramírez & Allende Prieto 2011; 2 Lawler et al. (2014).

Species	$\lambda$ (Å)	$\chi_{ex}$ (eV)	$gf_{Kurucz}$	$gf_{NIST}$	$gf_{VALD}$	$gf_{literature}$	$gf_{adopted}$
<sup>45</sup> ScI	5671.805/828N	1.447908	+0.640	+0.495	+0.495	—	+0.495
<sup>45</sup> ScI	5686.826/856	1.439588	+0.530	+0.376	+0.376	—	+0.276
<sup>45</sup> ScI	6210.676/658	0.000000	-1.570	-1.53	-1.529	—	-1.53
<sup>45</sup> ScII	5526.790/785	1.768298	+0.13	+0.02	+0.024	—	-0.28
<sup>45</sup> ScII	5552.224/235	1.455221	-2.270	—	-2.119	-2.28 <sup>1</sup>	-2.27
<sup>45</sup> ScII	5657.896/907	1.507058	-0.50	-0.60	-0.603	—	-0.60
<sup>45</sup> ScII	5684.202/214	1.507508	-1.050	-1.07	-1.074	-1.07 <sup>1</sup>	-1.07
<sup>45</sup> ScII	6245.637/641	1.507508	-0.98	—	-1.030	-1.04 <sup>1</sup>	-1.18
<sup>45</sup> ScII	6300.698/746	1.507508	-1.840	—	-1.887	-1.95 <sup>1</sup>	-1.99
<sup>45</sup> ScII	6320.851/843	1.500496	-1.770	—	-1.819	-1.92 <sup>1</sup>	-1.97
<sup>45</sup> ScII	6604.601/578	1.357044	-1.48	-1.31	-1.309	-1.31 <sup>1</sup>	-1.41
<sup>51</sup> VI	5703.560	1.050919	—	-0.211	-0.211	-0.21 <sup>2</sup>	-0.211
<sup>51</sup> VI	6081.440	1.050919	—	-0.578	-0.579	-0.61 <sup>2</sup>	-0.578
<sup>51</sup> VI	6090.220	1.080616	—	-0.062	-0.062	-0.07 <sup>2</sup>	-0.162
<sup>51</sup> VI	6119.520	1.063602	—	-0.320	-0.320	-0.36 <sup>2</sup>	-0.47
<sup>51</sup> VI	6199.190	0.286572	—	-1.28	-1.300	-1.46 <sup>2</sup>	-1.48
<sup>51</sup> VI	6243.100	0.300634	—	-0.98	-0.980	-0.94 <sup>2</sup>	-0.88
<sup>51</sup> VI	6251.820	0.286572	—	-1.34	-1.340	-1.37 <sup>2</sup>	-1.44
<sup>51</sup> VI	6274.650	0.266964	—	-1.67	-1.670	-1.70 <sup>2</sup>	-1.72
CuI	5105.537	1.389035	-1.516	-1.50	-1.542	—	-1.52
CuI	5218.197	3.816948	+0.476	+0.26	+0.364	—	+0.0

Atomic lines are as described in Sect. 3.2, and molecular lines of CN A<sup>2</sup>Π-X<sup>2</sup>Σ, C<sub>2</sub> Swan A<sup>3</sup>Π-X<sup>3</sup>Π and TiO A<sup>3</sup>Φ-X<sup>3</sup>Δ γ and B<sup>3</sup>Π-X<sup>3</sup>Δ γ' systems are taken into account. The atmospheric models were obtained by interpolation in the grid of MARCS Local Thermodynamic Equilibrium (LTE) models (Gustafsson et al. 2008), adopting their spherical and mildly CN-cycled ([C/Fe]= -0.13, [N/Fe]= +0.31) subgrid. These models consider [α/Fe]=+0.20 for [Fe/H]=-0.50 and [α/Fe]=+0.40 for [Fe/H] ≤ -1.00.

In Figures 3.3, 3.4, and 3.5 are shown examples of fitting of synthetic spectra to the observed lines.

### 3.3.2 Uncertainties

The final adopted atmospheric parameters for all programme stars were based on Fe I and Fe II lines in the papers cited above, and we have adopted their estimated uncertainties

Table 3.3 - Atmospheric parameters adopted.

Star (1)	$T_{\text{eff}}$ [K] (2)	$\log g$ (3)	[FeI/H] (4)	[FeII/H] (5)	[Fe/H] (6)	$v_t$ [kms $^{-1}$ ] (7)	[C/Fe] (8)	[N/Fe] (9)	[O/Fe] (10)
<b>47 Tucanae</b>									
M8	4086	1.48	-0.62	-0.65	-0.64	+1.42	+0.20	+0.50	+0.45
M11	3945	1.20	-0.62	-0.62	-0.62	+1.49	+0.00	+0.50	+0.25
M12	4047	1.45	-0.63	-0.68	-0.66	+1.45	+0.00	+0.50	+0.45
M21	5100	2.46	-0.77	-0.82	-0.80	+1.42	+0.20	+0.50	+0.30
M25	4200	1.65	-0.64	-0.67	-0.66	+1.37	-0.10	+0.20	+0.35
<b>NGC 6553</b>									
II-64	4500	2.20	-0.20	-0.20	-0.20	+1.45	+0.00	+0.50	+0.45
II-85	3800	1.10	-0.23	-0.29	-0.26	+1.38	+0.00	+0.50	+0.30
III-8	4600	2.40	-0.17	-0.17	-0.17	+1.40	+0.00	+0.50	+0.30
267092	4600	2.50	-0.21	-0.22	-0.22	+1.50	+0.00	+1.00	—
<b>NGC 6528</b>									
I-18	4700	2.00	-0.05	-0.11	-0.08	+1.50	-0.20	+0.30	+0.30
I-36	4200	1.50	-0.13	-0.09	-0.11	+1.50	-0.30	+0.80	+0.00
I-42	4100	1.60	-0.14	-0.08	-0.11	+1.20	+0.00	+0.20	+0.05
<b>HP 1</b>									
HP 1-2	4630	1.70	-1.02	-0.97	-1.00	+1.60	+0.00	+0.20	+0.30
HP 1-3	4450	1.75	-0.99	-0.95	-0.97	+ 1.40	+0.00	+0.20	+0.30
2115	4530	2.00	-0.98	-1.02	-1.00	+ 1.45	+0.00	+0.70	+0.40
2461	4780	2.05	-1.13	-1.09	-1.11	+ 1.90	+ 0.00	+0.50	+0.50
2939	4525	2.00	-1.07	-1.07	-1.07	+ 1.65	+0.00	+0.50	+0.50
3514	4560	1.80	-1.18	-1.19	-1.18	+ 2.00	+0.00	+0.80	+0.40
5037	4570	2.15	-0.98	-1.03	-1.00	+ 1.20	+0.00	+0.50	+0.35
5485	4920	2.07	-1.18	-1.18	-1.18	+ 1.80	+0.00	+0.50	+0.40
<b>NGC 6522</b>									
B-107	4990	2.00	-1.11	-1.14	-1.13	+ 1.40	+0.00	+0.70	+0.30
B-122	4900	2.70	-0.80	-0.82	-0.81	+1.55	-0.20	+0.70	+0.40
B-128	4800	2.50	-0.81	-0.82	-0.82	+1.25	+0.10	+0.70	+0.50
B-130	4850	2.20	-1.03	-1.04	-1.04	+1.45	+0.10	+0.70	+0.50
<b>NGC 6558</b>									
283	4840	2.50	-1.14	-1.16	-1.15	+1.05	+0.10:	+0.70	+0.50
364	4880	2.35	-1.18	-1.13	-1.15	+1.90	+0.10	+0.80	+0.20
1160	4890	2.35	-1.03	-1.04	-1.04	+0.73	+0.20	+1.00	+0.50
1072	4850	2.60	-1.20	-1.26	-1.23	+1.10	+0.10	+1.00	+0.55

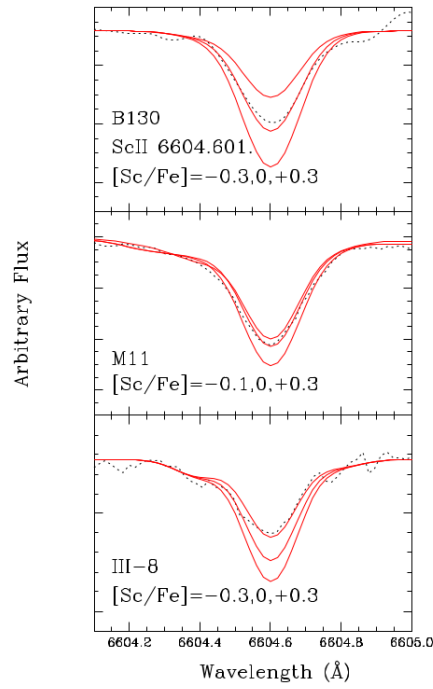


Figure 3.3: Fits of best lines of Sc I, Sc I 6604.601 Å for some sample stars.

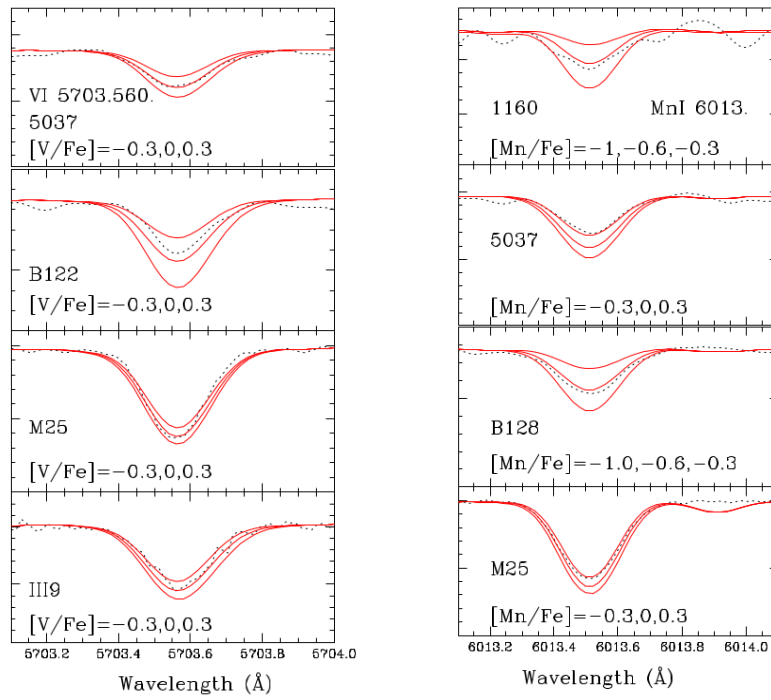


Figure 3.4: Fits of best lines of V I, V I 5703.560 Å, and, Mn I 6013.513 Å for some sample stars.

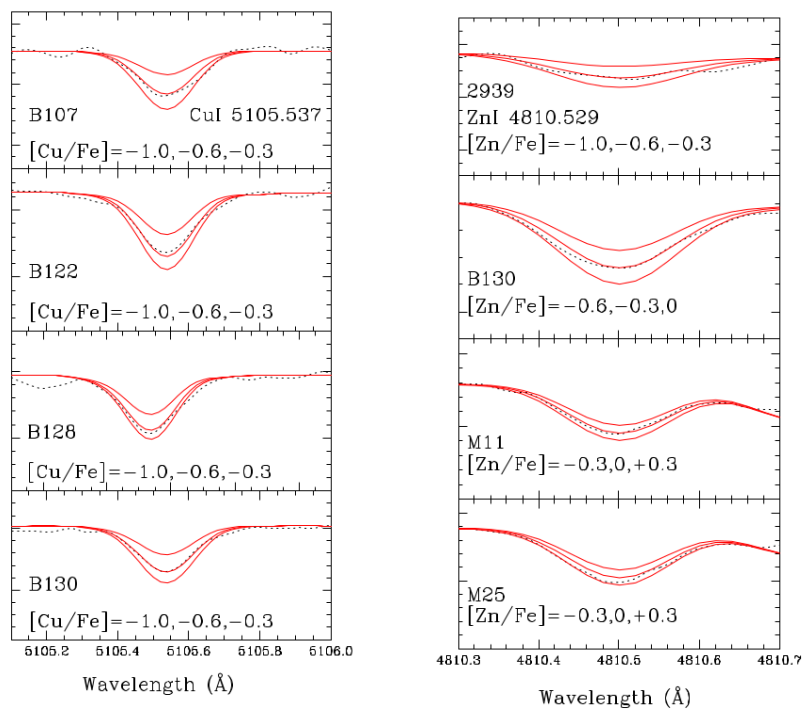


Figure 3.5: Fits of best lines of Cu I, Cu I 5105.537 Å, and Zn I, Zn I 4810.529 Å for some sample stars.

in the atmospheric parameters, i.e.  $\pm 100$  K for temperature,  $\pm 0.20$  for surface gravity,  $\pm 0.10$  dex for  $[\text{Fe}/\text{H}]$ , and  $\pm 0.20$   $\text{kms}^{-1}$  for microturbulent velocity, that impact the  $[\text{X}/\text{Fe}]$  values, and  $\pm 0.10$  dex for  $[\text{Fe}/\text{H}]$  is also added to result in errors in  $[\text{X}/\text{Fe}]$ . We note that the addition of the error in  $[\text{Fe}/\text{H}]$  overestimates the total error. In Table 3.4 the final uncertainties in the abundances of the iron-peak elements studied are reported for the metal-poor star HP-1:2115, and the metal-rich star NGC 6528:I36. Given that the stellar parameters are correlated among them, the covariance will be non-zero. Since we have taken into account only the diagonal terms of the covariance matrix, these errors are overestimated.

In order to further inspect the errors in stellar parameters, we applied NLTE corrections to abundances as given in Lind et al. (2012), and following suggestions given in Bergemann et al. (2013). For star HP1-2939 as an example, we show the LTE excitation and ionization potential plots in Fig. 3.6, restricting to lines with excitation potential  $\chi_{ex} \geq 2.0$  eV. We then applied

a) the NLTE abundance correction to each Fe I line, and ran the excitation and ionization equilibrium once more. This is shown in Fig. 3.7 (left panel). The result is a negligible change in metallicity from Fe I lines of about 0.015 dex.

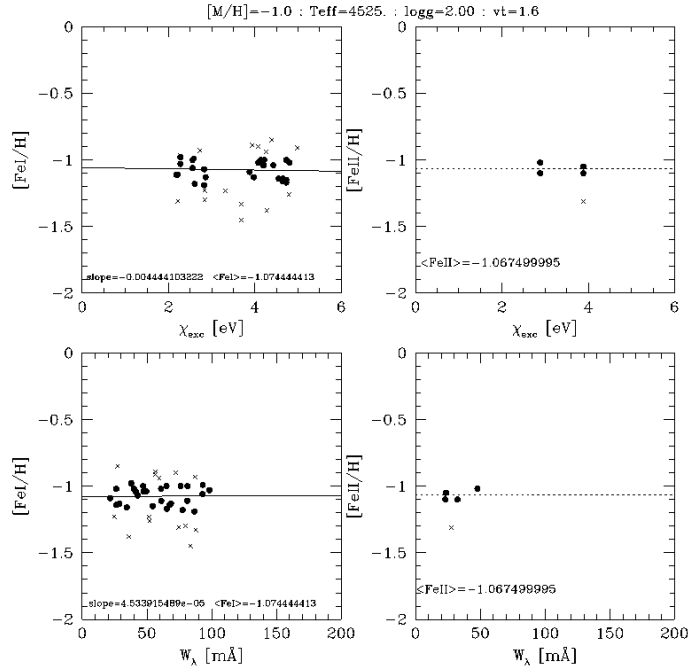


Figure 3.6: Excitation and ionization equilibria of Fe I and Fe II lines for the star 2939 in LTE.

b) the NLTE correction on gravity  $\log g$ , amounting to  $\Delta \log g = 0.04$  - see Fig. 3.7 (right panel). It can be seen that the difference in metallicity between Fe I and Fe II increased to 0.02 instead of the previous 0.01 difference.

c) the NLTE correction on temperature is negligible (6 K)

d) the NLTE on microturbulence velocity is also negligible at these metallicities.

As shown in Fig. 6 by Bergemann et al. (2013), the effects are not pronounced for stars of metallicity  $[\text{Fe}/\text{H}] \gtrsim -1.0$ , therefore they can be neglected for the present sample stars, given the other larger errors.

We must also take into account errors in S/N and equivalent widths. These errors are given by the Cayrel (1988) formula (see also Cayrel et al. 2004).  $\sigma = \frac{1.5}{S/N} \sqrt{FWHM * \delta x}$ . A mean FWHM = 12.5 pixels, or 0.184 Å is adopted. The CCD pixel size is 15 μm, or  $\delta x = 0.0147$  Å in the spectra. By assuming a mean S/N=100, we derive an error  $\Delta EW \sim 0.8$  mÅ (we note that this formula neglects the uncertainty in the continuum placement). In order to take the S/N and fitting error into account, we adopted  $\delta_{noise} = \frac{\sigma}{\sqrt{N-1}}$ . These are reported in Table 3.6.

The final error is given by the equation  $\delta([X/Fe]) = \sqrt{\delta_{noise}^2 + \delta_{parameters}^2}$  where for the error on stellar parameters the values given in Table 3.4 for the metal-poor stars HP1:2115

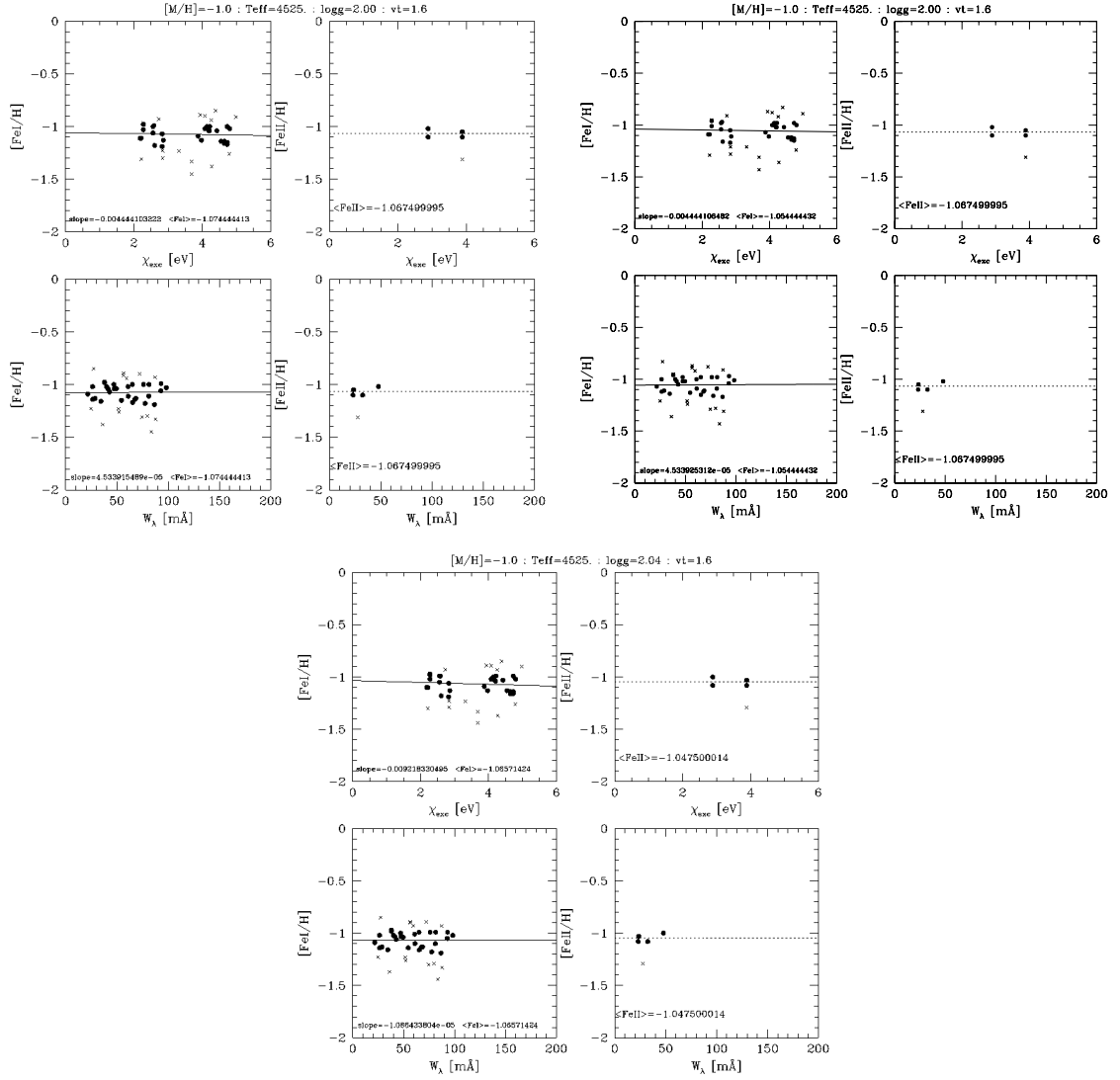


Figure 3.7: Upper left panel: LTE. Upper right panel: NLTE abundance corrected. Lower panel: NLTE gravity corrected. Excitation and ionization equilibria of Fe I and Fe II lines for star 2939. Upper left panel: applying NLTE abundance correction; upper right panel: applying NLTE gravity correction.

Table 3.4 - Sensitivity of abundances to changes of  $\Delta T_{\text{eff}} = 100$  K,  $\Delta \log g = +0.20$ , and  $\Delta v_t = 0.20$  km s<sup>-1</sup>. Error estimation usually take into account only these three stellar parameters,  $[X/\text{Fe}]_{sp}$ , as given in column (5). The error in  $\Delta[\text{Fe}/\text{H}] = 0.1$  dex is added in the last column, warning that this is an overestimation.

Species	$\Delta T$ (100 K)	$\Delta \log g$ (+0.20 dex)	$\Delta v_t$ (+0.20 kms <sup>-1</sup> )	$(\sum x^2)^{1/2}([X/\text{Fe}]_{sp})$	$(\sum x^2)^{1/2}([X/\text{Fe}])$ (+0.10 dex)
(1)	(2)	(3)	(4)	(5)	(6)
HP 1 : 2115					
ScII	-0.02	+0.10	-0.01	+0.10	+0.10
VI	+0.15	+0.01	-0.01	+0.15	+0.15
MnI	+0.01	+0.01	-0.02	+0.02	+0.03
CuI	+0.10	+0.02	-0.10	+0.14	+0.14
ZnI	-0.05	+0.10	-0.01	+0.12	+0.12
NGC 6528 : I-36					
ScII	-0.02	+0.10	-0.05	+0.11	+0.12
VI	+0.05	+0.01	-0.12	+0.13	+0.13
MnI	+0.01	+0.01	-0.10	+0.10	+0.10
CuI	+0.02	+0.01	-0.12	+0.12	+0.12
ZnI	+0.07	+0.07	-0.15	+0.18	+0.19

are applied to the stars more metal-poor than  $[\text{Fe}/\text{H}] < -0.5$ , and those for NGC 6528:I36 to the metal-rich stars. A detailed formalism on errors in abundances and abundance ratios was presented by McWilliam et al. (1995), and according to them, rigorously the error in  $[X/\text{Fe}]$  is given by their equation A19:  $\sigma[X/\text{Fe}]^2 = \sigma[X/\text{H}]^2 + \sigma[\text{Fe}/\text{H}]^2 - \sigma(X,\text{Fe})$ , where  $\sigma(X,\text{Fe})$  include the covariance terms between average abundances X and Fe. This term is, however, difficult to compute. In conclusion, by adding  $\sigma[\text{Fe}/\text{H}]$  to our error, the resulting error is overestimated. In Figs. 3.8, 3.9, 3.10, 3.12, and 3.14 the errors in  $[X/\text{Fe}]$  are those reported in column (6) from Table 3.4 plus the  $\delta_{\text{noise}}$ .

### 3.4 Results and discussion

Very few abundances are available for iron-peak elements in bulge stars. In this Section, we present results and discuss the available chemical evolution models, and associated nucleosynthesis of the studied species. We have included all chemical evolution models available for the Galactic bulge for these elements. The abundances of Sc I, Sc II, V I, Mn I, Cu I, and Zn I for each sample star are listed in Table 3.5. In Figures 3.8, 3.9, 3.10, 3.12, and 3.14 we plot the element-to-iron ratio versus the metallicity  $[\text{Fe}/\text{H}]$ .

### 3.4.1 Scandium, vanadium and manganese

Scandium is intermediate between the alpha-elements and the iron-peak elements.  $^{45}\text{Sc}$  is produced in central He burning and in C-burning shell, in a so-called weak-s process, and during neon burning and as the radioactive progenitor  $^{45}\text{Ti}$  in explosive oxygen and silicon burning (WW95,LC03). V, Cr, and Mn are mainly produced in incomplete explosive Si burning in outer layers of massive stars (WW95, Limongi & Chieffi 2003, hereafter LC03).

Figure 3.8 compares the present  $[\text{Sc}/\text{Fe}]$  values with metal-poor bulge stars by Howes (2015, 2016) for thick disk and halo stars by Nissen et al. (2000) and Ishigaki et al. (2013) and thin and thick disk stars by Battistini & Bensby (2015). The data show a considerable spread, but it is possible to interpret the metal-poor side from Howes et al. and Ishigaki et al. as somewhat enhanced with  $[\text{Sc}/\text{Fe}] \sim 0.2$ . Fishlock et al. (2017) confirm the findings by Nissen et al. (2000), that high- and low-alpha halo stars show high and low Sc abundances respectively. Data by Nissen et al. (2000) tend to show a trend of decreasing  $[\text{Sc}/\text{Fe}]$  with increasing metallicity. Contrarily to the Sc enhancement in the more metal-poor stars from Howes et al. (2015, 2016), the present results on moderately metal-poor bulge clusters do not show a significant Sc enhancement. Our resulting values are lower than those of Nissen et al. (2000), and fit well the level of  $[\text{Sc}/\text{Fe}]$  values by Battistini & Bensby (2015) for thin and thick disk stars. The metal-rich globular clusters NGC 6528 and NGC 6553 show a spread in Sc abundances at  $[\text{Fe}/\text{H}] \sim -0.2$ , that might be considered as a decrease with increasing metallicity at the high metallicity end.

Figure 3.9 shows that V varies in lockstep with Fe. There are no V abundances for bulge stars other than the present data. The thin and thick disk data from Reddy et al. (2003, 2006) are overplotted. The thick disk V abundances from Reddy et al. (2006) appear to be enhanced with respect to thin disk stars (Reddy et al. 2003), as well as to the present results, whereas they seem to be at the same level as thin and thick disk stars by Battistini & Bensby (2015). For the more metal-rich stars the bulge globular cluster stars tend to decrease with increasing metallicity, which could be due to enrichment in Fe by Supernovae of type Ia (SNIa). Due to uncertainties, the spread in the data do now allow us to derive further conclusions from V abundances.

Kobayashi et al. (2006, hereafter K06) have shown that Sc, and V yields are underabundant by 1 dex based on previous nucleosynthesis prescriptions. Umeda & Nomoto

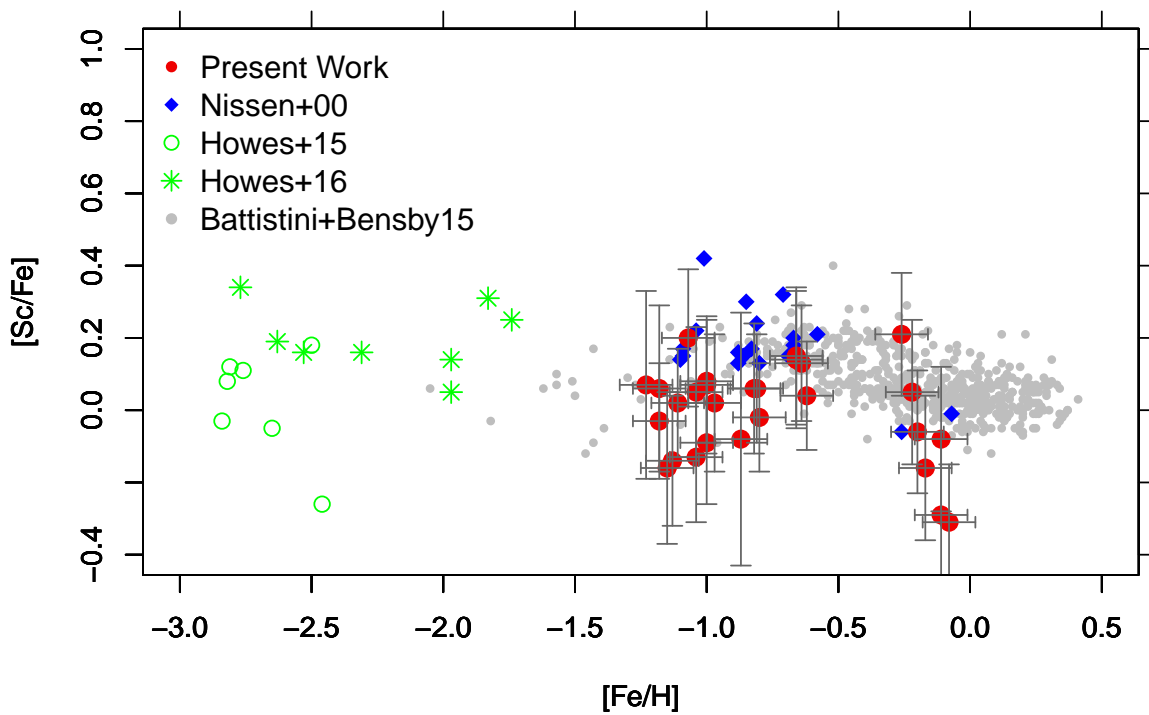


Figure 3.8:  $[\text{Sc}/\text{Fe}]$  vs.  $[\text{Fe}/\text{H}]$ . Symbols: present work (filled red circles), Bensby et al. (2017) (black filled circles), Nissen et al. (2000) (filled blue diamonds), Howes et al. (2015) (open green circles), Howes et al. (2016) (green crosses); Battistini & Bensby (2015) (grey filled circles). Error bars on  $[\text{Sc}/\text{Fe}]$  are indicated. Errors in  $[\text{Fe}/\text{H}]$  can be assumed to be constant, of the order of  $\Delta[\text{Fe}/\text{H}] = \pm 0.17$  dex.

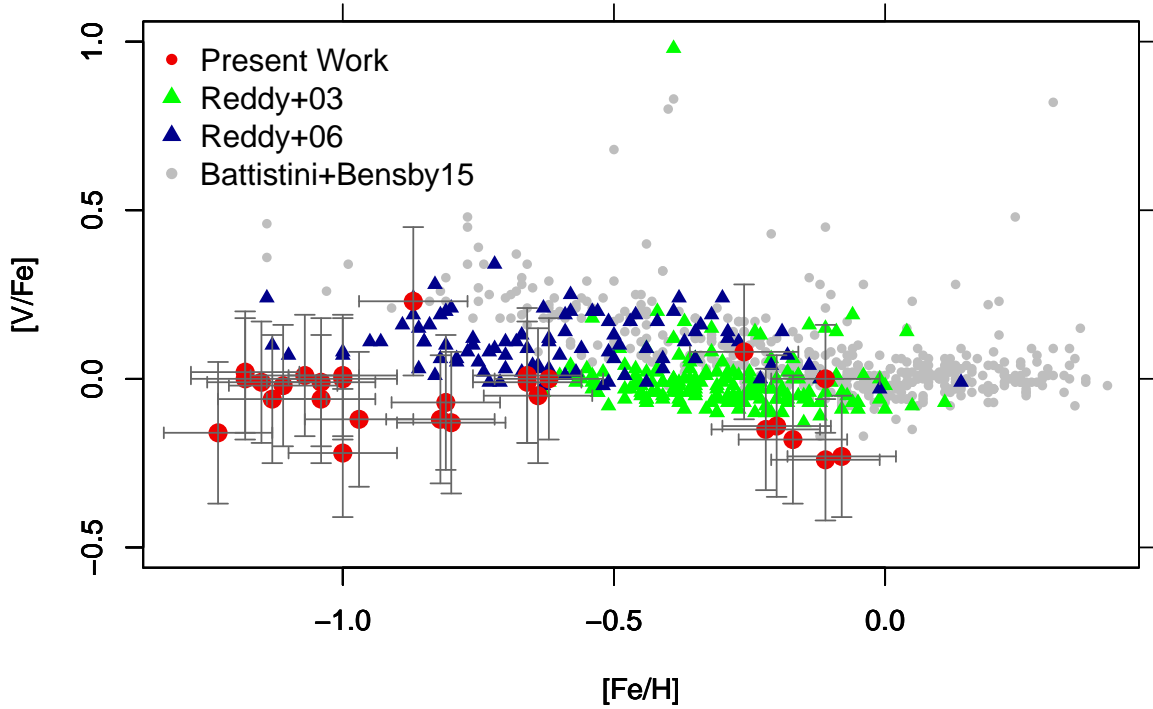


Figure 3.9:  $[V/Fe]$  vs.  $[Fe/H]$ . Symbols: present work (filled red circles); Reddy et al. (2003) (green filled triangles), Reddy et al. (2006) (navyblue filled triangles) Battistini & Bensby (2015) (grey filled circles). Errors are assumed as in Fig. 3.8.

(2005), Kobayashi et al. (2006), Nomoto et al. (2013) have introduced a low-density model, during explosive burning, enhancing Sc abundance through the alpha-rich freezeout. Yoshida et al. (2008) applied a  $\nu$ -process to Si explosive nucleosynthesis, producing larger amounts of Sc, V, and Mn production by a factor of ten. Fröhlich et al. (2006) showed that a delayed neutrino mechanism leading to an electron fraction value of  $Y_e \gtrsim 0.5$  in the innermost region gives larger production of Sc, Ti, and Zn. In conclusion, given that the available models do not reproduce the observations (Kobayashi et al. 2006) for both Sc and V, due to low yields from nucleosynthesis yields, these models are not overplotted on the data.

Figure 3.10 shows  $[Mn/Fe]$  vs.  $[Fe/H]$  for the present results, together with previous results in Galactic bulge stars measured by McWilliam et al. (2003), Barbuy et al. (2013), and Schultheis et al. (2017), and results for thin and thick disk stars by Battistini & Bensby (2015). We note that NLTE corrections in the range of parameters of the present

data are small (Bergemann & Gehren 2008). The only available bulge chemical evolution models by Cescutti et al. (2008) and Kobayashi et al. (2006) are overplotted. Cescutti et al. (2008) computed models for Mn enrichment in the Galactic bulge, adopting a star formation rate 20 times faster than in the solar neighbourhood, and a flatter Initial Mass Function (IMF). Their preferred model adopts metallicity dependent yields from WW95 for massive stars, and Iwamoto et al. (1999) for intermediate mass stars. K06 produced a grid of yields, including both supernovae of type II (SNII) and hypernovae, and further have built chemical evolution models for Galaxy components, including the bulge.

The present Mn abundances in globular cluster stars follow the trend of field stars, i.e. with  $[\text{Mn}/\text{Fe}] \sim -0.5$  at  $[\text{Fe}/\text{H}] \sim -1.5$ , increasing steadily with increasing metallicity, and they are well reproduced by the models. Finally, Fig. 3.11 shows  $[\text{Mn}/\text{O}]$  vs.  $[\text{Fe}/\text{H}]$ , revealing differences between thin, thick and bulge stars, as previously pointed out by Feltzing et al. (2007) and Barbuy et al. (2013). This is of great importance since  $[\text{Mn}/\text{O}]$  can be used as a discriminator between different stellar populations, that otherwise have a similar behaviour.

### 3.4.2 Copper

The  $^{63,65}\text{Cu}$  isotopes are mainly produced through neutron-capture during core He burning and convective shell carbon burning, therefore Cu may be classified as produced in a weak s-process component (LC03). Some primary  $^{65}\text{Cu}$  is also made as  $^{65}\text{Zn}$  in explosive nucleosynthesis through alpha-rich freezeout (WW95, Pignatari et al. 2010). Cu is not significantly produced in SNIa, nor in Asymptotic Giant Branch (AGB) stars or through the r-process (Pignatari et al. 2010).

Johnson et al. (2014) derived copper abundances for a large sample of bulge red giants. Their results show a low Cu abundance ratio at low metallicities that increases with increasing  $[\text{Fe}/\text{H}]$ . For supersolar metallicities,  $[\text{Cu}/\text{Fe}]$  values appear to be enhanced relative to other stellar populations.

The present results are plotted in Fig. 3.12, together with data from Johnson et al. (2014) for the bulge, and Ishigaki et al. (2013) for the thick disk. Our results tend to be less enhanced than those by Johnson et al. (2014). There is good agreement between the data and the models by Kobayashi et al. (2006). The metal-poor clusters show very low  $[\text{Cu}/\text{Fe}]$ .

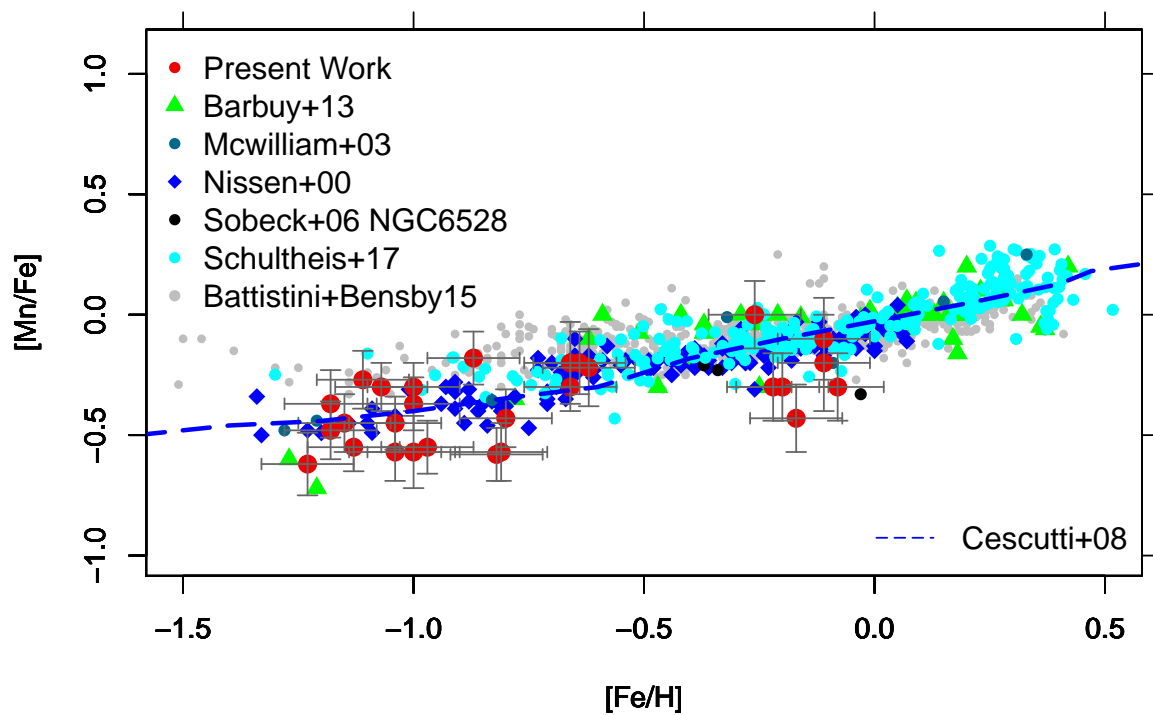


Figure 3.10:  $[\text{Mn}/\text{Fe}]$  vs.  $[\text{Fe}/\text{H}]$  for the sample stars and literature data: the present sample (red filled circles), Nissen et al. (2000) (blue filled diamonds), Sobeck et al. (2006) (black filled circles), McWilliam et al. (2003) (deep sky blue filled circles), Barbuy et al. (2013) (green filled triangles), Schultheis et al. (2017) (blue filled circles), and Battistini & Bensby (2015) (grey filled circles). Chemical evolution models by Cescutti et al. (2008) (blue dashed line); are overplotted. Errors are assumed as in Fig. 3.8.

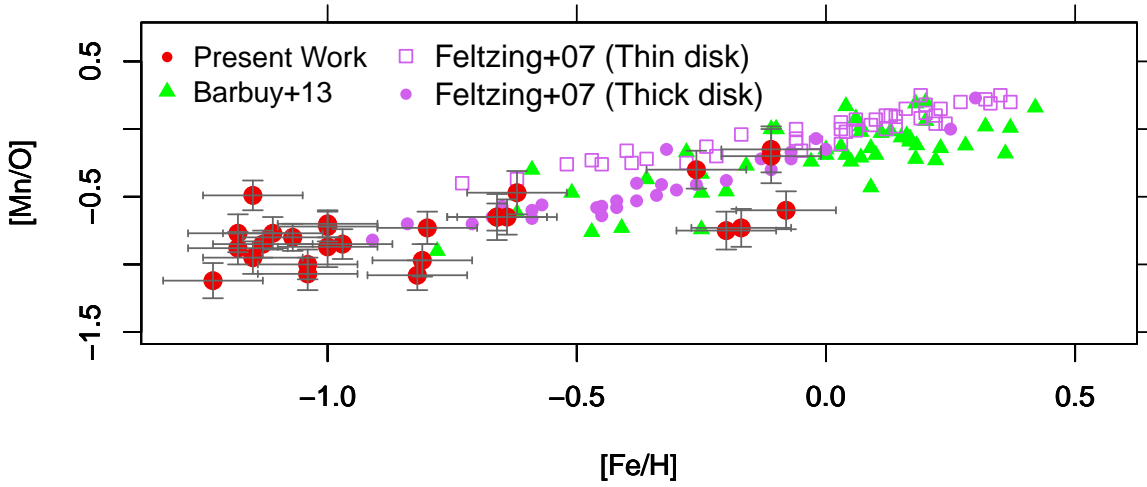


Figure 3.11:  $[\text{Mn}/\text{O}]$  vs.  $[\text{Fe}/\text{H}]$ . Symbols: present work (red filled circles), Barbuy et al. (2013) (green filled triangles), Feltzing et al. (2007) thin disk (violet open squares), Feltzing et al. (2007) thick disk (violet filled circles). Errors are assumed as in Fig. 3.8.

According to McWilliam (2016)  $[\text{Cu}/\text{O}]$  has much less spread than  $[\text{Cu}/\text{Fe}]$  data, Fig. 3.13 shows  $[\text{Cu}/\text{O}]$  vs.  $[\text{Fe}/\text{H}]$ , where the behaviour of the sample cluster stars track well the Johnson et al. (2014) field stars data. This rather straight correlation between Cu and O, indicates the production of Cu and O in the same massive stars.

### 3.4.3 Zinc

The main isotopes of Ti, Co, Ni, Cu, and Zn are produced only or mainly in the zone that undergoes explosive Si burning with complete Si exhaustion (LC03). The relevant Zn isotopes  $^{64,66,67,68}\text{Zn}$  are produced in core He burning but  $^{64}\text{Zn}$  is destroyed in convective C shell; they are also produced in  $\alpha$ -rich freeze-out layers in complete explosive Si-burning (LC03, WW95, Woosley et al. 2002, Nomoto et al. 2013). These contributions do not, however, explain the high  $[\text{Zn}/\text{Fe}]$  observed in metal-poor stars. Umeda & Nomoto (2002, 2005), Nomoto et al. (2013) suggested that  $^{64}\text{Zn}$  is produced in energetic explosive nucleosynthesis so-called hypernovae.

Figure 3.14 shows  $[\text{Zn}/\text{Fe}]$  vs.  $[\text{Fe}/\text{H}]$  for the present sample, and bulge field stars from Barbuy et al. (2015), Bensby et al. (2013, 2017), and metal-poor stars from Howes et al. (2015, 2016), Casey & Schlafman (2016) and Koch et al. (2016), and for thick disk stars

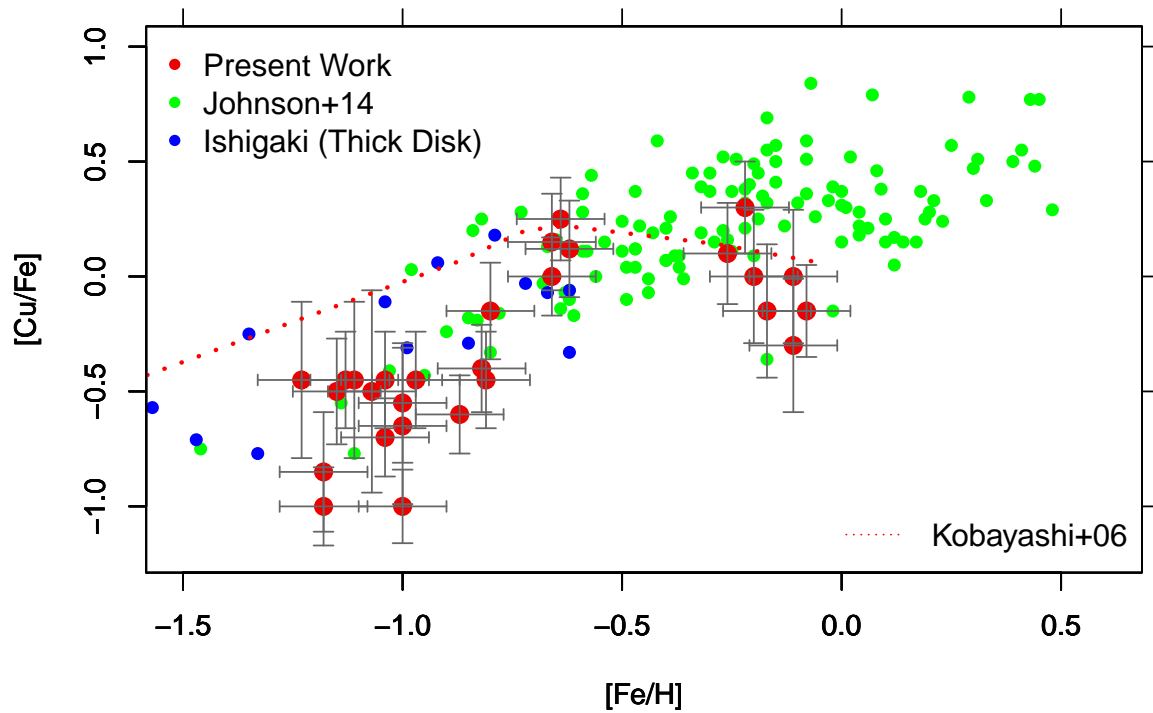


Figure 3.12:  $[Cu/Fe]$  vs.  $[Fe/H]$  for the present sample (red filled circles), Johnson et al. (2014) (green filled circles), and Ishigaki et al. (2013) (blue filled circles). Chemical evolution models by and Kobayashi et al. (2006) (red dotted lines) are overplotted. Errors are assumed as in Fig. 3.8.

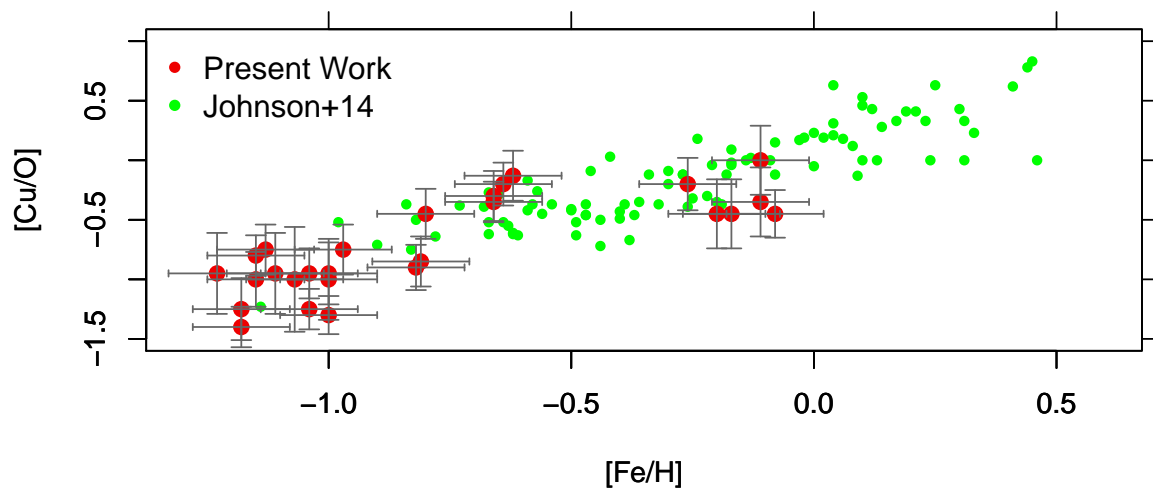


Figure 3.13:  $[Cu/O]$  vs.  $[Fe/H]$ . Data from the present work (red filled circles), and from Johnson et al. (2014) (green filled circles) are plotted.

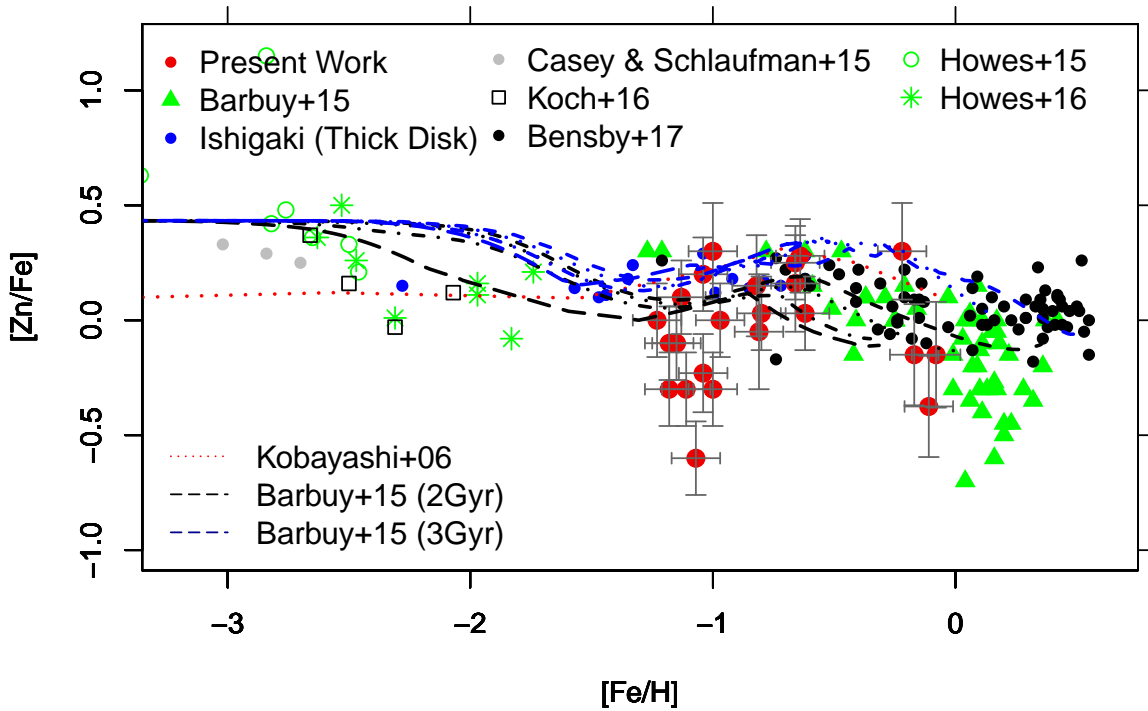


Figure 3.14:  $[Zn/Fe]$  vs.  $[Fe/H]$ . Symbols: present work (filled red circles), Barbuy et al. (2015) (green filled triangles), Ishigaki et al. (2013) (blue filled circles), Howes et al. (2015) (green open circles), Howes et al. (2016) (green crosses), Casey & Schlafman (2016) (grey filled circles), Koch et al. (2016) (black open squares), Bensby et al. (2017) (black filled circles). Chemical evolution models by Kobayashi et al. (2006) (red dotted line). The Barbuy et al. (2015) models are shown for enrichment timescales of 2 (black) and 3 (blue) Gyr. In each case, the models for radius with respect to the Galactic centre of  $r < 0.5$  kpc (dashed lines),  $0.5 < r < 1$  kpc (dotted lines),  $1 < r < 2$  kpc (dash-dotted lines),  $2 < r < 3$  kpc (long-dashed lines) are overplotted. Errors are assumed as in Fig. 3.8.

data from Ishigaki et al. (2013) and Nissen et al. (2011).

A high Zn abundance is found for bulge metal-poor stars in the range  $-3.0 \lesssim [\text{Fe}/\text{H}] \lesssim -0.8$ . This behaviour is similar to that previously reported in metal-poor halo and disk stars (e.g. Sneden et al. 1991; Nissen & Schuster 2011). In all samples  $[\text{Zn}/\text{Fe}]$  decreases with increasing metallicity, reaching a solar value at  $[\text{Fe}/\text{H}] > -0.4$ .

The nucleosynthesis taking place in hypernovae is needed to reproduce this Zn enhancement in metal-poor stars, as proposed by Umeda & Nomoto (2005), and Nomoto et al. (2013, and references therein). The contribution in Zn by hypernovae in the chemical evolution models by Barbuy et al. (2015) proved to be needed to reproduce the data (see their Fig. 12). As for the present results  $[\text{Zn}/\text{Fe}]$  is enhanced in the metal-poor clusters and decreases with metallicity, following the literature data. The exception is the globular cluster HP 1, showing low  $[\text{Zn}/\text{Fe}]$  at its metallicity of  $[\text{Fe}/\text{H}] \sim -1.0$ . A further inspection of this cluster would be of great interest, given that it has characteristics of being very old, and could reveal particularities due to its early formation.

Figure 3.14 compares  $[\text{Zn}/\text{Fe}]$  vs.  $[\text{Fe}/\text{H}]$  for bulge stars with chemodynamical evolution models of the Galactic bulge by Barbuy et al. (2015), further described in Friaça & Barbuy (2017). The hypernovae yields are suitable for metallicities more metal-poor than  $[\text{Fe}/\text{H}] \lesssim -2.0$ , as adopted in these models (Barbuy et al. 2015; Friaça & Barbuy 2017; da Silveira 2017). For this reason these models in the range  $-2.0 < [\text{Fe}/\text{H}] < -1.0$  are interrupted. Models by Kobayashi et al. (2006) taking into account hypernovae also reproduce well the Zn behaviour.

For disk stars with  $[\text{Fe}/\text{H}] > 0.0$ , Reddy et al. (2003, 2006) obtained  $[\text{Zn}/\text{Fe}] \sim 0.0$ , Bensby et al. (2003, 2005) found  $[\text{Zn}/\text{Fe}]$  essentially constant, whereas Allende-Prieto et al. (2004) found increasing  $[\text{Zn}/\text{Fe}]$  with increasing metallicity. The Bensby et al. (2013, 2017) results for microlensed dwarf bulge stars also give a solar  $[\text{Zn}/\text{Fe}]$  at all metallicities, differently from Barbuy et al. (2015), where  $[\text{Zn}/\text{Fe}]$  decreases sharply at the high metallicity end. The present results for the metal-rich clusters also appear to decrease with increasing metallicity, despite some spread. This decrease implies the action of SNIa, and could be an evidence of differences in the chemical enrichment of bulge giants and a thick disk sample. It is interesting that Duffau et al. (2017) also found decreasing  $[\text{Zn}/\text{Fe}]$  for red giants, and constant  $[\text{Zn}/\text{Fe}]$  for dwarfs, at the supersolar metallicities. They interpreted this discrepancy in terms of stellar populations, i.e. that their red giants should be younger

than the dwarfs, and for this reason, to contain Fe enriched from SNIa. The age explanation does not fit the present data, because our sample consists of old globular clusters. Stars in NGC 6528 have subsolar  $[Zn/Fe]$ , whereas NGC 6553 has  $[Zn/Fe] \sim +0.3$  for one star, and subsolar in the other star. In particular, at its location in the Galaxy, NGC 6553 has kinematical characteristics compatible with bulge or disk stars (Zoccali et al. 2001b), whereas NGC 6528 is located in the bulge, so that they might be different from each other. In conclusion, there seems to be a trend to have decreasing Zn-to-Fe with increasing metallicity, despite it not being clear for NGC 6553. Another aspect is the suggestion that the local metal-rich thick disk consists of stars having migrated from the inner regions of the Galaxy (Adibekyan et al. 2013, Anders et al. 2017, by Grisoni et al. 2017). Recio-Blanco et al. (2017) has also advanced a possibility of this population corresponding to a dwarf galaxy that previously merged with the Milky Way in the solar vicinity. One question that comes to mind is whether it would be possible that the metal-rich bulge stars either by Barbuy et al. (2015), or those by Bensby et al. (2017) correspond to the alpha-enhanced thick disk by Grisoni et al. (2017). To test this it would be of interest to derive Zn abundances in these metal-rich thick disk stars.

Skúladóttir et al. (2017) derived Zn abundances in stars of the dwarf galaxy Sculptor. Skúladóttir et al. (2018) further analyse the behaviour of  $[Zn/Fe]$ , and find  $[Zn/Fe]$  decreasing with increasing metallicities, and verified that the same occurs with other dwarf galaxies studied in the literature such as Sagittarius, Sextans, Draco and Ursa Minor. The authors suggest that it is more naturally explained by the enrichment of Fe, and no Zn enrichment from SNIa, therefore a behaviour similar to that of alpha-elements, although other less likely possibilities are discussed.

Finally, a general comment is that there is a trend for the cluster stars to be deficient relative to field bulge stars for Sc, V, and Zn. In particular at the metal-rich end, it could be attributed to noise in the spectra. For the metal-poor clusters, on the other hand, further inspection would be of great interest, because it could have an impact in the interpretation of enrichment of these globular clusters.

Table 3.5 - Line-by-line abundance ratios of Sc, V, Mn, Cu, and Zn for the sample.

Line	$\lambda(\text{\AA})$	47 Tucanae					NGC 6553				NGC 6528			HP 1	
		M8	M11	M12	M21	M25	II-64	II-85	III-8	267092	I-18	I-36	I-42	2	3
ScI	5671.805	+ 0.00	+ 0.03	+ 0.05	+ 0.00	-0.10	-0.30	-0.30	-0.30	-0.15	-0.30	-0.30	+ 0.00	—	+ 0.00
ScI	5686.826	+ 0.00	+ 0.00	+ 0.10	—	+ 0.00	-0.30	+ 0.00	-0.30	-0.25	-0.30	-0.50	+ 0.00	+ 0.00	—
ScI	6210.676	-0.25	-0.30	-0.10	—	-0.20	-0.30	—	-0.30	-0.30	-0.50	-0.60	-0.30	+ 0.00	+ 0.00
ScII	5526.790	+ 0.00	-0.30	+ 0.05	+ 0.00	+ 0.00	-0.30	+ 0.00	-0.30	+ 0.00	-0.40	-0.30	-0.30	-0.15	+ 0.00
ScII	5552.224	+ 0.00	+ 0.00	—	—	+ 0.10	+ 0.00	+ 0.30	+ 0.00	—	—	—	—	—	+ 0.00
ScII	5657.896	+ 0.20	+ 0.15	+ 0.30	+ 0.00	+ 0.30	+ 0.00	+ 0.30	+ 0.00	+ 0.30	-0.30	+ 0.00	+ 0.00	+ 0.00	+ 0.00
ScII	5684.202	+ 0.30	+ 0.05	+ 0.30	+ 0.00	+ 0.30	-0.10	+ 0.30	-0.25	+ 0.00	-0.30	-0.30	+ 0.00	+ 0.00	+ 0.00
ScII	6245.637	+ 0.10	+ 0.00	+ 0.00	+ 0.00	+ 0.25	+ 0.00	+ 0.10	-0.30	+ 0.00	-0.30	-0.30	—	+ 0.00	+ 0.00
ScII	6300.698	+ 0.15	+ 0.00	+ 0.10	—	+ 0.00	+ 0.00	+ 0.25	-0.15	—	-0.30	-0.40	+ 0.00	+ 0.00	+ 0.30
ScII	6320.851	+ 0.15	+ 0.10	+ 0.25	+ 0.00	+ 0.20	+ 0.00	—	+ 0.00	+ 0.00	-0.30	-0.30	+ 0.00	+ 0.00	+ 0.00
ScII	6604.601	+ 0.15	+ 0.00	+ 0.05	-0.10	+ 0.00	-0.15	—	-0.30	+ 0.00	-0.35	-0.45	-0.30	-0.20	-0.15
VI	5703.560	+ 0.10	+ 0.00	+ 0.10	-0.20	+ 0.00	+ 0.00	+ 0.25	-0.25	+ 0.00	-0.12	-0.10	+ 0.00	-0.30	+ 0.00
VI	6081.440	-0.10	+ 0.00	-0.05	-0.30	-0.10	-0.10	—	-0.10	-0.15	-0.30	-0.15	+ 0.00	-0.30	-0.25
VI	6090.220	+ 0.00	+ 0.00	+ 0.15	-0.05	+ 0.00	-0.25	+ 0.00	-0.15	-0.15	-0.25	-0.30	+ 0.00	-0.30	-0.10
VI	6119.520	+ 0.00	+ 0.05	+ 0.12	-0.05	+ 0.00	+ 0.00	+ 0.00	+ 0.00	-0.15	-0.10	-0.30	+ 0.00	—	-0.20
VI	6199.190	-0.15	+ 0.00	-0.10	-0.10	+ 0.00	-0.30	—	-0.10	-0.30	-0.30	-0.30	+ 0.00	-0.10	-0.12
VI	6243.100	-0.10	+ 0.00	+ 0.00	+ 0.00	+ 0.00	-0.35	—	-0.25	-0.15	-0.20	-0.30	+ 0.00	-0.15	-0.10
VI	6251.820	-0.10	+ 0.00	+ 0.00	-0.30	+ 0.00	+ 0.00	—	-0.30	-0.15	-0.30	-0.30	+ 0.00	-0.30	-0.05
VI	6274.650	-0.10	+ 0.00	-0.10	-0.15	+ 0.00	-0.15	—	-0.30	-0.15	-0.20	-0.15	+ 0.00	-0.10	—
VI	6285.160	+ 0.00	-0.05	+ 0.00	+ 0.00	+ 0.00	—	—	—	—	-0.30	—	—	—	—
MnI	6013.513	-0.10	-0.05	+ 0.00	-0.40	-0.30	-0.30	+ 0.00	-0.45	-0.30	-0.30	+ 0.00	+ 0.00	-0.60	-0.50
MnI	6016.640	-0.30	-0.30	-0.30	-0.40	-0.30	-0.30	—	-0.45	-0.30	-0.30	-0.30	—	-0.60	-0.55
MnI	6021.800	-0.20	-0.30	-0.30	-0.50	-0.30	-0.30	+ 0.00	-0.40	—	-0.30	-0.30	-0.20	-0.50	-0.60
CuI	5105.537	+ 0.20	+ 0.00	+ 0.00	-0.30	+ 0.00	-0.30	-0.10	-0.30	+ 0.00	-0.30	-0.30	-0.60	—	-0.60
CuI	5218.197	+ 0.30	+ 0.30	+ 0.30	+ 0.00	+ 0.00	—	—	-0.15	+ 0.30	-0.15	-0.45	—	-1.00	-0.30
ZnI	4810.529	+ 0.25	+ 0.00	+ 0.02	+ 0.05	+ 0.25	—	—	-0.05	+ 0.30	+ 0.00	-0.30	—	—	+ 0.00
ZnI	6362.339	+ 0.30	+ 0.05	+ 0.30	+ 0.05	+ 0.25	—	—	-0.00	+ 0.30	+ 0.00	-0.30	—	—	+ 0.00

Line	$\lambda(\text{\AA})$	HP-1					NGC 6522				NGC 6558				
		2115	2461	2939	3514	5037	5485	B-107	B-122	B-128	B-130	283	364	1072	1160
ScI	5671.805	-0.10	—	+0.12	+0.05	-0.12	—	—	+0.00	-0.30	—	—	—	—	—
ScI	5686.826	+0.10	—	+0.25	—	—	—	—	—	—	—	—	—	—	—
ScI	6210.676	+0.15	—	+0.15	—	-0.05	—	—	—	-0.05	—	—	—	—	—
ScII	5526.790	-0.15	+0.00	+0.00	-0.30	-0.18	-0.30	+0.00	+0.00	+0.00	-0.05	-0.30	-0.15	-0.15	-0.15
ScII	5552.224	+0.30	—	—	—	—	—	-0.30	—	—	+0.30	—	—	—	—
ScII	5657.896	+0.00	+0.00	+0.30	+0.00	+0.10	+0.15	+0.00	+0.05	+0.00	+0.00	-0.3	-0.15	+0.30	-0.10
ScII	5684.202	+0.00	+0.00	+0.00	-0.15	+0.00	+0.00	-0.15	+0.10	+0.00	+0.00	+0.00	-0.10	+0.30	—
ScII	6245.637	+0.10	+0.00	+0.30	+0.00	+0.12	+0.03	-0.10	+0.15	+0.00	+0.00	-0.03	—	-0.30	-0.20
ScII	6300.698	+0.30	+0.00	—	+0.30	+0.30	—	—	+0.00	+0.00	+0.00	—	+0.60	—	+0.00
ScII	6320.851	+0.00	+0.15	+0.30	+0.30	+0.15	+0.00	-0.15	+0.15	+0.30	+0.15	+0.00	—	+0.15	-0.30
ScII	6604.601	+0.00	+0.00	+0.30	+0.30	+0.00	-0.05	-0.30	+0.05	+0.15	+0.00	+0.00	—	+0.10	-0.05
VI	5703.560	+0.00	-0.10	+0.00	+0.00	+0.00	+0.00	—	-0.20	-0.10	-0.05	-0.05	+0.00	-0.30	+0.00
VI	6081.440	+0.00	—	+0.00	+0.02	+0.00	+0.00	—	-0.25	-0.10	-0.15	+0.05	+0.30	+0.00	+0.00
VI	6090.220	+0.00	+0.00	+0.00	+0.00	+0.00	—	+0.00	+0.00	-0.15	-0.1	-0.05	+0.00	-0.15	-0.10
VI	6119.520	+0.05	+0.00	+0.00	+0.00	+0.00	—	+0.00	+0.00	-0.15	+0.0	-0.05	+0.00	+0.00	-0.10
VI	6199.190	+0.00	-0.05	+0.00	+0.05	+0.00	—	—	+0.00	+0.00	+0.0	+0.00	—	-0.30	+0.05
VI	6243.100	+0.00	+0.00	+0.00	+0.05	+0.00	+0.00	-0.15	+0.00	-0.10	+0.0	+0.00	—	-0.20	+0.00
VI	6251.820	+0.00	+0.00	+0.05	+0.00	+0.00	+0.00	—	-0.10	+0.0	-0.05	+0.00	+0.15	-0.15	+0.10
VI	6274.650	—	+0.00	+0.00	+0.00	+0.00	—	-0.10	+0.00	-0.25	-0.15	—	—	-0.15	+0.00
VI	6285.160	—	—	—	—	—	—	—	—	—	—	—	—	—	—
MnI	6013.513	-0.30	-0.3	-0.30	-0.30	-0.35	-0.40	-0.55	-0.50	-0.55	-0.50	-0.50	-0.25	-0.60	-0.50
MnI	6016.640	-0.30	-0.3	-0.30	-0.30	-0.35	-0.55	-0.55	-0.60	-0.60	-0.60	—	-0.32	-0.60	-0.35
MnI	6021.800	-0.30	-0.2	-0.30	-0.50	-0.40	-0.50	-0.55	-0.60	-0.60	-0.60	-0.40	-0.30	-0.65	-0.50
CuI	5105.537	-0.80	-0.8	-1.00	-1.10	-1.00	-1.00	-0.60	-0.60	-0.50	-0.60	-0.70	-0.60	-0.80	-0.70
CuI	5218.197	-0.30	-0.1	+0.00	-0.60	-0.30	—	-0.30	-0.30	-0.30	-0.30	-0.30	—	-0.1	—
ZnI	4810.529	—	-0.30	-0.60	-0.10	-0.30	-0.30	+0.05	-0.25	+0.00	-0.30	-0.10	—	+0.00	+0.20
ZnI	6362.339	—	—	—	—	—	—	+0.15	+0.15	+0.30	-0.15	—	—	—	—

Table 3.6 - Mean abundances of Sc, V, Mn, Cu, and Zn for the sample.

Stars	Mean abundances												
	[Fe/H]	[Sc/Fe]	$\delta_{[ScI/Fe]}$	[ScII/Fe]	$\delta_{[ScII/Fe]}$	[V/Fe]	$\delta_{[VI/Fe]}$	[Mn/Fe]	$\delta_{[MnI/Fe]}$	[Cu/Fe]	$\delta_{[CuI/Fe]}$	[Zn/Fe]	$\delta_{[ZnI/Fe]}$
47Tuc													
M8	-0.64	-0.08	0.12	+0.13	0.08	-0.05	0.07	-0.20	0.08	+0.25	0.04	+0.28	0.03
M11	-0.62	-0.09	0.15	+0.04	0.06	+0.00	0.02	-0.22	0.12	+0.12	0.12	+0.03	0.03
M12	-0.66	+0.02	0.08	+0.15	0.12	+0.01	0.09	-0.20	0.14	+0.15	0.12	+0.16	0.14
M21	-0.80	+0.00	0.08	-0.02	0.04	-0.13	0.11	-0.43	0.05	-0.15	0.12	+0.03	0.03
M25	-0.66	-0.10	—	+0.14	0.12	-0.01	0.03	-0.30	0.00	+0.00	0.00	+0.25	0.00
NGC 6553													
II-64	-0.20	-0.30	0.00	-0.06	0.06	-0.14	0.13	-0.30	0.00	+0.00	0.24	—	—
II-85	-0.26	-0.15	0.15	+0.21	0.08	+0.08	0.12	+0.00	0.00	+0.10	0.16	—	—
III-8	-0.17	-0.30	0.00	-0.16	0.13	-0.18	0.10	-0.43	0.02	+0.15	0.24	-0.15	0.03
III-9	-0.22	-0.23	0.06	+0.05	0.12	-0.15	0.08	-0.30	0.00	+0.30	0.12	+0.30	0.00
NGC 6528													
I-18	-0.08	-0.37	0.09	-0.32	0.02	-0.23	0.08	-0.30	0.00	-0.15	0.12	-0.15	0.08
I-36	-0.11	-0.47	0.12	-0.29	0.14	-0.24	0.08	-0.20	0.14	+0.00	0.24	-0.37	0.03
I-42	-0.11	-0.10	0.14	-0.10	0.12	+0.00	0.00	-0.10	0.10	-0.30	0.24	—	—
HP 1													
2	-1.00	+0.00	—	-0.05	0.07	-0.22	0.09	-0.57	0.05	-1.00	—	+0.30	—
3	-0.97	+0.00	—	-0.02	0.12	-0.12	0.08	-0.55	0.04	-0.45	0.12	+0.00	—
2115	-1.00	+0.05	0.11	+0.07	0.13	+0.01	0.02	-0.30	0.00	-0.55	0.20	—	—
2461	-1.11	—	—	+0.02	0.06	-0.02	0.04	-0.27	0.05	-0.45	0.29	-0.30	—
2939	-1.07	+0.17	0.06	+0.20	0.12	+0.01	0.02	-0.30	0.00	-0.50	0.41	-0.60	—
3514	-1.18	+0.05	—	+0.06	0.18	+0.02	0.02	-0.37	0.09	-0.85	0.20	-0.10	—
5037	-1.00	-0.09	0.04	+0.08	0.10	+0.00	0.00	-0.37	0.02	-0.65	0.29	-0.30	—
5485	-1.18	—	—	-0.03	0.07	+0.00	0.00	-0.48	0.06	-1.00	—	-0.30	—
NGC 6522													
B-107	-1.13	—	—	-0.11	0.12	-0.06	0.06	-0.55	0.00	-0.45	0.12	+0.10	0.05
B-122	-0.81	+0.00	—	+0.07	0.06	-0.07	0.10	-0.57	0.05	-0.45	0.12	-0.05	0.20
B-128	-0.82	-0.18	0.13	+0.06	0.11	-0.12	0.07	-0.58	0.02	-0.40	0.08	+0.15	0.15
B-130	-1.04	—	—	+0.05	0.11	-0.06	0.06	-0.57	0.05	-0.45	0.12	-0.23	0.08
NGC6558													
283	-1.15	—	—	-0.16	0.16	-0.01	0.03	-0.45	0.05	-0.50	0.16	-0.10	—
364	-1.15	—	—	+0.05	0.32	+0.09	0.12	-0.29	0.03	-0.60	—	—	—
1072	-1.23	—	—	+0.07	0.22	-0.16	0.11	-0.62	0.07	-0.45	0.29	+0.00	—
1160	-1.04	—	—	-0.13	0.11	-0.01	0.06	-0.45	0.02	-0.70	—	+0.20	—

### 3.5 Summary

Globular clusters of the Galactic bulge should trace the formation process of the central parts of the Galaxy. They are also tracers of the older stellar populations in the bulge. Chemical tagging is a next big step for the understanding of the Milky Way formation. The iron-peak elements have been little studied so far, but their study should help understanding: a) nucleosynthesis of these elements is complex and observations can help constraining their formation; b) Sc and V appear to vary in lockstep with Fe in the present sample, but Sc has been found to be alpha-like in thick disk and halo stars, and further studies are needed; c) Mn is deficient in metal-poor stars, and steadily increases with metallicity due to enrichment from SNIa; d) Cu shows a secondary-like behaviour, in principle indicating its production in a weak s-process in massive stars; e) Zn is alpha-like in halo and thick disk stars, and also in the bulge, as concerns metal-poor stars. For metal-rich stars there is a controversy as to whether it decreases with increasing metallicity, or if  $[Zn/Fe]$  maintains a solar value.

We have derived abundances of the iron-peak elements Sc, V, Mn, Cu, and Zn, in 28 red giants in the five bulge globular clusters NGC 6553, NGC 6528, HP 1, NGC 6522, NGC 6558, and five red giants in the reference inner halo or thick disk cluster 47 Tucanae. The work was based on FLAMES-UVES high-resolution spectra obtained at the VLT UT2

telescope.

Vanadium varies in lockstep with Fe. Sc behaves similarly to V, not showing a clear enhancement, which was previously suggested by Nissen et al. (2000) for alpha-rich halo and thick disk stars. Both  $[\text{Sc}/\text{Fe}]$  and  $[\text{V}/\text{Fe}]$  seem to decrease with increasing metallicity at the high metallicity end.

Manganese is deficient in metal-poor stars and increases to solar values for the more metal-rich stars, indicating that it is underproduced in massive stars, and later produced in SNIa. Copper shows a behaviour as a secondary element, having low values at low metallicities, and steadily increasing with increasing metallicity, indicating an enrichment through a weak-s process in massive stars, and in good agreement with chemical evolution models.

Zinc is enhanced in metal-poor stars, likewise an alpha-element, and decreases with increasing metallicity. At the high metallicity end the behaviour of the present data is different from that found by Bensby et al. (2013, 2017), that show solar ratios at the high metallicities. This could be a discriminator of having the contribution of SNIa or not. This is made less clear given the difference in  $[\text{Zn}/\text{Fe}]$  found by Duffau et al. (2017) for red giants and dwarfs. It is important to stress that Skúladóttir et al. (2017, 2018) also found  $[\text{Zn}/\text{Fe}]$  decreasing with metallicity for dwarf galaxies. It is of great interest to pursue abundance derivation of iron-peak elements, and in particular Sc in all stellar populations, and Zn in bulge stars.



## Cobalt and Copper in bulge field stars

### *4.1 Introduction: Iron-peak elements Cobalt and Copper in bulge field stars*

The detailed study of element abundances in the Milky Way bulge can inform on the chemical enrichment processes in the Galaxy, and on the early stages of the Galaxy formation. Field stars in the Galactic bulge are old (Renzini et al. 2018, and references therein), and bulge globular clusters, in particular the moderately metal-poor ones, are very old (e.g. Kerber et al. 2018, 2019, Oliveira et al. 2020). The study of bulge stars can therefore provide hints on the chemical enrichment of the earliest stellar populations in the Galaxy.

Abundance ratio indicators have been extensively used in the literature and interpreted in terms of nucleosynthesis typical of different types of supernovae and chemical evolution models. The studies are most usually based on the alpha-elements O, Mg, Ca, and Si, and on Al and Ti, which behave like alpha-elements that are enhanced in metal-poor stars (e.g. Mishenina et al. 2002, Cayrel et al. 2004, Lai et al. 2008), in the Galactic bulge (e.g. McWilliam 2016, Friaça & Barbuy 2017), and elliptical galaxies (e.g. Matteucci & Brocato 1990). The alpha-element enhancement in old stars is due to a fast chemical enrichment by type II supernovae (SNII). Other independent indicators have so far been less well studied, notably iron-peak elements, s-elements, and r-elements. Ting et al. (2012) aimed to identify which groups of elements are independent indicators of the supernova type that produced them. Their study reveals two types of SNII: one that produces mostly  $\alpha$ -elements and one that produces both  $\alpha$ -elements and Fe-peak elements with a large enhancement of heavy Fe-peak elements, which may be the contribution from hypernovae.

This shows the importance of deriving Fe-peak element abundances.

Our group previously analysed the iron-peak elements Mn and Zn (Barbuy et al. 2013, 2015, da Silveira et al. 2018) in the same sample of field stars studied in the present work, as well as Sc, V, Cu, Mn, and Zn in bulge globular cluster stars (Ernandes et al. 2018). In this chapter we analyse abundances of the iron-peak elements cobalt and copper. These two elements, and copper in particular, deserve attention because the nucleosynthesis processes that produce them have been discussed over the years in the literature. The production of Cu in massive stars as a secondary product was only challenged by Mishenina et al. (2002), who argued that a sum of a secondary and a primary process would be needed to explain the behaviour of  $[\text{Cu}/\text{Fe}]$  versus  $[\text{Fe}/\text{H}]$  in metal-poor stars. Bisterzo et al. (2004) concluded that most Cu derives from a secondary weak-s process in massive stars; a small primary contribution of  $\sim 5\%$  in the Sun would be due to the decay of  $^{63,65}\text{Zn}$ , and this becomes dominant for  $[\text{Fe}/\text{H}] < -2.0$ . On the other hand, asymptotic giant branch (AGB) stars and SNIa contribute little to Cu. Pignatari et al. (2010) presented nucleosynthesis calculations showing an increased production of Cu from a weak-s process in massive stars. Romano & Matteucci (2007) concluded that Cu enrichment is due to a primary contribution from explosive nucleosynthesis in SNII, and a weak s-process in massive stars. Lai et al. (2008) data on halo stars agreed with these models.

According to WW95, Limongi et al. (2003), and Woosley et al. (2002), the upper iron-group elements are mostly synthesized in two processes: either neutron capture on iron-group nuclei during He burning and later burning stages (also called the weak *s*-component); or the  $\alpha$ -rich freezeout in the deepest layers. Both cobalt and copper are produced as primary elements in the  $\alpha$ -rich freezeout and as secondary elements in the weak *s*-process in massive stars. The relative efficiency of these two contributions to the nucleosynthesis of Co and Cu can be tested by deriving their abundances in the Galaxy. Abundances gathered so far, in the Galactic bulge in particular, indicate that copper behaves as a secondary element, therefore with a significant contribution from the weak *s*-process. Cobalt, which appears to vary in lockstep with Fe, seems instead to be mostly contributed from the  $\alpha$ -rich freezeout mechanism (Barbuy et al. 2018a, Woosley, private communication).

Very few previous analyses of iron-peak elements in Galactic bulge stars are available in the literature. For copper, Johnson et al. (2014) and Xu et al. (2019) are so far the only

available data derived from moderately high-resolution spectra. For cobalt, Johnson et al. (2014) present results from moderately high-resolution spectra, Schultheis et al. (2017) from near-infrared (NIR) spectra, and Lomaeva et al. (2019) from high-resolution spectra.

As presented in Chapter 2, the sample consists of 43 red giants from Zoccali et al. (2006), and 13 red clump giants from Hill et al. (2011). The description of the sample selected to carry out this analysis of Co and Cu abundances is described in the section 2. Our sample of bulge red giant stars had the abundances of O, Na, Mg, and Al studied in Zoccali et al. (2006) and Lecureur et al. (2007). The C, N, and O abundances were revised in Friaça & Barbuy (2017). The iron-peak elements Mn and Zn were studied in Barbuy et al. (2013, 2015) and da Silveira et al. (2018), and heavy elements in van der Swaelmen et al. (2016). In summary, the abundances of C, N, O, Na, Mg, Al, Mn, Zn, and heavy elements were derived. González et al. (2011) derived abundances of Mg, Si, Ca, and Ti for a GIRAFFE counterpart of the sample, obtained at  $R \sim 22\,000$ ). Da Silveira et al. (2018) derived O and Zn from GIRAFFE data in two fields.

It is interesting to note that this data set, including both the high-resolution UVES data as well as the moderately high-resolution GIRAFFE data, has become an important reference for bulge studies; from this same ESO programme, Johnson et al. (2014) analysed GIRAFFE data for 156 red giants in the Blanco and near-NGC 6553 fields, and Xu et al. (2019) reanalysed 129 of these same stars. Jönsson et al. (2017) reanalysed UVES spectra of a sub-sample of 33 stars from our sample of 43 red giants, and additionally analysed two other stars, BW-b1 and B2-b8, that were observed but not included in the studies by Zoccali et al. (2006, 2008). A comparison of stellar parameters between Zoccali et al. (2006) and Lecureur et al. (2007) relative to Jönsson et al. (2017) is discussed in da Silveira et al. (2018). The same sub-sample that was reanalysed by Jönsson et al. (2017) was further analysed by Forsberg et al. (2019), Lomaeva et al. (2019), and Grisoni et al. (2020) for different elements, adopting their own stellar parameters. Finally, Schultheis et al. (2017) compared APOGEE (Apache Point Observatory Galactic Evolution Experiment) results with stars in common with Zoccali et al. (2008)’s results for stars observed with GIRAFFE.

## 4.2 Abundance analysis

The abundance analysis was carried out following the same method described in the chapter 3.3.1. The stellar parameters adopted from previous studies (Zoccali et al. 2006, 2008, Lecureur et al. 2007), which we summarize below.

The equivalent widths for selected lines of Fe, Na, Mg, Al, Si, Ca, Sc, Ti, and Ni were measured using the code DAOSPEC (Stetson and Pancino 2008). The selection of clean Fe lines and their atomic parameters was compiled using a spectrum of  $\mu$  Leo as reference (Lecureur et al. 2007).

The LTE abundance analysis was performed using an updated version of the code ABON2 (Spite 1967) and MARCS models (Gustafsson et al. 2008). Excitation equilibrium was imposed on the Fe I lines in order to refine the photometric  $T_{\text{eff}}$ , while photometric gravity was imposed even if ionization equilibrium was not fulfilled.

Elemental abundances were obtained through line-by-line spectrum synthesis calculations. The calculations of synthetic spectra were carried out using the PFANT code described in Barbuy et al. (2018b), where molecular lines of the CN  $A^2\Pi-X^2\Sigma$ ,  $C_2$  Swan  $A^3\Pi-X^3\Pi$  and TiO  $A^3\Phi-X^3\Delta$   $\gamma$ , and  $B^3\Pi-X^3\Delta$   $\gamma'$  systems are taken into account. The MARCS model atmospheres are adopted (Gustafsson et al. 2008).

The abundances derived line-by-line are reported in Table 4.2. The final mean abundances are given in the last three columns of Table 4.3, where the final mean values of  $[Cu/Fe]$  and  $[Co/Fe]$  in LTE and NLTE-corrected are reported.

Figure 4.1 shows the fit to the eight Co I lines in star BWc-4. Figure 4.2 shows the fit to the Cu I 5105.537 and 5218.197 Å lines for star BL-7.

### 4.2.1 Line parameters: hyperfine structure, oscillator strengths

We derive cobalt and copper abundances for the 56 sample stars using the lines of Co I and Cu I reported in Table 4.1. The oscillator strengths and the hyperfine structure (HFS) we adopted are described below.

#### *Cobalt: Co I lines*

Cobalt has the unique species  $^{59}\text{Co}$  (Asplund et al. 2009). The HFS was taken into account by applying the code made available by McWilliam et al. (2013) together with the A and B constants reported in Table D.2 that were adopted from Pickering et al. (1996).

Cobalt has a nuclear spin  $I = 7/2$ . Central wavelengths and excitation potential values from Kurucz (1993)<sup>1</sup>, the oscillator strengths from Kurucz (1993), NIST<sup>2</sup> (Martin et al. 2002), and VALD (Piskunov et al. 1995), and the final values adopted are presented in Table 4.1.

Tables D.6, D.7, and D.8 show the HFS components of the Co I lines studied. All these lines were checked by comparing synthetic spectra to high-resolution spectra of the Sun (using the same instrument settings as the present sample of spectra<sup>3</sup>), Arcturus (Hinkle et al. 2000), and the metal-rich giant star  $\mu$  Leo (Lecureur et al. 2007). We adopted the following stellar parameters: effective temperature ( $T_{\text{eff}}$ ), surface gravity ( $\log g$ ), metallicity ( $[\text{Fe}/\text{H}]$ ), and microturbulent velocity ( $v_t$ ) of (4275 K, 1.55, -0.54, 1.65 km.s<sup>-1</sup>) for Arcturus from Meléndez et al. (2003), and (4540 K, 2.3, +0.30, 1.3 km.s<sup>-1</sup>) for  $\mu$  Leo from Lecureur et al. (2007).

#### *Copper: Cu I lines*

Copper abundances were derived from the two Cu I lines at 5105 and 5218 Å already employed and described in detail in Ernandes et al. (2018). The 5782 Å line is not available in the UVES spectra. Isotopic fractions of 0.6894 for <sup>63</sup>Cu and 0.3106 for <sup>65</sup>Cu (Asplund et al. 2009), as well as the HFS structure as given in Ernandes et al. (2018), are adopted.

Figures 4.1 and 4.2 show the fits to the spectra of the Sun, Arcturus, and  $\mu$  Leo. The Cu I atomic parameters and fits to these reference stars were already extensively discussed in Ernandes et al. (2018).

#### *4.2.2 Non-local thermodynamic equilibrium corrections*

We applied the NLTE corrections for each cobalt line following the same method used by Kirby et al. (2018), with the formalism of Bergemann & Cescutti (2010) and Bergemann et al. (2010)<sup>4</sup>. The derivation of corrections from the online code made available requires the choice of atmospheric model, inclusion of stellar parameters of each star, and the line list, followed by the atomic number ( $Z$ ) under study. The corrections so derived line-by-line for the Co abundances are reported in Table 4.2, and final NLTE-corrected Co abundance values are given in Table 4.3.

<sup>1</sup> <http://kurucz.harvard.edu/atoms.html>

<sup>2</sup> [http://physics.nist.gov/PhysRefData/ASD/lines\\_form.html](http://physics.nist.gov/PhysRefData/ASD/lines_form.html)

<sup>3</sup> [http://www.eso.org/observing/dfo/quality/UVES/pipeline/solar\\_spectrum.html](http://www.eso.org/observing/dfo/quality/UVES/pipeline/solar_spectrum.html)

<sup>4</sup> [http://nlte.mpia.degui-siuAC\\_secE.php](http://nlte.mpia.degui-siuAC_secE.php)

Table 4.1 - Central wavelengths and total oscillator strengths.

species	$\lambda$ (Å)	$\chi_{ex}$ (eV)	gf <sub>Kurucz</sub>	gf <sub>NIST</sub>	gf <sub>VALD</sub>	gf <sub>adopted</sub>
CoI	4749.669	3.053457	-0.321	—	-0.236	-0.321
CoI	5212.691	3.514439	-0.110	-0.11	-0.110	-0.110
CoI	5280.629	3.628984	-0.030	-0.03	-0.030	-0.030
CoI	5301.039	1.710426	-2.000	-1.99	-2.000	-2.000
CoI	5342.695	4.020881	0.690	—	0.741	0.690
CoI	5454.572	4.071888	-0.238	—	+0.238	+0.238
CoI	5647.234	2.280016	-1.560	-1.56	-1.560	-1.560
CoI	6117.000	1.785283	-2.490	-2.49	-2.490	-2.490
CoI	6188.996	1.710426	-2.450	-2.46	-2.450	-2.450
CuI	5105.537	1.389035	-1.516	-1.50	hfs	-1.52
CuI	5218.197	3.816948	0.476	0.264	hfs	+0.124

### 4.2.3 Uncertainties

The estimated uncertainties in the atmospheric parameters (i.e.  $\pm 100$  K for temperature,  $\pm 0.20$  for surface gravity, and  $\pm 0.20$  kms<sup>-1</sup> for microturbulent velocity). In Table 4.4 we compute Co and Cu abundances for the metal-rich star B6-f8 and the metal-poor star BW-f8 by changing their parameters by these amounts. The errors computed by adopting models with  $\Delta T_{eff}=+100$ K,  $\Delta \log g=+0.2$ , and  $\Delta v_t=+0.2$  km.s<sup>-1</sup>, as well as final errors, are shown in Table 4.4.

For comparison purposes, we have listed the stars that were also analysed by Johnson et al. (2014) and Jönsson et al. (2016) in Table 4.5, reporting the respective stellar parameters they adopted. Johnson et al. (2014) analysed their corresponding GIRAFFE spectra, while Jönsson et al. (2016) reanalysed the same UVES data as Zoccali (2006, 2008) and Lecureur et al. (2007); these data and stellar parameters are the same as given in Lomaeva et al. (2019).

The differences in stellar parameters between the present ones adopted from Zoccali et al. (2006, 2008), Lecureur et al. (2007), and the reanalysis by Jönsson et al. (2017) were discussed in da Silveira et al. (2018). As reported in Sect. 3, the present parameters (see Sect. 3) were obtained by applying excitation equilibrium imposed on the Fe I lines in order to refine the photometric  $T_{eff}$ , and photometric gravity was imposed.

The Lomaeva et al. (2019) parameters, adopted from Jönsson et al. (2017), were obtained by using the software Spectroscopy Made Easy (SME; Valenti & Piskunov 1996). The SME software simultaneously fits stellar parameters and/or abundances by fitting

calculated synthetic spectra to an observed spectrum. All the stellar parameters ( $T_{\text{eff}}$ ,  $\log g$ ,  $[\text{Fe}/\text{H}]$ , and  $v_t$ ) were derived simultaneously using relatively weak, unblended Fe I, Fe II, and Ca I lines and gravity-sensitive Ca I-wings.

On average, the differences in parameters amount to  $\Delta T_{\text{eff}}(\text{Jönsson+17-Zoccali+06}) = -94$  K in effective temperatures and  $\Delta \log g(\text{Jönsson+17-Zoccali+06}) = +0.46$  in gravities. The gravities adopted by Jönsson et al. (2017) are possibly too high because the sample stars were chosen to have one magnitude brighter than the red clump or horizontal branch. It is well known that the red clump stars have rather homogeneous gravity values of  $\log g \sim 2.2$  that can go up to  $\log g \sim 2.5$  at most, depending on metallicity (Girardi 2016), and should be around  $\log g \sim 2.3$  for the stellar parameters of the present metallicities. Therefore, it appears natural that red giants located at one magnitude above the red clump should have gravities around  $\log g \sim 2.0$  (or lower). On the other hand, the patchy extinction towards the bulge might arguably accommodate larger gravities for the sample stars, as assumed by Jönsson et al. (2017). In any case, we prefer to keep the parameters from our group for the sake of homogeneity of elemental abundances between this chapter and the previous ones. Furthermore, since we have 56 stars, including 33 in common with Jönsson et al. (2017), it is also important to have an internal consistency in the analysis of the 56 stars.

A check of lines used by each author can explain some differences in the results, as follows. (i) Comparison of lines used for cobalt: Johnson et al. (2014) used the Co I 5647.23 and 6117.00 Å lines. Lomaeva et al. (2019) only used the UVES spectra from the red arm and relied on the Co I 6005.020, 6117.000, 6188.996, and 6632.430 Å. We have used lines from both the red arm and the blue arm spectra, as listed in Table 4.1; (ii) Comparison of lines used for copper: Johnson et al. (2014) and Xu et al. (2019) used the same Cu I 5782.11 Å line for the same stars, which is a well-known suitable line with identified HFS structure.

### 4.3 Chemical evolution models

We have computed chemodynamical evolution models for cobalt and copper for a small classical spheroid with a baryonic mass of  $2 \times 10^9 M_{\odot}$  and a dark halo mass  $M_H = 1.3 \times 10^{10} M_{\odot}$ , with the same models presented in Barbuy et al. (2015) and Friaça & Barbuy (2017).

Table 4.2 - LTE abundances of Co and Cu derived in the present work.

Star	[Fe/H]	[Cu/Fe]	[Cu/Fe]	[Co/Fe]							
		5105.5374 Å	5218.1974 Å	5212.691 Å	5280.629 Å	5301.047 Å	5342.708 Å	5454.572 Å	5647.234 Å	6117.000 Å	6188.996 Å
B6-b1	0.07	-0.30	-0.10	-0.15	-0.25	-0.30	-0.30	-0.30	-0.15	-0.15	0.00
B6-b2	-0.01	-0.15	0.20	-0.20	+0.00	+0.00	-0.30	-0.25	-0.25	+0.00	-0.20
B6-b3	0.10	0.05	0.00	-0.20	0.00	0.00	-0.15	-0.10	0.00	0.00	0.05
B6-b4	-0.41	0.00	-0.15	-0.15	-0.15	0.00	-0.15	0.00	0.00	0.00	0.00
B6-b5	-0.37	0.35	-0.10	0.00	0.00	-0.15	-0.15	0.00	0.00	-0.15	+0.05
B6-b6	0.11	-0.05	0.00	-0.15	0.00	-0.10	-0.10	-0.15	-0.15	-0.10	+0.10
B6-b8	0.03	-0.30	0.00	-0.28	0.00	-0.30	-0.30	-0.30	-0.10	-0.30	-0.05
B6-f1	-0.01	-0.30	-0.10	-0.15	0.00	-0.15	-0.30	-0.15	-0.10	-0.30	0.00
B6-f2	-0.51	-0.30	-0.10	0.00	0.00	—	0.00	-0.15	0.00	-0.30	—
B6-f3	-0.29	0.10	0.00	0.00	0.00	0.00	0.00	-0.10	+0.10	0.00	+0.10
B6-f5	-0.37	-0.30	0.15	-0.10	0.00	0.00	-0.15	-0.15	-0.05	0.00	+0.15
B6-f7	-0.42	-0.35	0.00	0.00	0.00	0.00	-0.35	0.00	0.00	0.00	0.00
B6-f8	0.04	0.30	-0.10	0.00	0.00	+0.10	0.00	-0.15	+0.05	-0.15	+0.08
BW-b2	0.22	—	-0.15	0.00	0.00	-0.15	—	-0.20	-0.20	-0.25	0.00
BW-b4	0.07	—	-0.30	-0.20	-0.10	-0.30	+0.05	-0.30	-0.15	+0.15	-0.15
BW-b5	0.17	—	-0.35	0.00	0.00	-0.05	-0.10	0.00	0.00	0.00	0.00
BW-b6	-0.25	—	-0.30	0.00	-0.05	-0.15	-0.10	0.00	0.00	-0.15	0.00
BW-b7	0.10	—	-0.25	-0.30	0.00	-0.30	0.00	-0.30	-0.30	-0.15	-0.10
BW-f1	0.32	-0.40	-0.40	0.00	—	0.00	-0.30	0.00	0.00	0.00	0.00
BW-f4	-1.21	-1.00	-0.60	—	—	—	0.00	0.00:	0.00:	0.00	0.00
BW-f5	-0.59	0.00	-0.30	+0.05	0.00	-0.30	0.00	-0.15	0.00	-0.10	0.00
BW-f6	-0.21	—	-0.50	0.00	0.00	-0.10	-0.15	-0.05	0.00	0.00	+0.30
BW-f7	0.11	—	—	-0.12	0.00	-0.30	—	-0.30	-0.30	-0.25	0.00
BW-f8	-1.27	-0.70	-0.60	0.00:	—	—	0.00	+0.30	0.00	-0.10:	—
BL-1	-0.16	0.00	0.10	0.00	+0.15	+0.35	+0.30	0.00	+0.30	-0.15	0.00
BL-3	-0.03	0.10	-0.30	0.00	0.00	0.00	+0.05	0.00	+0.05	-0.25	0.00
BL-4	0.13	0.30	0.15	0.00	0.00	+0.10	-0.10	-0.10	+0.12	-0.15	+0.12
BL-5	0.16	0.00	0.00	0.00	0.00	0.00	-0.15	-0.15	-0.15	-0.15	0.00
BL-7	-0.47	0.15	0.00	+0.05	+0.10	+0.10	+0.15	+0.10	+0.10	-0.10	-0.05
B3-b1	-0.78	—	—	+0.10	—	—	—	—	+0.30	-0.30	-0.15
B3-b2	0.18	0.00	-0.30	-0.22	-0.20	+0.15	0.00	-0.20	0.00	-0.18	-0.25
B3-b3	0.18	—	—	-0.07	0.00	+0.10	+0.30	0.00	0.00	-0.25	-0.05
B3-b4	0.17	0.05	-0.30	-0.12	+0.15	-0.05	-0.20	-0.10	+0.25	0.00	-0.07
B3-b5	0.11	0.30	-0.20	-0.10	-0.10	-0.10	0.00	0.00	+0.10	-0.30	+0.05
B3-b7	0.20	0.30	-0.05	0.00	+0.25	0.00	0.00	-0.15	0.00	-0.10	0.00
B3-b8	-0.62	0.20	0.00	0.00	0.00	0.00	0.00	0.00	0.00	-0.03	0.00
B3-f1	0.04	-0.05	-0.20	-0.10	+0.15	-0.30	0.00	-0.10	+0.20	-0.30	0.00
B3-f2	-0.25	0.30	0.30	0.00	-0.20	+0.25	0.00	-0.25	+0.30	0.00	0.00
B3-f3	0.06	-0.30	0.30	-0.23	0.00	0.00	+0.15	-0.15	-0.15	-0.30	-0.05
B3-f4	0.09	-0.40	0.00	—	-0.30	0.00	0.00	0.00	-0.15	-0.30	+0.05
B3-f5	0.16	-0.40	-0.40	-0.15	0.00	-0.30	0.00	+0.15	-0.15	0.00	+0.20
B3-f7	0.16	0.00	0.00	-0.10	+0.15	-0.30	0.00	-0.30	0.00	-0.30	+0.25
B3-f8	0.20	0.50	0.30	-0.10	-0.10	-0.05	-0.07	-0.20	+0.10	0.00	+0.25
BWc-1	0.09	0.00	0.00	-0.10	0.00	0.00	0.00	-0.05	0.00	+0.10	0.00
BWc-2	0.18	-0.60	-0.60	-0.30	0.00	-0.15	—	-0.10	-0.30	-0.30	-0.20
BWc-3	0.28	0.35	0.00	-0.20	0.00	0.00	0.00	-0.30	+0.12	-0.20	0.00
BWc-4	0.05	-0.30	-0.10	-0.10	0.00	0.00	0.00	0.00	0.00	-0.15	0.00
BWc-5	0.42	0.00	-0.20	0.00	0.00	0.00	0.00	-0.25	+0.15	-0.20	+0.20
BWc-6	-0.25	0.30	-0.30	0.00	0.00	0.00	0.00	—	+0.15	-0.08	0.00
BWc-7	-0.25	-0.30	0.00	0.00	+0.10	0.00	0.00	-0.30	+0.10	-0.25	—
BWc-8	0.37	0.00	-0.10	-0.18	-0.12	0.00	0.00	-0.15	-0.15	-0.20	0.00
BWc-9	0.15	0.30	0.30	0.00	0.00	0.00	0.00	0.00	-0.15	-0.15	+0.15
BWc-10	0.07	-0.30	-0.30	-0.15	0.00	0.00	0.00	-0.15	-0.10	-0.30	-0.05
BWc-11	0.17	0.00	-0.30	0.00	0.00	0.00	0.00	—	-0.05	—	-0.30
BWc-12	0.23	-0.35	0.00	-0.18	0.00	-0.05	-0.20	0.00	0.00	-0.15	0.00
BWc-13	0.36	-0.20	-0.30	—	-0.05	0.00	0.00	—	0.00	—	-0.20

Table 4.3 - Atmospheric parameters and radial velocities adopted from Zoccali et al. (2006) and Lecureur et al. (2007), and resulting Co and Cu abundances.

Star	OGLE no.	$\alpha$ (J2000)	$\delta$ (J2000)	$T_{\text{eff}}$	logg	[Fe/H]	$v_t$	$v_r$	$v_{\text{helio}}$	[Cu/Fe] <sub>LTE</sub>	[Co/Fe] <sub>LTE</sub>	[Co/Fe] <sub>NLTE</sub>
				[K]			[kms <sup>-1</sup> ]	[kms <sup>-1</sup> ]	[kms <sup>-1</sup> ]			
B6-b1	29280c3	18 09 50.480	-31 40 51.61	4400	1.8	0.07	1.6	-88.3	11.59	-0.20	-0.20	-0.07
B6-b2	83500c6	18 10 33.980	-31 49 09.15	4200	1.5	-0.01	1.4	17.0	11.66	0.03	-0.15	-0.04
B6-b3	31220c2	18 10 19.060	-31 40 28.19	4700	2.0	0.10	1.6	-145.8	11.64	0.03	-0.05	0.08
B6-b4	60208c7	18 10 07.770	-31 52 41.36	4400	1.9	-0.41	1.7	-20.3	11.61	-0.08	-0.06	0.03
B6-b5	31090c2	18 10 37.380	-31 40 29.14	4600	1.9	-0.37	1.3	-4.2	11.67	0.13	-0.05	0.06
B6-b6	77743c7	18 09 49.100	-31 50 07.66	4600	1.9	0.11	1.8	44.1	11.58	-0.03	-0.08	0.05
B6-b8	108051c7	18 09 55.950	-31 45 46.33	4100	1.6	0.03	1.3	-110.3	11.59	-0.15	-0.20	-0.11
B6-f1	23017c3	18 10 04.460	-31 41 45.31	4200	1.6	-0.01	1.5	38.4	10.95	-0.20	-0.14	-0.03
B6-f2	90337c7	18 10 11.510	-31 48 19.28	4700	1.7	-0.51	1.5	-98.5	10.96	-0.20	-0.08	0.05
B6-f3	21259c2	18 10 17.720	-31 41 55.20	4800	1.9	-0.29	1.3	90.2	10.97	0.05	+0.01	0.14
B6-f5	33058c2	18 10 41.510	-31 40 11.88	4500	1.8	-0.37	1.4	22.1	11.02	-0.08	-0.04	0.06
B6-f7	100047c6	18 10 52.300	-31 46 42.18	4300	1.7	-0.42	1.6	-10.4	11.03	-0.18	0.00	0.09
B6-f8	11653c3	18 09 56.840	-31 43 22.56	4900	1.8	0.04	1.6	58.5	10.94	0.10	-0.01	0.14
BW-b2	214192	18 04 23.950	-30 05 57.80	4300	1.9	0.22	1.5	-19.2	-6.15	-0.15	-0.11	0.00
BW-b4	545277	18 04 05.340	-30 05 52.50	4300	1.4	0.07	1.4	85.6	-6.18	-0.30	-0.13	0.00
BW-b5	82760	18 04 13.270	-29 58 17.80	4000	1.6	0.17	1.2	68.8	-6.17	-0.35	-0.02	0.05
BW-b6	392931	18 03 51.840	-30 06 27.90	4200	1.7	-0.25	1.3	140.4	-6.21	-0.30	-0.06	0.04
BW-b7	554694	18 04 04.570	-30 02 39.60	4200	1.4	0.10	1.2	-211.1	-6.19	-0.25	-0.18	-0.06
BW-f1	433669	18 03 37.140	-29 54 22.30	4400	1.8	0.32	1.6	202.6	-2.73	-0.40	0.09	0.02
BW-f4	537070	18 04 01.400	-30 10 20.70	4800	1.9	-1.21	1.7	-144.1	-2.68	-0.80	0.00	0.22
BW-f5	240260	18 04 39.620	-29 55 19.80	4800	1.9	-0.59	1.3	-6.1	-2.61	-0.15	-0.06	0.08
BW-f6	392918	18 03 36.890	-30 07 04.30	4100	1.7	-0.21	1.5	182.0	-2.73	-0.50	0.00	0.08
BW-f7	357480	18 04 43.920	-30 03 15.20	4400	1.9	0.11	1.7	-139.5	-2.60	—	-0.17	-0.05
BW-f8	244598	18 03 30.490	-30 01 44.80	5000	2.2	-1.27	1.8	-24.8	-2.74	-0.65	+0.05	0.35
BL-1	1458c3	18 34 58.643	-34 33 15.241	4500	2.1	-0.16	1.5	106.6	-6.37	0.05	+0.12	0.22
BL-3	1859c2	18 35 27.640	-34 31 59.353	4500	2.3	-0.03	1.4	50.6	-6.32	-0.10	-0.02	0.09
BL-4	3328c6	18 35 21.240	-34 44 48.217	4700	2.0	0.13	1.5	117.9	-6.34	0.23	+0.00	0.14
BL-5	1932c2	18 36 01.148	-34 31 47.913	4500	2.1	0.16	1.6	57.9	-6.27	0.00	-0.08	0.05
BL-7	6336c7	18 35 57.392	-34 38 04.621	4700	2.4	-0.47	1.4	108.1	-6.27	0.08	+0.06	0.16
B3-b1	132160C4	18 08 15.840	-25 42 09.83	4300	1.7	-0.78	1.5	-123.8	2.32	—	-0.01	0.07
B3-b2	262018C7	18 09 14.062	-25 56 47.35	4500	2.0	0.18	1.5	7.8	2.43	-0.15	-0.11	0.03
B3-b3	90065C3	18 08 46.405	-25 42 44.40	4400	2.0	0.18	1.5	12.2	2.38	—	0.00	0.13
B3-b4	215681C6	18 08 44.472	-25 57 56.85	4500	2.1	0.17	1.7	78.6	2.37	-0.13	-0.03	0.10
B3-b5	286252C7	18 09 00.527	-25 48 06.78	4600	2	0.11	1.5	-51.3	2.41	0.05	-0.06	0.07
B3-b7	282804C7	18 09 16.540	-25 49 26.08	4400	1.9	0.20	1.3	159.7	2.44	0.13	0.00	0.14
B3-b8	240083C6	18 08 24.602	-25 48 44.39	4400	1.8	-0.62	1.4	-9.6	2.34	0.10	0.00	0.09
B3-f1	129499C4	18 08 16.176	-25 43 19.18	4500	1.9	0.04	1.6	29.4	3.35	-0.13	-0.06	0.06
B3-f2	259922C7	18 09 15.609	-25 57 32.75	4600	1.9	-0.25	1.8	3.4	3.46	0.30	+0.01	0.11
B3-f3	95424C3	18 08 49.628	-25 40 36.93	4400	1.9	0.06	1.7	-19.1	3.41	0.00	-0.09	0.03
B3-f4	208959C6	18 08 44.293	-26 00 25.05	4400	2.1	0.09	1.5	-81.9	3.40	-0.20	-0.10	0.08
B3-f5	49289C2	18 09 18.404	-25 43 37.41	4200	2.0	0.16	1.8	-34.7	3.47	-0.40	-0.03	0.00
B3-f7	279577C7	18 09 23.694	-25 50 38.19	4800	2.1	0.16	1.7	-9.2	3.48	0.00	-0.08	0.05
B3-f8	193190C5	18 08 12.632	-25 50 04.45	4800	1.9	0.20	1.5	11.0	3.34	0.40	0.00	0.15
BWc-1	393125	18 03 50.445	-30 05 31.993	4476	2.1	0.09	1.5	—	111.8	0.00	0.00	0.12
BWc-2	545749	18 03 56.824	-30 05 37.390	4558	2.2	0.18	1.2	—	62.6	-0.60	-0.15	-0.01
BWc-3	564840	18 03 54.730	-30 01 06.096	4513	2.1	0.28	1.3	—	237.6	0.18	-0.07	0.08
BWc-4	564857	18 03 55.416	-30 00 57.314	4866	2.2	0.05	1.3	—	1.1	-0.20	-0.03	0.10
BWc-5	575542	18 03 56.021	-29 55 43.716	4535	2.1	0.42	1.5	—	65.0	-0.10	-0.01	0.14
BWc-6	575585	18 03 56.543	-29 55 11.787	4769	2.2	-0.25	1.3	—	104.9	0.00	0.00	0.11
BWc-7	67577	18 03 56.543	-29 55 11.787	4590	2.2	-0.25	1.1	—	0.0	-0.15	-0.05	0.05
BWc-8	78255	18 03 12.494	-30 03 59.111	4610	2.2	0.37	1.3	—	-4.2	-0.05	-0.10	0.05
BWc-9	78271	18 03 16.683	-30 03 51.406	4539	2.1	0.15	1.5	—	47.8	0.30	-0.02	0.11
BWc-10	89589	18 03 18.914	-30 01 09.983	4793	2.2	0.07	1.3	—	188.0	-0.30	-0.09	0.04
BWc-11	89735	18 03 04.749	-29 59 35.301	4576	2.1	0.17	1.0	—	98.0	-0.15	-0.06	0.09
BWc-12	89832	18 03 20.102	-29 58 25.785	4547	2.1	0.23	1.3	—	-47.6	-0.18	-0.07	0.07
BWc-13	89848	18 03 04.612	-29 58 14.080	4584	2.1	0.36	1.1	—	-201.1	-0.25	-0.06	0.10

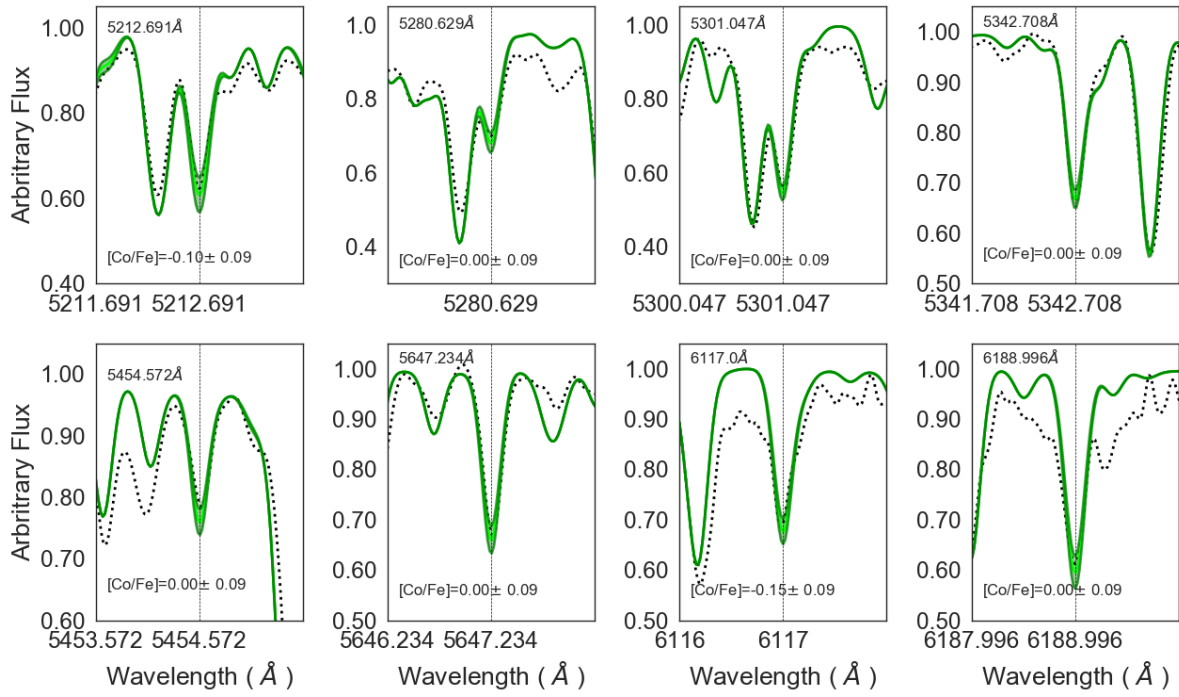


Figure 4.1: Fits of synthetic spectra to the eight observed lines of Co I in star BWc-4. The dotted line is the observed spectrum. The green lines correspond to the value adopted, and with  $[\text{Co}/\text{Fe}] = +0.09$  and  $-0.09$ .

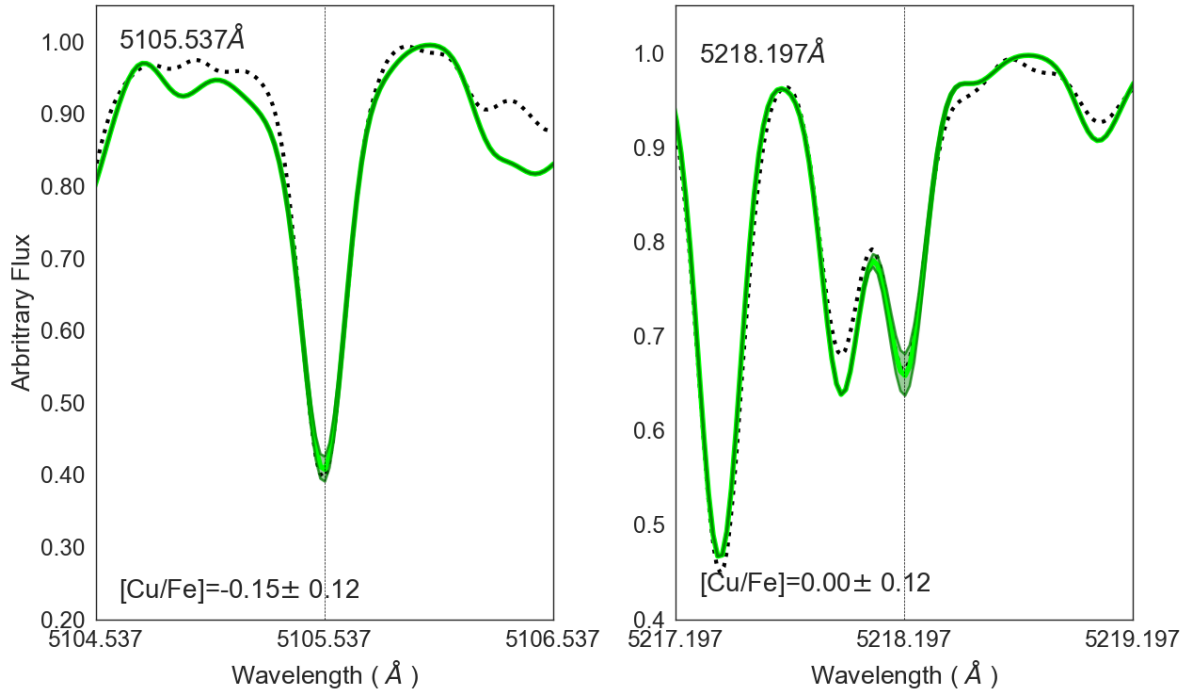


Figure 4.2: Fits of synthetic spectra to the two observed lines of Cu I in star BL-7. The dotted line is the observed spectrum. The green lines correspond to the value adopted, and with  $[\text{Cu}/\text{Fe}] = +0.12$  and  $-0.12$ .

Table 4.4 - Abundance uncertainties for the metal-rich star B6-f8 and the metal-poor star BW-f8 for uncertainties of  $\Delta T_{\text{eff}} = 100$  K,  $\Delta \log g = 0.2$ , and  $\Delta v_t = 0.2$  km s $^{-1}$ , and corresponding total error. The errors are to be added to reach the reported abundances.

Element	$\Delta T$ 100 K	$\Delta \log g$ 0.2 dex	$\Delta v_t$ 0.2 kms $^{-1}$	$(\sum x^2)^{1/2}$
(1)	(2)	(3)	(4)	(5)
B6-f8				
[CoI/Fe]	+0.09	+0.01	+0.01	0.09
[CuI/Fe]	+0.12	+0.02	+0.00	0.12
BW-f8				
[CoI/Fe]	+0.03	+0.00	+0.00	0.03
[CuI/Fe]	+0.10	+0.00	-0.02	0.10

The code allows inflow and outflow of gas, treated with hydrodynamical equations coupled with chemical evolution.

As described in detail in Friaça & Barbuy (2017), metallicity dependent yields from SNe II, SNe Ia, and intermediate mass stars (IMS) are included. The core-collapse SNII yields are adopted from WW95. For lower metallicities we also adopt, in a second calculation, yields from high explosion-energy hypernovae from Nomoto et al. (2013, and references therein). Yields of SNIa resulting from Chandrasekhar mass white dwarfs are taken from Iwamoto et al. (1999), namely their models W7 (progenitor star of initial metallicity  $Z=Z_{\odot}$ ) and W70 (initial metallicity  $Z=0$ ). The yields for IMS ( $0.8 - 8 M_{\odot}$ ) with initial  $Z=0.001$ , 0.004, 0.008, 0.02, and 0.4 are from van den Hoek & Groenewegen (1997) (variable  $\eta_{AGB}$  case).

Specific star formation rates (SFR) are defined as the inverse of the timescale for the system formation, represented by  $\nu_{\text{SFR}}$  and given in Gyr $^{-1}$ . It is the ratio of the SFR in  $M_{\odot}$  Gyr $^{-1}$  over the gas mass in  $M_{\odot}$  available for star formation. In the present models we assume  $\nu_{\text{SFR}} = 3$  and 1 Gyr $^{-1}$ , corresponding to fast timescales of 0.3 and 1 Gyr, respectively, for the chemical enrichment of the bulge.

The model calculations overplotted to the data are shown in Fig. 4.3. Models where only the WW95 yields for massive stars are included are shown in black, together with a specific star formation rate of 3 Gyr $^{-1}$ . The models in green have a specific star formation rate of 1 Gyr $^{-1}$  and adopting yields from hypernovae (Kobayashi et al. 2006, Nomoto et al. 2013) instead of yields from WW95 for metallicities lower than  $[\text{Fe}/\text{H}] < -4.0$ . We have

concluded that for these elements (Co, Cu) the inclusion of hypernovae makes essentially no difference. Since the yields from core-collapse SNII by WW95 underestimate the Co abundance, as recognized by Timmes et al. (1995), we have multiplied the yields of Co by a factor of two for all metallicities  $Z/Z_{\odot}$ .

In Figure 4.3  $[\text{Co}/\text{Fe}]$  versus  $[\text{Fe}/\text{H}]$  is shown with the present results in LTE and corrected for NLTE in the upper panel;  $[\text{Cu}/\text{Fe}]$  versus  $[\text{Fe}/\text{H}]$  is shown in the lower panel. Literature data include: a) Johnson et al. (2014) and b) Xu et al. (2019), where stars are the same but they are plotted as if there were different samples; c) Lomaeva et al. (2019) only for the stars not in common with the present sample, which are 11 stars from the SW field (see Jönsson et al. 2017). We do not plot the stars in common with the present work in order to avoid too much clutter in the plot; d) ErnanDES et al. (2018) for bulge globular clusters.

In conclusion, Co is well reproduced by the models, whereas Cu is overproduced. Chemical evolution models from Kobayashi et al. (2006) show a similar Co abundance compatible with the observations, and also overproduce Cu.

#### 4.4 Discussion of results

Our main interest in the present analysis is to compare the behaviour of cobalt and copper. They are produced both in the alpha-rich freezeout as primary elements (Sukhbold et al. 2016) and in the weak-s process in massive stars as secondary elements. The iron-peak elements are mostly formed during explosive oxygen and silicon burning in massive supernovae (WW95). For the larger values of the neutron fraction  $\eta$ , the main products of silicon burning are completed. On the other hand, if the density is low and the supernova envelope expansion is fast,  $\alpha$  particles will be frozen and not captured by the heavier elements (Woosley et al. 2002). This so-called  $\alpha$ -rich freezeout will produce  $^{59}\text{Co}$ . As pointed out by S. Woosley (private communication) and Barbay et al. (2018a), their abundances as a function of Fe can reveal the relative efficiencies of these two contributions.

In thick-disc and halo stars, Nissen et al. (2000), Cayrel et al. (2004), and Ishigaki et al. (2013), among others, derived abundances of iron-peak elements. Nissen et al. (2000) observed that Sc might be enhanced in metal-poor stars, and that Mn decreases with decreasing metallicities. Ishigaki et al. (2013) has also shown that most Fe-peak elements

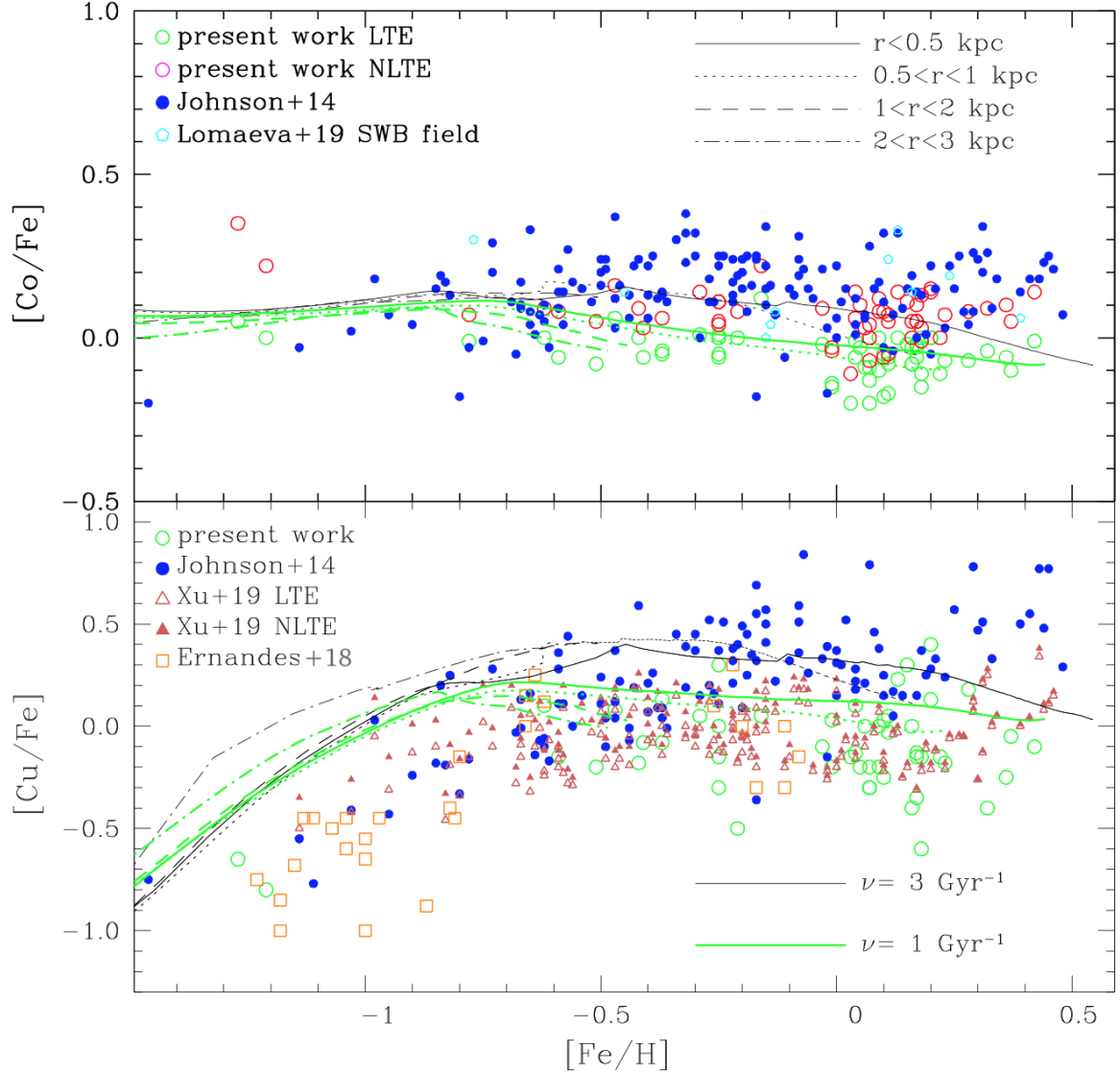


Figure 4.3: Upper panel:  $[\text{Co}/\text{Fe}]$  vs.  $[\text{Fe}/\text{H}]$  with the present results in LTE and corrected for NLTE, together with literature data. Lower panel:  $[\text{Cu}/\text{Fe}]$  vs.  $[\text{Fe}/\text{H}]$  with the present results and literature data. Shown are: the present results in LTE (open green circles); present results in NLTE (open magenta circles); Johnson et al. (2014) (filled blue circles); Lomaeva et al. (2019) for the SW field (open cyan circles); Xu et al. (2019) in LTE (open Indian red triangles); Xu et al. (2019) in NLTE (filled Indian red triangles); Ernandes et al. (2018) for bulge globular clusters (open dark orange squares) and chemodynamical evolution models are overplotted; specific star formation rates of  $3 \text{ Gyr}^{-1}$ , with SNII yields from WW95 (black lines); specific star formation rates of  $1 \text{ Gyr}^{-1}$ , with SNII yields from WW95 and from Kobayashi et al. (2006) for  $[\text{Fe}/\text{H}] < -4.0$  (green lines). Models are for distances to the Galactic center of:  $r < 0.5 \text{ kpc}$  (solid lines),  $0.5 < r < 1 \text{ kpc}$  (dotted lines),  $1 < r < 2 \text{ kpc}$  (dashed lines), and  $2 < r < 3 \text{ kpc}$  (dash-dotted lines).

show solar abundance ratios as a function of metallicity, with the exception of Mn, Cu, and Zn. In particular as regards Co and Cu, Ishigaki et al. finds that Co varies in lockstep with Fe for  $[\text{Fe}/\text{H}] > -2.0$ , but appears enhanced for  $[\text{Fe}/\text{H}] < -2.0$ , as previously already found by Cayrel et al. (2004), and that Cu decreases with decreasing metallicities. Barbuy (2013, 2015) and da Silveira et al. (2018) derived Mn and Zn for the present sample of 56 UVES spectra of red giants, and confirmed that Mn decreases with decreasing metallicity and that Zn is enhanced in metal-poor stars. Ernandes et al. (2018) discussed Sc, V, Mn, Cu, and Zn in bulge globular-cluster stars from UVES spectra, with Sc and V varying in lockstep with Fe, Mn; Cu, increasing with metallicity; and Zn enhanced in metal-poor stars. We will now examine the  $[\text{Co}/\text{Fe}]$  and  $[\text{Cu}/\text{Fe}]$  versus  $[\text{Fe}/\text{H}]$  behaviour.

Before drawing conclusions, we present literature results here on Co and Cu in bulge stars. Johnson et al. (2014) derived abundances of Cr, Co, Ni, and Cu in 156 giants, and Xu et al. (2019) derived Cu abundances for 129 of these same stars, applying NLTE corrections. Recently, Lomaeva et al. (2019) derived Sc, V, Cr, Mn, Co, and Ni for bulge giants that include 33 stars in common using the same UVES data as the present sample. Schultheis et al. (2017) derived abundances of Cr, Co, Ni, and Mn from APOGEE results, which show, however, a large spread and are not considered here.

#### 4.4.1 Comments on results for cobalt

Figure 4.3 shows that  $[\text{Co}/\text{Fe}]$  varies in lockstep with  $[\text{Fe}/\text{H}]$ , and this appears in all samples. It appears therefore that the nucleosynthesis process dominating the formation of cobalt is the alpha-rich freezeout.

Figure 4.3 shows that the mean  $[\text{Co}/\text{Fe}]$  value differs among the different authors. The Johnson et al. (2014) and Lomaeva et al. (2019) results are in the mean 0.2 dex, more Co-rich than the present results. A main reason for the discrepancies might be the location of continuum. In order to further investigate the disagreement on the level of Co deficiency or over-enhancement, it is interesting to note the deficiency in Co relative to Fe in the Sagittarius dwarf galaxy. In Fig. 4.4 we compare the present results for Co in LTE and NLTE, compared with Co abundances in 158 red giants of the Sagittarius dwarf galaxy by Hasselquist et al. (2017). These authors used the H-band from APOGEE data and found that Co is deficient with respect to stars in the Milky Way. Hasselquist et al. (2017) did not consider NLTE effects; therefore, we compare our results in LTE and theirs, which leads

to a difference in Co abundances of  $\Delta[\text{Co}/\text{Fe}] \sim 0.3$ , reduced by 0.2 with respect to results by Johnson et al. (2014) and Lomaeva et al. (2019). Therefore, the deficiency of Co in Sagittarius relative to the present chapter is not as drastic as in previous results discussed in the literature. A possible explanation of the deficiency in Co in Sagittarius, previously already suggested by McWilliam et al. (2013), is that Sagittarius was less enriched by SNe II relative to the Milky Way, which could be caused by a top-light initial mass function (IMF).

#### 4.4.2 Comments on results for copper

In Fig. 4.3 all data agree on  $[\text{Cu}/\text{Fe}]$  versus  $[\text{Fe}/\text{H}]$  having a flat behaviour between  $-0.8 < [\text{Fe}/\text{H}] < +0.1$ . For  $[\text{Fe}/\text{H}] < -0.8$ , copper-to-iron clearly decreases with decreasing metallicity, indicating the behaviour of a secondary element. For the metal-rich stars, our data would be compatible with a flat trend, or a slightly decreasing trend with metallicity, but this is not shown in the Johnson et al. and Xu et al. results. Finally, there is a shift in enhancements between Johnson et al. and Xu et al. Since they use the same spectra of the same stars, and the same line, this could be due to a different placement of continua. Our results fit the abundance values from Xu et al. better and we note that the NLTE corrections from Xu et al. are small.

The behaviour of  $[\text{Cu}/\text{Fe}]$  versus  $[\text{Fe}/\text{H}]$ , which shows a decrease in  $[\text{Cu}/\text{Fe}]$  towards decreasing metallicities, confirms that  $[\text{Cu}/\text{Fe}]$  essentially has a secondary-element behaviour and that its production should be dominated by a weak s-process. Another characteristic, as noted by McWilliam (2016), is that  $[\text{Cu}/\text{O}]$  has much less spread than  $[\text{Cu}/\text{Fe}]$  data, indicating a production of Cu and O in the same massive stars. This is confirmed in Fig. 4.5, where our data are plotted in NLTE together with data from Johnson et al. (2014) and Ernan-des et al. (2018), the latter corresponding to red giants in bulge globular clusters. It is clear that the spread of points is lower, confirming the suggestion by McWilliam (2016).

### 4.5 Summary of Co and Cu abundances in the bulge

In this work we analysed a sample of high-quality spectroscopic data for 56 Galactic bulge red giants. The present results show  $[\text{Co}/\text{Fe}] \sim \text{constant} \sim 0.0$ , indicating cobalt mostly produced from the  $\alpha$ -rich freezeout. Copper instead shows a secondary element

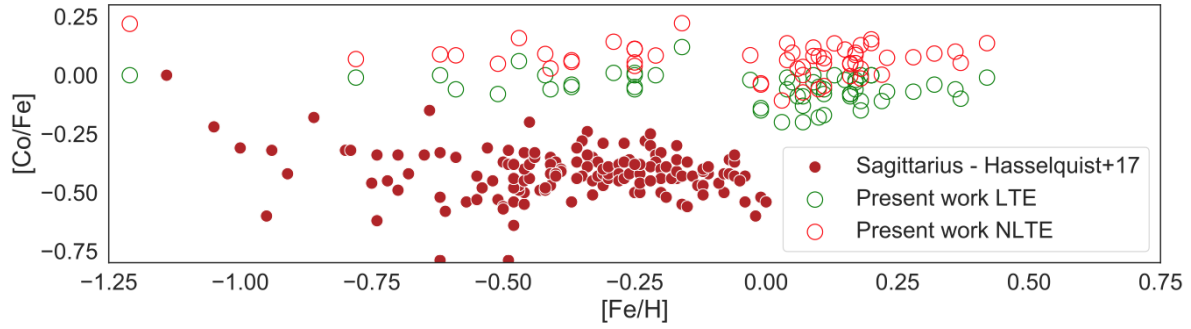


Figure 4.4:  $[\text{Co}/\text{Fe}]$  vs.  $[\text{Fe}/\text{H}]$ : present results in LTE and corrected for NLTE, compared with data from Hasselquist et al. (2017) for the Sagittarius dwarf galaxy. Symbols: open green circles represent present results in LTE; red circles represent present results in NLTE; filled blue dots represent Hasselquist et al. (2017).

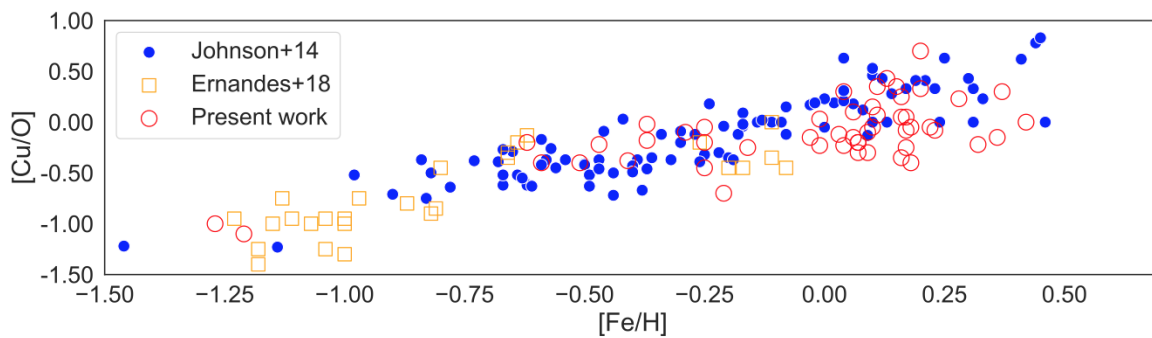


Figure 4.5:  $[\text{Cu}/\text{O}]$  vs.  $[\text{Fe}/\text{H}]$  for the present results in NLTE and literature data. Symbols: open magenta circles represent present results in NLTE; filled blue dots represent Johnson et al. (2014); open orange squares represent Ernandes et al. (2018).

Table 4.5 - Comparison of stellar parameters and Co and Cu abundances of the present work with Johnson et al. (2014) and Lomaeva et al. (2019).

Star	OGLE	$T_{\text{eff}}$	logg	[Fe/H]	$v_t$	[Co/Fe] <sub>LTE</sub>	[Co/Fe] <sub>NLTE</sub>	[Cu/Fe]	$T_{\text{eff}}$	logg	[Fe/H]	[Co/Fe]	[Cu/Fe]
Present work									Johnson et al. 2014				
B3-b2	262018C7	4500	2.0	0.18	1.5	-0.11	0.03	-0.15	4700	2.75	0.08	0.15	0.46
B3-b4	215681C6	4500	2.1	0.17	1.7	-0.03	0.10	-0.13	4800	2.75	0.31	0.20	0.51
B3-b5	286252C7	4600	2.0	0.11	1.5	-0.06	0.07	0.05	4700	3.10	0.43	0.18	0.77
B3-b7	282804C7	4400	1.9	0.20	1.3	0.00	0.14	0.13	4575	2.50	0.10	0.11	0.25
B3-b8	240083C6	4400	1.8	-0.62	1.4	0.00	0.09	0.10	4425	1.65	-0.58	0.04	—
B3-f1	129499C4	4500	1.9	0.04	1.6	-0.06	0.06	-0.13	4900	2.75	0.13	0.32	—
B3-f8	193190C5	4800	1.9	0.20	1.5	0.00	0.15	0.40	4675	2.75	0.24	0.22	—
Star	OGLE	$T_{\text{eff}}$	logg	[Fe/H]	$v_t$	[Co/Fe] <sub>LTE</sub>	[Co/Fe] <sub>NLTE</sub>	[Cu/Fe]	$T_{\text{eff}}$	logg	[Fe/H]	$v_t$	[Co/Fe] <sub>LTE</sub>
Present work									Lomaeva et al. 2019				
B3-b1	132160C4	4300	1.7	-0.78	1.5	-0.01	0.07	—	4414	1.35	-0.89	1.41	0.04
B3-b5	286252C7	4600	2.0	0.11	1.5	-0.06	0.07	0.05	4425	2.70	0.25	1.43	-0.25
B3-b7	282804C7	4400	1.9	0.20	1.3	0.00	0.14	0.13	4303	2.36	0.08	1.58	-0.08
B3-b8	240083C6	4400	1.8	-0.62	1.4	0.00	0.09	0.10	4287	1.79	-0.67	1.46	0.67
B3-f1	129499C4	4500	1.9	0.04	1.6	-0.06	0.06	-0.13	4485	2.25	-0.15	1.88	0.15
B3-f2	259922C7	4600	1.9	-0.25	1.8	+0.01	0.11	0.30	4207	1.64	-0.66	1.74	0.66
B3-f3	95424C3	4400	1.9	0.06	1.7	-0.09	0.03	0.00	4637	2.96	0.24	1.89	-0.24
B3-f4	208959C6	4400	2.1	0.09	1.5	-0.10	0.08	-0.20	4319	2.60	-0.12	1.50	0.12
B3-f7	279577C7	4800	2.1	0.16	1.7	-0.08	0.05	0.00	4517	2.93	0.17	1.55	-0.17
B3-f8	193190C5	4800	1.9	0.20	1.5	0.00	0.15	0.40	4436	2.88	0.24	1.54	-0.24
BW-b1									4042	2.39	0.46	1.43	-0.46
BW-b2	214192	4300	1.9	0.22	1.5	-0.11	0.00	-0.15	4367	2.39	0.18	1.68	-0.18
BW-b5	82760	4000	1.6	0.17	1.2	-0.02	0.05	-0.35	3939	1.68	0.25	1.31	-0.25
BW-b6	392931	4200	1.7	-0.25	1.3	-0.06	0.04	-0.30	4262	1.98	-0.32	1.44	0.32
BW-b8									4424	2.54	0.30	1.52	-0.30
BW-f1	433669	4400	1.8	0.32	1.6	-0.04	0.09	-0.40	4359	2.51	0.28	1.93	-0.28
BW-f5	240260	4800	1.9	-0.59	1.3	-0.06	0.08	-0.15	4818	2.89	-0.51	1.29	0.51
BW-f6	392918	4100	1.7	-0.21	1.5	0.00	0.08	-0.50	4117	1.43	-0.43	1.69	0.43
B6-b1	29280c3	4400	1.8	0.07	1.6	-0.20	-0.07	-0.20	4372	2.59	0.25	1.57	-0.25
B6-b3	31220c2	4700	2.0	0.10	1.6	-0.05	0.08	0.03	4468	2.48	0.05	1.67	-0.05
B6-b4	60208c7	4400	1.9	-0.41	1.7	-0.06	0.03	-0.08	4215	1.38	-0.62	1.68	0.62
B6-b5	31090c2	4600	1.9	-0.37	1.3	-0.05	0.06	0.13	4340	2.02	-0.48	1.34	0.20
B6-b6	77743c7	4600	1.9	0.11	1.8	-0.08	0.05	-0.03	4396	2.37	0.19	1.77	0.23
B6-b8	108051c7	4100	1.6	0.03	1.3	-0.20	-0.11	-0.15	4021	1.90	0.06	1.45	0.06
B6-f1	23017c3	4200	1.6	-0.01	1.5	-0.14	-0.03	-0.20	4149	2.01	0.10	1.65	0.10
B6-f3	21259c2	4800	1.9	-0.29	1.3	+0.01	0.14	0.05	4565	2.60	-0.35	1.28	0.17
B6-f5	33058c2	4500	1.8	-0.37	1.4	-0.04	0.06	-0.08	4345	2.32	-0.33	1.41	0.29
B6-f7	100047c6	4300	1.7	-0.42	1.6	0.00	0.09	-0.18	4250	2.10	-0.31	1.65	0.25
B6-f8	11653c3	4900	1.8	0.04	1.6	-0.01	0.14	0.10	4470	2.78	0.13	1.30	0.13
BL-1	1458c3	4500	2.1	-0.16	1.5	+0.12	0.22	0.05	4370	2.19	-0.19	1.50	0.10
BL-3	1859c2	4500	2.3	-0.03	1.4	-0.02	0.09	-0.10	4555	2.48	-0.09	1.53	0.16
BL-4	3328c6	4700	2.0	0.13	1.5	+0.00	0.14	0.23	4476	2.94	0.27	1.41	0.19
BL-5	1932c2	4500	2.1	0.16	1.6	-0.08	0.05	0.00	4425	2.65	0.28	1.68	0.22
BL-7	6336c7	4700	2.4	-0.47	1.4	+0.06	0.16	0.08	4776	2.52	-0.5	1.53	0.19

behaviour, with [Cu/Fe] decreasing with decreasing metallicity, indicating its production is dominated by the weak *s*-process. The yields of Co and Cu considered in the models appear to include these two mechanisms in the right proportions, and the chemodynamical models reproduce their behaviour well.



## The faint old bulge globular cluster Terzan 9

### 5.1 Introduction: Terzan 9

Globular clusters in the central parts of the Galaxy are among the oldest extant stellar populations in the Milky Way (e.g. Barbuy et al. 2018a; Kunder et al. 2018). Terzan 9 is a very compact cluster located at 4d12 and 0.7 kpc (Bica et al. 2006) from the Galactic center, which is, thus, in the inner bulge volume, and it is among the globular clusters closest to the Galactic center. Terzan 9 appears to show a blue horizontal branch (BHB) in the ground-based color-magnitude diagrams (CMDs) by Ortolani et al. (1999). The clusters identified with a moderate metallicity and a BHB are very old as deduced from proper-motion cleaned CMDs for example for NGC 6522 and HP 1 (Kerber et al. 2018, 2019). A proper-motion cleaned CMD for Terzan 9 is presented in Rossi et al. (2015), with the cluster proper motions derived. Orbit calculations by Pérez-Villegas et al. (2018) reveal that Terzan 9 remains confined within 1 kpc of the Galactic center with an orbit co-rotating with the bar, it has a bar shape in the (x - y) projection, and a boxy shape in (x - z), which indicates that these clusters are trapped by the bar. With absolute proper motions from Gaia DR2, a new orbital analysis was carried out (Pérez-Villegas et al. 2019) using a Monte Carlo method to take into account the effect of the uncertainties in the observational parameters. These calculations confirm that Terzan 9 belongs to the bulge globular cluster group and that most of its probable orbits follow the bar. Since the bulge clusters are typically old, they were probably formed early in the Galaxy and were later trapped by the bar (see also Renzini et al. 2018). As a matter of fact, the bar should have formed at about  $8 \pm 2$  Gyr ago, according to Buck et al. (2018).

A metallicity of  $[\text{Fe}/\text{H}] \sim -2.0$  is deduced by Ortolani et al. (1999) and  $[\text{Fe}/\text{H}] \sim -1.2$

by Valenti et al. (2007) from CMDs. Armandroff & Zinn (1988) obtained  $[\text{Fe}/\text{H}] = -0.99$  from measurements of CaT lines. Vásquez et al. (2018) (ESO proposal 089.D-0493) measured the CaT lines for six stars and obtained  $[\text{Fe}/\text{H}] \sim -1.08, -1.21,$  and  $-1.16$  following calibrations from Dias et al. (2016), Saviane et al. (2012), and Vásquez et al. (2015), respectively. In the compilations by Harris (1996, Edition of 2010)<sup>1</sup> and Carretta et al. (2009), metallicities of  $[\text{Fe}/\text{H}] = -1.05$  and  $-2.07$  are respectively reported. Given that spectroscopic results are more reliable for metallicity derivations, it appears that a value of around  $[\text{Fe}/\text{H}] \sim -1.0$  should be preferred. The aim of this work is to obtain the metallicity derivation for Terzan 9, together with its radial velocity. The coordinates and typical photometric parameters for Terzan 9 are reported in Table 1.

In Figure 5.1 is shown an image of Terzan 9 obtained at the NTT in 2012, with an excellent seeing of  $0.5''$ . Figure 2.1 shows an image created from MUSE cube where the data cubes are added up combing the colours red, green, and blue (RGB).

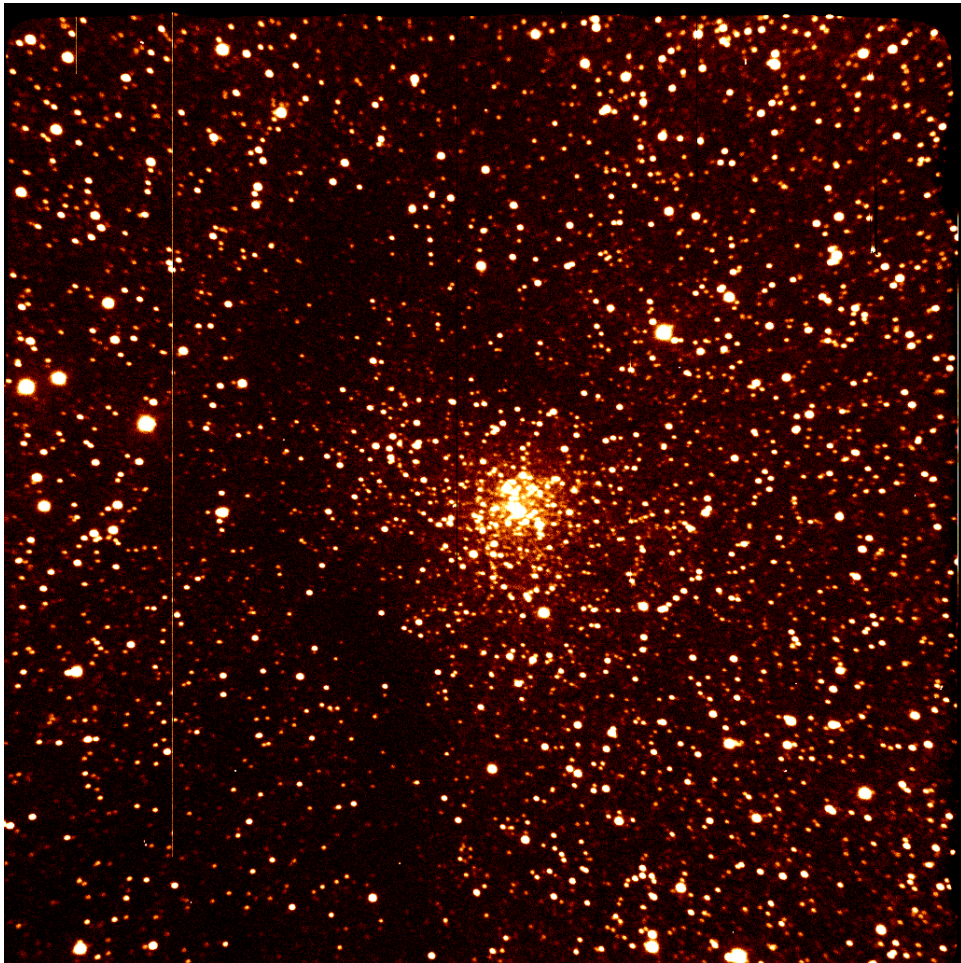
Some general informations about Terzan 9 are reported in Table 5.1. The log of observations reported in 2.2.

Table 5.1 - Terzan 9: data from literature. References: (1) Rossi et al. (2015), (2) Bica et al. (2006), (3) Ortolani et al. (1999), (4) Harris (1996, 2010 Edition).

RA J2000	18 01 38.80
DEC J2000	-26 50 23.0
l(°)	3.60
b(°)	-1.99
R <sub>Sun</sub> (kpc)	7.7 (1,2)
R <sub>GC</sub> (kpc)	0.7 (2)
E(B-V)	1.87 (2)
V <sub>tip</sub> /V <sub>HB</sub>	17.5/20.35 (3)
M <sub>0 V,t</sub>	-3.71 (4)

The code ETOILE (Katz et al. 2011, Dias et al. 2015) is used to derive the stellar parameters effective temperature, gravity, metallicity, and  $[\text{Mg}/\text{Fe}]$  ratio for each sample star. This code corrects for radial velocity, compares the observed spectra of a sample star to all spectra from a grid of spectra, and indicates which ones are the most similar. The procedure proved to work well, as demonstrated in Dias et al. (2015, 2016), where the method is applied to 800 red giants in 51 globular clusters, observed with FORS2 at a similar resolution as MUSE, which is of the order of  $R \sim 2000$  at  $6000 \text{ \AA}$ .

<sup>1</sup> [www.physic.mcmaster.ca/~harris/mwgc.dat](http://www.physic.mcmaster.ca/~harris/mwgc.dat)



*Figure 5.1:* Terzan 9: I image of Terzan 9 obtained at NTT in 2012, with seeing of 0.5 arcsec. Size is  $2.2 \times 2.2$  arcmin<sup>2</sup>.

### 5.1.1 Extraction of Stellar Spectra

To extract the data from the MUSE datacubes, we employed the PampelMUSE<sup>2</sup> code (Kamann et al. 2013) which is specific to stellar spectra extraction in crowded fields of data cubes such as MUSE. This software aptly deals with the observation of a densely populated stellar field such as a globular cluster. One challenge is the seeing-limited angular resolution of the instrument. A single object is represented by a point spread function (PSF), and the stellar field is a sum of many overlapping PSFs. Even in cases of heavily blended regions, the objects can be recovered using a PSF model if the distance between two neighbor stars is larger than  $0.3 \times \text{FWHM}$ .

This code written in python executes many tasks. In a simplified picture, a datacube is a sum of layers in wavelength of the image. A spaxel contains the entire spectrum, hence contributes to all layers. This method consists in analysing the datacube, layer by layer, performing PSF photometry individually on each layer. In the end all photometric solutions for each layer are combined, building spectra for each of the objects.

In order to get the spectra of sources of interest from the datacube, it is needed to provide an input catalogue with the position and magnitude of these objects, or else a selection by hand on the image. The coordinates are identified in the list of stars from the NTT 2012 observations (Sect. 2), and the proper motion cleaned CMDs by Rossi et al. (2015). The code locates the stars through a PSF fitting; a degree of confidence is assigned to each object, that can then be resolved in the crowded stellar field, and the spectra to be extracted.

To find a PSF in a crowded field, the program selects a number of relatively isolated objects and fits to them an analytical function. Then an Hermitian of order two is used to smooth the PSF parameters as a function of wavelength.

The last step in the data handling before the analysis is the removal of emission lines and non-stellar features left behind in the previous steps. These lines could introduce noise to the results in the minimum distance method which is the basis of the code ETOILE. The elimination of emission lines was made using a python code, which identifies the lines and cuts them in a region between their two edges, as illustrated in Fig. 5.2. We proceeded with the elimination of the emission line [O I] 5577.338 Å (Osterbrock et al. 1996) from

<sup>2</sup> <https://gitlab.gwdg.de/skamann/pampelmuse>

all sample spectra. A future version of ETOILE may have the option of masking out undesired regions, such as those with their emission lines remaining after the cosmic ray cleaning and sky subtraction.

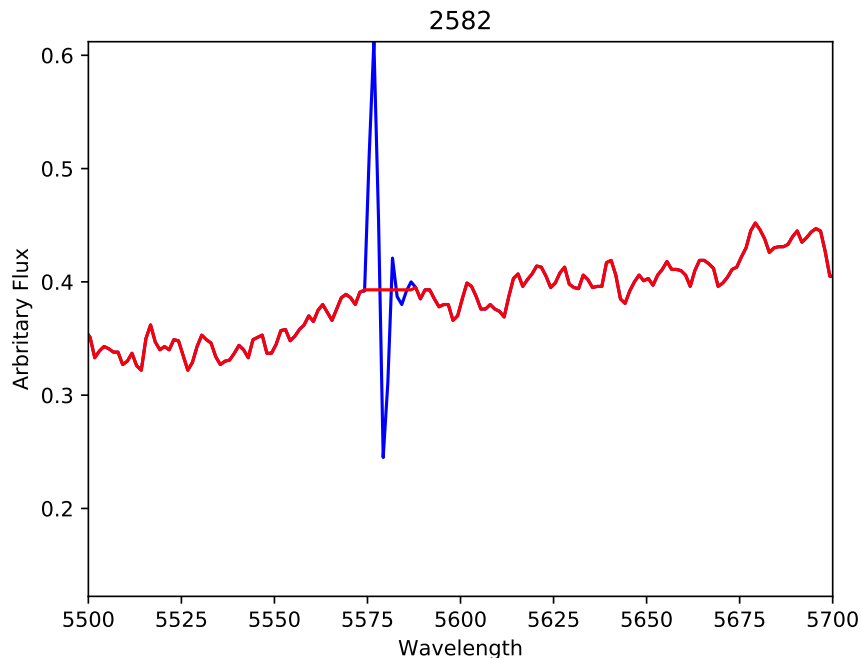


Figure 5.2: Emission line subtraction from spectrum of star 2582.

Finally, the extracted spectra for each star observed in different nights were combined to get a final 1D spectrum with higher S/N for each star. The combination is done following these steps: Fig. 5.3 shows the difference in flux levels in the spectra of a same star observed on different nights with the same exposure time but different weather conditions. We accounted for the difference in flux by normalizing them at 5000 Å and adding up all with no airmass-based or S/N-based weight, given that for the same star, there is little variation in S/N.  $S/N \sim 110$  for  $V \sim 17$ , and  $S/N \sim 90$  for  $V \sim 20$ . All S/N values are given in Table A.2.

## 5.2 Analysis

We derived atmospheric parameters via full spectrum fitting with the ETOILE code (Katz et al. 2011). This method is very robust in finding the absolute minimum in a  $\chi^2$  map (e.g. Recio-Blanco et al. 2014; Jofre et al. 2018). The code written in C is a modified

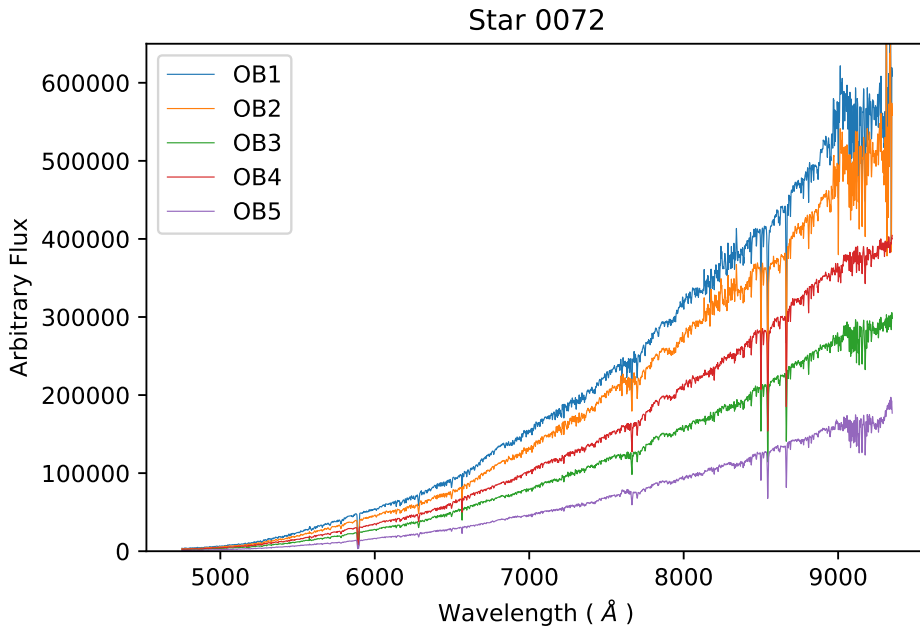


Figure 5.3: Spectra of Terzan 9 star id 0072 from different data cubes obtained with PampelMUSE.

version of the HALO (Cayrel et al. 1991) and TGMET (Katz et al. 1998) codes, which is obtained by changing the main four procedures: a) the sample star spectrum is compared with the full list of reference spectra, b) the input data are in ascii format, c) the target spectrum does not need to be normalized or calibrated in absolute flux, and d) no input parameters are given. More details on the method for extracting the fundamental stellar parameters ( $T_{\text{eff}}$ ,  $\log g$ ,  $[\text{Fe}/\text{H}]$ ) from the spectra are given in Katz et al. (1998, 2001). In the original code, high resolution spectra of 2000 stars obtained with the ELODIE spectrograph, as presented in Katz et al. (2011), were adopted as reference.

Dias et al. (2015, 2016) implemented two other grids of spectra suitable for the analysis of medium-resolution spectra in the wavelength range 4600-5600 Å: the synthetic spectra by Coelho et al. (2005, hereafter Coelho05) and the MILES grid of observed spectra (Sánchez-Blázquez et al. 2006). We implemented a wavelength-extended version to be run with the Coelho05 library, encompassing the range 3000-18000 Å that covers the region of the MUSE spectra 4800-9300 Å, and it was used in different ways, as explained below.

In summary, the ETOILE code compares the observed spectrum to a list of reference spectra, either observed or synthetic, and finds the most similar ones through a least square of Euclidean distance measure. An example of a fit to a sample spectrum is given in Fig. 5.4.

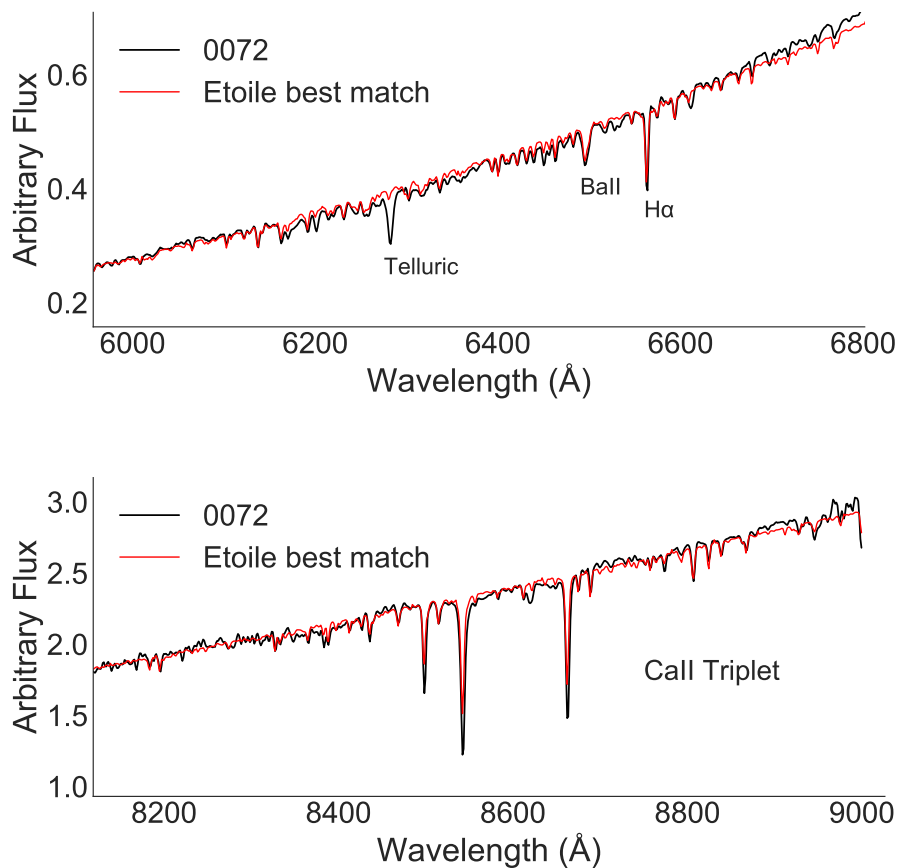


Figure 5.4: Fit obtained with ETOILE for star 0072 with a good  $S/N = 129.80$ . Upper panel: region 6000- 6800 Å where the strongest lines (telluric feature at 6282 Å, BaII 6496.9 Å and  $H\alpha$ ) are indicated; lower panel: calcium triplet region.

### 5.2.1 Sample extraction and radial velocities

We were able to extract and combine spectra from the five data cubes for 614 stars. After a selection based on  $S/N$  ( $S/N \geq 85$ ) of all final spectra, 90 of them were retained for analysis. The choice of this high  $S/N$  was due to better reliability in the parameter derivation. The ETOILE code was run for these spectra in order to derive their stellar parameters. The code first corrects for radial velocity ( $v_r$ ) through cross-correlation with a template spectrum from the library in use. In the present case, we used the MILES library in the wavelength range 4600 - 5600 Å, the synthetic Coelho05 library in the full MUSE range 4860 - 9300 Å, and in the region of the CaII triplet (CaT) 8400 - 8750 Å. The use of these different libraries and wavelength regions has shown that the most reliable method to derive radial velocities is the comparison of the sample spectra with

Table 5.2 - Comparison of radial velocity and metallicity for two stars in common with Vásquez et al. (2018, V+18). The metallicity from V+18 adopts the metallicity scale by Dias et al. (2016).

ID	ID <sub>V+18</sub>	$v_r$ km.s <sup>-1</sup>	$v_r(V+18)$ km.s <sup>-1</sup>	[Fe/H] ETOILE	[Fe/H] CaT	[Fe/H] <sub>V+18</sub>
1322	1_399	75.9±1.1	74.8±0.7	-1.52	-1.14	-1.25
1378	1_745	60.8±1.1	61.9±0.6	-1.23	-1.34	-1.26

the synthetic spectra in the CaT region. We concluded this from inspecting a series of spectra from the full initial sample and comparing them individually to reference spectra, verifying the wavelength region with that particular radial velocity value. The results are shown in Fig. 5.5 as smoothed histograms of radial velocities obtained in the three cases described above.

Fig. 5.6 shows the radial velocity distribution using the CaT region analysed through the Coelho05 library, for the 90 selected stars. A gaussian fit results in a mean radial velocity value of  $v_r = 49.7 \text{ km s}^{-1}$  and a sigma of  $22 \text{ km s}^{-1}$ . The mean heliocentric radial velocity is  $v_r^h = 58.1 \text{ km s}^{-1}$ . The radial velocity of  $v_r^h = 71.4 \pm 0.4 \text{ km s}^{-1}$  from six stars by Vásquez et al. (2018) is compatible with the present value within uncertainties. A comparison with two stars in common with Vásquez et al. (2018) is reported in Table 5.2, showing excellent agreement in terms of radial velocities. In conclusion, we suggest that the present value is more accurate given the larger sample of stars taken into account.

For these two stars in common, the metallicities from the present work, derived with ETOILE and from CaT with the same method as Vásquez et al. (2018), that is, by applying their Equation 5 for the metallicity scale by Dias et al. (2016) and their reported values, given in Table 5.2, show good agreement within uncertainties. The full explanation on how the metallicities are calibrated is given on Sect. 5.2.4

In Table A.3 are reported the selection for a  $S/N = 85$ . Finally, the spectra are corrected for the adopted results of radial velocity, which are reported in Table A.1.

### 5.2.2 Coordinates and proper motions

The X,Y position of stars in the NTT image used to identify the stars in the MUSE data, were transformed to right ascension (RA) and declination (DEC) and matched with the Gaia Data Release 2 (DR2, Gaia collaboration 2018) coordinates, therefore the coordinate values reported in Table A.2 have a high astrometric precision. For the list of 90 selected stars, Gaia data are available.

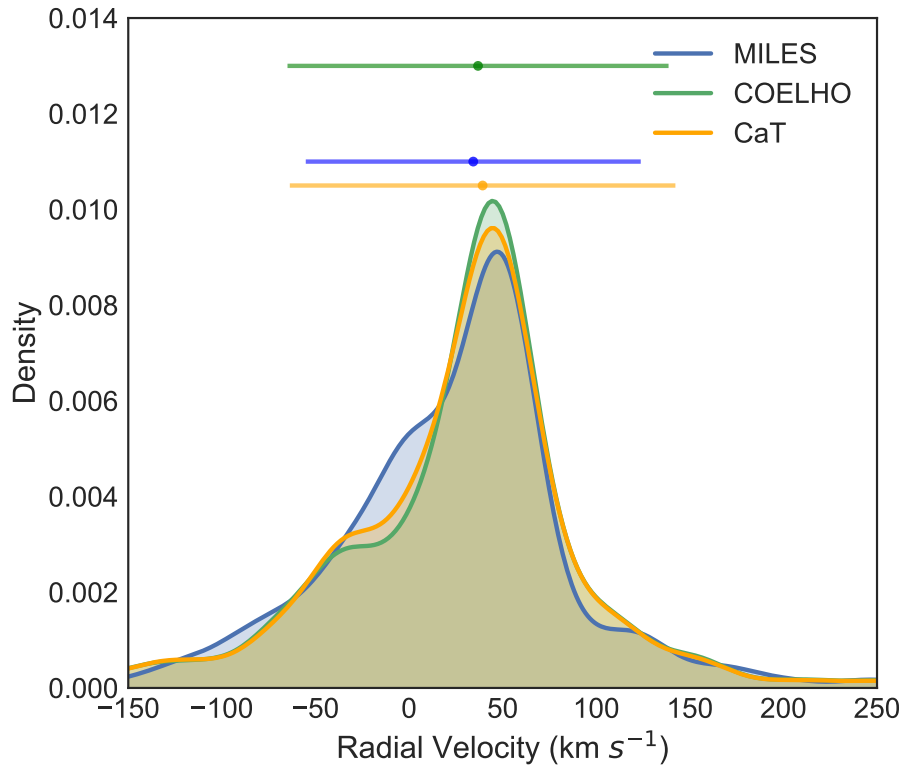


Figure 5.5: Histograms of radial velocities obtained in the cases: green distribution: MILES library in the range 4860 - 5600 Å; blue distribution: Coelho05 library in the range 4860 - 9000 Å; and yellow distribution: Coelho05 library in the CaT region at 8400 - 8750 Å.

In the MUSE field, there are 371 stars in the Gaia data that are shown in Fig. 5.7, where we see a clear cluster, seen as the feature highlighted in blue. Among the 371 Gaia stars, we identified 236 stars with proper motion (PM) information. For this sample, the mean proper motion values derived are:  $\text{pmRA} = -2.212 \pm 0.0851$  mas/yr, and  $\text{pmDE} = -7.425 \pm 0.0851$  mas/yr, in good agreement with derivations by Pérez-Villegas et al. (2019) of  $(-2.314 \pm 0.108, -7.434 \pm 0.068)$  mas/yr and  $(-2.225 \pm 0.038, -7.492 \pm 0.029)$  mas/yr from Vasiliev (2018). Note that the PM value derived uses 236 stars from Gaia which are present in the MUSE field. The values are the same as for the 90 selected member stars, as made evident in the corner plot given in Fig. 5.12. We note that the previous values by Rossi et al. (2015) of  $(0.0 \pm 0.38, -3.07 \pm 0.49)$  were different from these data, which are more accurate.

In order to identify a final list of member stars, we selected stars from their radial velocity of  $v_r = 58.1 \pm 1.1$  km s<sup>-1</sup>, combined with proper motions of  $\text{pmRA} = -2.21 \pm 0.10$

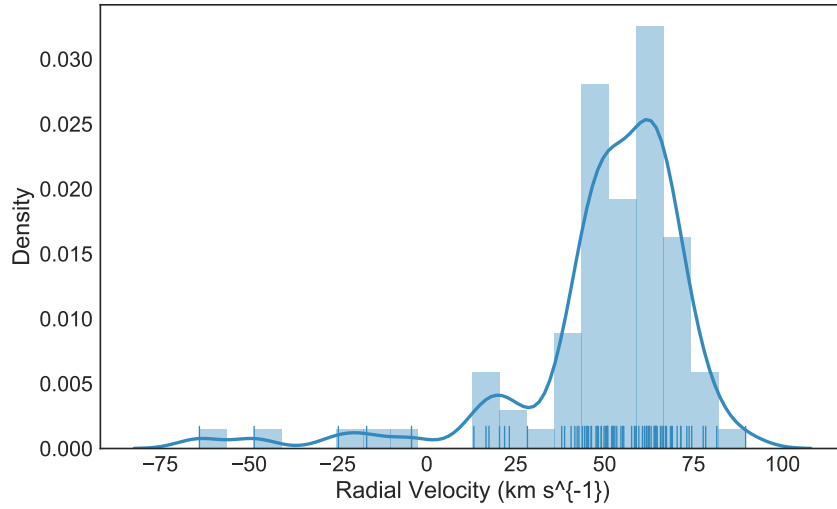


Figure 5.6: Smoothed histogram of radial velocities obtained with the Coelho05 library in the CaT region at 8400 - 8750 Å. A kernel density estimation (KDE) gaussian fitting the main peak of radial velocity distribution is overplotted.

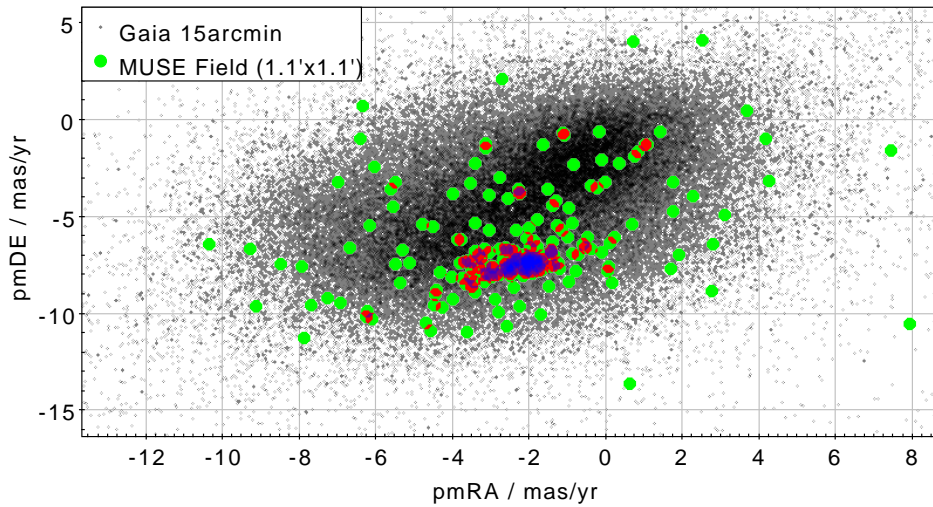


Figure 5.7: Proper motions from Gaia. Symbols: gray dots: Gaia stars contained within a radius of 15 arcmin from the cluster center; Green dots: Gaia stars in a density representation enclosed in the MUSE field (1.1'×1.1'). The clustering of stars from Terzan 9 can be seen in red and blue, where blue is the densest part.

and  $\text{pmDEC} = -7.42 \pm 0.07$ . We ended up with 67 stars, that are reported in Table A.2.

### 5.2.3 Stellar parameters

After radial velocity correction, the stellar spectrum is compared with the spectra of all stars in both libraries: Coelho05 and MILES. The ETOILE code ranks all spectra from

the library by similarity ( $S$ ) to the target spectrum.  $S$  is related to  $\chi^2$ , i.e., the most similar spectra have the smallest  $S$  value (for a definition of the similarity parameter, see Katz et al. 1998, and Dias et al. 2015). A weighted mean of the stellar parameters  $T_{\text{eff}}$ ,  $\log g$ ,  $[\text{Fe}/\text{H}]$ , and  $[\alpha/\text{Fe}]$  of the most similar reference spectra is taken as the derived parameter of the target spectrum. The threshold to select the most similar spectra is based on the normalized similarity,  $S/S(1) \leq 1.1$  (Dias et al. 2015), applied to results with both libraries.

The stellar parameters were first derived using the observed library MILES in the wavelength range of 4800-6000 Å, containing the MgI triplet lines, which is among the main features commonly used in spectra of galaxies (Mg2, Mgb, Fe5270, Fe5335, Faber et al. 1985). From this procedure we obtained our first set of results.

Using the Coelho05 library, we carried out tests in different spectral regions, as well as with the full spectral range of the MUSE spectra. As a check, we applied these calculations to spectra of the Sun, Arcturus and the metal-rich red giant  $\mu$  Leo (Lecureur et al. 2007). For the synthesis of these spectra, the PFANT code (Barbuy et al. 2018b) was applied. The result indicated that the most reliable region is 6000-6800 Å, which is, in fact, the region commonly used to derive stellar parameters from high-resolution spectra (e.g. Barbuy et al. 2018c). This is explained by the following facts: it is widely known that when bluer than 6000 Å, the continuum is progressively affected by molecular lines as well as a large number of faint lines. When redder than 6800 Å, there are fewer lines, and, particularly fewer lines with well-defined oscillator strengths, and more numerous telluric lines. The stellar parameters were then derived by running ETOILE with the library Coelho05 in the range 6000-6800 Å, obtaining a second set of results.

From the final stellar parameters from the two applications (MILES and Coelho05), a mean metallicity obtained from ETOILE along with the two libraries is  $[\text{Fe}/\text{H}] = -1.12 \pm 0.12$ , as shown in Fig. 5.8. It is important to note that there is a trend for lowering the metallicity as a function of lower S/N in this method. This is the reason for selecting only high S/N > 85 spectra; even so there is still a spread in metallicity values.

Finally, in Fig. 5.11 the metallicity distribution vs. radial velocity distribution is shown, clearly indicating the locus of the cluster member stars. There is no strong correlation between the possible two peaks in metallicity hinted at in Fig. 11 and radial velocity, meaning that these are not two distinguished groups of similar metallicity and radial

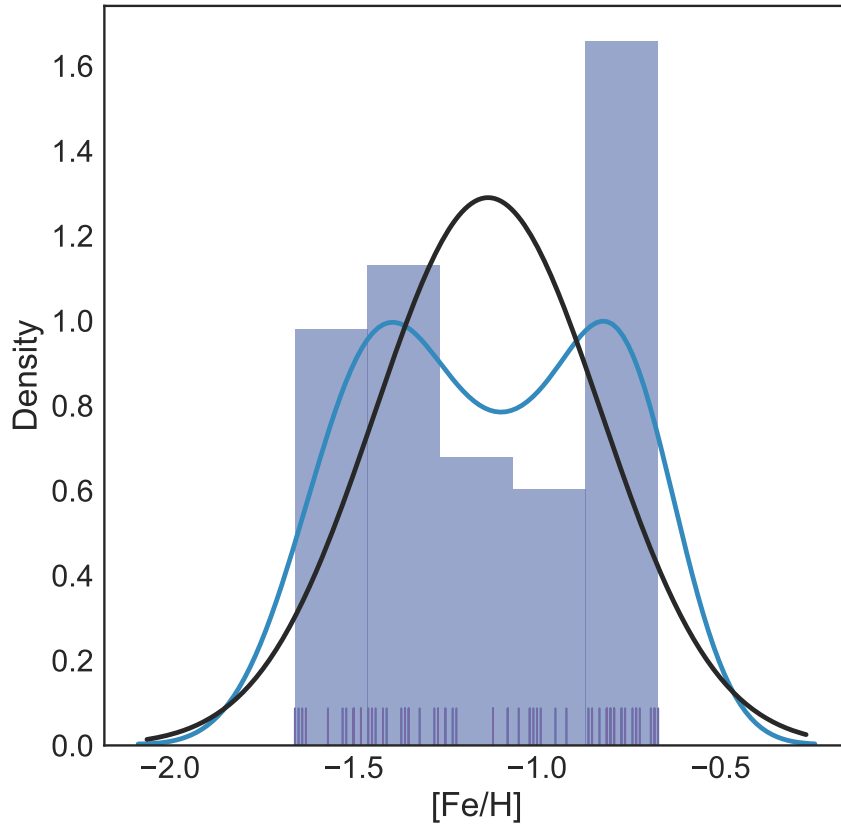


Figure 5.8: Metallicity distribution of sample stars based on the optical analysis. The black curve represents a gaussian fit centered at a mean value of  $[\text{Fe}/\text{H}] = -1.12 \pm 0.12$ . The blue curve is a KDE gaussian bandwidth estimated using Scott's rule

velocity values. In Fig. 5.12, the corner plot of different parameters of the member stars is given.

#### 5.2.4 Uncertainties

The uncertainties in this work regarding the stellar parameters are the same as those that have already been described in section 3.2.2 in Dias et al. (2015). The uncertainties on the stellar parameters are computed using the average of squared residuals with the weighted  $1/S^2$  as shown in the equation

$$\sigma_{par(N)} = \sqrt{\frac{1}{M} \frac{\sum_{m=1}^{M_{max}} (par_m - par)^2 \times 1/S_M^2}{\sum_{m=1}^{M_{max}} 1/S_n^2}}, \quad (5.1)$$

where  $par$  corresponds to the stellar parameters,  $T_{\text{eff}}$ ,  $\log g$ ,  $[\text{Fe}/\text{H}]$ , and  $[\alpha/\text{Fe}]$ , and  $N$  is

the number of stars. The  $m$ , and  $M$  are counted as the number of the most similar stars in the library after the criteria of similarity  $S \leq 1.1$  is applied.

### 5.2.5 Metallicities from CaT

We normalized the NIR portion of the spectra around the CaT lines in order to perform the techniques described in Vásquez et al. (2015, 2018). The two stronger lines ( $\lambda\lambda$  8542, 8662 Å) were fitted using a combination of a Gaussian and a Lorentzian profile, and the equivalent widths were summed ( $W = W_{8542} + W_{8662}$ ). Since we used the same script as in Vásquez et al. (2018), we were able to directly follow their calibrations, which we briefly describe here. The sum of the equivalent widths was first put into the same scale as Saviane et al. (2012) by applying the relation

$$W_{S12} = 0.97 \times W + 0.21.$$

The  $W_{S12}$  was then corrected by gravity and temperature effects by applying the correction, resulting into the reduced equivalent width

$$W' = W_{S12} + 0.55 \times (V - V_{HB})$$

where  $V_{HB} = 20.35$  mag (Ortolani et al. 1999). The  $W'$  was then converted into metallicity by applying the metallicity scale of Dias et al. (2016) represented by Eq. 5 of Vásquez et al. (2018), that is,

$$[Fe/H]_{D16} = 0.055 \times W'^2 + 0.13 \times W' - 2.68$$

Example of CaT lines are shown in Fig. 5.9 for star 1378. A typical error in metallicity is of  $\pm 0.1$  dex. The final list of cluster members where the metallicities derived from procedures using the ETOILE code and the CaT measurements are reported in Table A.1, which give a mean value of  $[Fe/H] = -1.09 \pm 0.15$ , as shown in Fig. 5.10.

Finally, a comparison of metallicities for the same stars from the ETOILE code and from CaT lines gives a mean difference of  $[Fe/H](ETOILE) - [Fe/H](CaT) \approx -0.03$  dex. In other words, from ETOILE we get a mean of  $[Fe/H] = -1.12 \pm 0.12$  and from CaT we get  $[Fe/H] = -1.09 \pm 0.15$ , which are, therefore in excellent agreement.

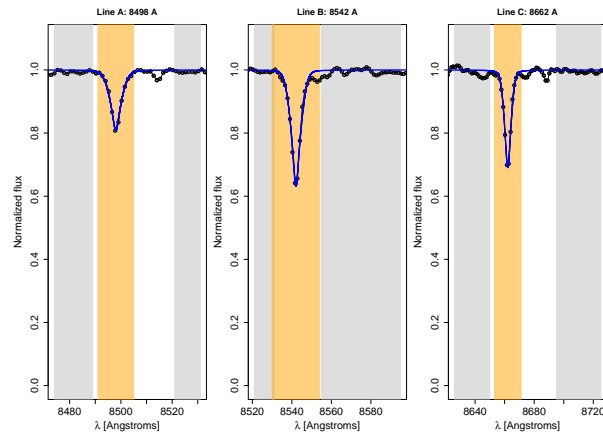


Figure 5.9: Fit to CaT lines A: 8498 Å; B: 8542 Å, and C: 8662 Å for star 1378 as example. The shaded gray areas show the local continuum regions and the shaded orange areas show the line region defined by (269). The black lines and dots trace the observed spectrum in the rest frame and the blue lines are the best model fit to the data, using a sum of Gaussian and Lorentzian functions. The spectrum has been locally normalized using the highlighted local continuum regions before the fitting. In this analysis we only use the sum of the equivalent widths of the two strongest lines (B+C) following the recipe of (269; 270).

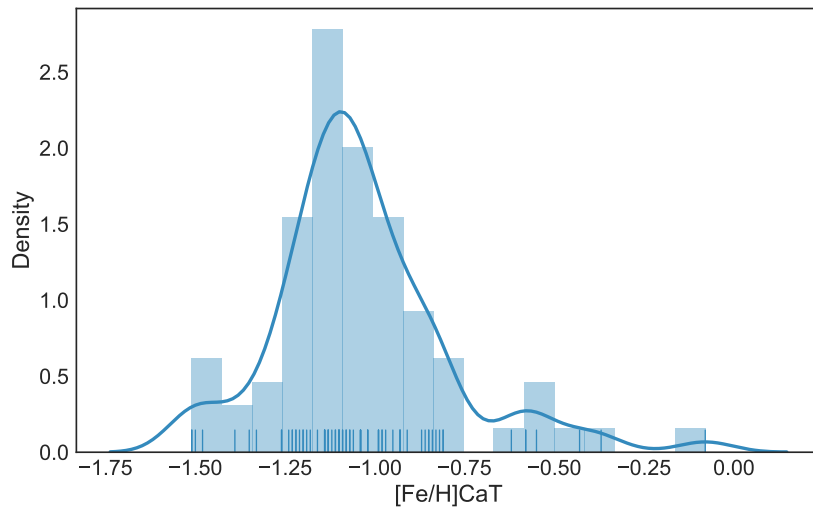


Figure 5.10: Metallicity distribution of sample stars based on CaT analysis.

Fig. 5.11 shows the metallicity distribution vs. the radial velocity distribution for the identified 67 member stars. Fig. 5.12 shows a corner plot relating metallicities, proper motions, and radial velocities.

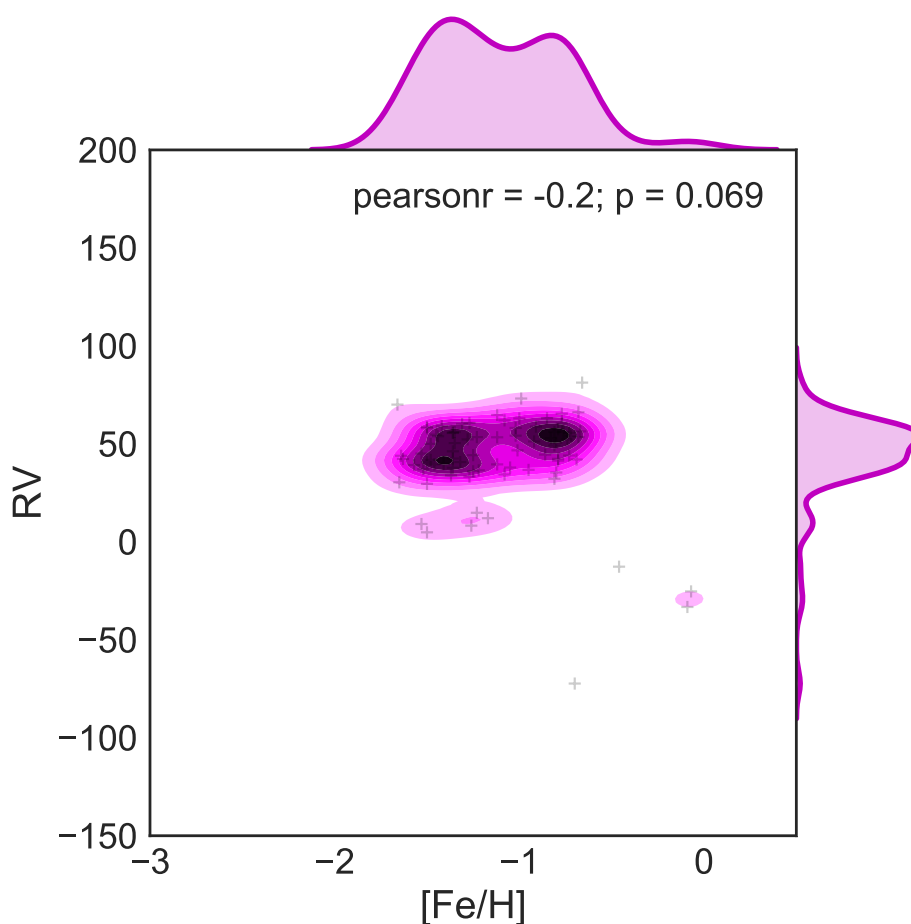


Figure 5.11: Metallicity distribution based on optical analysis vs. radial velocity distribution, for identified member stars.

### 5.2.6 Color-magnitude diagrams of member stars

In Fig. 5.13 we compare the I vs. V-I color-magnitude diagram showing all stars where the member stars are highlighted, and the resulting  $\log g$  vs.  $T_{\text{eff}}$  diagram. At the RGB base, a small trend towards high temperatures might be present. The brighter the RGB stars, the closer the isochrones get to the more metal-rich ones, again indicating that the metallicity is not bimodal and that the spread is due to S/N effects. On the right panel, member stars identified in the Gaia survey, are plotted with Gaia colors G vs. BR-RP. Dartmouth isochrones of 13 Gyr,  $[\text{Fe}/\text{H}]=-2.0$  and  $[\text{Fe}/\text{H}]=-1.0$  are overplotted. The I values were corrected by  $A_I$  cf. Schlafly & Finkbeiner (2011)<sup>3</sup>; for the Gaia magnitudes no corrections were applied. In this Fig. we clearly see the RGB stars. A BHB appears more

<sup>3</sup>

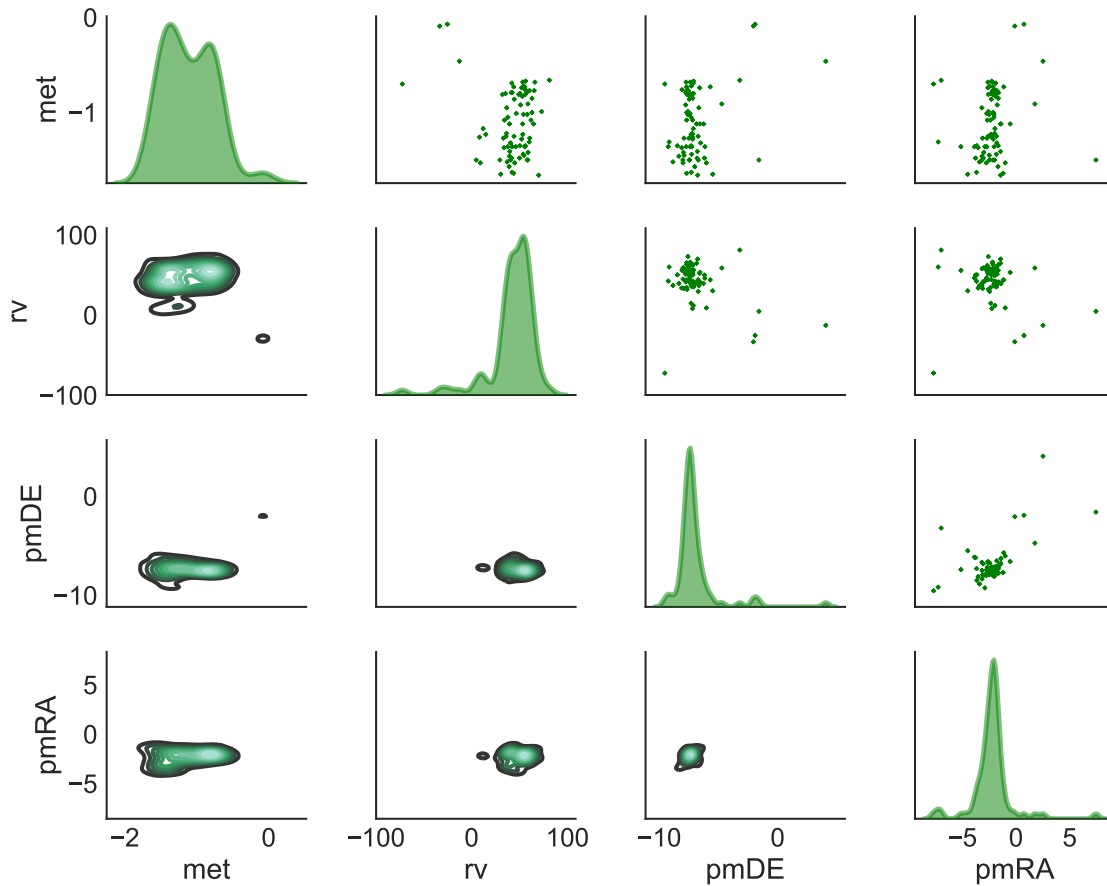


Figure 5.12: Corner plot: metallicity, proper motion and radial velocities.

clearly present in Fig. 5.13b, confirming earlier evidence by Ortolani et al. (1999).

### 5.3 Discussion

In the present work, the metallicity derived from the 67 selected member stars turned out to be of  $[\text{Fe}/\text{H}] = -1.12 \pm 0.12$  from the optical and  $[\text{Fe}/\text{H}] = -1.09 \pm 0.15$  from CaT lines, therefore, a final metallicity of  $[\text{Fe}/\text{H}] = -1.10 \pm 0.15$  was adopted.

The radial velocity of our sample stars was double-checked with synthetic spectra exhaustively, therefore, we suggest that our value of  $v_r^h = 58.1 \pm 1.1 \text{ km s}^{-1}$  is more robust than the higher value of  $v_r = 71.4 \text{ km s}^{-1}$ , given in Vásquez et al. (2018), due to the higher numbers of stars.

Terzan 9 is now included in the list of moderately metal-poor globular clusters with a BHB similar to HP 1 (Barbuy et al. 2016), NGC 6522 (Barbuy et al. 2014), and NGC

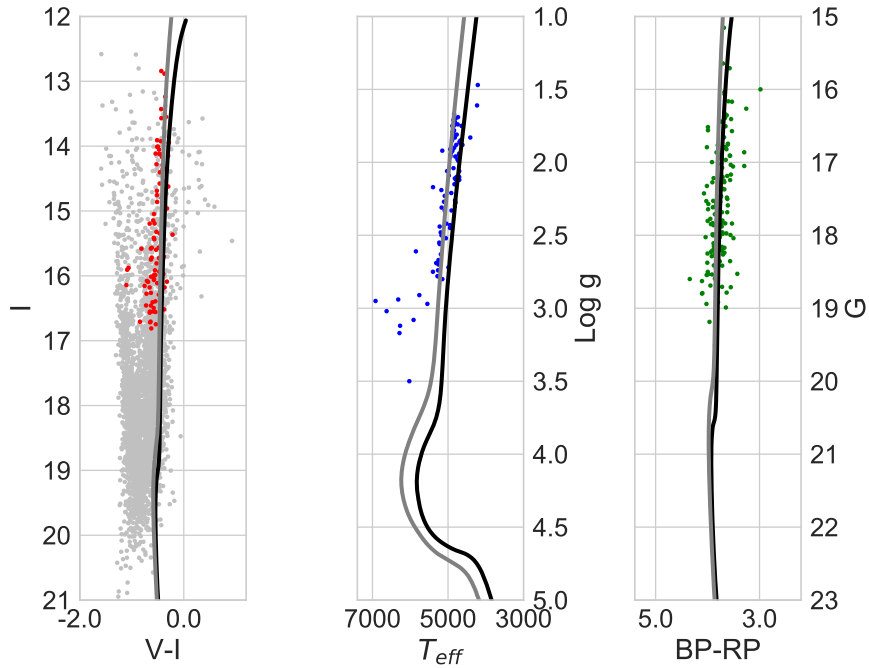


Figure 5.13: I vs. V-I color-magnitude diagram showing all stars (gray) and member stars (red) (left panel), compared with the log  $g$  vs.  $T_{\text{eff}}$  diagram (middle panel), and CMD in Gaia magnitudes and colors G vs. BP-RP for the stars in common (right panel). Dartmouth isochrones of 13 Gyr, and  $[\text{Fe}/\text{H}]=-1.0$  are overplotted in black and isochrones of 13 Gyr, and  $[\text{Fe}/\text{H}]=-2.0$  are overplotted in gray.

6558 (Barbuy et al. 2018c).

Terzan 9 has a blue HB, but not an extended one (see Ortolani et al. 1999). The moderately metal-poor metallicity found for Terzan 9 correspond essentially to the lower end of the metallicity distribution of the bulk bulge stellar population. As a matter of fact, due to a fast chemical enrichment in the Galactic bulge, such as the one modeled by e.g. Cescutti et al. (2008), the iron abundance of  $[\text{Fe}/\text{H}]\sim-1.3$  is reached very fast, and stellar populations start to form in more significant numbers from there on, as confirmed by metallicity distribution functions (MDF) given in Zoccali et al. (2008, 2017), Hill et al. (2011), Ness et al. (2013), Rojas-Arriagada et al. (2014, 2017) - see also Barbuy et al. (2018a).

The derivation of Mg-to-iron is based on the fitting of the MgI triplet lines (see Dias et al. 2015, 2016). In Fig. 5.14, the distribution of enhancement in the  $\alpha$ -element Mg is shown with a mean value of  $[\text{Mg}/\text{Fe}]=+0.27\pm 0.03$ . The sigma of the distribution results is also  $\pm 0.03$ . This enhancement is similar to those reported in the Galactic bulge by

Barbuy et al. (2018a) and Schultheis et al. (2017). This indicates that the stars in Terzan 9 were formed from gas resulting from an early fast chemical enrichment by core-collapse supernovae.

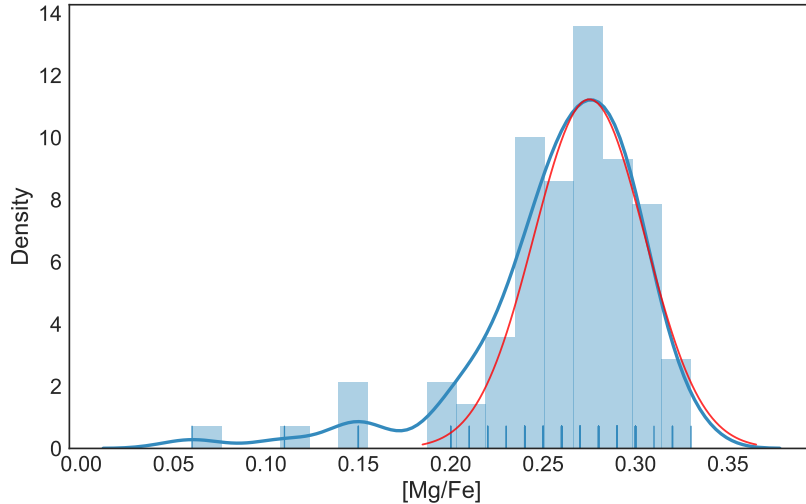


Figure 5.14: Distribution in  $[Mg/Fe]$ . A KDE plot indicates a mean value of  $[Mg/Fe]=+0.27$ .

#### 5.4 Summary of Terzan 9

We obtained MUSE datacubes for the bulge compact globular cluster Terzan 9. Using the software pampelMUSE by Kamann et al. (2013, 2018), we were able to extract the spectra of over 600 stars. The sample was reduced to 67 member stars by selecting spectra with  $S/N > 85$  and with compatible radial velocities and proper motions. These spectra were analysed based on a full spectrum fitting with the ETOILE code in the area of 4600-5600 Å, compared with a grid of observed spectra (MILES, Sánchez-Blázquez et al. 2006). In the area of 6000-6800 Å, they were compared with a grid of synthetic spectra by Coelho et al. (2005). The CaT lines were also measured in order to obtain an independent derivation of metallicity. Both methods give very close mean results, with an adopted mean of  $[Fe/H]=-1.10 \pm 0.15$ . This mean value is the outcome of the combination of a range of values where, in particular with regard to the optical region, two metallicity peaks are seen. In order to confirm metallicities, further observations with high resolution spectroscopy are of great interest. The present work allows for a reliable target selection for such studies.

---

From MUSE data we were able to derive a mean heliocentric radial velocity of  $v_r^h = 58.1 \pm 1.1 \text{ km s}^{-1}$ , which is somewhat lower than the value from Vásquez et al. (2018) based on 6 stars, but the values are in agreement within uncertainties. These metallicities place Terzan 9 as a new member of the moderately metal-poor clusters with a blue horizontal branch that are found in the Galactic bulge.



## The globular cluster AL 3

### 6.1 Introduction: Globular cluster AL 3

The globular clusters AL 3, NGC 6558, and HP 1 share the characteristics of having a metallicity of  $[\text{Fe}/\text{H}] \sim -1.0$  and of being located in the Galactic bulge. They are old and could represent the earliest stellar populations in the Galaxy (Ortolani et al. 2006; Barbuy et al. 2018c; Kerber et al. 2019).

The star cluster AL 3 was discovered by Andrews & Lindsay (1967) and was also cataloged as BH 261 by van den Bergh & Hagen (1975), reported as a faint open cluster. It is reported in the ESO/Uppsala catalogue (Lauberts 1982) as ESO 456-SC78. Ortolani et al. (2006) have shown that the star cluster shows B, V, I Colour-Magnitude Diagrams (CMD) typical of a globular cluster. It is centered at J2000  $\alpha = 18^{\text{h}}14^{\text{m}}06.6^{\text{s}}$ ,  $\delta = -28^{\circ}38'06''$ , with Galactic coordinates  $l = 3.36^{\circ}$ ,  $b = -5.27^{\circ}$ . It is located at 6d25 and 2 kpc from the Galactic center, therefore in the inner bulge volume. The cluster has a depleted Red Giant Branch (RGB), similarly to low mass Palomar clusters, indicating it to have been stripped along its lifetime. This cluster has not been further observed so far.

NGC 6558 is located in a window, identified by Blanco (1988), with equatorial coordinates (J2000)  $\alpha = 18^{\text{h}}10^{\text{m}}18.4^{\text{s}}$ ,  $\delta = -31^{\circ}45'49''$ , and Galactic coordinates  $l = 0.201^{\circ}$ ,  $b = -6.025^{\circ}$ . This cluster was analysed in terms of Colour-Magnitude Diagrams (CMD) by Rich et al. (1998). Rossi et al. (2015) obtained a proper-motion-cleaned CMD, and presented a proper motion analysis, from which a study of its orbits was given in Pérez-Villegas et al. (2018, 2020).

The globular cluster Cl Haute-Provence 1 or HP 1, also designated BH 229 and ESO 455-SC11, was discovered by Dufay et al. (1954). It is located at J2000  $\alpha = 17^{\text{h}}31^{\text{m}}05.2^{\text{s}}$ ,

$\delta = -29^{\circ}58'54''$ , with Galactic coordinates  $l = 357.42^{\circ}$ ,  $b = 2.12^{\circ}$ .

In the present work we study individual stars of these clusters, in a limited region of the spectrum in the H-band corresponding to the wavelength region of the Phoenix spectrograph at the Gemini-South telescope, centered at  $15555 \text{ \AA}$ , and covering  $15520\text{--}15590 \text{ \AA}$ , with a high spectral resolution of  $R \sim 75,000$ . This region was chosen for containing prominent lines of CN, CO and OH.

The description of the sample selected to carry out this analysis of the globular cluster AL 3 is described in the section 2.

## 6.2 The spectra of the AL 3 observed stars

There is a clear contrast between the spectra of HP1-5, AL3-3, and AL3-7, that have shallow lines, and AL3-6 and NGC6558-42, that show strong lines. Whereas NGC6558-42 is a typical red giant, the stars AL3-3, AL3-7, and HP1-5 show weak molecular lines. In Fig. 6.8, we show the observed spectrum in the selected wavelength regions containing CN, OH lines, and the CO bandhead at  $15578 \text{ \AA}$  for stars AL3-3, AL3-7, and HP1-5. The molecular lines are very shallow, due to a combination of warm temperatures and low metallicities. Clearly, the CNO abundances derived for these stars are less reliable than for the cool star NGC6558-F42. Their CNO abundances are compatible with being close to solar, but given the shallowness of the lines, it is clear that the molecular lines are not reliable for abundance measurements.

AL3-6 instead shows very strong CNO lines. Figure 7 indicates that  $[\text{C}/\text{Fe}] = +0.7$ ,  $+0.8$ ,  $[\text{N}/\text{Fe}] = +1.0$ ,  $[\text{O}/\text{Fe}] = +0.8$  for this star. We show two different renormalisations to illustrate the difficulty in analysing this spectrum. Additionally, the computations with two different carbon abundances illustrate the extreme sensitivity of the lines. Clearly, however, there is an urgent need to observe this star in the optical and/or in a more extended wavelength region in the H-band to obtain firm conclusions on the CNO abundances of AL 3.

## 6.3 Spectroscopy in the H-band: atomic and molecular lines

The H-band will be intensely observed in the near-future, given the new instruments giving emphasis on the near-infrared region, such as the James Webb Space Telescope

(JWST), and new spectrographs on ground-based telescopes such as MOONS@VLT (presently CRIFES@VLT is available), and MOSAIC@ELT. The project APOGEE (Apache Point Observatory Galactic Evolution Experiment), with observations at a resolution of  $R \sim 22,000$  carried out at the 2.5-meter Sloan Foundation Telescope at the Apache Point Observatory in New Mexico (APOGEE-2N), and the 2.5-meter du Pont Telescope at Las Campanas Observatory in Chile (APOGEE-2S) (Majewski et al. 2017) has been showing the power of the H-band.

Given the short wavelength range covering only  $70 \text{ \AA}$  of the Phoenix spectrograph, we faced the challenge of identifying the lines in moderately metal-poor stars of the Galactic bulge, for which only a few lines are available. Because the available lamps did not include lines in this region, and experience proved that sky lines yielded a better wavelength calibration, and given the short wavelength range, it is not straightforward to identify the lines.

For this reason, we have proceeded to a line identification, in the spectra of the reference stars Arcturus and  $\mu$  Leo, and created a shortened version of a line list, containing only detectable lines.

Meléndez & Barbuy (1999, hereafter MB99) worked on a list of atomic lines in the J and H bands. The list of lines corresponded to the detectable lines mostly. That previous line list needed to be largely completed. By checking the lines detectable, in the wavelength range  $15520\text{-}16000 \text{ \AA}$ , this was done by verifying the line lists from APOGEE (Shetrone et al. 2015), and VALD (Piskunov et al. 1995, Ryabchikova et al. 2015). Note that astrophysical oscillator strengths  $\log gf$  were applied to the APOGEE line list, wherefrom differences in  $\log gf$  are due. Through a line-by-line checking of its detectability in the Arcturus spectrum, we identified lines of Mg I, Si I, Ca I, Ti I, Mn I, Ni I, and could not find detectable lines from the species C I, O I, Sc I, V I, Cr I, Co I, Cu I, Y I, Y II. The spectra computed including all lines of all these elements, are entirely equivalent to the one computed with the shortened line list, therefore for practical purposes of identifying which are the lines really contributing to a feature, we created a table containing the detectable lines only. In this Table, available under request, are reported the oscillator strengths from MB99, APOGEE, VALD, and adopted values, where by order of preference we adopted NIST and MB99 preferentially.

Molecular electronic transition lines of CN  $A^2\Pi-X^2\Sigma$ , and vibration-rotation CO  $X^1\Sigma^+$ ,

OH X<sup>2</sup>Π lines were included in the synthetic spectra calculations. The line lists for CN were made available by S. P. Davis, the CO line lists were adopted from Goorvitch (1994), and the OH line list was made available by S. P. Davis and A. Goldman (Goldman et al. 1998). For more details on CN, CO and OH molecular lines we refer to Meléndez & Barbuy (1999), Meléndez et al. (2001), and Meléndez et al. (2002). TiO  $\phi$ -system b<sup>1</sup>Π-d<sup>1</sup>Σ lines are also present in the region. The line list by Jorgensen (1994) is included in the calculations as described in Schiavon & Barbuy (1999) and Barbuy et al. (2018a). The adopted dissociation potential of OH is 4.392 eV, D<sub>0</sub> = 11.092 eV for CO, and D<sub>0</sub> = 7.65 eV for CN (Huber & Herzberg 1979).

The code PFANT for calculations of synthetic spectra is described in Barbuy et al. (2018b), and the code, together with the atomic and molecular line lists are available<sup>1</sup>.

We identified the lines in the reference stars Arcturus and  $\mu$  Leo. For the reference star Arcturus, the spectrum atlas from Hinkle et al. (1995), and for the metal-rich reference giant star  $\mu$  Leo APOGEE spectra are used.

The adopted stellar parameters for Arcturus and  $\mu$  Leo are from Meléndez et al. (2003) and Lecureur et al. (2007).

## 6.4 Gaia cross-check

In order to verify the corresponding membership probability of observed stars in AL 3, we performed the cross-match with Gaia Early Data Release 3 (EDR3; Gaia Collaboration 2020). We selected stars within 20' from the cluster centre and used the renormalised unit weight error (RUWE)  $\leq 2.4$  to ensure the kinematics precision and the minimum match separation.

Having the high-precision EDR3 proper motions ( $\mu_{\alpha}^* = \mu_{\alpha} \cos \delta$  and  $\mu_{\delta}$ ), we obtain the mean proper motions for the cluster of  $\mu_{\alpha}^* = 3.59 \pm 0.03$  mas yr<sup>-1</sup> and  $\mu_{\delta} = -3.54 \pm 0.04$  mas yr<sup>-1</sup>. These values are compatible with those given in Baumgardt et al. (2019). We also computed the Gaussian membership probability distribution of AL 3. We found that the stars AL3-6 and AL3-7 have membership probabilities of 100%. Finally, the star AL3-3 has a relatively low membership probability of  $\sim 60\%$ , but still, it could be considered a member. Therefore, all three observed stars are probable members of AL 3. Table 6.1

<sup>1</sup> <http://trevisanj.github.io/PFANT>

Table 6.1 - Gaia magnitudes, proper motions and membership probability.

Star	$\alpha$ (J2000) deg	$\delta$ (J2000) deg	$G$ mag	$G_{RP}$ mag	$\mu_{\alpha}^*$ mas yr $^{-1}$	$\mu_{\delta}$ mas yr $^{-1}$	Memb %
AL3-3	273.5288067	-28.6357960	14.186 $\pm$ 0.003	13.323 $\pm$ 0.004	3.78 $\pm$ 0.09	-4.04 $\pm$ 0.07	59
AL3-6	273.5247404	-28.6346067	15.228 $\pm$ 0.003	14.303 $\pm$ 0.011	3.56 $\pm$ 0.06	-3.64 $\pm$ 0.04	100
AL3-7	273.5220767	-28.6380356	13.924 $\pm$ 0.003	13.062 $\pm$ 0.005	3.58 $\pm$ 0.03	-3.48 $\pm$ 0.03	100

provides the Gaia EDR3 cross-match and the membership probabilities.

### 6.5 Radial velocity of AL 3

We were able to derive radial velocities for the sample stars. We used the low S/N individual observations of each star (S/N $\sim$ 10.0) combined to increase the signal-to-noise to S/N $\sim$ 18.0, and S/N $\sim$ 22.0 for AL3-3 and AL3-7, respectively. Due to the stacking process, the most prominent features identified are FeI 15,534.26, OH 15,542.10, TiI 15,543.758, TiO/NiI 15,55.25 blend, CN 15,555.25, and FeI 15,591.49. We also used the OH sky lines, as listed in Table 2 by Meléndez et al. (2003). These features were used for AL3-3, giving a radial velocity of  $-67.65 \pm 3.65$  kms $^{-1}$ . In the combined spectrum of AL3-7, the same features result in a radial velocity of  $-68.93 \pm 4.83$  kms $^{-1}$ . The corresponding heliocentric velocities of  $-57.29$  km.s $^{-1}$  and  $-58.57$  km.s $^{-1}$  lead to a final mean heliocentric velocity of  $-57.93$  km.s $^{-1} \pm 4.28$  for AL 3. Figures 6.1 and 6.3 show the line identification and radial velocity derivation.

The star AL3-6 shows a very noisy spectrum, and we verified that it was observed under a high airmass of over 1.3, which also explains that it is plagued with telluric features. For AL3-6, we obtained a different heliocentric radial velocity, as shown in Fig. 6.2, of  $-29.57 \pm 5.85$  km.s $^{-1}$ , compatible with the value given by Baumgardt et al. (2019) of  $-29.38 \pm 0.60$  km.s $^{-1}$ .

The derived radial velocity is of crucial importance for the computation of the cluster's orbits. However, we obtained two different figures:  $v_r^{hel} = -57.93$  and  $-29.57$  km.s $^{-1}$ . In Fig. 6.2, we show the spectrum of AL3-6 compared with that of AL3-7. Therefore, we obtained two different radial velocities for AL 3.

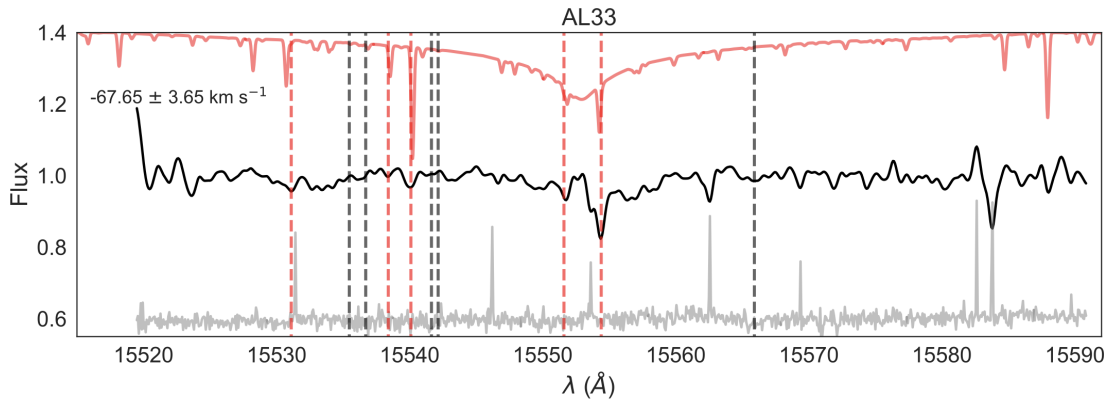


Figure 6.1: AL 3-3: radial velocity derivation. The solid black line is the observed spectrum, the solid grey line is the noise spectrum, the solid red line is the synthetic spectrum, the dashed red lines are those used to derive the radial velocity, and the dashed black lines are the OH sky lines.

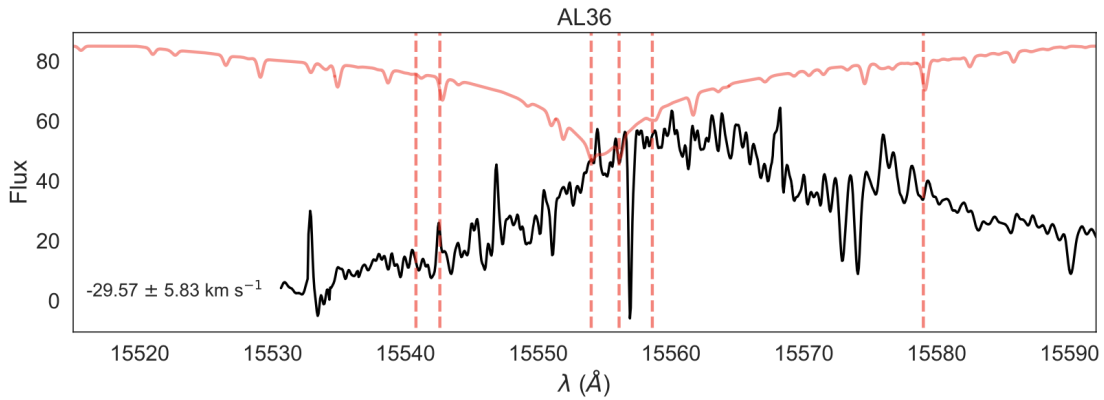


Figure 6.2: AL 3-6: radial velocity derivation. The solid black line is the observed spectrum, the solid grey line is the spectrum of star AL3-7, the dashed red lines are those used to derive the radial velocity, and the dashed black lines are the OH sky lines.

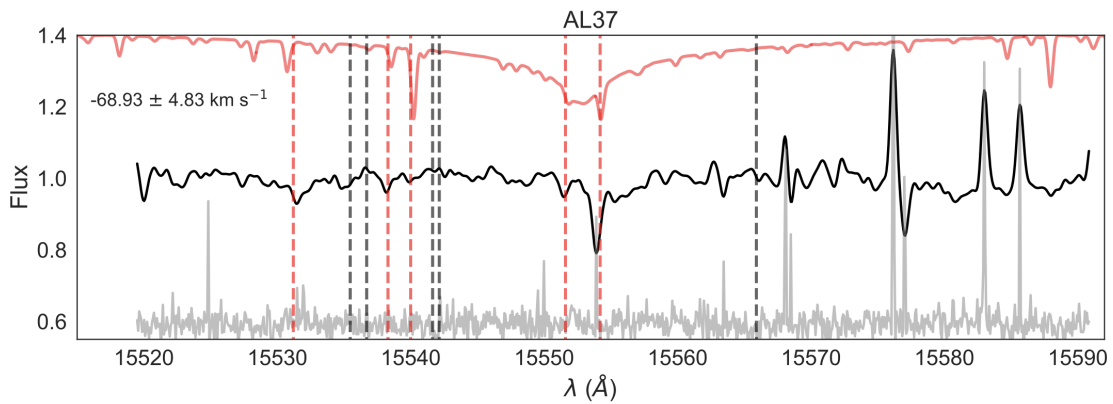


Figure 6.3: AL 3-7: radial velocity derivation. The solid black line is the observed spectrum, the solid grey line is the noise spectrum, the solid red line is the synthetic spectrum, the dashed red lines are those used to derive the radial velocity, and the dashed black lines are the OH sky lines.

## 6.6 Stellar parameters

### 6.6.1 NGC 6558 and HP 1

Individual stars of NGC 6558 were analysed with high-resolution spectroscopy by Barbuy et al. (2007, 2018b) and with moderate-resolution spectroscopy by Dias et al. (2015). The stars NGC6558-42 and NGC6558-64 are studied here.

Similar studies of HP 1 were carried out in Barbuy et al. (2006, 2016) and Dias et al. (2016). In the 2006 article, the bright red giants were labelled with numbers 1 to 6, for the purpose of identifying them in the cluster chart. In 2016, we adopted the identification numbers corresponding to the photometric reductions relative to observations obtained at the New Technology Telescope (NTT) at ESO, in 1994, as described in Ortolani et al. (1997). HP1-4 and HP1-5 are stars 2115 and 2939 in Barbuy et al. (2016). HP1-2 is the same as in Barbuy et al. (2006). In our study, we only analysed HP1-5.

### 6.6.2 AL 3

The magnitudes and colours as follows are indicated in Table 3: B, V from Ortolani et al. (2006), V, I from Rossi et al. (2015), JHK from the 2MASS catalogue (Skrutskie et al. 2006),<sup>2</sup> and JHK from the VVV survey (Saito et al. 2012).<sup>3</sup>

Effective temperatures were initially derived from  $B - V$ ,  $V - I$ ,  $V - K$ , and  $J - K$  using the colour-temperature calibrations of Alonso et al. (1999). V,I Cousins were transformed to V,I Johnson using  $(V - I)_C = 0.778(V - I)_J$  (Bessell 1979). The  $J$ ,  $H$ ,  $K_S$  magnitudes and colours were transformed from the 2MASS system to California Institute of Technology (CIT), and from this to Telescopio Carlos Sánchez (TCS), using the relations established by Carpenter (2001) and Alonso et al. (1998). The conversion of JHK VVV colours to the JHK 2MASS system was done using relations by Soto et al. (2013).

The temperatures resulting from photometry are of the order of 5000 K for the three stars. These temperatures, however, are not compatible with another indicator, which is the Hydrogen Brackett 16 line, centred at 15556.457 Å. A fit of this line for both AL 3 stars was carried out iteratively, after deriving their CNO abundances. The resulting temperatures, adopted in the following analysis, are 4250 K and 4500 K for AL3-3 and

<sup>2</sup> <http://ipac.caltech.edu/2mass/releases/allsky/>; <https://irsa.iapc.caltech.edu>

<sup>3</sup> [horus.roe.ac.uk/vsa](http://horus.roe.ac.uk/vsa)

AL3-7, respectively. The fits to the hydrogen line are shown in Figure 6.4. For AL3-6, the low quality of the spectrum does not allow the fit of the hydrogen line, in particular due to strong telluric absorptions in the region. It appears to be cooler and compatible with 4150 K. This incompatibility between photometric and hydrogen-wing-derived temperatures is a main source of uncertainty in the present study.

To derive the gravity, we used the PARSEC isochrones (Bressan et al. 2012).<sup>4</sup> To inspect the isochrones, we adopted a metallicity of  $[\text{Fe}/\text{H}] = -1.0$ , or overall metallicity  $Z = 0.00152$  (10 times below solar), and an age of 12 Gyr. Assuming a reddening of  $E(B - V) = 0.36$  (Ortolani et al. 2006, and present results), leading to  $E(V - I) = 0.478$  and  $A_V = 1.12$ , we transformed the apparent magnitudes to absolute magnitudes, as well as the colours ( $V - I_{\text{corr}} = V - I - E(V - I)$ ), and we identified the correspondence of the observed stars to the theoretical isochrone.

The metallicity resulting from the CMD fitting is  $[\text{Fe}/\text{H}] = -1.34$ , which was imposed as a prior. We inspected individual lines of Fe in the AL3-3 spectrum and the fits are more compatible with  $[\text{Fe}/\text{H}] = -1.0$ . There is also the evidence from other similar bulge globular clusters such as NGC 6558, NGC 6522, HP 1, and Terzan 9, which are found to have  $[\text{Fe}/\text{H}] \sim -1.0$  from high-resolution spectroscopy. Bica (2016) showed that there is a peak in metallicity at  $[\text{Fe}/\text{H}] \sim -1.0$  in the bulge, which we also adopted for AL 3. An isochrone fitting with this higher metallicity was tried, but appeared difficult to converge. This is a second source of uncertainty of the present study. Final adopted stellar parameters for program stars, and of the reference stars Arcturus (Meléndez et al. 2003) and  $\mu$  Leo (Lecureur et al. 2007), are reported in Table 6.6.2.

## 6.7 CNO abundances

The atmospheric models were interpolated in the grid of models by Gustafsson et al. (2008). The synthetic spectra were computed employing the PFANT code described in Barbuy et al. (2018b). In order to derive the C, N, O abundances, we fitted the CN, OH, and CO lines iteratively.

<sup>4</sup> <http://stev.oapd.inaf.it/cgi-bin/cmd>

Table 6.2 - AL 3: coordinates, magnitudes, and colours of sample stars.

Star	2MASS	$\alpha$ (J2000)	$\delta$ (J2000)	V	I	J	H		K	J	H		K
							2MASS	2MASS			VVV	VVV	
B11	18101902-3144506	18 10 19.01	-31 44 50.64	15.902	14.275	13.136	12.440	12.280	13.017	12.397	12.248		
B64	18101803-3145435	18 10 18.03	-31 45 43.55	15.703	14.180	13.064	12.456	12.277	13.055	12.529	12.384		
B73	18102150-3145268	18 10 21.50	-31 45 26.77	15.709	14.187	13.128	12.449	12.316	13.047	13.047	12.313		
F42	—	18 10 17.65	-31 45 38.93	16.054	14.442	—	—	—	—	—	—		
F97	18101520-3146014	18 10 15.21	-31 46 00.67	16.037	14.467	13.183	12.481	12.338	—	12.503	12.378		
HP1-2	17310585-2958354	17 31 05.60	-29 58 34.00	16.982	14.332	12.210	11.268	10.969	14.588	13.675	13.368		
HP1-4	17310538-2959199	17 31 05.30	-29 59 20.00	17.070	14.281	—	11.67	—	11.258	11.392	10.688		
HP1-5	17310729-2959021	17 31 07.20	-29 59 02.00	17.131	14.395	11.901	10.869	10.595	12.021	11.285	10.898		
AL3-3	18140691-2839087	18 14 06.90	-28 38 09.0	14.524	13.204	12.214	11.631	11.469	12.211	11.714	11.544		
AL3-6	18140592-2838049	18 14 05.80	-28 38 06.0	15.563	14.203	12.763	12.272	12.256	—	—	—		
AL3-7	18140529-2838168	18 14 05.30	-28 38 19.0	14.313	12.963	11.878	11.296	11.170	11.920	11.472	11.195		

Table 6.3 - Adopted stellar parameters for individual stars in NGC 6558, AL 3, and HP 1, and resulting C, N, O abundances. For NGC 6558, the stellar parameters are from Barbuy et al. (2007), and for HP 1 they are from Barbuy et al. (2016). Stellar parameters for the Sun, Arcturus, and  $\mu$  Leo are also included.

Name	$T_{\text{eff}}$ (K)	$\log g$	[Fe/H]	$v_t$ km/s	[C/Fe]	[N/Fe]	[O/Fe]
Program stars							
F42	3800	0.5	-1.05	1.65	-0.5	+0.8	+0.5
HP1-5	4525	2.0	-1.07	1.55	-0.1	0.8	0.5
AL3-3	4250	1.7	-1.00	1.2	-0.1	0.0	0.0
AL3-6	4150	1.3	-1.00	1.2	+0.8	+1.0	+0.8
AL3-7	4500	1.5	-1.00	1.2	-0.2	-0.1	0.0
Reference stars							
Sun	5770	4.44	+0.00	1.0	+0.00	+0.00	+0.00
Arcturus	4275	1.55	-0.54	1.65	+0.11	+0.40	+0.43
$\mu$ Leo	4540	2.3	+0.30	1.3	-0.1	+0.65	+0.00

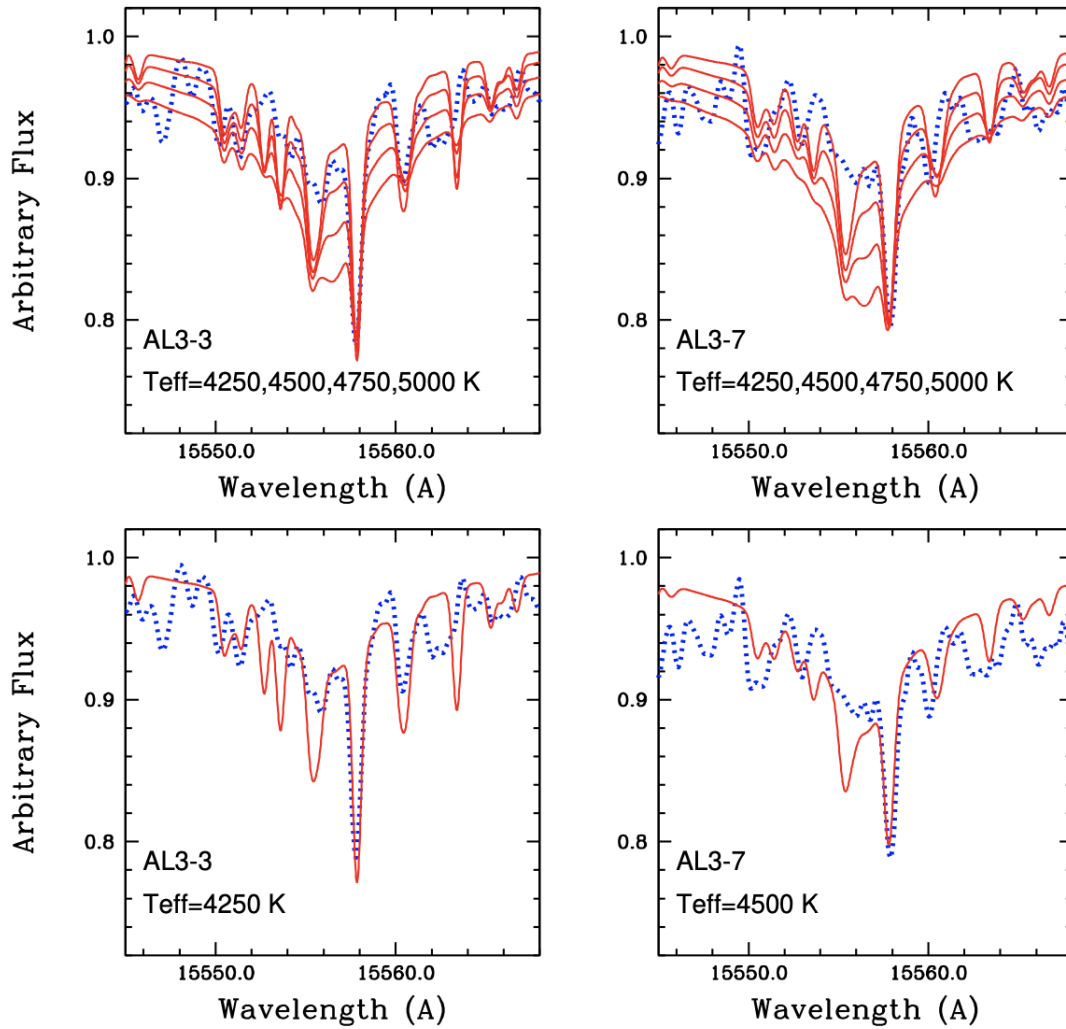


Figure 6.4: AL 3-3 and AL 3-7: Hydrogen Brackett 16 line computed for  $T_{eff} = 4250, 4500, 4750, 5000$  K (upper panels) and adopted values of 4250 K and 4750 K, respectively (lower panels). The dashed line is the observed spectrum



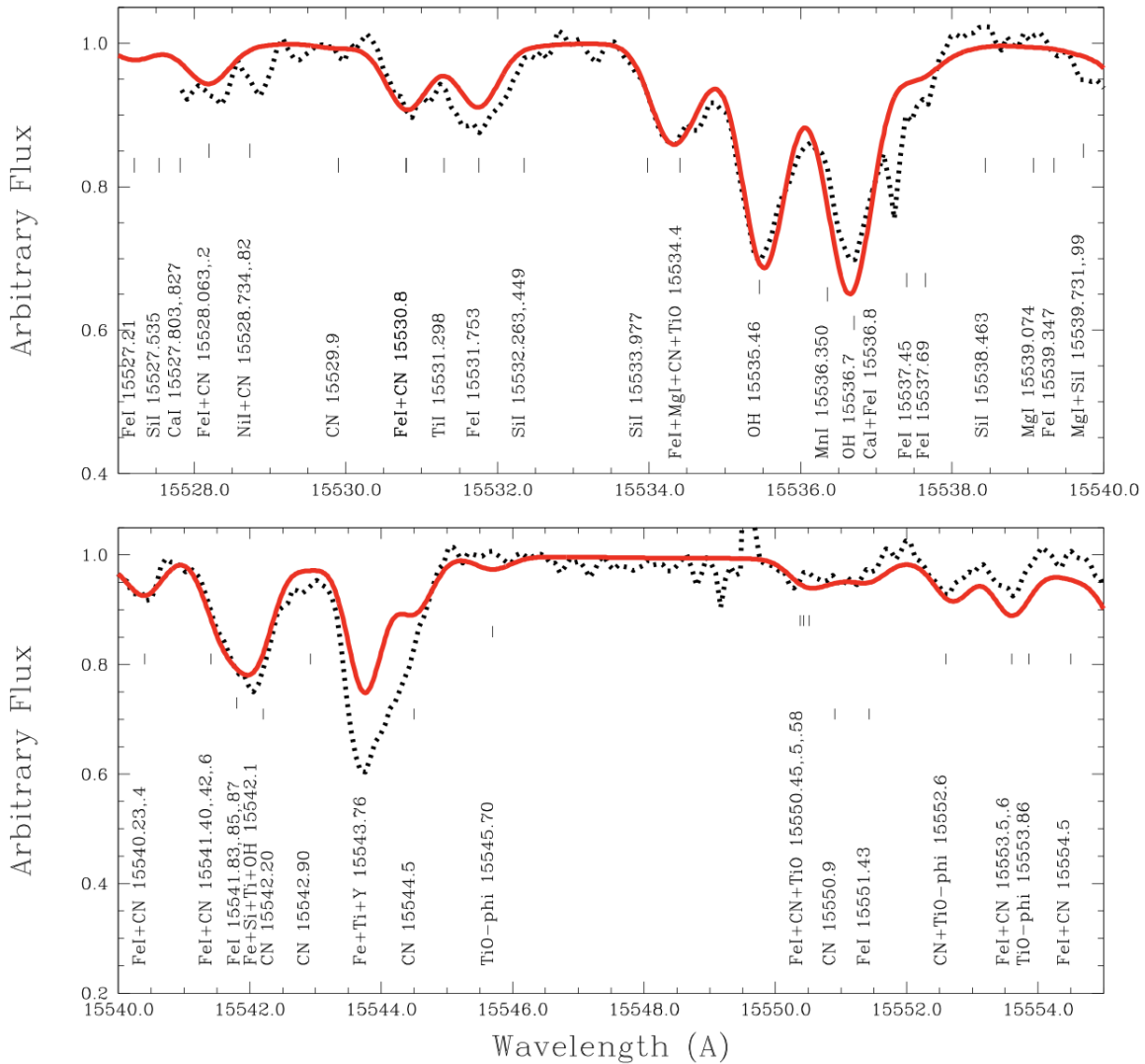


Figure 6.6: NGC 6558-42: Line identification in the range 15527-15555 Å. Dashed line: Observed spectrum. Solid red line: Synthetic spectrum. Synthetic spectrum computed with  $[C/Fe]=-0.5$ ,  $[N/Fe]=0.8$ ,  $[O/Fe]=+0.5$ .

### 6.7.1 The cool red giant N6558-42

The cool red giant, NGC6558-42, shows strong lines and is a typical red giant. For this reason, we show the fits to the spectrum of this star in detail in Figures 6.6 and 6.7.

The star NGC6558-64 instead, which would have an effective temperature of 4850 K according to the analysis from optical spectra by Barbuy et al. (2018b), could be as hot as 5500 K. This is seen from the profile of its Hydrogen Brackett 16 line; however, this should be taken with caution due to defects in the observed spectrum. For this reason, we could not converge on CNO abundances for this star.

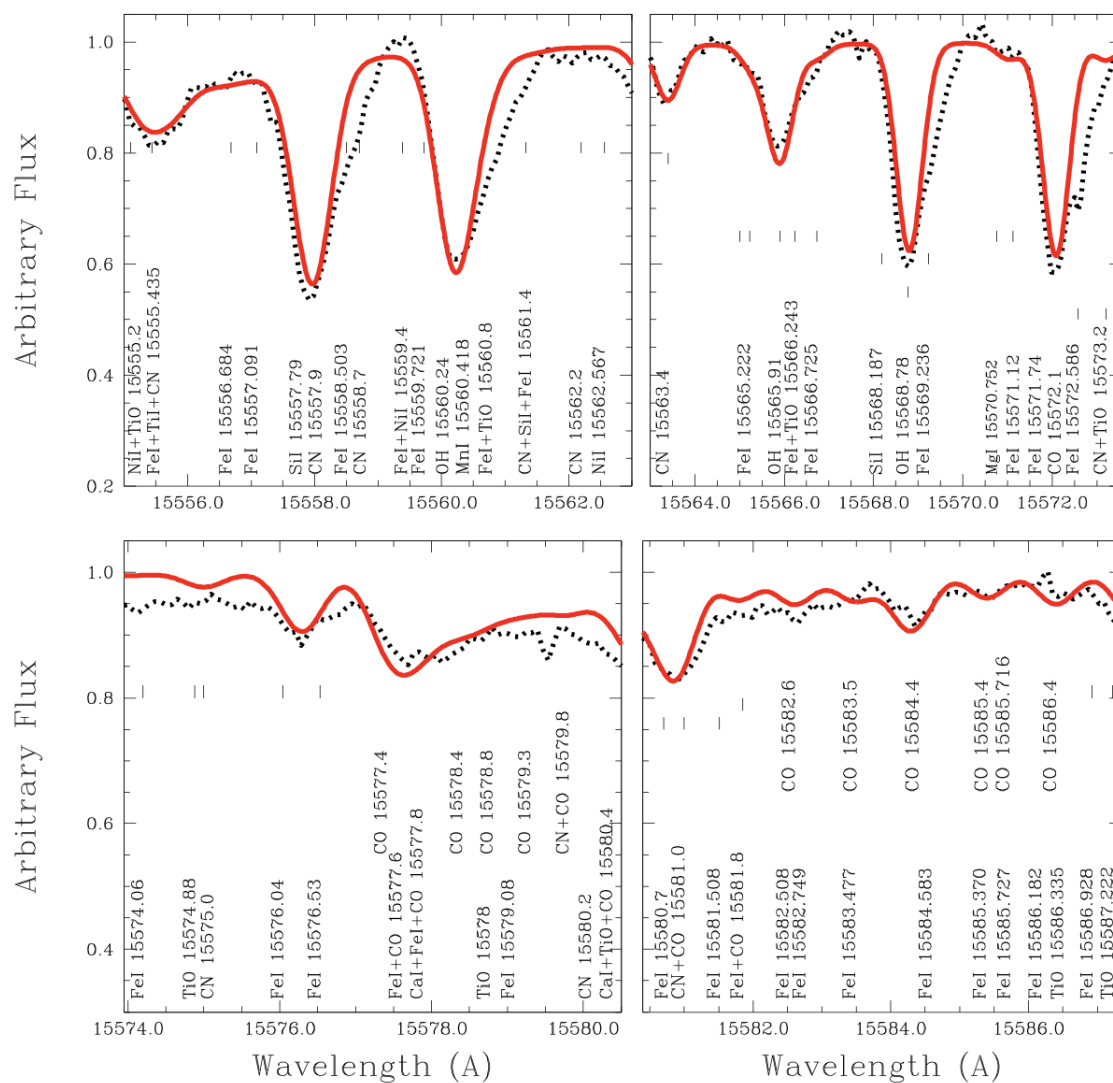


Figure 6.7: NGC 6558-42: Same as Fig. 6.6, in the range 15555-15587 Å.

### 6.7.2 AL-3 and HP 1

There is a clear contrast between the spectra of HP1-5, AL3-3, and AL3-7, that have shallow lines, and AL3-6 and NGC6558-42, that show strong lines. Whereas NGC6558-42 is a typical red giant, the stars AL3-3, AL3-7, and HP1-5 show weak molecular lines. In Fig. 6.8, we show the observed spectrum in the selected wavelength regions containing CN, OH lines, and the CO bandhead at 15578 Å for stars AL3-3, AL3-7, and HP1-5. The molecular lines are very shallow, due to a combination of warm temperatures and low metallicities. Clearly, the CNO abundances derived for these stars are less reliable than for the cool star NGC6558-F42. Their CNO abundances are compatible with being close to solar, but given the shallowness of the lines, it is clear that the molecular lines are not reliable for abundance measurements.

AL3-6 instead shows very strong CNO lines. Figure 6.5 indicates that  $[C/Fe]=+0.7$ ,  $0.8$ ,  $[N/Fe]=+1.0$ ,  $[O/Fe]=+0.8$  for this star. We show two different renormalisations to illustrate the difficulty in analysing this spectrum. Additionally, the computations with two different carbon abundances illustrate the extreme sensitivity of the lines. Clearly, however, there is an urgent need to observe this star in the optical and/or in a more extended wavelength region in the H-band to obtain firm conclusions on the CNO abundances of AL 3.

### 6.7.3 Uncertainties

The main uncertainty in the derivation of CNO abundances in AL 3 stems from the effective temperatures. Adopting a colour excess  $E(B-V)=0.36$  the photometric magnitudes results in temperatures of  $\sim 5000$  K. In order to be compatible with the wings of hydrogen lines, we would have to adopt  $E(B-V)=0.2$ , but the present fit of the CMD confirms the high reddening value.

Hydrogen wings that we adopted are a very good temperature indicator, and the temperatures can be roughly derived for the two stars showing the line, whereas for the cooler star AL3-6, the H line is not strong, indicating that it is cooler than the other two stars. For this star, we adopted  $T_{\text{eff}} = 4150$  K, compatible with its almost absent hydrogen-profile and a temperature compatible with its location in the RGB. With this temperature, we obtained high CNO values and could not converge with lower values. We note that the CN,

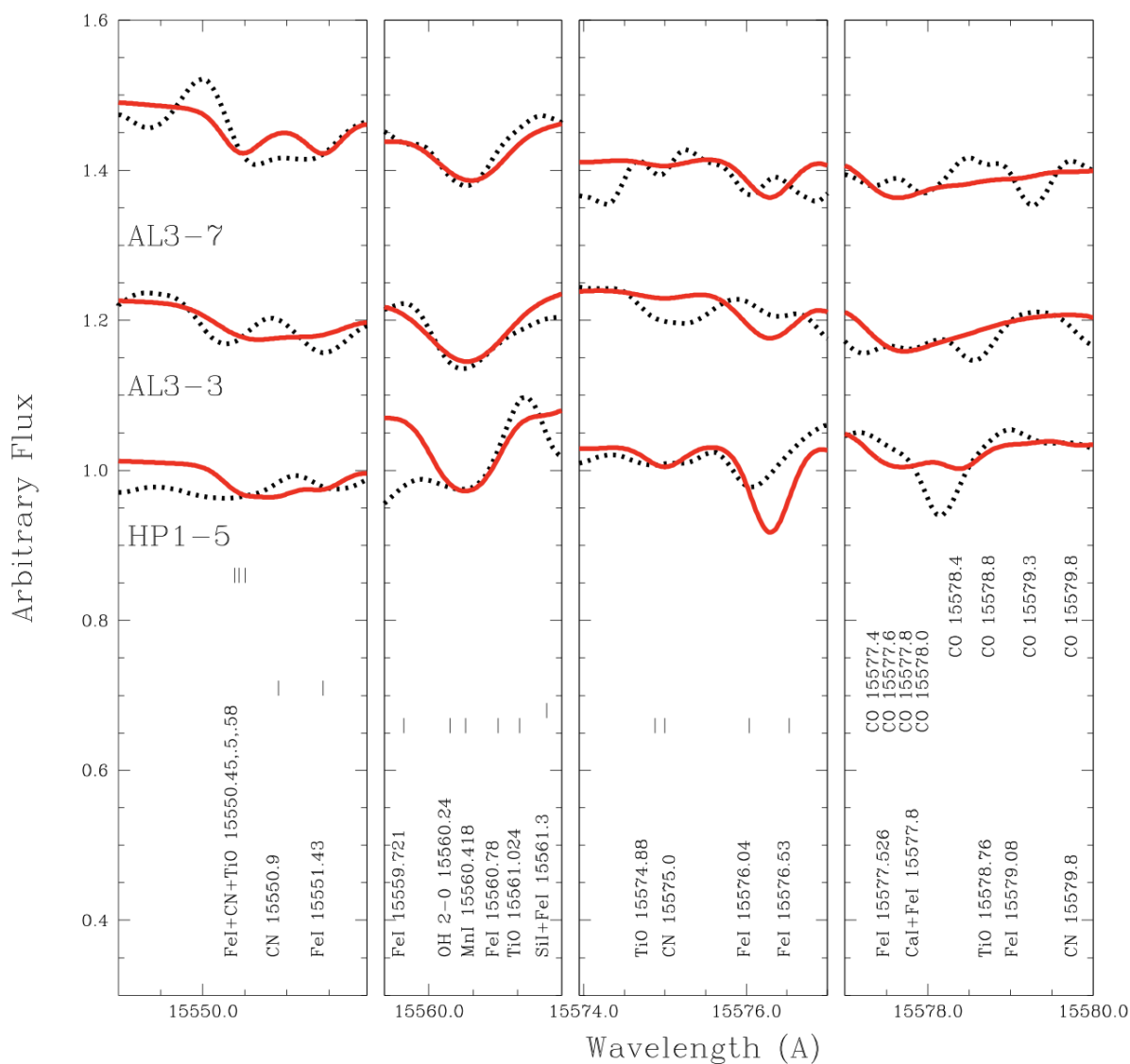


Figure 6.8: HP 1-5, AL 3-3, and AL 3-7: Spectrum in selected wavelength regions containing CN, OH lines and the CO bandhead. Synthetic spectra are computed for the CNO abundances given in Table 6.6.2.

CO, and OH dissociation equilibrium interplay gives a strong constraint on the result, but at the same time, these are very sensitive to abundance variations. We adopted effective temperature errors of  $\pm 250$  K for AL3-6, and  $\pm 150$  K for AL3-3 and AL3-7, errors of  $\pm 0.8$  for the gravity, and  $\pm 0.3$  for metallicity.

## 6.8 Summary of AL 3

We analysed spectra of individual stars of the globular clusters AL 3, NGC 6558, and HP 1, obtained with the PHOENIX spectrograph at the Gemini South telescope. With a high spectral resolution of  $R \sim 75,000$ , in the H band centred at  $15555 \text{ \AA}$ , the wavelength coverage is short ( $15520 - 15590 \text{ \AA}$ ).

In AL 3, this limited wavelength range means that it is difficult to use atomic lines to deduce the stellar parameters effective temperature, gravity, and metallicity. For this reason, the effective temperature from the Hydrogen Brackett 16 line, gravity from photometric data, and isochrones. The metallicity  $[\text{Fe}/\text{H}] \sim -1.3 \pm 0.3$  was deduced from the observed CMD given in Ortolani et al. (2006).

We note that we adopted  $[\text{Fe}/\text{H}] = -1.0$  for the analysed stars, due to spectroscopic evidence. For NGC 6558 and HP 1, the stellar parameters were adopted from previous analyses from optical spectra (Barbuy et al. 2007, 2018), and Barbuy et al. (2006, 2016) respectively. Adopting these stellar parameters, we computed the synthetic spectra in order to derive the abundances of C, N, and O. Since they vary interdependently, the fit was done iteratively, where particular attention was given to the CO bandhead. The stars analysed in NGC 6558 and HP 1 show typical CNO abundances of red giants, and confirm previous oxygen abundance derivation.

AL 3 is a more complex case: two stars analysed in AL 3 show solar CNO abundance ratios, but based on very shallow lines, and the location of these two stars in the CMD point to them being AGB stars. The star AL3-6 shows instead very strong CNO abundances of the order of  $[\text{C}/\text{Fe}] = +0.8$ ,  $[\text{N}/\text{Fe}] = +1.0$ ,  $[\text{O}/\text{Fe}] = +0.8$ . A strong CNO abundance indicated by this cooler star shows that AL 3 appears to be an extremely interesting old cluster. In conclusion, further investigation of this cluster are clearly needed. We also derived the cluster's radial velocity, which in turn allowed the orbits computation for the AL 3 in Pérez-Villegas et al. (2018, 2020). For the two AGB stars, we found a higher velocity,

---

whereas for the third cooler star, the radial velocity is compatible with the value from Baumgardt et al. (2019).

Therefore, we conclude that the cluster AL 3 appears to be an extremely interesting cluster that should be further investigated through more wavelength-extended spectra, and including larger samples of member stars.



## Near-UV study of the halo star CS 31082-001

### 7.1 Introduction of the metal-poor halo star CS 31082-001

Field stars in the Galactic halo are thought to have been formed in an early inner halo or accreted from disrupted dwarf galaxies. Detailed abundance studies (so-called ‘Galactic archaeology’) are a powerful technique to help us understand the origin of these halo populations. To date, the iron-peak elements have been less studied than alpha and neutron-capture elements, but they can be important indicators of both the processes and sources of nucleosynthesis (e.g. Minelli et al. 2021).

In their seminal work, Cayrel et al. (2004) described the ‘First Stars’ Large Programme at the European Southern Observatory (ESO), that included 37 nights of observations of metal-poor stars with the Ultraviolet and Visual Echelle Spectrograph (UVES, Dekker et al. 2000) on the Very Large Telescope (VLT). An important target in this programme was the metal-poor halo star CS 31082-001, with  $[\text{Fe}/\text{H}] = -2.9$  and  $V = 11.6$  mag. Its abundances were presented in a series of papers, including the first detection of uranium in a stellar spectrum (enabling an age estimate from the ratio of the U abundance to that of thorium, Cayrel et al. 2001), abundance determinations of lighter (Li to Zn) and heavy (Sr to U) elements (Hill et al. 2002), and further study of C to Zn (Cayrel et al. 2004). Ultraviolet (UV) observations with the Space Telescope Imaging Spectrograph (STIS) on the *Hubble Space Telescope (HST)* opened-up further abundance studies of the star, confirming it to be rich in both r-process elements and actinides (Barbuy et al. 2011; Siqueira-Mello et al. 2013).

A subset of metal-poor stars are found to be actinide rich. Holmbeck et al. (2020) recently redefined the r-II sub-class of r-process enhanced stars as those characterized by

$[\text{Eu}/\text{Fe}] \geq 0.7$ , instead of the previous definition of  $[\text{Eu}/\text{Fe}] \geq +1.0$  (Beers & Christlieb 2005), giving a total of 72 stars now classified as r-II. It has only been possible to measure the actinide uranium abundance in six stars (Holmbeck et al. 2018), namely, CS 31082-001 (Hill et al. 2002), BD +17°3248 (Cowan et al. 2002), HE1523-0901 (Frebel et al. 2007), RAVE J203843.2-002333 (Placco et al. 2017), CS 29497-004 (Hill et al. 2017) and 2MASS J09544277+5246414 (Holmbeck et al. 2018). Upper limits were reported for others, including CS22892-052 (Snedden et al. 2003) and J1538-1804 (Sakari et al. 2018). CS 31082-001 and J09544277+5246414 are clear actinide-boost stars, showing a large enhancement of the actinides relative to any other class of old stars. For this reason CS 31082-001 is a reference star in this respect (e.g. Sneden et al. 2008).

Given the limited efficiency of current facilities, the ground-UV region (300-400 nm) is less explored in the context of stellar abundances than longer, visible wavelengths. Partly motivated by the development of a new, UV-optimised spectrograph for the VLT, the Cassegrain U-Band Efficient Spectrograph (CUBES), here we revisit the UVES data of CS 31082-001 to investigate its abundances of three elements observed in the near-UV that were not included in previous analyses, namely beryllium, vanadium and copper.

Be, like Li, is a fragile element. In stellar interiors it is destroyed as soon as the temperature is higher than  $3.5 \times 10^6 \text{K}$ . But, unlike Li, Be is not significantly produced by primordial nucleosynthesis. In very metal-poor stars it is formed through cosmic-ray spallation, with the latter probably emitted by the first supernovae (Reeves et al. 1970). V and Cu are iron-peak elements, that are gaining importance in their use as indicators of the early nucleosynthesis processes that enriched old stars. We also compare abundances estimated from the near-UV for other iron-peak elements with those published from diagnostic lines at longer optical wavelengths.

We use the mean of three UVES spectra centered at 340 nm, cited in section 2, these spectra were not used in Hill et al. (2002), but later in Spite et al. (2005), Barbuy et al. (2011) and Siqueira-Mello et al. (2013). In the common range of wavelengths ( $300 \text{ nm} < \lambda < 307 \text{ nm}$ ), the co-added spectrum has a higher resolution ( $R = 75\,000$ ) than the HST spectrum, with a signal-to-noise ratio of about 20 at 300 nm and 100 at 340 nm.

Table 7.1 - Stellar parameters adopted for CS 31082-001 (Hill et al. 2002), HD 122563 (Cayrel et al. 2004), and the reference star Arcturus (Meléndez et al. 2003).

Star Name	$T_{\text{eff}}$ (K)	$\log g$	[Fe/H]	$v_t$ (km.s $^{-1}$ )
CS 31082-001	4825 $\pm$ 50	1.5 $\pm$ 0.3	-2.9 $\pm$ 0.1	1.8 $\pm$ 0.2
HD 122563	4600 $\pm$ 50	1.1 $\pm$ 0.4	-2.8 $\pm$ 0.1	2.0 $\pm$ 0.2
Arcturus	4275 $\pm$ 50	1.55 $\pm$ 0.1	-0.54 $\pm$ 0.06	1.65 $\pm$ 0.05

## 7.2 The halo star CS 31082-001

For our abundance analysis we adopted the stellar parameters from Hill et al. (2002), as summarised in Table 7.1. Model atmospheres were interpolated in the MARCS grids (Gustafsson et al. 2008). For the spectral synthesis calculations we employed the `Turbospectrum` code (Alvarez & Plez, 1998; Plez, 2012), in which the atomic line lists are essentially those from VALD (Ryabchikova et al. 2015) and also including molecular lines of CH, OH, CN and NH. It is important to note that this code includes scattering in the continuum, that significantly depresses the continuum in the UV region (e.g. Fig. 1 from Barbuy et al. 2011). This effect needs to be taken into account because, when measuring weak lines such as the Be II doublet, the lowered continuum decreases the line depth and the abundance can be underestimated.

Here we focus on the lines of Be and iron-peak elements in the 300-400 nm region. Prior to our analysis we compiled the existing results from the First Stars series for light(er) elements (Table 7.2) and neutron-capture elements (Table 7.3)<sup>1</sup>

The nitrogen abundance was tentatively deduced from the CN band, although noting that this is very weak in CS 31082-001 and that only an upper limit of  $A(\text{N}) < 5.22$  was possible (Hill et al. 2002; Cayrel et al. 2004). Spite et al. (2005) later estimated  $A(\text{NH}) = 4.90$  using the molecular data of the NH band from Kurucz linelists. In the same paper it was shown that, in general, there is a systematic difference of  $\sim 0.4$  dex between the abundance deduced from the CN and the NH bands. Therefore, Spite et al. (2005) adopted  $A(\text{N}) = 4.50$  after correction. We carried out a new measurement of the NH band based on a recent NH linelist (Fernando et al. 2018) and concluded that  $A(\text{N}) = 4.57$ .

In Table 7.3 we also include abundance estimates from Barbuy et al. (2011) and Siqueira-Mello et al. (2013) obtained from the *HST* data alone (i.e. using lines at  $< 300$  nm,

<sup>1</sup> Small differences of 0.01 dex between the  $[X/\text{Fe}]$  values from Hill et al. (2002), and Cayrel et al. (2004) or Spite et al. (2005) arise from adopting a metallicity of  $[\text{Fe I}/\text{H}] = -2.90$  or a mean of  $[(\text{Fe I} + \text{Fe II})/\text{H}] = -2.91$ .

Table 7.2 - Published light-element abundances for CS 31082-001. Refs: 1) Hill et al. (2002); 2) Cayrel et al. (2004); 3) Spite et al. (2005); 4) NLTE calculations from Spite et al. (2011), 5) present work.

Species	Z	A(X)	[X/Fe]
Li I	3	0.85 <sup>1,2,3</sup>	...
C	6	5.82 <sup>1,2,3</sup>	+0.2 <sup>1</sup> , +0.21 <sup>2,3</sup>
N	7	<5.22 <sup>1,2,3</sup> , 4.90 <sup>3</sup> , 4.57 <sup>5</sup>	+0.21 <sup>1,2,3</sup> , -0.11 <sup>3</sup> , -0.49 <sup>5</sup>
O I	8	6.52 <sup>1</sup> , 6.46 <sup>2</sup>	+0.66 <sup>1</sup> , +0.6 <sup>2,3</sup>
Na I	11	3.70 <sup>1,2</sup>	+0.27 <sup>1</sup> , +0.28 <sup>2</sup>
Mg I	12	5.04 <sup>1,2</sup>	+0.36 <sup>1</sup> , +0.37 <sup>2</sup>
Al I	13	2.83 <sup>1,2</sup>	-0.74 <sup>1</sup> , -0.73 <sup>2</sup>
Si I	14	4.89 <sup>1,2</sup>	+0.24 <sup>1</sup> , +0.25 <sup>2</sup>
S	16	4.54 <sup>4</sup>	+0.36 <sup>4</sup>
K I	19	2.87 <sup>1,2</sup>	+0.65 <sup>1</sup> , +0.66 <sup>2</sup>
Ca I	20	3.87 <sup>1,2</sup>	+0.41 <sup>1</sup> , +0.42 <sup>2</sup>
Sc II	21	0.28 <sup>1,2</sup>	+0.01 <sup>1</sup> , +0.02 <sup>2</sup>
Ti I	22	2.37 <sup>1,2</sup>	+0.25 <sup>1</sup> , +0.26 <sup>2</sup>
Ti II	22	2.43 <sup>1,2</sup>	+0.31 <sup>1</sup> , +0.32 <sup>2</sup>
Cr I	24	2.43 <sup>1,2</sup>	-0.34 <sup>1</sup> , -0.33 <sup>2</sup>
Mn I	25	2.14 <sup>1</sup> , 1.98 <sup>2</sup>	-0.35 <sup>1</sup> , -0.50 <sup>2</sup>
Fe I	26	4.60 <sup>1,2,3,4</sup>	0.00 <sup>1,2,3,4</sup>
Fe II	26	4.58 <sup>1,2,3,4</sup>	0.00 <sup>1,2,3,4</sup>
Co I	27	2.28 <sup>1,2</sup>	+0.26 <sup>1</sup> , +0.27 <sup>2</sup>
Ni I	28	3.37 <sup>1,2</sup>	+0.02 <sup>1</sup> , +0.03 <sup>2</sup>
Zn I	30	1.88 <sup>1,2</sup>	+0.18 <sup>1</sup> , +0.19 <sup>2</sup>

hence some of the values quoted here are slightly different from the final results from Siqueira-Mello et al.).

### 7.3 Beryllium abundance in CS 31082-001

The derivation of Be abundances for metal-poor stars is challenging because the Be II doublet (see Table 7.4 for details) is weak and blended with other nearby absorption lines. Lines of Mn, Cr, Ni, Ge, Ta, Gd, Tm, Mo are all present in the region but they do not contribute significantly to the blends. In contrast, weak lines of Fe, V, Ti, Th, Os and molecular CNO lines (mainly from OH) do contribute as blends to the Be lines. In particular, the longer-wavelength Be II line is blended with Th II 3131.07 Å and Os I 3131.12 Å. Fig. 7.1 shows the spectral synthesis calculation without including Be and with  $A(\text{Be}) = -2.5, -2.4, -2.1,$  and  $-2.0$ , suggesting abundances of  $A(\text{Be}) = -2.5$  and  $-2.4$  for CS 31082-001 from the Be II 3130.42 and 3131.07 Å lines, respectively.

The Be abundance measured in CS 31082-001 does not, however, indicate its primordial Be abundance. Be is a fragile element destroyed as soon as the temperature reaches  $3.5 \times 10^6$  K. Nonetheless, Be is less fragile than Li, which is destroyed at  $2.5 \times 10^6$  K. All

Table 7.3 - Published heavy-element abundances for CS 31082-001. Refs: 1) Hill et al. (2002); 2) Plez et al. (2004); 3) Barbuy et al. (2011); 4) Siqueira-Mello et al. (2013).

Ele.	Z	A(X) <sub>VLT</sub>	A(X) <sub>HST</sub>	[X/Fe]
Ge	32	+0.10 <sup>4</sup>	...	-0.55 <sup>4</sup>
Sr	38	+0.72 <sup>1</sup>	...	+0.65 <sup>1</sup>
Y	39	-0.23 <sup>1</sup> , -0.15 <sup>4</sup>	...	+0.43 <sup>1</sup> , +0.53 <sup>4</sup>
Zr	40	+0.43 <sup>1</sup>	+0.55 <sup>4</sup>	<+0.73 <sup>1</sup> , +0.85 <sup>4</sup>
Nb	41	-0.55 <sup>1</sup>	-0.52 <sup>4</sup>	+0.93 <sup>1</sup> , +0.96 <sup>4</sup>
Mo	42	...	-0.11 <sup>4</sup>	+0.90 <sup>4</sup>
Ru	44	+0.36 <sup>1</sup>	+0.65 <sup>4</sup>	+1.42 <sup>1</sup> , +1.71 <sup>4</sup>
Rh	45	-0.42 <sup>1,4</sup>	...	+1.36 <sup>1,4</sup>
Pd	46	-0.05 <sup>1</sup> , -0.09 <sup>4</sup>	...	+1.16 <sup>1</sup> , +1.12 <sup>4</sup>
Ag	47	-0.81 <sup>1</sup> , -0.84 <sup>4</sup>	...	+1.15 <sup>1</sup> , +1.12 <sup>4</sup>
Ba	56	+0.40 <sup>1</sup>	...	+1.17 <sup>1</sup>
La	57	-0.60 <sup>1</sup>	...	+1.13 <sup>1</sup>
Ce	58	-0.31 <sup>1,4</sup>	...	+1.01 <sup>1,4</sup>
Pr	59	-0.86 <sup>1</sup>	...	+1.33 <sup>1</sup>
Nd	60	-0.13 <sup>1</sup> , -0.21 <sup>4</sup>	...	+1.27 <sup>1</sup> , +1.19 <sup>4</sup>
Sm	62	-0.51 <sup>1</sup> , -0.42 <sup>4</sup>	...	+0.00 <sup>1</sup> , +0.11 <sup>4</sup>
Eu	63	-0.76 <sup>1</sup>	-0.75 <sup>4</sup>	+1.63 <sup>1</sup> , +1.64 <sup>4</sup>
Gd	64	-0.27 <sup>1</sup>	-0.22 <sup>4</sup>	+1.51 <sup>1</sup> , +1.46 <sup>4</sup>
Tb	65	-1.26 <sup>1</sup>	-0.50 <sup>4</sup>	+1.74 <sup>1</sup> , +0.98 <sup>4</sup>
Dy	66	-0.21 <sup>1</sup> , -0.12 <sup>4</sup>	...	+1.55 <sup>1</sup> , +1.46 <sup>4</sup>
Er	68	-0.27 <sup>1</sup>	-0.20 <sup>4</sup>	+1.70 <sup>1</sup> , +1.63 <sup>4</sup>
Tm	69	-1.24 <sup>1</sup> , -1.18 <sup>4</sup>	...	+1.66 <sup>1</sup> , +1.60 <sup>4</sup>
Hf	72	-0.59 <sup>1</sup> , -0.73 <sup>4</sup>	...	+1.43 <sup>1</sup> , +1.29 <sup>4</sup>
Os	76	+0.43 <sup>1</sup>	-0.07 <sup>4</sup>	+1.30 <sup>1</sup> , +1.72 <sup>4</sup>
Ir	77	+0.20 <sup>1</sup>	+0.18 <sup>4</sup>	+1.75 <sup>1</sup> , +1.72 <sup>4</sup>
Pt	78	...	+0.30 <sup>3</sup>	+1.46 <sup>3</sup>
Au	79	...	-1.00 <sup>3</sup>	+0.89 <sup>3</sup>
Pb	82	-0.55 <sup>2</sup>	-0.65 <sup>3</sup>	+0.40 <sup>2</sup> , +0.30 <sup>3</sup>
Bi	83	...	-0.40 <sup>3</sup>	+1.83 <sup>3</sup>
Th	90	-0.98 <sup>1</sup>	...	+1.83 <sup>1</sup>
U	92	-1.92 <sup>1</sup>	...	+1.49 <sup>1</sup>

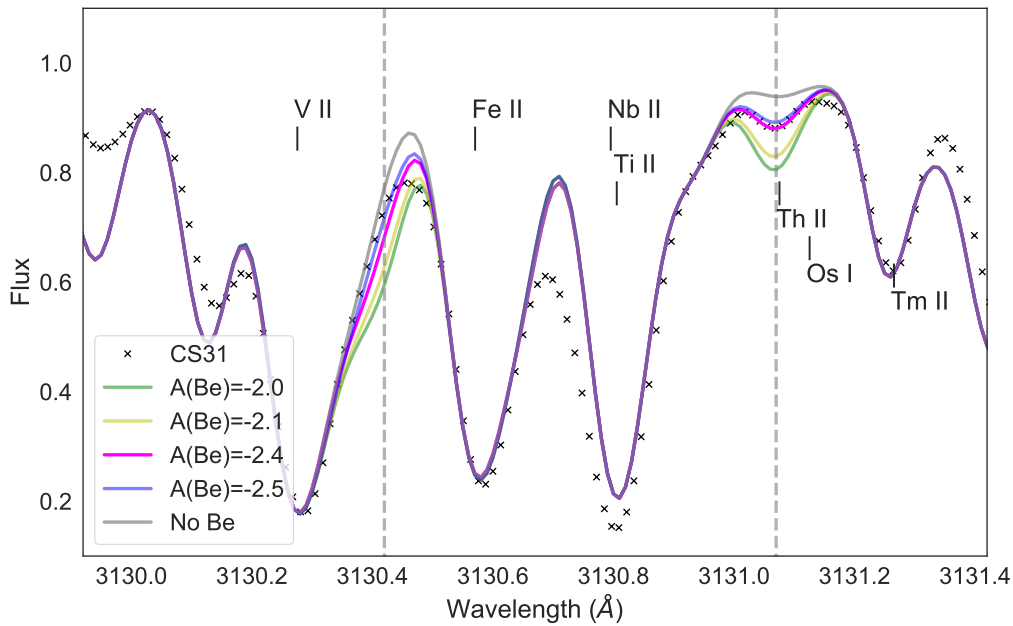


Figure 7.1: Fits to the Be II 3130.42 and 3131.07 Å doublet. Blue, magenta, yellow and green model spectra correspond to  $A(\text{Be}) = -2.5$ ,  $-2.4$ ,  $-2.1$  and  $-2.0$ , respectively. The grey line is the model spectrum without Be.

the stars in the Spite’s Li plateau (Spite & Spite 1982) have effective temperatures higher than 5900 K. At lower temperatures the convective zone is deeper and, as a consequence, Li is brought to deep layers where it is gradually destroyed, and the same process affects also Be. At the metallicity of CS 31082-001, following e.g. Boesgaard et al. (2011), its original abundance should be about  $A(\text{Be}) = -2.2$ . Destruction of Be in CS 31082-001 is thus confirmed, as might be expected by its low Li abundance ( $A(\text{Li}) = 0.85$ ), which is much below the Spite plateau at  $A(\text{Li}) \sim +2.2$ .

During their evolution, metal-poor giants undergo a first mixing (1st dredge-up) when they leave the subgiant branch. Later, at the level of the bump, they undergo extra mixing: C is transformed into N and Li practically disappears. It has been shown that CS 31082-001 has not yet undergone this extra mixing (Spite et al. 2005), therefore some Li and Be appear to be still present. In contrast, HD 122563 was another giant star observed by the First Stars programme but located after the bump (see stellar parameters in Table 7.1). In this star Li is not measurable ( $A(\text{Li}) < 0.6$ , Spite et al. 2005), and we verified that the Be line appears also to be absent.

The estimated Be abundance in CS 31082-001 is the first measurement of a Be abundance in a metal-poor giant. Results in the literature are for stars with effective temperatu-

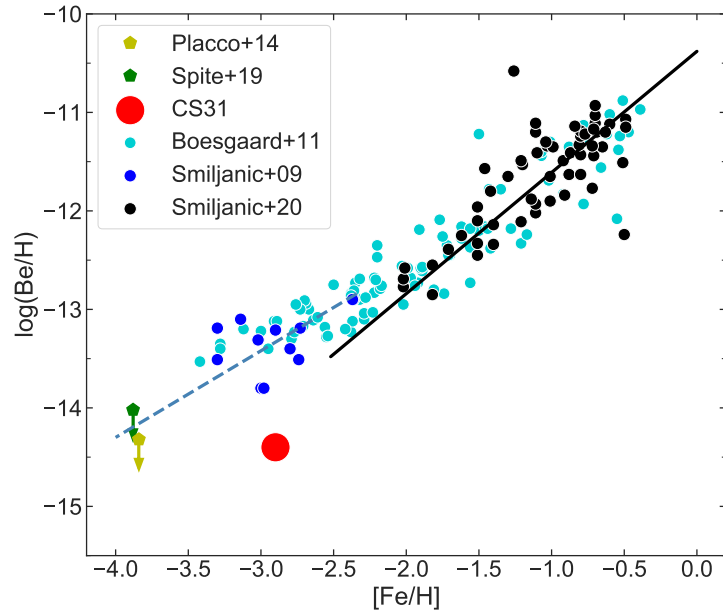


Figure 7.2:  $\log(\text{Be}/\text{H})$  vs.  $[\text{Fe}/\text{H}]$  for CS 31082-001 (red circle) compared with literature data as follows: solid blue circles, Smiljanic et al. (2021); solid black circles, Smiljanic et al. (2009); solid green pentagons, Spite et al. (2019); solid yellow pentagons, Placco et al. (2014); solid cyan circles, Boesgaard et al. (2011). The solid line is a fit to the data by Smiljanic et al. (2009). The dashed line is the locus of dwarf metal-poor stars (Spite et al. 2019).

res greater than  $\sim 5500$  K, and with gravities around the turn-off. In Fig. 7.2 we show literature values for dwarf stars from Boesgaard et al. (2011), Placco et al. (2014), Smiljanic et al. (2009, 2021) and Spite et al. (2019), where it can be seen that the Be abundance increases with  $[\text{Fe}/\text{H}]$ . In CS 31082-001 with  $[\text{Fe}/\text{H}] = -2.9$  we would expect  $\log(\text{Be}/\text{H}) \approx -13.8$  for a dwarf star, to be compared with our estimate of  $\log(\text{Be}/\text{H}) = -14.5$  for CS 31082-001. In fact, Be (like Li) has been partially destroyed during the first dredge up. This destruction depends mainly on the extension of the convective zone. The combination of the Be and Li depletion in metal-poor giants observed after the first dredge-up, could bring important constraints on the maximum depth of the convective layer.

## 7.4 Iron-peak elements in CS-31082-001

Table 7.4 gives the list of near-UV lines of iron-peak elements considered here, together with oscillator strengths from Kurucz (1993)<sup>2</sup>, NIST<sup>3</sup>, VALD<sup>4</sup> (Piskunov et al. 1995, Ryab-

<sup>2</sup> <http://kurucz.harvard.edu/atoms.html>

<sup>3</sup> <https://physics.nist.gov/PhysRefData/ASD/lines.form.html>

<sup>4</sup> <http://vald.astro.uu.se/>

chikova et al. 2015), and literature values. A more extensive list of the most prominent lines in the near-UV can be found in Ernandes et al. (2020).

We included lines of the elements from Sc to Ge. Note that Germanium is considered the last of the iron-peak elements (WW95), but it is sometimes considered as part of the heavy neutron-capture elements, or else as a trans-iron element (e.g. Peterson et al. 2020).

#### 7.4.0.1 Hyperfine structure

To accurately model the near-UV lines of Sc II, V II, Mn II, Co I, and Cu I we investigated their hyperfine structure (HFS) using the code from McWilliam et al. (2013). The magnetic dipole A-factor and electronic quadrupole B-factor hyperfine constants used to compute the HFS for each species are given in Table D.3 with details as follows:

- Scandium:  $^{45}\text{Sc}$  is the only stable nuclide, with nuclear spin  $I = 7/2$ . Hyperfine constants are from Villemoes et al. (1992) and Kurucz (1993).
- Vanadium: abundances correspond to 99.75% of  $^{51}\text{V}$  and only 0.25% of  $^{50}\text{V}$  (Asplund et al. 2009). We therefore adopted  $^{51}\text{V}$  as a unique isotope, with nuclear spin  $I = 7/2$ . Hyperfine constants are from Wood et al. (2014). Following Ou et al. (2020), HFS splitting was not applied to the V II 3715.46 Å line.
- Manganese:  $^{55}\text{Mn}$  is the only nuclide that contributes to the abundance (Woodgate & Martin 1957), with nuclear spin  $I = 5/2$ . Hyperfine constants are from Den Hartog et al. (2011).
- Cobalt:  $^{59}\text{Co}$  is the only nuclide (Asplund et al. 2009), with nuclear spin  $I = 7/2$ . Hyperfine constants are from Pickering (1996).
- Copper: Isotopic fractions for Cu I are 0.6894 for  $^{63}\text{Cu}$  and 0.3106 for  $^{65}\text{Cu}$  (Asplund et al. 2009). The nuclear spin is  $I = 3/2$ . Abundances were derived from the Cu I 3247.53 and 3273.95 Å lines. Hyperfine constants are from Biehl (1976) and Kurucz (1993).

After calculating the line splits and intensities of the HFS lines, we computed synthetic lines for the reference star Arcturus, adopting stellar parameters from Meléndez et al. (2003), and then comparing them with the observed lines in a near-UV UVES spectrum

Table 7.4 - List of near-UV absorption lines considered. Refs: 1) Wood et al. (2014); 2) Den Hartog et al. (2011); 3) Li et al. (1999); 4) Lawler et al. (2013); 5) VALD3; 6) Ou et al. (2020). Adopted log gf values are indicated in bold face.

Ion	Wavelength (Å)	$\chi_{\text{ex}}$	$\log \text{gf}_{\text{Kur}}$	$\log \text{gf}_{\text{VALD}}$	$\log \text{gf}_{\text{NIST}}$	$\log \text{gf}_{\text{lit}}$	[X/Fe]	$\Delta[\text{X}/\text{Fe}]_{\text{NLTE}}$	Ref.
Be II	3130.42	+0.00	-0.168	-0.168	<b>-0.178</b>	...	-0.98	...	5
Be II	3131.07	+0.00	-0.468	-0.468	<b>-0.479</b>	...	-0.98	...	5
Sc II*	3576.34	+0.0084	+0.130	+0.007	<b>+0.01</b>	...	+0.03	...	5
Sc II*	3590.47	+0.022	-0.500	-0.552	<b>-0.55</b>	...	+0.52	...	5
Ti I	3199.914	+0.048	+0.200	+0.310	<b>+0.20</b>	+0.31	+0.35	...	4
Ti I	3717.391	+0.000	-1.210	-1.228	<b>-1.20</b>	-1.19	+0.35	...	4
Ti I	3729.807	+0.000	-0.340	-0.280	<b>-0.289</b>	-0.28	+0.35	...	4
Ti I	3924.526	+0.021	-0.937	-0.870	<b>-0.883</b>	-0.87	+0.35	...	4
Ti I	3962.851	+0.000	-1.167	-1.232	<b>-1.110</b>	-1.10	+0.35	...	4
Ti I*	3998.64	+0.048	-0.056	+0.02	<b>+0.016</b>	...	+0.02	...	4
Ti II*	3321.70	+1.231	-0.320	-0.340	<b>-0.313</b>	...	+0.35	...	4
Ti II*	3343.76	+0.151	-1.270	-1.180	<b>-1.149</b>	...	+0.35	...	4
Ti II*	3491.05	+0.113	-1.130	-1.100	<b>-1.153</b>	...	+0.35	...	4
V II	3517.299	+1.128	-0.310	...	<b>-0.24</b>	-0.24	+0.22	...	6
V II	3545.196	+1.096	-0.390	...	<b>-0.32</b>	-0.32	+0.22	...	6
V II	3715.464	+1.575	-0.380	...	<b>-0.22</b>	-0.22	+0.22	...	6
V II*	3951.96	+1.4764	-0.740	-0.730	<b>-0.73</b>	-0.73	+0.22	...	1
Cr I*	3578.68	+0.00	+0.409	+0.42	<b>+0.408</b>	...	-0.31	+0.678	5
Mn II*	3441.99	+1.776	-0.270	-0.332	<b>-0.346</b>	-0.346	-0.39	...	2
Mn II*	3460.32	+1.809	-0.615	-0.615	<b>-0.632</b>	-0.631	-0.39	...	2
Mn II*	3482.90	+1.833	-0.740	-0.826	<b>-0.837</b>	-0.837	-0.39	...	2
Mn II*	3488.68	+1.847	-0.860	-0.921	<b>-0.937</b>	-0.937	-0.39	...	2
Mn II*	3495.83	+1.855	-1.200	-1.257	<b>-1.282</b>	-1.280	-0.39	...	2
Mn II*	3497.53	+1.847	-1.330	-1.397	<b>-1.414</b>	-1.418	-0.39	...	2
Co I*	3412.34	+0.5136	+0.030	+0.030	<b>+0.03</b>	...	+0.19	...	5
Co I*	3412.63	+0.00	-0.780	-0.780	<b>-0.78</b>	...	+0.19	...	5
Co I*	3449.16	+0.5815	-0.090	-0.090	<b>-0.09</b>	...	+0.19	...	5
Co I*	3529.03	+0.1744	-0.880	-0.880	<b>-0.88</b>	...	+0.19	...	5
Co I*	3842.05	+0.9227	-0.770	-0.770	<b>-0.76</b>	...	+0.19	...	5
Co I*	3845.47	+0.9227	+0.010	+0.010	<b>+0.01</b>	...	+0.19	+0.749	5
Ni I*	3437.28	+0.00	-1.150	-1.20	<b>-1.15</b>	...	+0.05	...	5
Ni I*	3483.77	+0.2748	-1.110	-1.110	<b>-1.12</b>	...	+0.05	...	5
Ni I*	3500.85	+0.1652	-1.370	-1.270	<b>-1.37</b>	...	+0.05	...	5
Ni I*	3597.71	+0.2124	-1.090	-1.10	<b>-1.09</b>	...	+0.05	...	5
Ni I*	3807.14	+0.4228	-1.180	-1.230	<b>-1.18</b>	...	+0.05	...	5
Ni I*	3807.14	+3.8983	...	-2.816	<b>-1.18</b>	...	...	...	Blend
Cu I*	3247.53	+0.00	-0.062	-0.008	<b>-0.054</b>	...	-0.79	...	5
Cu I*	3273.95	+0.00	-0.359	-0.311	<b>-0.354</b>	...	-0.79	...	5
Zn I*	3075.90	+0.00	-3.900	-3.900	<b>-3.80</b>	...	...	...	5
Zn I*	3302.58	+4.0297	-0.057	-0.057	<b>-0.01</b>	...	+0.22	...	5
Zn I*	3345.01	+4.0778	+0.246	+0.246	<b>+0.30</b>	...	+0.22	...	5
Ge I*	3039.07	+0.8834	...	+0.49	<b>+0.07</b>	-0.08	...	...	3

1) Symbols: \* Near-UV iron-peak element lines considered by Ernandes et al. 2020;

2) The Ge I line is included for completeness, where its abundance was derived by Siqueira-Mello et al. (2013).

from the ESO archive<sup>5</sup>. Figures E.1 and E.2 show the fits to Co and Cu for the Arcturus spectrum. For Sc II and Mn II the calculations including the HFS are a poorer match to the observations than those without, possibly because some atomic constants cannot be accounted for; we therefore did not include HFS for these two elements in our analysis of CS 31082-001. We add that for many of the lines studied here, the surrounding lines in the Arcturus spectrum are saturated. The adopted HFS components and corresponding oscillator strengths for the Co I and Cu I lines are reported in Tables D.4, D.5 and D.9.

#### 7.4.0.2 Non-LTE abundance corrections

As demonstrated by Bergemann & Cescutti (2010) and Bergemann et al. (2010), NLTE corrections are needed for the Cr and Co lines, with corrections available for two of our diagnostic lines<sup>6</sup>. For the adopted stellar parameters of CS 31082-001, the NLTE corrections for the Cr I 3578.68 Å and Co I 3845.47 Å lines are +0.678 dex and +0.749 dex, respectively. In particular, Bergemann & Cescutti (2010) analysed the discrepancies between abundances derived from Cr I and Cr II lines, showing that deficiencies of Cr in metal-poor stars are related to only NLTE effects, and that the Cr/Fe ratio is essentially solar.

#### 7.4.1 Abundances: Sc, Ti, Cr, Mn, Co, Ni and Zn

Adopting the published stellar parameters of CS 31082-001 and varying the abundances of each species to fit the relevant diagnostic lines, our fits to Sc, Ti, Mn, Co, Ni and Zn are shown in Figs. E.3 to E.9, with the fit to the Cr I 3578.68 Å line shown in Fig. 7.3.

The fits to the Cr I, Mn II, Co I and Ni I lines are excellent (Figs. 7.3, E.6, E.7, and E.8), while those to Sc II and Ti I (Figs. E.3 and E.4, respectively) both have problems. For Sc II, the two diagnostic lines lead to quite different abundances ( $\Delta A(\text{Sc}) = 0.49$ ); the Sc II 3590.47 Å line appears to be a saturated blend that only has a small dependence on the abundance, so we adopt the value from the Sc II 3576.34 Å line.

A similar discrepancy also arises between the Ti I 3998.64 Å and 3924.526 Å lines (see Fig. E.4), where there are blends present in the redward wing. However, the estimated abundance from the Ti I 3924.526 Å line also matched that from the four other Ti I lines in Table 7.4. These other lines were included from the line list of Lawler et al. (2013);

<sup>5</sup> <http://archive.eso.org/dataset/ADP.2020-08-04T15:12:16.253>

<sup>6</sup> [http://nlte.mpia.de/gui-siuAC\\_secE.php](http://nlte.mpia.de/gui-siuAC_secE.php)

Table 7.5 - Comparison of our derived abundances with results from Hill et al. (2002). Solar abundances are from Grevesse & Sauval (1998).

Species	Z	A(X) <sub>⊙</sub>	[X/Fe] <sub>Hill</sub>	[X/Fe] <sub>present</sub>	A(X)
BeII	4	1.15	...	-0.90	-2.4
ScII	21	3.17	+0.02	+0.01	0.28
TiI	22	5.02	+0.25	+0.28	2.40
TiII	22	5.02	+0.31	+0.28	2.40
VII	23	4.00	...	+0.15	1.25
CrI	24	5.67	-0.34	-0.34	2.43
MnII	25	5.39	-0.35	-0.35	2.14
CoI	27	4.92	+0.27	+0.26	2.28
NiI	28	6.25	+0.03	+0.02	3.37
CuI	29	4.21	...	-0.81	0.50
ZnI	30	4.60	+0.19	+0.18	1.88
GeI	32	3.41	-0.55	...	...

additional Ti I lines at 3725.1 and 3926.3 Å were not strong enough in CS 31082-001 to estimate the abundance. Fig E.4 shows the fits to the Ti I lines, giving an abundance of  $A(\text{Ti}) = 2.40$ . This is similar to the value obtained from the Ti II lines (Fig. E.5), so we adopt this value. Compared to the results from optical lines, this result is higher by 0.15 dex for Ti I and 0.05 dex for Ti II, but still in reasonable enough agreement given the uncertainties.

A summary of the present abundance results with previous values is given in Table 7.5. The values for each species are in general agreement within errors.

#### 7.4.2 Abundances: V and Cu

Our fits to the V and Cu lines are shown in Figs. 7.4 and 7.5. From their large sample of metal-poor stars, Ou et al. (2020) found a discrepancy between abundance estimates from V I and V II, with mean values of  $[V \text{ I}/\text{Fe}] = -0.10$  and  $[V \text{ II}/\text{Fe}] = +0.13$ . The difference is thought to arise from NLTE effects in the V I lines, so for CS 31082-001 we used the V II lines.

For Cu, Bonifacio et al. (2010) found a discrepancy between the abundances for turn-off stars from the multiplet 1 line in the UV at 3247.5 Å and multiplet 2 at 5105.5 Å. To see if the same discrepancy is present in CS 31082-001, we also fitted the Cu I 5105.5 and 5218.2 Å lines (see Fig. 7.6) taking into account the HFS from Ernandes et al. (2018). In this case the UV and optical abundances agree.

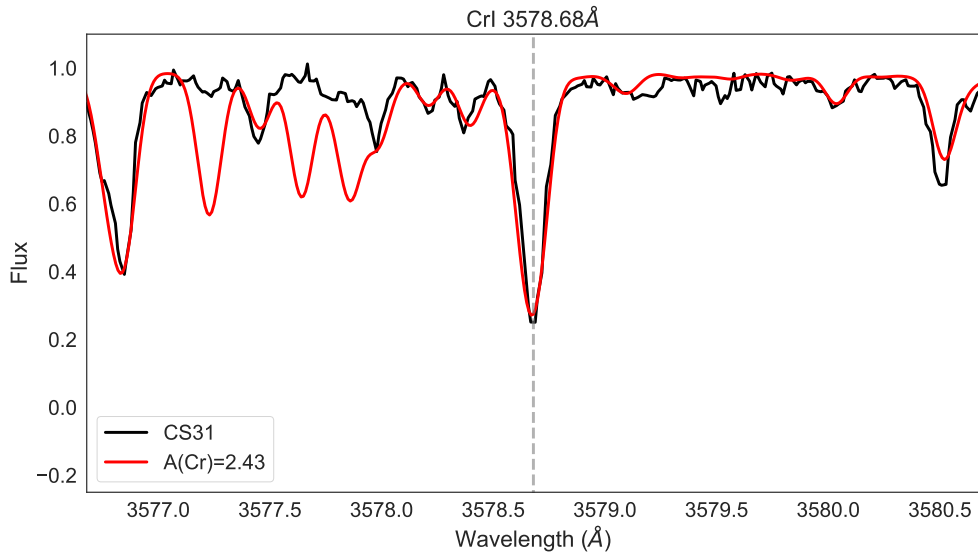


Figure 7.3: Best-fit abundance for the Cr I 3578.68 Å line, computed with  $[\text{Cr}/\text{Fe}] = -0.31$ , without NLTE correction (see Sect. 7.4.0.2).

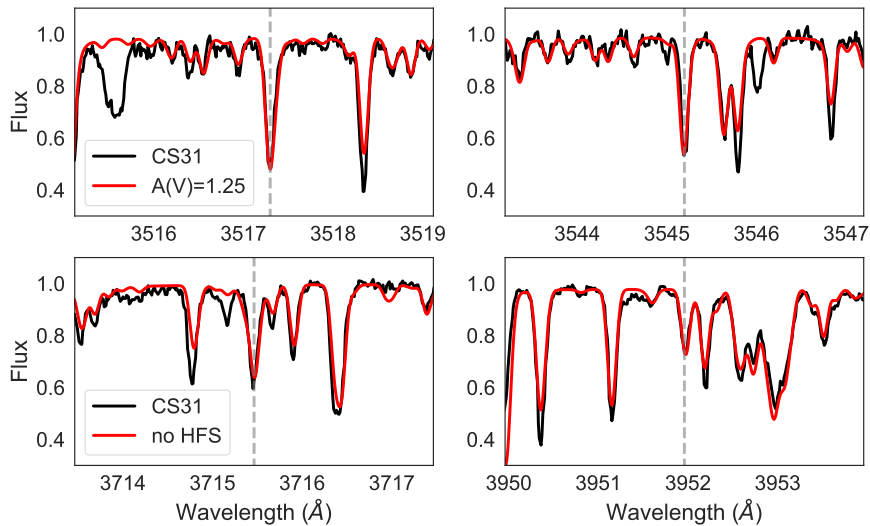


Figure 7.4: Best fit abundance for V II 3517.299, 3545.196, 3715.464 and 3951.96 Å lines, computed with  $[\text{V}/\text{Fe}] = +0.22$ . HFS was not applied to the V II 3715.464 Å line.

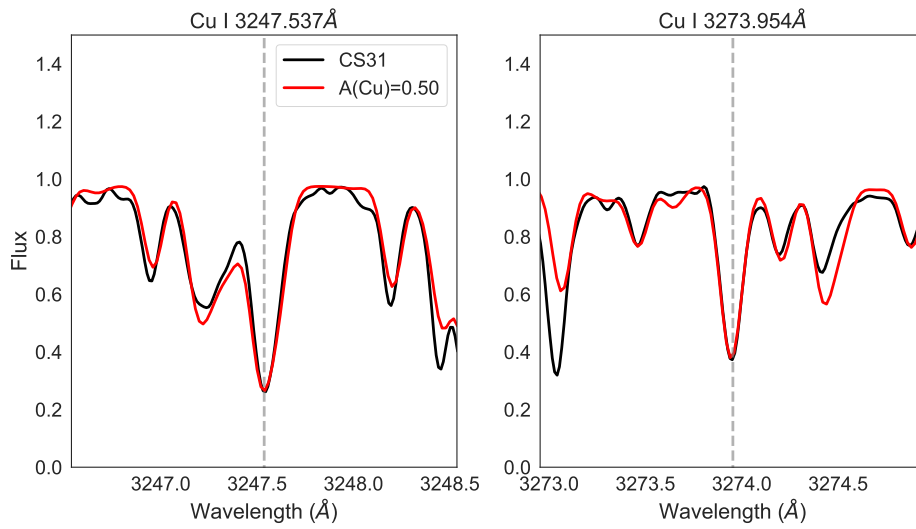


Figure 7.5: Best fit for the Cu I 3247.537 and 3273.954 Å lines, computed with  $[\text{Cu}/\text{Fe}] = -0.79$  (including hyperfine structure).

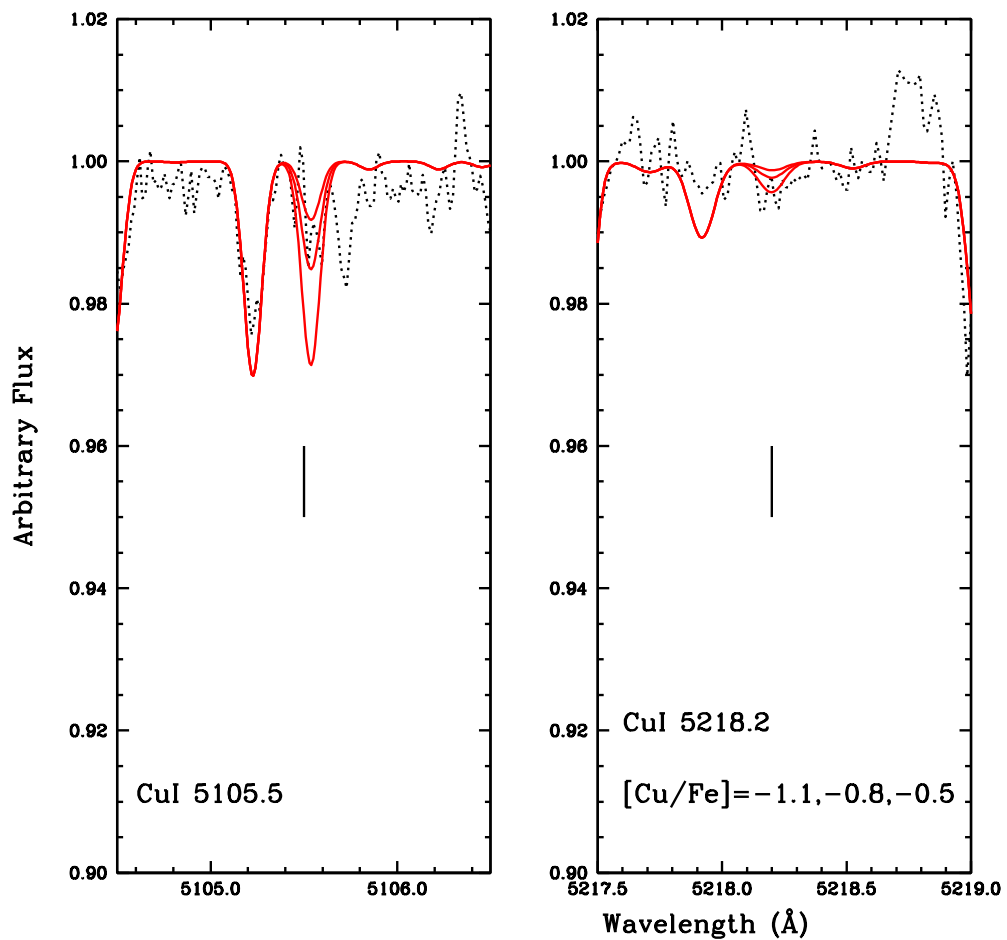


Figure 7.6: Best fit to the Cu I 5105.5 and 5218.2 Å lines, computed with  $[\text{Cu}/\text{Fe}] = -0.80$ .

## 7.5 Chemical evolution models

To investigate our estimated V and Cu abundances in the context of nucleosynthesis, we have employed the disk/halo chemical-evolution model from Lanfranchi & Friaça (2003, hereafter LF03), which has been used to investigate the origin of damped Lyman- $\alpha$  systems in galaxy disks and of Lyman-limit systems in galactic halos (Viegas et al. 1999). It is assumed that the infall of gas from the halo into the Milky Way disk feeds the disk star formation and that the star-formation rate (SFR) follows power laws on mass surface density and gas fraction. The formalism and basic equations of the model can be found in LF03. An exponential mass surface density profile is adopted for the disk,  $\sigma \propto e^{-r/r_G}$ , with  $r_G = 2.6$  kpc (Boissier & Prantzos 2000). In the adopted SFR law, the specific SFR (i.e. the inverse of the local star-formation timescale) depends on the gas density as  $\nu \propto \rho^{1/2}$ . The normalizations of the SFR are  $\tilde{\nu}_H = 0.2 \text{ Gyr}^{-1}$  for the initial halo and  $\tilde{\nu}_D = 0.5 \text{ Gyr}^{-1}$  for the disk at the age of the Galaxy ( $t_G = 13.5 \text{ Gyr}$ ) and at the solar Galactocentric distance ( $r_\odot = 8 \text{ kpc}$ ).

The history of gas infall into the Galactic disk presents two phases, in line with scenarios such as the two-infall model (Chiappini et al. 2001). The infall rate into the disk is assumed to decline with time as  $e^{-t/\tau_D}$ . The first phase of the infall is rapid, with the infall timescale  $\tau_D = 1 \text{ Gyr}$ , from  $t = 0$  until  $t = 1 \text{ Gyr}$ . In the late infall,  $\tau_D$  is given by  $\tau_D(r) = 1 + 7/6(r-2)$ , for  $2 \leq r \leq 8 \text{ kpc}$ , and  $\tau_D(r) = 8 + 0.5(r-8)$ , for  $r > 8 \text{ kpc}$ . The inner and the outer boundaries of the disk are set at 2 and 18 kpc. At these radii,  $\tau_D = 1$  and 13 Gyr, respectively, and  $\tau_D = 8$  at  $r_\odot$ . In contrast to Chiappini et al. (2001), we do not consider a threshold for star formation, fixed by adjusting its value in order to reproduce the observations, but we included inhibition of star formation by considering fundamental processes (see LF03 and Friaça & Terlevich 1998)

With respect to the nucleosynthesis prescriptions of our model, we adopt metallicity-dependent yields from core-collapse supernovae (SNe II), high explosion-energy hypernovae, type Ia supernovae (SNe Ia), and intermediate-mass stars (IMS) (for more details, see Friaça & Barbuy 2017). The SN II yields are adopted from WW95. For low metallicities ( $Z < 0.01Z_\odot$ ), we also considered the yields from hypernovae (Umeda & Nomoto 2002, 2003, 2005; Nomoto et al. 2006, 2013). The yields of SNIa resulting from Chandrasekhar mass white dwarfs are taken from Iwamoto et al. (1999), specifically models W7 (progenitor

star of initial metallicity  $Z = Z_{\odot}$ ) and W70 (zero initial metallicity). The yields for IMS (0.8-8  $M_{\odot}$ ) with initial  $Z = 0.001, 0.004, 0.008, 0.02,$  and  $0.4$  are from van den Hoek & Groenewegen (1997) (variable  $\eta_{AGB}$  case).

### 7.5.1 Abundances and chemical-evolution models for V

The upper panel of Fig. 7.7 shows V abundance estimates derived by Ou et al. (2020) for the sample of halo stars from Roederer et al. (2014), and the results from Ishigaki et al. (2013) for halo and thick disk stars; our best fit abundance, derived from the V II 3951.96 Å line in CS 31082-001 is shown by the red circle.

Vanadium is synthesized in explosive Si-burning during core-collapse supernovae (SNe). Its abundances are known to be underpredicted by chemical evolution models (at all metallicities) when compared to observations (WW95, Kobayashi et al. 2006, 2020), as highlighted by the model from Kobayashi et al. (2020) in the upper panel of Fig. 7.7 compared to the observational results.

Multidimensional effects could increase the abundances of Sc, Ti and V (Maeda & Nomoto 2003; Tominaga 2009). To mimic these effects, the K15 model of Kobayashi et al. (2020) considered a 0.3 dex enhancement in the V yields. Indeed, Timmes et al. (1995) pointed out that the V yields of WW95 should be increased by a factor of  $\sim 3$  to reproduce the observational data. Therefore, in our chemical-evolution models, we applied this factor to the V yields of WW95 from  $Z = Z_{\odot}$  to  $0.01 Z_{\odot}$ . Including an enhancement by a constant factor accounts for the flat behaviour of  $[V/Fe]$  for  $[Fe/H] > -2$ . However, as V varies in lockstep with iron, the models do not reproduce the high  $[V/Fe]$  ratios seen in extremely metal-poor and very metal-poor stars, including CS 31082-001.

Core-collapse SNe release large amounts of energy as neutrinos ( $> 10^{53}$  erg). The interaction of neutrinos with matter represents an additional nucleosynthetic source (WW95, Heger et al. 2005, Yoshida et al. 2008). In very low metallicity stars, neutrino processes contribute significantly to the production of odd-Z elements such as V, Mn, Sc, K, F and B (Yoshida et al. 2008, Kobayashi et al. 2011a). Following the prescriptions of Yoshida et al. (2008), our models therefore also include enhancement of V yields by neutrino processes during the SN explosion. These phenomena can be important at very low metallicities but would be ineffective for the yields of hypernovae. The total neutrino energy  $E_{\nu}$  released when the core of a massive star collapses to form a neutron star is a free parameter. In

our models we adopted the standard case of  $E_\nu = 3 \times 10^{53}$  erg from Yoshida et al. (2008), which corresponds to the gravitational binding energy of a  $1.4M_\odot$  neutron star (Lattimer & Prakash 2001). We also consider the cases of a larger neutrino energy  $E_\nu = 9 \times 10^{53}$  erg, and the standard case of  $E_\nu = 3 \times 10^{53}$  erg but with a neutrino temperature of  $T_\nu = 8$  Mev (as assumed by WW95). As shown by Fig. 7.7, inclusion of the neutrino processes better reproduces the rising trend of  $[V/Fe]$  for  $[Fe/H] < -2.0$  in the results from Ou et al. (2020) as well as our result for CS 31082-001.

We have considered neutrino processes as an additional nucleosynthetic source of vanadium. Although this effect reproduces the rise of  $[V/Fe]$  for  $[Fe/H] \lesssim -2.5$ , it falls short of the highest observed values of  $[V/Fe]$  around  $+1.5$ , obtained by Ou et al. (2020). In this context it is worth considering the possibility of observational errors. Following Ou et al. (2020) the vanadium abundance for CS 31082-001 was derived from the V II lines. The highest value of  $[V/Fe]$  derived by Ou et al. (2020) using the V II line is 1.63 for G238–030. If using the V I line instead, the derived  $[V/Fe]$  is 1.46. On the theoretical side, it could be that other processes are at work, e.g., the above mentioned multidimensional effects. Even considering the sole neutrino process, our models have been conservative, and higher neutrino energies would increase the  $[V/Fe]$  ratio.

### 7.5.2 Abundances and chemical evolution models for Cu

Copper is produced both in the alpha-rich freeze-out as a primary element (Sukhbold et al. 2016) and in the weak-s process in massive stars as a secondary element. The iron-peak elements are mainly formed during explosive oxygen and silicon burning in massive supernovae (WW95). For larger values of the neutron fraction, the main products of silicon burning are completed. On the other hand, if the density is low and the supernova envelope expansion is fast,  $\alpha$  particles will be frozen and not captured by the heavier elements (Woosley et al. 2002). The trend of Cu abundance with the metallicity  $[Fe/H]$  could reveal the relative efficiencies of these two contributions.

The secondary-like behaviour of Cu has led Sneden et al. (1991) to suggest that it could mainly be attributed to the weak s-process. However, as more data has been accumulated and chemical evolution models have been tested, a more complex picture has emerged (Mishenina et al. 2002, Kobayashi et al. 2006, 2011b, 2020). The relation of  $[Cu/Fe]$  versus  $[Fe/H]$  for  $-2 < [Fe/H] < -0.5$  is well described by a secondary process, but if we

consider a wider range in metallicity, from  $[\text{Fe}/\text{H}] \sim -4$  to  $\sim 0$ , the behavior of  $[\text{Cu}/\text{Fe}]$  is more complex than that expected from purely primary or secondary processes. The general curve has a wavy shape, and for  $[\text{Fe}/\text{H}] < -2.5$ ,  $[\text{Cu}/\text{Fe}]$  increases or, at least, reaches a plateau, indicating the presence of a primary process. In fact, the Cu content of extremely metal-poor stars is basically determined by explosive nucleosynthesis in massive stars, and by hypernovae in particular. On the other hand, the form of the trend of  $[\text{Cu}/\text{Fe}]$  with  $[\text{Fe}/\text{H}]$  for higher metallicities, tells us about the role of longer lived sources of Cu enrichment. At  $[\text{Fe}/\text{H}] \sim -1$ ,  $[\text{Cu}/\text{Fe}]$  shows another plateau, which is explained by SNe Ia. In addition to that, besides an origin in massive stars, Cu is also formed through the s-process acting in AGB stars. However, this contribution is negligible at  $[\text{Fe}/\text{H}] \sim -2$  and amounts to only 0.03 dex at  $[\text{Fe}/\text{H}] = 0$  (Kobayashi et al. 2020).

In the lower panel of Fig. 7.7 we show the Cu abundances derived by Mishenina et al. (2002), Cohen et al. (2013), and Ishigaki et al. (2013) for halo and thick disk stars and our best fit abundance to the Cu I 3247.54 and 3273.95 Å lines of CS 31082-001 compared to the predictions of the LF03 model used in this work. The data points from Ishigaki et al. (2013) are systematically below those from Mishenina et al. (2002) and, although their scatter is large, they suggest a sinuous behavior of  $[\text{Cu}/\text{Fe}]$  with  $[\text{Fe}/\text{H}]$ , as predicted by the LF03 model. The abundances we derived for CS 31082-001 (red circle) are well fitted by our model. The plateau of  $[\text{Cu}/\text{Fe}]$  at  $[\text{Fe}/\text{H}] < 2.5$  appears to mainly be the result of hypernovae.

The thick solid line in the lower panel of Fig. 7.7 refers to the halo in our model and the thin lines to the disk at the radii  $r = 4, 8$  and  $12$  kpc. The neutrino process follows the fiducial case ( $E_\nu = 3 \times 10^{53}$  erg), but it has little impact on the Cu abundances. The results in Fig. 7.7 also include the predictions for Cu abundances from Kobayashi et al. (2020), whose models include AGBs, core-collapse SNe and type Ia SNe. This model accounts for the  $[\text{Cu}/\text{Fe}]$  ratio of CS 31082-001 but overestimates the Cu abundances around  $[\text{Fe}/\text{H}] = -2.0$ . To assess the effect of the s-process in AGB stars on Cu production, their model without the AGB contribution is also plotted (dotted-dashed line in Fig. 7.7). This process contributes with only a very modest increase of Cu near  $[\text{Fe}/\text{H}] = 0.0$ , and removing the AGB contribution does not alleviate the overestimate of  $[\text{Cu}/\text{Fe}]$  at  $[\text{Fe}/\text{H}] \sim -2.0$ .

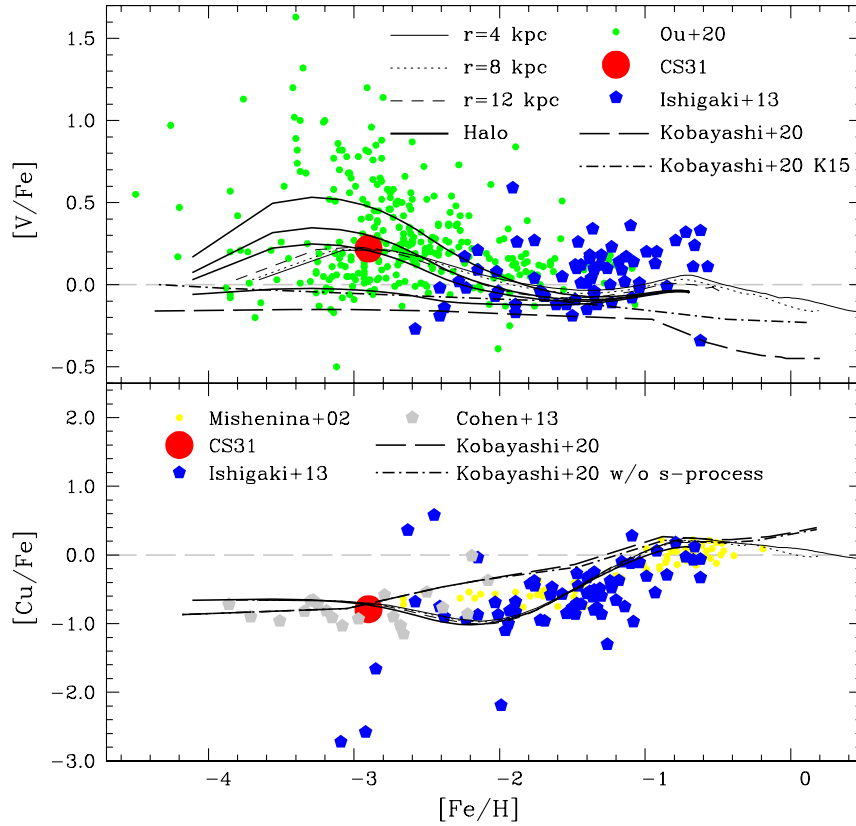


Figure 7.7: *Upper panel:* Relation of  $[V\ II/Fe]$  vs.  $[Fe/H]$ . Symbols: red dots: present work; green dots: Ou et al. (2020), blue pentagons: Ishigaki et al. (2013). Our chemical evolution model for the halo/disk (LF03) is shown for several Galactocentric radii and for the halo (thick solid lines). Our fiducial model includes neutrino processes with  $E_\nu = 3 \times 10^{53}$  erg. The various curves for the halo correspond to different assumptions for the neutrino process. From bottom to top: 1) no neutrino process; 2) the fiducial model ( $E_\nu = 3 \times 10^{53}$  erg); 3)  $E_\nu = 3 \times 10^{53}$  erg and  $T_\nu = 8$  Mev; 4)  $E_\nu = 9 \times 10^{53}$  erg. As we can see from the comparison of the LF03 model with the data, inclusion of the neutrino process could account for the high  $[V/Fe]$  ratios of extremely metal-poor and very metal-poor stars. The solid long-dashed line refers to the predictions of the fiducial model of Kobayashi et al. (2020), while the K15 model from Kobayashi et al. (2020), which includes an 0.3 dex enhancement of the V yields, is also shown (dotted-dashed line). *Lower panel:* Relation of  $[Cu\ I/Fe]$  vs.  $[Fe/H]$ . Symbols: red dots: present work; yellow dots: Mishenina et al. (2002); blue pentagons: Ishigaki et al. (2013); gray pentagons: Cohen et al. (2013). The thick solid line refers to the halo in the LF03 model and the thin lines to the disk in the model at the radii  $r = 4, 8$  and  $12$  kpc. The neutrino process follows the fiducial case ( $E_\nu = 3 \times 10^{53}$  erg). The LF03 model not only reproduces the CS 31082-001 data point but also predicts the wave shape of the  $[Cu/Fe]$  versus  $[Fe/H]$  curve. The resulting evolution of Cu abundance predicted by the model of Kobayashi et al. (2020) for the solar neighborhood is given by the black long-dashed line, and the dotted-dashed line refers to the model without production of Cu by the s-process in AGB stars.

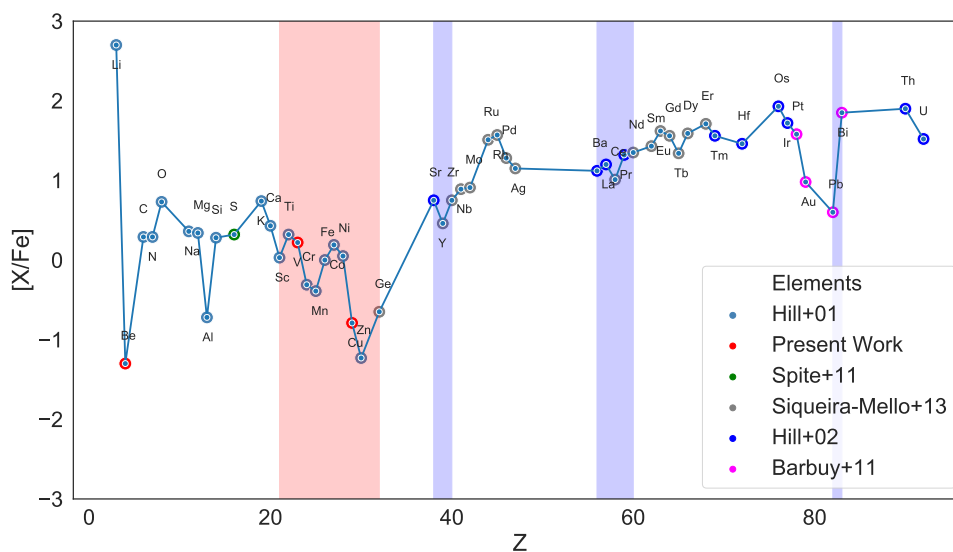


Figure 7.8: Elemental abundances of CS 31082-001, with the symbol colours showing the source of the result, as indicated in the legend. The red shaded region highlights the iron-peak elements, with the blue regions highlighting the first, second and third peaks of s-process elements

### 7.5.3 Abundances: Summary

The iron-peak abundance pattern of CS 31082-001 is shown in Fig. 7.8, including results from Hill et al. (2001, 2002), Cayrel et al. (2004), Plez et al. (2004), Spite et al. (2005, 2011), Barbuy et al. (2011), Siqueira-Mello et al. (2013), and our new results for V and Cu.

In the upper panel of Fig. 7.9 we compare the iron-peak abundances in CS 31082-001 with those for the similarly r-process-rich star CS 22892-052 (Snedden et al. 2003). These two halo metal-poor stars appear to have not only the same abundance patterns for the neutron-capture elements but also have the same pattern for the iron-peak elements, indicating that the same kind of process produced the iron-peak elements in both stars. To confirm the chemical evolution models developed above, in the lower panel of Fig. 7.9 we show the abundances of iron-peak elements compared with the predicted SNe yields from Nomoto et al. (2013) for a faint supernova (black, dashed line) and a hypernova (green, dashed line). The latter is a better fit to the iron-peak elements (e.g. for Co, Ni, Cu, and Zn) but both models underestimate the production for Sc, Ti, V, Mn, and Ge, and overestimate the yield for Cr. This is the reason why we combined yields from hypernovae and added neutrino processes in our chemical evolution models. In particular for V, it

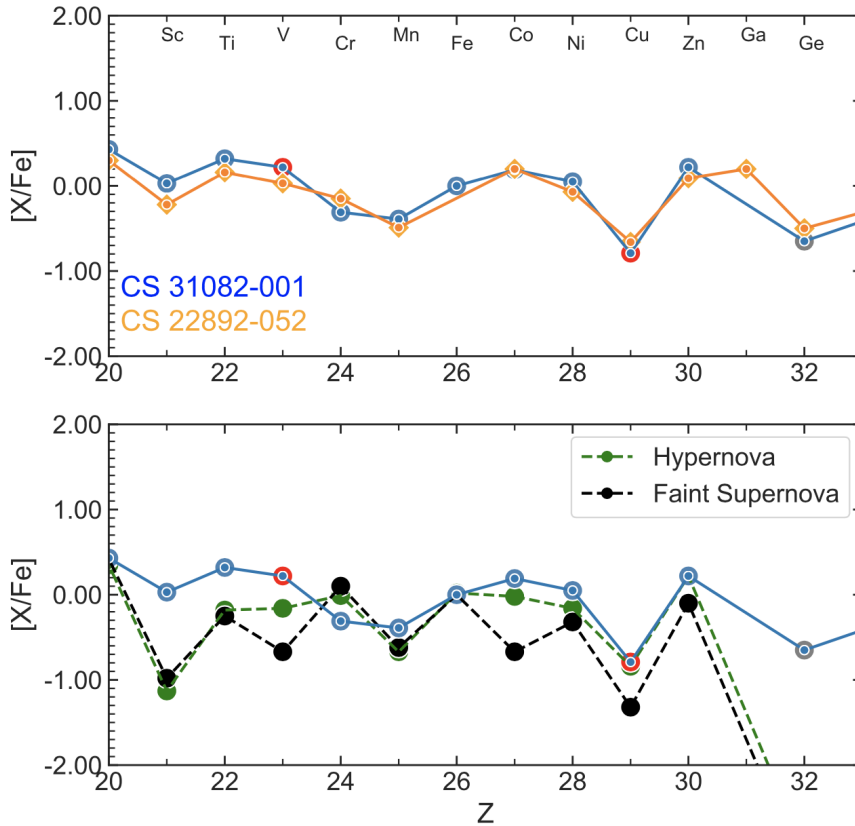


Figure 7.9: *Upper panel:* Elemental abundances of CS 31082-001. Symbols: red circles are from the present work; blue circles, Hill et al. (2002); gray circles, Siqueira-Mello et al. (2013). The orange diamonds are the elemental abundances of CS 22892-052 from Sneden et al. (2003). *Lower panel:* Iron-peak abundances of CS 31082-001 with the same symbol colours as the upper panel. The predicted abundance yields from for Nomoto et al. (2013) for faint supernovae and hypernovae are shown by the green and black dashed lines, respectively.

adjusts the lower  $[V/Fe] = -0.1$  yield to reach  $[V/Fe] = +0.3$ .

The underestimates in the production of the Sc, V, Mn, and Co in the hypernovae models can be explained by the  $\nu$ -process not being included in the model from Nomoto et al. (2013). According to Yoshida et al. (2008) the hypernovae models can be improved by adding the  $\nu$ -process – especially for the odd- $Z$  elements where the neutrino process plays a significant role. One of these elements is V, which is mainly synthesized in the incomplete Si-burning region as  $^{51}\text{Mn}$ . However, in the hypernovae models it is synthesized in the complete Si-burning region along with the  $\nu$ -process from  $^{52}\text{Fe}$  in the incomplete Si-burning region. The  $[Ge/Fe]$  abundances are significantly underestimated by the faint SNe and the hypernovae models. However, it is also underproduced in the models from

Wanaajo (2007), as described by Siqueira-Mello (2013) in a previous analysis of CS 31082-001, where they concluded that the r-process considered by Wanaajo (2007) cannot explain the observed Ge abundance. On the other hand, the model of high entropy winds by Farouqi et al. (2010), with an electron abundance of  $Y_e = 0.498$ , can explain the abundance of the trans-iron elements Ge, As, Se, Mo, and Ru (Peterson et al. 2020).

## 7.6 Summary of CS 31082-001

We have used the near-UV region of high-resolution spectra from VLT-UVES and *HST*-STIS to estimate Be, V and Cu abundances in the metal-poor star CS 31082-001 for the first time. Beryllium in CS 31082-001 appears to be low, with  $A(\text{Be}) = -2.4$  to  $-2.5$ , and not following the linear trend seen for unmixed, metal-poor stars. This is expected for a cool red giant, due to diffusion effects and consequent destruction of the light elements (Li and Be) in the atmospheric layers.

Our estimated abundances of the iron-peak elements V and Cu agree well with other data in the literature, and we present new chemo-dynamical models for these elements. We can only reproduce the observed V abundance by adding an extra nucleosynthesis source to the models to include the interaction of neutrinos with matter. For Cu we found that the behaviour of  $[\text{Cu}/\text{Fe}]$  for metal-poor stars confirms a decreasing Cu-to-Fe abundance with decreasing metallicity. As pointed out by Sukhbold et al. (2016), Co and Cu are both produced in the alpha-rich freezeout as primary elements, and as well in the weak-s process in massive stars, in the latter case with a secondary element behaviour (see also Barbuy et al. 2018a). A dominant weak-s process origin is therefore confirmed for copper.

We have also investigated the abundances estimated for iron-peak elements from near-UV diagnostics compared with published values from longer-wavelength lines in the visible, finding good agreement. This validation is important in the context of future near-UV observations of metal-poor stars with the CUBES instrument. In a future paper we will investigate the detectability of heavy elements in the UV region in CS 31082-001, to further investigate the future opportunities with CUBES in studies of stellar nucleosynthesis.



## Simulations on upcoming instruments

### 8.1 *The CUBES spectrograph*

#### 8.1.1 *Introduction*

The CUBES (Cassegrain U-Band Efficient Spectrograph) is a forthcoming ESO VLT spectrograph focusing on achieving high efficiency in the ground-UV, observing in the 300nm-400nm window with mid-resolution. Since the ground-based ultraviolet (UV) spectroscopy is a treasure trove for stellar astrophysics (Evans et al. 2018). This part of the near-UV domain (300-400 nm) is rich with diagnostic lines from both light- and heavy-elements, from which precision abundances can be determined for a broad range of stars, in particular metal-poor stars, characterising their CNO abundances using CN, NH, and OH features in the UV and measuring abundances of key elements as Be and heavy elements. Some of those neutron-capture elements only have lines in the near UV (see, e.g. Sneden et al. 2003).

Our observational efforts in this region are currently limited by the efficiencies of instruments such as UVES (Dekker et al. 2000) on the Very Large Telescope (VLT). UVES has an end-to-end efficiency of only a few percent over the near-UV range. As such, detailed chemical abundances from lines in this region for metal-poor stars, have generally been limited to relatively bright (10<sup>th</sup> or 11<sup>th</sup> magnitude) targets, or have required significant integration times, e.g. the 20 hr total exposure of BPS BS 16968-061 ( $V = 13.2$  mag) (Smiljanic et al. 2021).

Advanced simulations to finalise the instrument requirements and quantify the performance of CUBES are now underway as part of the Phase A study. Here we present analysis that provided the starting point of the conceptual design. The over-arching design goal

for CUBES is to maximise the instrument efficiency in the near UV, while still enabling quantitative stellar abundances, so spectral resolving power ( $R$ ) is a key parameter. One of the leading instruments for stellar abundances at such wavelengths has been the Ultraviolet and Visual Echelle Spectrograph (UVES) on the VLT (Dekker et al. 2000), typically providing  $R = 40000$  with a  $1''$  slit. Abundances for many elements can potentially be estimated at lower resolution, but we need to investigate their feasibility on a line-by-line basis.

Here we firstly present a first study of the impact of spectral resolution on a broad range of elemental diagnostic lines in the near UV (over the range 3020-4000Å). Specifically, we investigate which are accessible with  $R = 20000$  from CUBES compared to  $R = 40000$  with UVES.

Secondly we investigate the performance of CUBES for heavy-element abundances in a more quantitative approach, here we present simulations undertaken using the metal-poor ( $[Fe/H] = -2.9$ ), r-process-enriched star CS 31082-001 as a spectral template. This star was observed extensively with UVES within the ‘First Stars’ Large Programme at the European Southern Observatory (ESO), as well as with the *Hubble Space Telescope* (*HST*). The U/Th abundance ratio derived from the optical spectra was used to estimate the age of the star (Cayrel et al. 2001), and a series of papers then presented its light- and heavy-element abundances from the ground-based spectroscopy (115; 57; 204; 252) and the *HST* data (Barbuy et al. 2011 and Siqueira-mello et al. 2013).

Using the UVES data of CS 31082-001 we investigate the near-UV diagnostics for several light elements compared to published values, as well as presenting the first abundances for Be, Cu, and V (76). Here we present simulations investigating the detectability of selected heavy elements at the lower spectral resolving power of CUBES compared to that of UVES. In particular, we consider lines from Ge and Bi that are at the shortward end of the ground-UV domain, and which helped to motivate the blueward coverage of the instrument design. We also investigated two other neutron-capture elements of interest in studies of metal-poor stars (Hf, U) to further characterise the performance of the CUBES.

### 8.1.2 Science motivation: stellar nucleosynthesis

Determine the element abundance in stars atmospheres not only help us understand the origins of the elements in the periodic table but the origin of these stars and how

their birth environment assembled and enriched. Each isotope has a complex production channel, which includes numerous nuclear reactions in several astrophysical sites.

The elements can be grouped together by their formation mechanisms. For instance, the lightest elements (H, He, Li) were formed in the first minutes after the Big Bang (with some debate remaining as to whether trace amounts of Be are also primordial). He is also produced via the proton-proton chain in main-sequence stars, whereas Li and Be are produced and destroyed by this process, which depletes them even further than their otherwise low relative abundances (see Fig. 8.1). The light  $\alpha$ -elements typically have spectral lines in the visible and infrared, but elements around the iron-peak ( $21 \leq Z \leq 30$ , highlighted in pink in Fig. 8.1, in which the most abundant element is Fe itself), also have absorption lines in the near-UV regime.

Beyond the iron peak many elements only have detectable lines at ground-UV wavelengths and into the space UV (e.g. Sneden et al. 2003). Fusion reactions beyond the iron peak (i.e.  $Z > 30$ ) are endothermic and would also have to overcome the Coulomb barrier, so these elements are generally not formed by proton capture. Production of such elements therefore occurs via neutron-capture nucleosynthesis, which is described by two major mechanisms, the rapid and slow capture of neutrons (r-process and s-process, respectively). The s-process occurs when the neutron-capture timescale is much lower than that for  $\beta$ -decay ( $\tau_n \gg \tau_\beta$ ), hence this process flows in the valley of beta stability. The three peaks of the s-process (highlighted by the blue panels in Fig. 8.1) appear due to the bottleneck effect of the magic numbers 50, 82 and 126. The r-process is defined by the converse,  $\tau_n \ll \tau_\beta$ , where neutron capture occurs before nuclei have time to undergo  $\beta$ -decay. Given these timescales, the two processes are associated with very different astrophysical environments.

To address fundamental questions such as the origins of the heavy elements and their complex nucleosynthesis we need access to the wealth of information that near-UV spectra contain. For example, the chemical abundances of metal-poor stars provide us with valuable probes of the nucleosynthesis processes of the first stars and the early evolution of the Milky Way, but near-UV observations are limited to only small samples (tens of stars) with current instrumentation. Stars with  $[\text{Fe}/\text{H}] < -2.0$  are generally referred to as very metal-poor stars (VMP), while those with  $[\text{Fe}/\text{H}] < -3.0$  are called Extremely metal-poor stars (EMP). Ahead of investigating the required spectral resolution for near-UV spectroscopy

and to identify key diagnostic lines.

For a quantitative analysis Ge and Bi were selected due their importance and region their lines are within. We also selected two neutron-capture Hf and U due their relevance in evaluation nucleosynthesis process to summarise some of the key points for our selected elements.

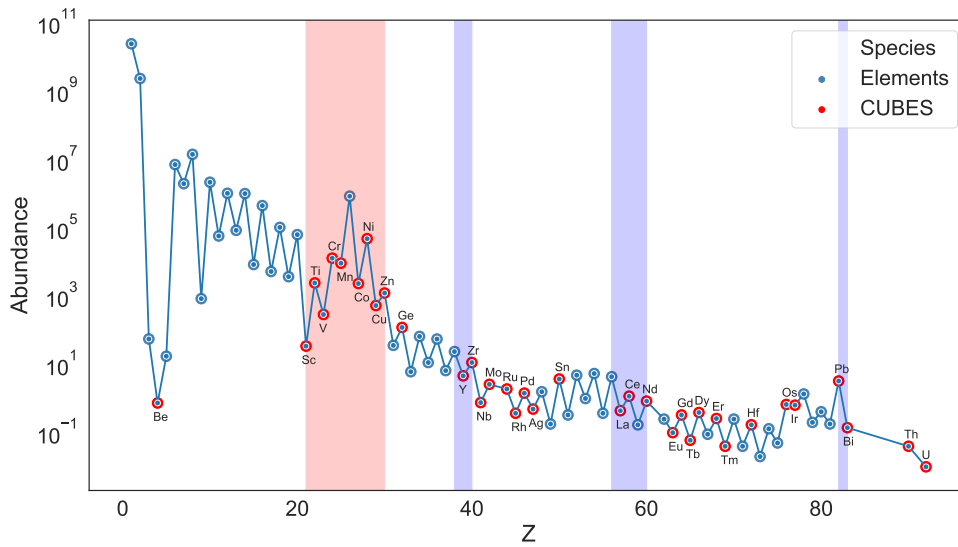


Figure 8.1: Abundances of elements in the Solar System vs. atomic number ( $Z$ ) normalised by the abundance of  $^{28}\text{Si}$  to  $10^6$  (Lodders, 2003). Iron-peak elements and the three peaks of the s-process are highlighted by the pink and blue panels, respectively. Elements with near-UV (3020-4000Å) spectral lines and observable with CUBES (at  $R=20000$ ) are indicated in red.

### 8.1.2.1 Beryllium

Although one of the lightest, simplest elements, there remain profound questions regarding the production of Beryllium in the early Universe. For instance, the recent upper limit for the Be abundance in an extremely metal-poor star ( $[\text{Fe}/\text{H}]=-3.84$ ) from Spite et al. (2019) is consistent with no primordial production, but larger samples of very metal-poor stars are required to constrain its formation channels. Moreover, Be is a potentially powerful tracer of Galactic and stellar physics in a range of different contexts, including stellar evolution, the formation of globular clusters, and the star-formation rate and chemical evolution of the Galaxy (Smiljanic 2014).

The only Be lines available from the ground for abundance estimates are two BeII resonance lines at 3130.42, 3131.06Å, which require good S/N ( $\gtrsim 50$ ) and sufficient resolution to clearly discern them from nearby, relatively strong V II ( $\lambda 3130.3$ ) and TiII ( $\lambda 3130.8$ )

absorption. There are only  $\sim 200$  stars with estimated Be abundances (from Keck-HIRES and VLT-UVES), which span near-solar metallicities down to  $[\text{Fe}/\text{H}] < -3$  (Boesgaard et al. 1999, 2011; Primas et al. 2000a,b; Smiljanic et al. 2009). The limiting magnitude of current observations is  $V \sim 12$  mag; observations down to at least three magnitudes deeper with CUBES will provide the large homogeneous samples required, particularly at the metal-poor end given discoveries from ongoing wide-field, multi-band photometric surveys (e.g. Pristine, Starkenburg et al. 2017; SkyMapper, Da Costa et al. 2019; Wolf et al. 2018).

### 8.1.2.2 Iron-peak elements

The iron-peak group is divided in two: the lower group ( $21 \leq Z \leq 26$ ), which is mainly produced by explosive oxygen and silicon burning (Nomoto, Kobayashi & Tominaga, 2013) and the upper group ( $27 \leq Z \leq 32$ ) which are synthesized in two processes:  $\alpha$ -rich freeze-out and the weak s-process (Woosley, Heger & Weaver, 2002; LC03); see also the review by Barbuy et al. (2018) and recent results for Sc, V, Mn, Cu, and Zn in globular clusters in the Galactic bulge (Ernandes et al. 2018). The near UV is less critical for these elements, but can still provide useful information for species such as ZnI.

Ge in special is often considered as either the heaviest of the iron-peak elements, or as the lightest of the trans-iron, neutron-capture elements (e.g. Peterson et al. 2020). Critically, in the context of the CUBES design requirements, the only diagnostic line available to us is the Ge I 3039.07 Å line, which is close to the atmospheric cut-off.

### 8.1.2.3 Heavy elements

As previously mentioned, heavy elements (i.e.  $Z > 30$ ) are produced by two major mechanisms, the r-process and s-process. The s-process is typically associated with stars on the Asymptotic Giant Branch (AGB, e.g. Busso, Gallino & Wasserburg, 1999) and includes the elements highlighted by the blue panels in Fig. 8.1. The s-process also occurs in massive stars during their He-burning phase. They mainly produce first-peak s-process elements (Sr, Y and Zr), and have an impact at low metallicity thanks to rapid rotation (Frischknecht et al. 2012, Limongi & Chieffi 2018), although  $^{96}\text{Mo}$  and  $^{204}\text{Pb}$  are only identified as such due to a stable isobar of charge, at  $Z-2$ , blocking the r-process; Sneden, Cowan & Gallino, 2008.

The formation channels for the r-process are particularly topical given the detection of the GW170817 kilonova from a binary neutron-star merger (Pian et al. 2017; Smartt et al. 2017; Watson et al. 2019). The r-process is thought to occur both during the merging and in the milliseconds afterwards (e.g. Bovard et al. 2017), and is thought to play an important role in the chemical evolution of the Galaxy (Matteucci et al. 2014; Cescutti et al. 2015). Other predicted sites of r-process nucleosynthesis include magnetohydrodynamically-driven jets from core-collapse SNe, resulting from rapidly-rotating massive stars with a strong magnetic field (Winteler et al. 2012; Nishimura, Takiwaki & Thielemann, 2015) and accretion discs in the supernova-triggering collapse of rapidly-rotating massive stars (or collapsars, Siegel et al. 2019).

Some metal-poor stars display enhanced actinide abundances compared to the expected r-process distribution (‘actinide-boost’ stars). This is usually traced via the Th/Eu ratio, but Th/Hf is also responsive to the initial conditions, in particular the electron fraction (78). There are two Hf II lines (3399.79, 3719.28 Å) that are well within the CUBES range, so we investigated their detectability.

The only Bi line available is at 3024.64 Å, even closer to the atmospheric cut-off than the Ge line, making it incredibly difficult to detect with a ground-based facility. Moreover, it is just shortwards of the region covered by the bluest standard setting of UVES, and in the case of CS 31082-001 the Bi abundance was determined from *HST* observations (Barbuy et al. 2011). U I 3859.57 Å is a strongly blended line that requires high spectral resolution and sensitivity to be detected, and has only been detected in six stars so far (Holmbeck et al. 2018). Bi and U abundances combined is of fundamental importance to understand the nucleosynthesis of very heavy elements, created by the same mechanism in an r-process event. These elements can therefore provide useful constraints on the production rates of r-process elements. Moreover, Pb and Bi are direct decay products of U and Th. For this reason, the U/Bi and U/Th ratios are frequently used as cosmochronometers (115; 16).

#### 8.1.2.4 CNO abundances

Abundances of CNO bring a wealth of information on stellar evolution and the chemical evolution of the Galaxy. In contrast to the atomic transitions of the elements discussed above, CNO features in the near UV are dominated by a series of molecular bands (see Fig. 8.2), which include the A-X OH transitions at the shortest wavelengths can be used

to estimate oxygen abundances.

Many potential targets in this context will be drawn from the so-called Carbon-enhanced metal-poor (CEMP) stars, which have  $[C/Fe] > +1.0$  (see Beers & Christlieb, 2005). Although rare, they demonstrate a diverse range of abundances of neutron-capture elements, commonly grouped as: ‘CEMP-no’ (no over-abundance of r-process elements), ‘CEMP-r’ and ‘CEMP-s’ (stars with over-abundances of r- and s-processed elements, respectively) and ‘CEMP-r/s’ (with apparent contributions from both processes enriching their photospheres).

A range of scenarios have been explored to investigate these patterns, including rotational mixing in rapidly rotating, low-metallicity stars (e.g. Chiappini, 2013; Choplin et al. 2016) and supernova models which include both mixing and fallback of material to yield the observed abundance ratios (e.g. Umeda & Nomoto, 2002, 2005; Tominaga, Iwamoto & Nomoto, 2014). In short, the CEMP stars are perfect probes to investigate nucleosynthesis from the first stars (including production of neutron-capture elements) as well as mass transfer in binary systems (e.g. Abate et al. 2015). However, comprehensive near-UV spectroscopy of CEMP stars to date has been limited by the sensitivity of current facilities to a few relatively bright targets (e.g. Placco et al. 2015; T. Hansen et al. 2015; Hansen et al. 2019).

### 8.1.3 Spectral Analysis

#### 8.1.3.1 Simulated spectra

To investigate the feasibility of abundance estimates for different elements as a function of spectral resolving power, we created small grids of synthetic spectra with the PFANT code, using model atmospheres interpolated from the grid of 1D, hydrostatic, LTE MARCS models from Gustafsson et al. (2008). Atomic data for the calculations were taken from the VALD database (Ryabchikova et al. 2015). We calculated two sets of spectra that will be illustrative of CUBES observations, with effective temperatures ( $T_{\text{eff}}$ ) and surface gravities ( $\log g$ ) appropriate for a G-type dwarf and a K-type giant, with two metallicities (as traced by the iron abundance,  $[Fe/H]$ ), as summarised in Table 8.1. A microturbulence ( $v_{\text{turb}}$ ) of  $2.0 \text{ km s}^{-1}$  was adopted in all calculations.

Relative to the solar-scaled abundances (defined by  $[Fe/H]$ ), the abundances for a broad

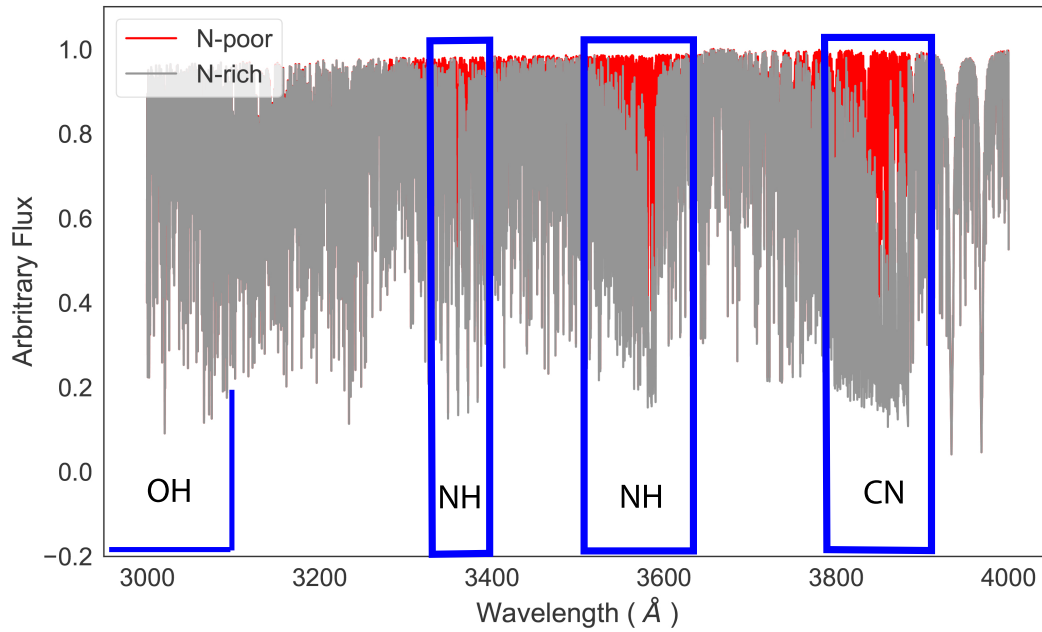


Figure 8.2: *Red*: Synthetic spectrum of a metal-poor star generated using the TURBOSPECTRUM radiative transfer code (Plez, 2012), adopting physical parameters as for CS31082-001 (Cayrel et al. 2001; Hill et al. 2002) including  $[\text{Fe}/\text{H}] = -2.9$ . *Grey*: Synthetic spectrum of the same star, but now N-rich ( $\Delta[\text{N}/\text{H}] = +2.0\text{dex}$ ).

Table 8.1 - Summary of models used to investigate the diagnostic lines.

Parameter	Dwarf	Giant
$T_{\text{eff}}$ [K]	5500	4500
$\log g$ [dex]	4.0	2.0
$v_{\text{turb}}$ [ $\text{kms}^{-1}$ ]	2.0	
$[\text{Fe}/\text{H}]$	-3.0, -1.0	
$R$	20000, 40000	

range of elements with near-UV absorption lines were varied to investigate the feasibility of observations (and responsiveness of the lines to abundance changes). We calculated models for both the dwarf and giant templates, at both metallicities and spectral resolving powers, varying the abundances of 39 elements<sup>1</sup> simultaneously by  $-0.5$ ,  $0.0$ ,  $+0.5$ , and  $+1.0\text{dex}$ . The full list of elements and absorption lines considered are detailed in Table C.1 in the Appendix.

The models were convoluted by a Gaussian with a full-width half maximum matched to that of the resolution at  $3120\text{\AA}$  ( $\Delta\lambda = 0.156\text{\AA}$  at  $R = 20000$ ,  $\Delta\lambda = 0.078\text{\AA}$  at  $R = 40000$ ) and then binned to mimic the sampling by the detector, assuming 2.6 pixels per resolution

<sup>1</sup> Be, Sc, Ti, V, Cr, Mn, Co, Ni, Cu, Zn, Ge, Y, Zr, Nb, Mo, Ru, Rh, Pd, Ag, Sn, Ba, La, Nd, Sm, Eu, Gd, Tb, Dy, Ho, Er, Tm, Yb, Hf, Os, Ir, Pb, Bi, Th, and U.

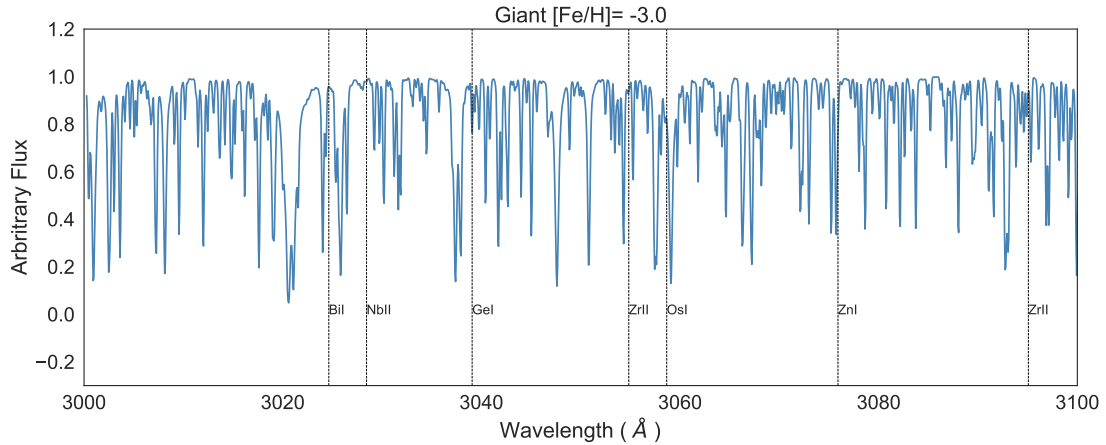


Figure 8.3: Example section of metal-poor ( $[\text{Fe}/\text{H}]=-3.0$ ) giant spectrum at  $R=20000$ , prior to introduction of noise.

element. To mimic real observations we introduced random noise in each of our models, to give simulated spectra with signal-to-noise (S/N) ratios of 50, 100, and 200 (per pixel). To illustrate the spectral richness of the near UV at the shortest wavelengths, an example section of one of the model spectra at  $R=20000$  (prior to adding noise) is shown in Fig. 8.3. Examples of specific lines (GeI, CoI, NiI, YII) in the simulated spectra of the giant star, varying  $R$  at fixed S/N=100, are shown in Fig. 8.4.

#### 8.1.4 Quantitative analysis

To investigate the potential performance of CUBES for studies of heavy elements in metal-poor stars we first synthesized a model spectrum for CS 31082-001 using the `TURBOSPECTRUM` code (4; 205) and adopting published physical parameters of  $T_{\text{eff}} = 4825$  K,  $\log g = 1.5$  and  $[\text{Fe}/\text{H}] = -2.9$  (from Hill et al. 2002). We smoothed and rebinned the model spectrum to match the lowest resolution and sampling of the CUBES design, i.e.  $R \sim 22,000$  and a full-width half maximum (FWHM) of  $\sim 0.14$  Å (sampled by 2.3 pixels). Using this model instead of an observed spectrum in our tests gave us full control of the noise, stellar parameters, and chemical abundances in our tests.

To mimic a CUBES observation we used this template as our input to the CUBES end-to-end (E2E) simulator that is provided in a Jupyter-notebook (93). The E2E simulator uses a model point-spread function (PSF) to generate simulated science images. The PSF is then sliced into six narrower slices to deliver the required spectral resolving power. The sky spectrum, atmospheric extinction models, instrument throughput and detector cha-

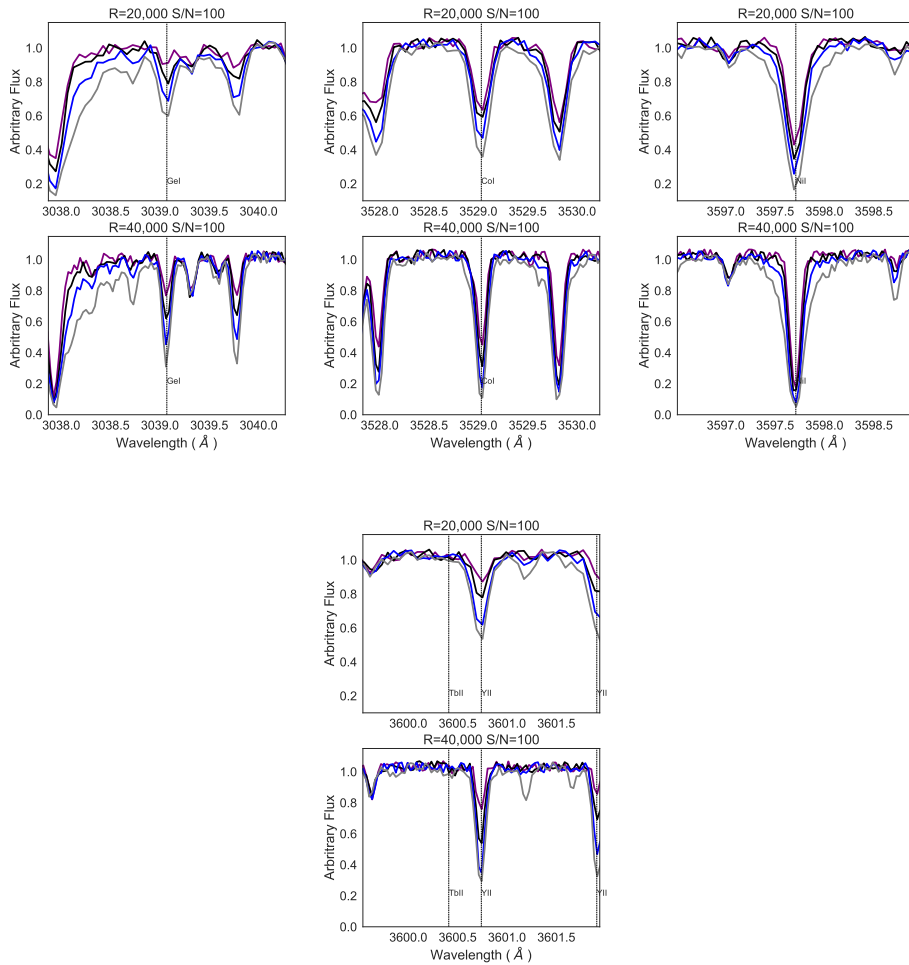


Figure 8.4: Simulated giant spectra ( $[\text{Fe}/\text{H}] = -3.0$ ) for example diagnostic lines, GeI  $\lambda 3039.07$ , CoI,  $\lambda 3529.03$ , NiI  $\lambda 3597.71$ , YII  $\lambda 3600.74$  at  $R = 20000$  and  $40000$  (with  $S/N=100$ ). Abundance variations of  $-0.5$ ,  $0.0$ ,  $+0.5$  and  $+1.0$  dex (in  $[\text{X}/\text{H}]$ ) for the elements in Table C.1 are shown in purple, black, blue and grey, respectively.

racteristics are then applied to the source spectra of each slice to simulate the appearance of the extracted and co-added data. In this regard, the end-to-end simulator helped us to reach the maximum verisimilitude of a CUBES observation.

We undertook detailed tests for the Ge I and Hf II lines. To evaluate the detectability of these lines we first synthesised models for the published abundances,  $\log_{\epsilon}(\text{Ge}) = +0.10$  (Siqueira-mello et al. 2013) and  $\log_{\epsilon}(\text{Hf}) = -0.59$  (Hill et al. 2002). We also synthesised models with larger abundances (+0.35 and +0.65 for Ge, and -0.30 and 0.00 for Hf) to investigate the sensitivity of the recovered abundances from the CUBES simulations to the input values. These models were used as inputs for the E2E simulator, adopting the default values of airmass = 1.16 and seeing = 0.87", for six different exposure times (ranging from 5 min to 4 hrs) and for target magnitudes of  $U_{\text{E2E}} = 16$  and 18 mag; for comparison, CS 31082-001 has  $U = 12.5$  mag. However, note that the models are continuum normalised (i.e. have a flat spectral slope), which has consequences on the interpretation of the results, as discussed in Section 8.1.6.3.

We then fit the simulated CUBES observations with the reference model spectrum (smoothed and rebinned to the same sampling as CUBES), while varying the abundance of the chosen element in the model. The adopted abundance for each simulated observation is the value that minimises the  $\chi^2$ -statistic when compared to the synthetic spectra. Initial models were fit varying the abundance of the selected element in steps of 0.1 dex. Once a first minimum in  $\chi^2$  was found, a finer grid with abundance variations of 0.01 dex was calculated to arrive at the final estimate.

### 8.1.5 Abundance estimates

Differential abundances,  $\Delta A(X)$ , between the input values and those estimated from the simulated observations with  $U_{\text{E2E}} = 16$  mag. for Ge and Hf are shown in Fig. 8.7. For observations of  $>1$  hr, the uncertainty on the Hf abundance is of order  $\pm 0.1$  dex, with an even smaller dispersion for the longest (4 hr) integration. Compared to the S/N estimates from Table 8.3, these results argue that with  $S/N \gtrsim 100$  we can recover estimates of Hf abundances to  $\pm 0.1$  dex.

Given the lower S/N at the shorter wavelengths, the dispersion on the Ge results is larger for shorter exposures, but with reasonable *differential* agreement (to  $\pm 0.1$  dex) for the longest simulated exposure (with  $S/N = 89$  from Table 8.3). However, we note the

systematic offset to larger estimated abundances for the Ge results (and, to a lesser extent, Hf too). This is not surprising for a weak line such as Ge I 3039 Å, and is probably a consequence of the challenges of continuum normalisation in these rich spectral regions, where the real continuum level can be underestimated due to the pseudo-continuum from the line blends (thus requiring an enhanced abundance value to reproduce a given line feature). Nonetheless, for the current purpose, our tests suggest that differential Ge abundances (to  $\pm 0.1$  dex) should be possible for a star similar to CS 31082-001 with  $U \sim 14.25$  mag. within a few hours.

### 8.1.6 Results

Each line in Table C.1 was visually inspected for all four relative abundances (i.e.  $-0.5$ ,  $0.0$ ,  $+0.5$ ,  $+1.0$ ) for both the dwarf and giant models at both resolving powers. For the purposes of the current study, we subjectively assessed the feasibility of obtaining an abundance estimate from each line on the basis of whether a ‘by-eye’ fit to the simulated spectrum would enable constraints on the abundance (either a direct estimate or upper/lower limits). In the appendix we show which lines are feasible/useful in Table 8.4, summarising the number of lines available for each ion at  $R=20000$ .

If the gains are sufficiently good in terms of sensitivity to work at  $R=20000$  (cf. 40000), one might sensibly ask if even lower resolution observations are feasible. We therefore also investigated simulated spectra with  $R=10000$  to assess the impact of another factor of two in resolution. As demonstrated by the spectra in Fig. 8.5, this results in significant loss of information. Many close lines become strongly blended (e.g. the CoI doublet in the right-hand panel of the figure), and no constraint is possible on Be (left-hand panel). Indeed, at this lower resolution approximately 80% of the lines in Table C.1 are lost as useful abundance diagnostics, with only the most isolated and strongest lines remaining available. We therefore did not pursue such a low resolution any further.

#### 8.1.6.1 Performance comparison

As indicated by the results in Table 8.4, the majority of the diagnostic lines are accessible at  $R = 20000$  (provided there is sufficient S/N). Aside from optimisation of the instrument design, what the above comparisons neglect is the inherent loss in sensitivity of working at higher dispersion, i.e. a fairer comparison for the simulations shown in Fig. 8.4

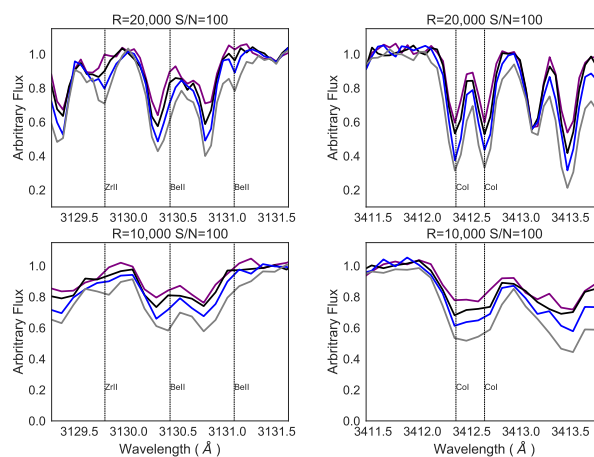


Figure 8.5: Illustrative comparison of BeII (upper panel) and CoI  $\lambda 3412$  (lower panel) diagnostic lines at  $R=10000$  and  $20000$  (at  $S/N=100$ , for the  $[\text{Fe}/\text{H}]=-3.0$  giant model). Abundance variations of  $-0.5$ ,  $0.0$ ,  $+0.5$  and  $+1.0$  dex (in  $[X/\text{H}]$ ) for the elements in Table C.1 are shown in purple, black, blue and grey, respectively.

would be to show the resulting spectra for the same integration time.

The design philosophy for CUBES is to maximise the end-to-end efficiency of the instrument. It is unlikely that a similar efficiency could be obtained at the present time for a design at the higher resolving power. In short,  $R=20000$  provides a combination of excellent sensitivity with sufficient resolution to undertake quantitative analysis of the large majority of the lines considered here.

The faintest stars observed with VLT-UVES and Keck-HIRES to date for quantitative analysis in the near UV have  $V \sim 12$  mag. For example, 2MASS J18082002–5104378 ( $V=11.93$ , Schlafman, Thompson & Casey, 2018) was observed with ten 1h UVES exposures by Spite et al. (2019), giving  $S/N \sim 70$  near the Be lines. It is clear that going to fainter magnitudes (and to obtain better  $S/N$ ) with UVES quickly starts to demand prohibitively long exposures/programmes of tens of hours per star. For comparison, using a developmental version of the CUBES Exposure Time Calculator (ETC)<sup>2</sup>, observations of a metal-poor dwarf with  $V=16$  mag should provide a  $S/N=100$  at  $3130\text{\AA}$  in approximately  $3 \times 1$ h exposures.

### 8.1.6.2 Expected uncertainties on measured equivalent widths

Given the resolution and pixel sampling of CUBES, we used the arguments from Cayrel et al. 1988 to estimate the limiting equivalent width ( $W$ ) that could be obtained from high

<sup>2</sup> <http://archives.ia2.inaf.it/cubes/#/etc>

Table 8.2 - Differential equivalent widths ( $\Delta EW$ ) for simulated CUBES observations of the Ge I 3039.07 Å and Hf II 3399.79, 3719.28 Å lines compared to the published values for CS 31082-001 (used here as the input model abundances).

$t_{\text{exp}}$ (min)	$ \Delta EW $ (m Å)		
	Ge I 3039 Å	Hf II 3400 Å	Hf II 3719 Å
30	2.57	7.22	6.33
60	3.35	5.46	1.67
120	3.16	1.67	4.38
240	1.93	1.54	2.22

S/N ( $>200$ ) observations. Defining the spectral line as a Gaussian profile and assuming the spectrum is correctly calibrated (corrected for bias and dark levels, flat-field correction), then:

$$W = \int_{-\infty}^{+\infty} r(x) dx = \sum_{i=i_1}^{i_2} r_i \delta x = \delta x \sum_{i=i_1}^{i_2} r_i, \quad (8.1)$$

where  $r_i$  is the flux array and  $\delta x$  the pixel size. The uncertainty in the measured widths is then (from Cayrel et al. 2004):

$$\sigma_w = \frac{1.5}{S/N} \sqrt{FWHM \times \delta x}. \quad (8.2)$$

Considering the CUBES FWHM of 0.14 Å and  $\delta x = 0.06$  Å/pixel, a S/N of 200 would yield  $\sigma_w = 0.7$  mÅ. However, the above formula neglects the uncertainty on the continuum placement (which can be particularly challenging at these short wavelengths), and the expected uncertainty is usually a factor of two or three larger (see Cayrel et al. 2004), i.e. an uncertainty of  $\gtrsim 1.5$  mÅ for CUBES (assuming excellent S/N).

Example models of the Ge I 3039 Å and Hf II 3400 Å lines and their measured equivalent widths are shown in the left-hand panels of Fig. 8.6. Alongside them are similar plots for simulated observations of 30 and 240 min, with the difference between the measured (‘observed’) width and that from the model indicated. Note that the uncertainties for the longest exposures are already approaching the expected limit. Absolute values of the differential widths for all three lines are given in Table 8.2.

### 8.1.6.3 Results: Ge & Hf

We first estimated the continuum S/N (per pixel) for the simulated spectra in regions close to the Ge I 3039 Å and Hf II 3719 Å lines for insight into the exposure times required

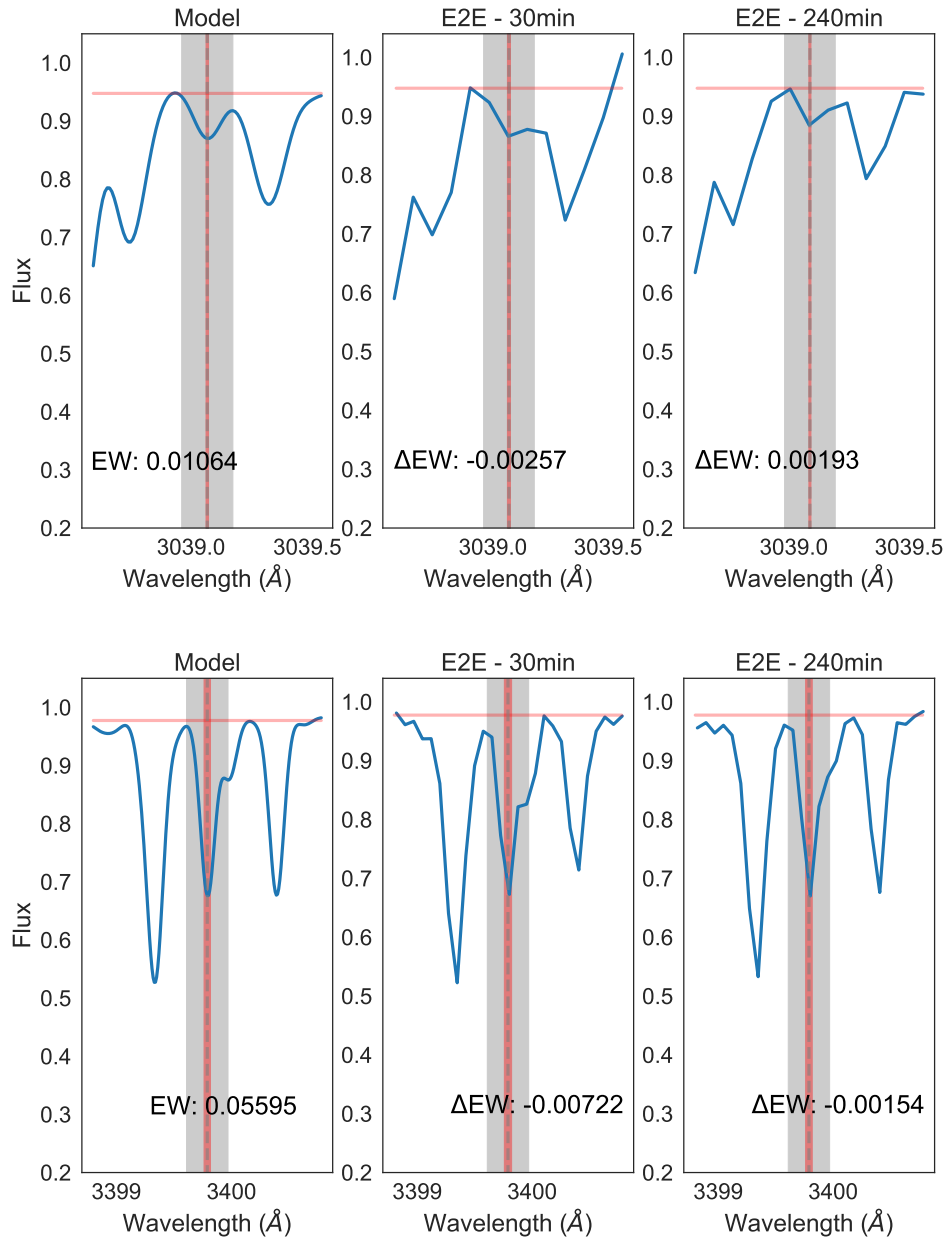


Figure 8.6: Equivalent widths of Ge I 3039 Å (upper panels) and Hf II 3400 Å (lower panels) for an input stellar model in the left-hand panels. The centre and right-hand panels show the output spectra from the end-to-end (E2E) simulator for  $U = 16$  mag. for 30 and 240 min, respectively. Differences between the measured width from the simulations compared to the models are given by  $\Delta EW$ . The regions considered for the estimates are shown in grey.

to recover robust abundances. These estimates (for the initial abundance models, i.e.  $A(\text{Ge}) = +0.10$  and  $A(\text{Hf}) = -0.59$ ) are summarised in Table 8.3.

Caution is required in interpreting the S/N estimates from the E2E simulations at the bluewards end of the CUBES range as we have (necessarily) used continuum-normalised model spectra which have been scaled to the desired  $U$ -band magnitudes. The Johnson  $U$ -band filter has an effective central wavelength of 366 nm, with a width of 65 nm (e.g. Bessell et al. 2005). Thus, when our model spectra were scaled to  $U = 16$  and 18 mag., the resulting model flux will be a good enough approximation to the real astrophysical flux for the Hf II 3719 Å line as it is close to the centre of the photometric band (i.e. the estimated S/N value is realistic for the true flux distribution of a star such as CS 31082-001).

However, this is not the case for the Ge I 3039 Å line, which is located in the bluewards tail of the  $U$ -band filter curve. Given its low effective temperature ( $T_{\text{eff}} = 4825$  K), the flux distribution of CS 31082-001 declines rapidly towards shorter wavelengths across the  $U$ -band filter. This means that use of continuum-normalised models as inputs to the E2E simulator give an unrealistically large estimate of the flux at short wavelengths when they are scaled to the desired  $U$ -band magnitude. This does not impact on the ability to recover the targeted abundance as a function of the S/N from the E2E simulations, but means that the realistic observed magnitude for which this level of performance can be achieved needs to be quantified. In summary, the effective  $U$ -band magnitude ( $U_{\text{eff}}$ ) for the appropriate flux level for a star similar to CS 31082-001 at 3039 Å will be brighter than the values used in the E2E simulations.

To estimate of the scale of this effect, we used the CUBES Exposure Time Calculator (ETC) (93), adopting the same conditions as the E2E simulations (airmass = 1.16, seeing = 0.87") and using one of the standard template spectra ( $T_{\text{eff}} = 4500$  K,  $\log(g) = 1.5$ ,  $[M/H] = -3.5$ ), that is a reasonable match to the parameters of CS 31082-001. The S/N predicted by the ETC matches that from the E2E by adopting  $\Delta U \sim -1.75$  mag. That is, using the  $T_{\text{eff}} = 4500$  K template, the S/N predicted by the ETC for  $U_{\text{ETC}} = 14.25$  matches the E2E result for  $U_{\text{E2E}} = 16$  (and similarly for  $U_{\text{ETC}} = 16.25$  for  $U_{\text{E2E}} = 18$ ). We emphasise that this is due to the difference in the spectral slope of the models at the short wavelengths, and that the E2E and ETC results at 3730 Å are in good agreement.

Results for the simulations with  $U_{\text{E2E}} = 18$  mag. are shown in Fig. 8.8. Mirroring the results in terms of the S/N estimates for  $U_{\text{E2E}} = 16$  mag., the Hf abundance can be recovered

Table 8.3 - Predicted continuum signal-to-noise (S/N) per pixel from the end-to-end (E2E) CUBES simulations near the Ge I 3039 Å line and the redder Hf II line (3719 Å). The adopted magnitudes for the E2E simulations were  $U_{\text{E2E}} = 16$  and 18 mag. For simulations of CS 31082-001 these values are a good approximation to the real flux at 3730 Å, but given the use of continuum-normalised model spectra, the effective observed magnitudes ( $U_{\text{eff}}$ ) for the Ge I 3039 Å line are  $\sim 1.75$  mag brighter (see Section 8.1.6.3 for discussion).

$t_{\text{exp}}$ (min)	S/N $_{\lambda 3050}$ ( $U_{\text{eff}} \sim 14.25$ )	S/N $_{\lambda 3730}$ ( $U_{\text{E2E}} = 16$ )	S/N $_{\lambda 3050}$ ( $U_{\text{eff}} \sim 16.25$ )	S/N $_{\lambda 3730}$ ( $U_{\text{E2E}} = 18$ )
5	7	24	1	7
10	12	34	3	11
30	25	65	6	23
60	36	92	10	37
120	53	148	15	47
240	89	190	20	70

to better than  $\pm 0.1$  dex for the 4 hr exposures (with  $S/N = 70$ ). The Ge abundance is more challenging for such a faint target as we are limited to  $S/N = 20$  even in a 4 hr observation. Nonetheless, even at such modest  $S/N$  (see results for 30 min in Fig. 8.7) we can potentially constrain the Ge abundance to  $\sim 0.2$ - $0.3$  dex. Achieving even this level of precision for such faint stars would be remarkable compared to our current capabilities.

Example fits for the  $U_{\text{E2E}} = 16$  mag. simulations are shown in Figs. 8.9, 8.10 and 8.11, in which the simulated CUBES data (in black) and model spectra (in red, prior to binning for display purposes) have been continuum normalised.

#### 8.1.6.4 Results: Bi & U

We also used the E2E software to simulate CUBES observations of the Bi I 3024.64 Å and U II 3859.57 Å lines, in which we varied the model abundances around the published values of  $A(\text{Bi}) = -0.4$  (Barbuy et al. 2011) and  $A(\text{U}) = -1.92$  (Hill et al. 2002). Simulated spectra from 4 hr exposures for  $U_{\text{E2E}} = 16$  mag. for the Bi and U regions are shown in Figs. 8.12 and 8.13, respectively. Given the weakness of these lines combined with the impact of nearby blends and difficulty of continuum normalisation, precise abundance determinations are particularly challenging for these elements. To emphasise this in the case of the weak U II line, the upper panel of Fig. 8.13 shows the input models and identifies the stronger, nearby lines that influence the final appearance of the U II line in the CUBES simulations<sup>3</sup>.

<sup>3</sup> Nd II 3859.413 Å, V I 3859.337 Å, Sc II 3859.358 Å, and Fe I 3859.213, 3859.911 Å as well as a contribution from a CN feature.

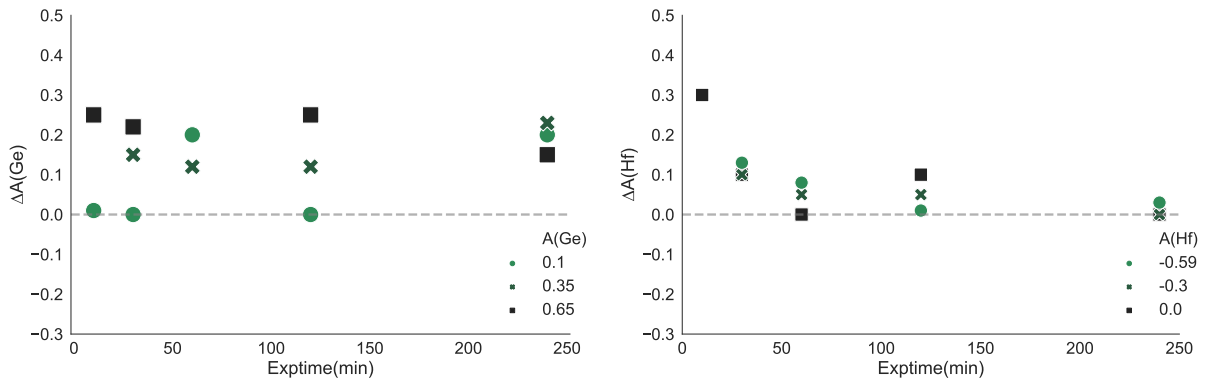


Figure 8.7: Abundance uncertainties ( $\Delta A$ ) compared to the input values for the  $U_{E2E} = 16$  mag. CS31082-001 simulations. *Left:* Ge I 3039 Å, *Right:* Hf II 3400.

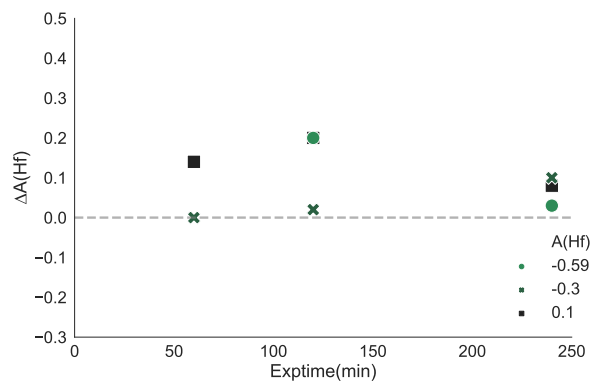


Figure 8.8: Abundance uncertainties ( $\Delta A$ ) compared to the input values for the  $U_{E2E} = 18$  mag. CS31082-001 simulations for Hf II 3400.

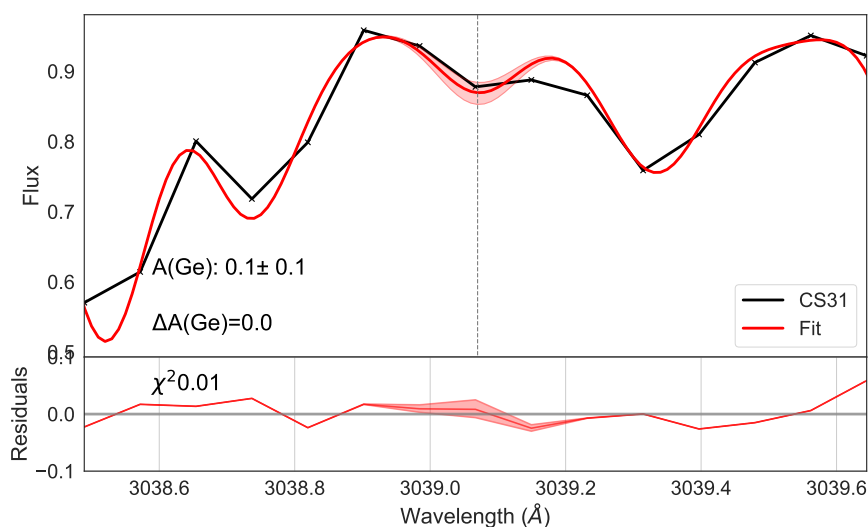


Figure 8.9: Simulated 2 hr CUBES spectrum of CS 31082-001 (with  $U_{E2E} \sim 16$  mag.) for the Ge I 3039 Å region. The reference model ( $A(\text{Ge}) = +0.10$ ) is plotted in black, with the best fit model ( $A(\text{Ge}) = +0.1$ ) in red. The red shaded area indicates  $\pm 0.1$  dex in Ge abundance.

Nonetheless, given good S/N ( $>100$ ), CUBES observations of both the Bi and U lines should be able to place initial constraints on their abundances, even if just upper limits in the case the lower abundances considered in the examples here.

### 8.1.7 Summary of CUBES analysis

Near UV spectroscopy enables the study of a diverse range of elements for stellar astrophysics and of the chemical evolution of the Galaxy. Many of these are uniquely observable in the near UV, such as Be, Bi, and Os. Our study of the elements accessible with observations at  $R = 20\,000$  compared to  $R = 40\,000$  reveals that nearly all species are feasible. In most instances the more dominant factor is S/N rather than resolving power, but the accuracy owing to blends may be reduced for some lines and requires more detailed simulations (e.g. C. Hansen et al. 2015). Reducing the resolution by a factor of two (to  $R = 10\,000$ ) would render most of the diagnostic lines unusable for abundance analysis.

Informed by these results, the conceptual design of CUBES adopted  $R \sim 20\,000$  as its baseline. Quantifying the tolerances on this specification, including its variation with wavelength and performance for the light-element molecular features, is now underway as part of the Phase A study. From initial performance estimates, quantitative spectroscopy in the near-UV will be possible to at least three magnitudes deeper than current programmes

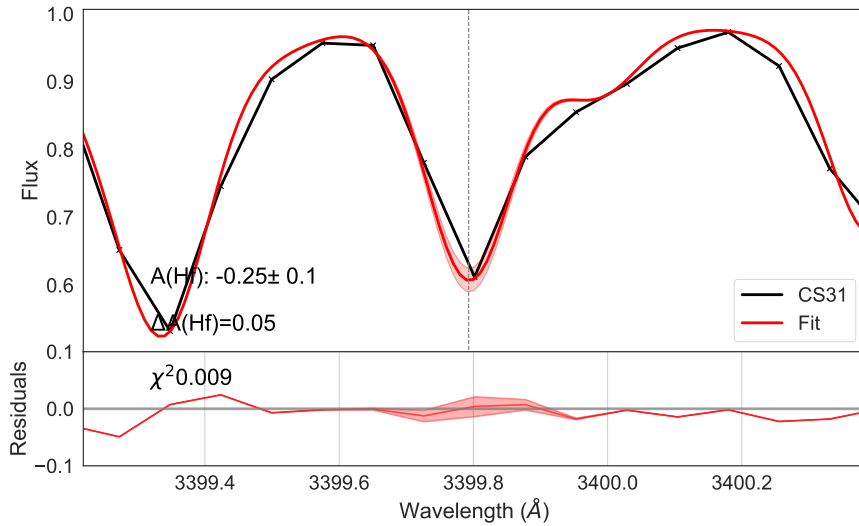


Figure 8.10: Simulated 2 hr CUBES spectrum of CS 31082-001 (with  $U_{\text{E2E}} = 16$  mag.) for the Hf II 3400 Å region. The reference model ( $A(\text{Hf}) = -0.30$ ) is plotted in black, with the best fit model ( $A(\text{Hf}) = -0.25$ ) in red. The red shaded area indicates  $\pm 0.1$  dex in Hf abundance.

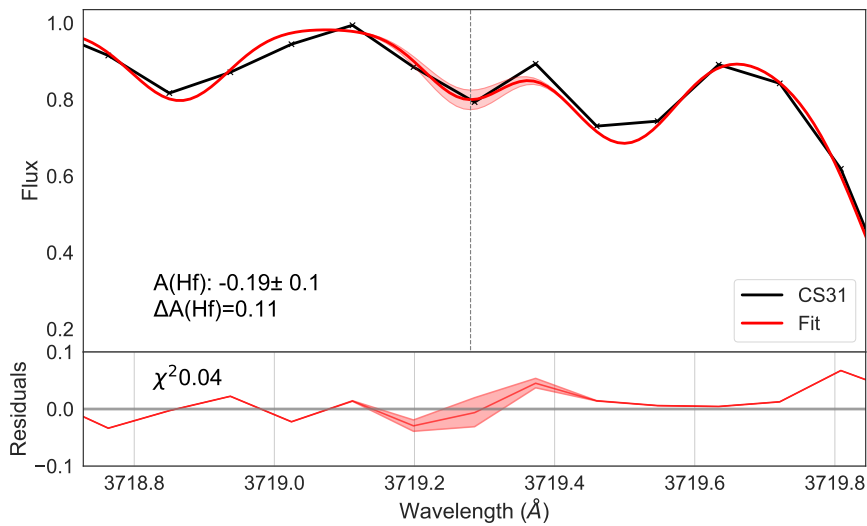


Figure 8.11: Simulated 2 hr CUBES spectrum of CS 31082-001 (with  $U_{\text{E2E}} = 16$  mag.) for the Hf II 3719 Å region. The reference model ( $A(\text{Hf}) = -0.30$ ) is plotted in black, with the best fit model ( $A(\text{Hf}) = -0.19$ ) in red. The red shaded area indicates  $\pm 0.1$  dex in Hf abundance.

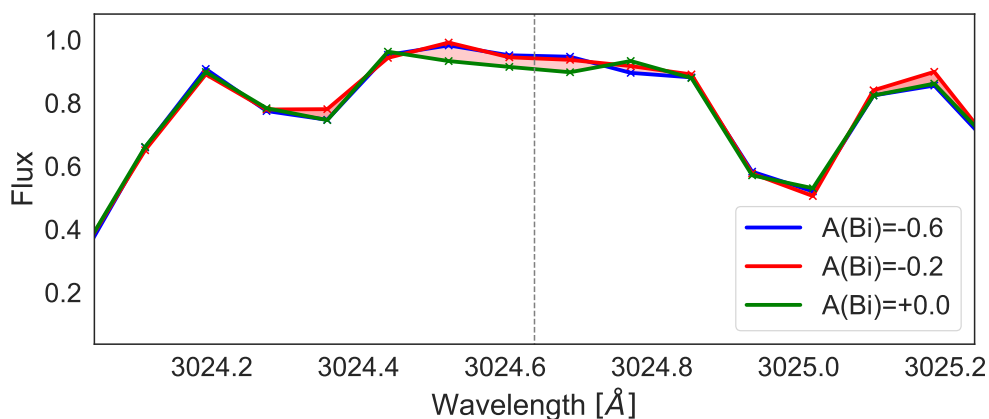


Figure 8.12: Simulated 4 hr CUBES observation of the Bi I 3024.64 Å line for  $U_{E2E} = 16$  mag. and models with  $A(\text{Bi}) = -0.6, -0.2,$  and  $0.0$ . The pink shaded regions are to highlight the differences between the models (where both abundance and S/N contribute).

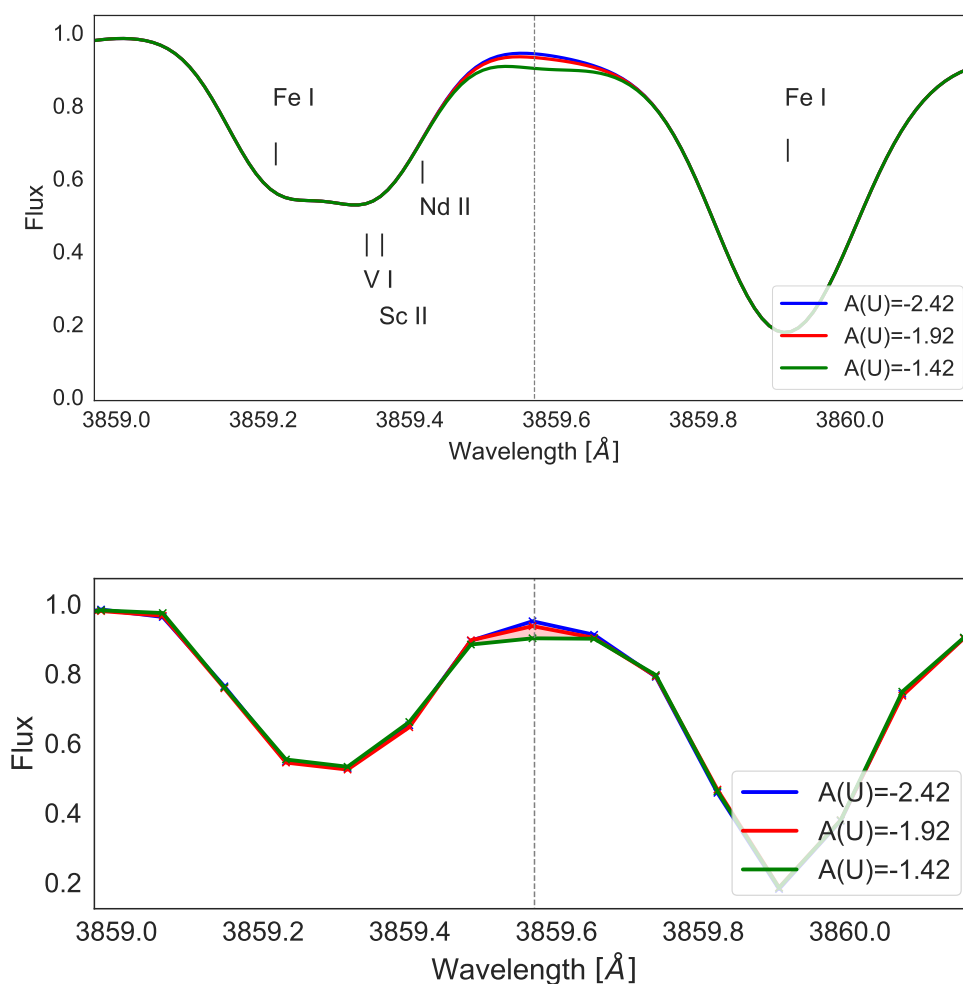


Figure 8.13: *Upper panel:* Model spectra in the region of U II 3859.57 Å for  $U_{E2E} = 16$  mag. and with  $A(\text{U})$  as indicated in the legend. The spectra have been convolved to  $R = 22,000$  but are left oversampled to better highlight the other contributing lines. *Lower panel:* Simulated 4 hr CUBES observation of the same region. As in Fig. 8.12, the shaded regions highlight the differences between the models.

(in the same exposure time). This will enable exciting new insights in our understanding of nucleosynthesis and the old stellar populations of the Milky Way.

We also presented a quantitative analysis of simulated CUBES observations of faint ( $U_{E2E} = 16$  and  $18$  mag.) metal-poor stars, using the well-studied CS 31082-001 star as a template. We selected two elements (Ge and Hf) with relatively isolated lines to investigate the performance of CUBES near the blueward limit of the instrument (Ge) and at longer wavelengths (Hf) in detailed abundance studies of metal-poor stars. We also investigated the weak Bi I and U II lines, which are two of the most challenging lines for abundance estimates with current facilities. Our key findings are:

- Ge: From a 4 hr integration for  $U_{E2E} = 16$  mag. we recover sufficient S/N to obtain differential Ge abundances to  $\sim \pm 0.1$  dex. Given the discussion in Section 8.1.6.3, this translates to an effective  $U$ -band magnitude for a star similar to CS 31082-001 of  $U \sim 14.25$  mag.
- Hf: Given the better transmission of the atmosphere at longer wavelengths, we can recover Hf abundances (from the Hf II 3400, 3719 Å lines) to  $\sim 0.1$  dex in just 1 hr for  $U = 16$  mag., and in 4 hr for  $U = 18$  mag.
- Bi and U: Our simulated 4 hr observations indicate we should be able to place initial constraints on the abundances (even if just upper limits) of these more challenging, weak lines.

A critical factor in arriving at accurate (rather than precise) abundances in the CUBES range is the ability to correctly estimate the continuum level when calibrating and analysing the spectra (as evidenced by the systematic offset in the Ge results in Fig. 8.7, and even more critical for the weak Bi and U lines). As such, quantitative abundance studies of metal-poor stars with CUBES will require the physical properties of future targets (temperatures, gravities, metallicity, microturbulence etc) to be well constrained from other observations, which could include simultaneous observations with the fibrelink to UVES that was included in the Phase A design (289).

In summary, by combining unprecedented near-UV sensitivity with sufficient spectral resolution for quantitative stellar studies, table 8.4 based in the list C.1, CUBES will provide an exciting and unique capability for studies of chemical abundances and stellar

nucleosynthesis. The simulations presented here for a faint analogue of CS 31082-001 have demonstrated the high-precision, differential abundances will be possible for both Ge and Hf for targets that are two-to-three magnitudes fainter than possible with current facilities. In terms of the  $U$ -band magnitude achievable, the predicted performance at  $<350$  nm is strongly dependent on the spectral energy distribution of the target. The temperature of CS 31082-001 is quite cool compared to those of the stars that will comprise the majority of future CUBES targets, so even greater gains can be anticipated for elements such as Ge and Bi in studies of hotter stars.

## 8.2 MOSAIC

MOSAIC is a multi-object spectrograph in preparation for the Extremely Large Telescope. It is going to start Phase B (PDR) in 2022. MOSAIC makes it possible to observe beyond the current limits of observations. Accessing the low-metallicity tail in the metallicity distribution function (MDF) can give more reliable constraints in the formation models of the Galaxy. With studies combining chemical compositions and kinematics characterise the contributions of each population that formed the bulge. This new facility has the potential to enlighten the formation of the Galactic bulge which is still a controversial topic.

According to a new study that analysed bulge dwarfs stars using microlensing methods the bulge for this sample are more metal-rich than expected before (Bensby et al. 2017), but this has to be further studied with larger samples. Considering that MOSAIC will be able to access large samples of dwarfs in the Galactic bulge. This will bring a new debate to the conundrum that is the formation of the bulge.

Firstly to test the MOSAIC performance we use the COMputing Platform for Adaptive optics SystemS (COMPASS) code. The code requires a PSF library together with a spectral library. Combining the PSF, design parameter of ELT and MOSAIC, associated with the spectra from Starckenburg et al. 2017 we are able to reproduce an observation from that check the observation limits of MOSAIC.

Secondly we intend to test the abundance derivation capability of MOSAIC. To approach this problem we made use of the `Chem-I-Calc` code (249). Which estimates quantitatively the stellar parameters and abundances precision.

Table 8.4 - Number of our selected lines that are detectable for each ion in the CUBES wavelength range for both a G-type dwarf and a K-type giant with  $[\text{Fe}/\text{H}] = -3.0$  and  $[\text{Fe}/\text{H}] = -1.0$  with  $R \sim 20\,000$ . Those flagged with an asterisk are ions for which no lines are feasible for quantitative analysis in our simulated spectra.

Ions	$[\text{Fe}/\text{H}] = -3.0$		$[\text{Fe}/\text{H}] = -1.0$	
	Giant	Dwarf	Giant	Dwarf
Be II	2/2	2/2	2/2	2/2
Sc II	2/2	2/2	2/2	2/2
Ti I	1/1	1/1	1/1	1/1
Ti II	3/3	3/3	3/3	3/3
V II	1/1	1/1	1/1	1/1
Cr I	1/1	1/1	0/1	1/1
Mn II	4/6	5/6	4/6	4/6
Co I	6/6	6/6	6/6	6/6
Ni I	5/5	5/5	5/5	4/5
Cu I	2/2	2/2	0/2	2/2
Zn I	1/3	3/3	1/3	3/3
Ge I	1/1	1/1	1/1	1/1
Y II	3/6	4/6	4/6	4/6
Zr II	29/34	30/34	12/34	19/34
Nb II	3/3	1/3	2/3	2/3
Mo I	1/1	0/1	1/1	1/1
Ru I	3/5	0/5	3/5	3/5
Rh I	2/4	0/4	1/4	1/4
Pd I	3/3	0/3	2/3	2/3
Ag I	2/2	0/2	2/2	0/2
Sn I	1/1	0/1	0/1	0/1
Ba II*	0/1	0/1	0/1	0/1
La II	3/4	2/4	1/4	2/4
Ce II	1/1	1/1	1/1	1/1
Nd II	4/4	0/4	3/4	4/4
Sm II*	0/3	0/3	0/3	0/3
Eu II	1/3	1/3	1/3	2/3
Gd II	0/4	0/4	1/4	0/4
Tb II	2/2	0/2	1/2	2/2
Dy II	8/8	0/8	6/8	5/8
Ho II*	0/3	0/3	0/3	0/3
Er II	3/6	0/6	2/6	2/6
Tm II	0/3	0/3	0/3	0/3
Yb II*	0/1	0/1	0/1	0/1
Hf II	1/3	0/3	1/3	1/3
Os I	1/1	0/1	1/1	1/1
Ir I	2/2	0/2	1/2	2/2
Pb I	0/1	0/1	0/1	1/1
Bi I	0/1	0/1	1/1	1/1
Th II	0/6	0/6	1/6	1/6
U II	1/1	1/1	0/1	1/1

The simulations with COMPASS were made considering the High multiplex mode in the visible (HMM-VIS) and the High multiplex mode in the near-infrared (HMM-NIR), while the `Chem-I-Calc` simulations we only considered the HMM-VIS. The HMM-VIS mode can observe in the visible 200 targets simultaneously with medium ( $R \sim 5000$ ) and high resolution ( $R \sim 20,000$ ). The HMM-NIR similarly to the HMM-VIS can observe in medium and high spectral resolution. Particularly the HMM-NIR will simultaneously observe 80 targets with each fiber having a dedicated sky fiber to improve the sky subtraction in the H band. For this work we only considered the medium resolution modes.

### 8.2.1 COMPASS

The COMPASS code was designed to create simulations taking into account systematic convolution of the spectra by a PSF that is defined by a simple Gaussian with FWHM sampled by a number of pixels that is specified by the user. It also includes a Paranal sky model of airglow continuum, emission lines of upper atmosphere, molecular emission of lower atmosphere, and an updated higher resolution absorption curve. In order to assist in the projects, evaluating designs and trade-offs to achieve the proposed science cases.

### 8.2.2 Stellar spectral library

To create the simulations using COMPASS in the I band we selected metal-poor stars spectra from Pristine table 8.5 (Starkenburger et al. 2017) varying the I magnitude between 20 and 24 to verify the limits in magnitude in a MOSAIC observation for each synthetic spectra. fig 8.14 shows the red giant branch stellar models and fig 8.15 shows the main sequence stellar models. For the H band in order to evaluate how the signal-to-noise drops in function of magnitude we create the COMPASS simulations based in a flat spectrum, presented in fig 8.16.

### 8.2.3 Chemcalc

The `Chem-I-Calc` code from Sandford et al. 2020 derives the abundance and stellar parameters precision of a given instrument using a Fisher information matrix and the Cramér-Rao inequality to find the Cramér-Rao Lower Bound. This is a method to find the lower bound to the root-mean-square of an unknown, non-biased variable. The `Chem-I-Calc` use a full-spectral fitting method, adopting 1D LTE models from an internal

Table 8.5 - Pristini's spectral library models from Starkenburg et al. 2017.

Pristini models			
$T_{eff}$	$\log g$	[Fe/H]	$\alpha$
6000	4.00	-1.00	0.40
6000	4.00	-1.50	0.40
6000	4.00	-2.00	0.40
6000	4.00	-2.50	0.40
6000	4.00	-3.00	0.40
6000	4.00	-4.00	0.40
4500	1.00	-1.00	0.40
4500	1.00	-1.50	0.40
4500	1.00	-2.00	0.40
4500	1.00	-2.50	0.40
4500	1.00	-3.00	0.40
4500	1.00	-4.00	0.40

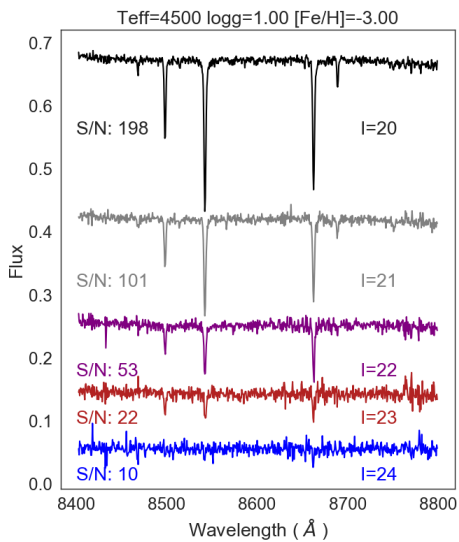


Figure 8.14: Simulated RGB spectra with different magnitudes in I band showing the impact in S/N in a MOSAIC observation.

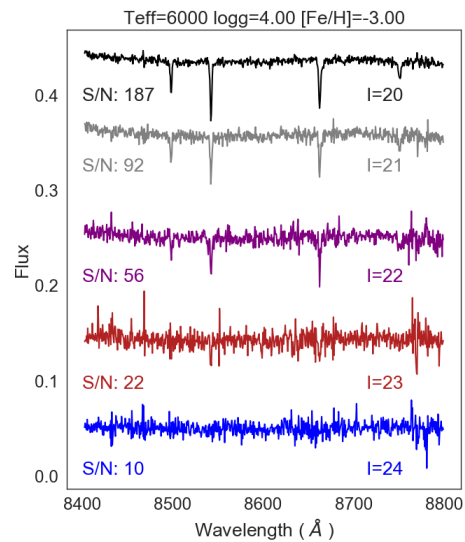


Figure 8.15: Simulated main-sequence turn-off spectra with different magnitudes in I band showing the impact in S/N in a MOSAIC observation.

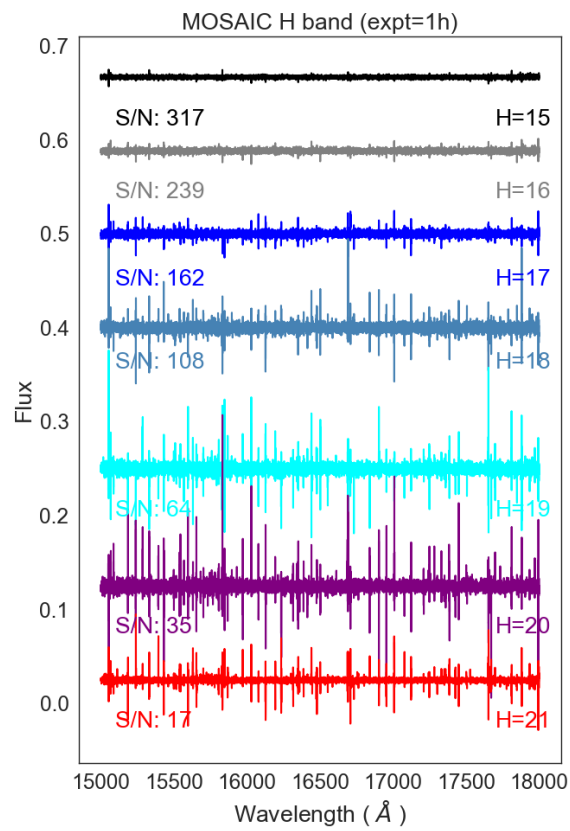


Figure 8.16: Simulated RGB spectra with different magnitudes in H band showing the impact in S/N in a MOSAIC observation.

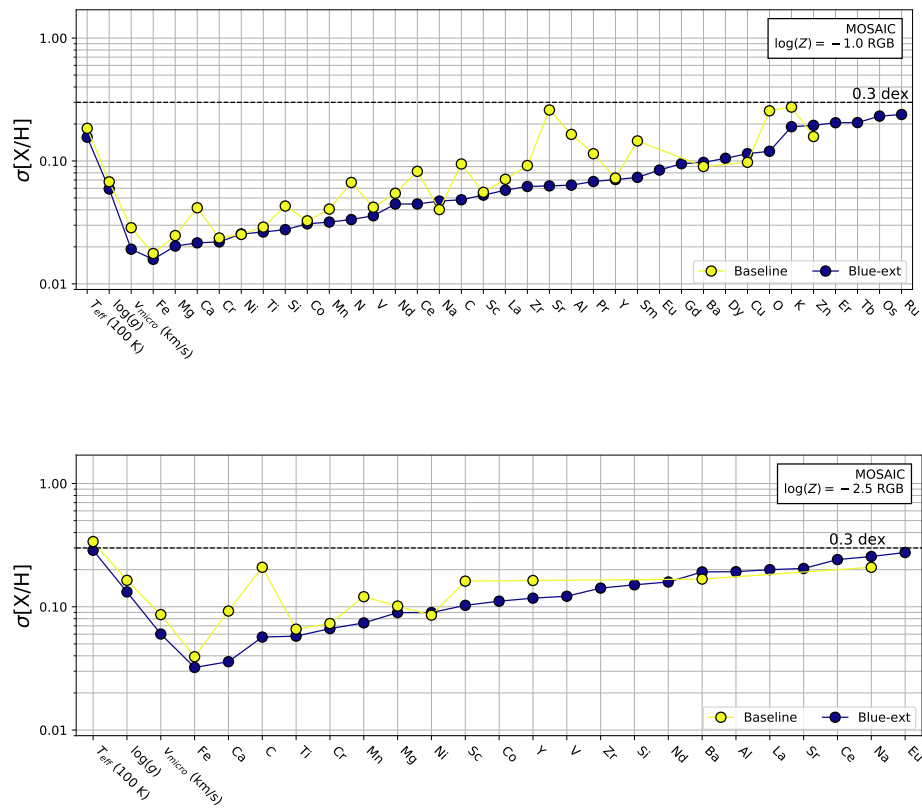


Figure 8.17: Cramér-Rao Lower Bound for the two considered designs for MOSAIC, Baseline in yellow and Blue-extension in blue showing the precision in the determination of the stellar parameters and elemental abundances.

library in the package. The code requires as input the spectral resolution ( $R$ ), the S/N ratio (wavelength dependent or not), and the wavelength coverage of the instrument.

In fig. 8.17 two possible designs of MOSAIC are considered. The baseline of MOSAIC (450 - 592nm; 587-770nm.  $R = 4500$  at  $S/N = 50$ ) plotted in yellow and the blue extension (390 - 499nm; 486 - 621nm; 608 - 778nm.  $R = 4500$ .  $S/N = 50$ ) in navy blue. The upper panel in fig. 8.17 is presented the a model of a  $[Fe/H] = -1.0$  star while the lower panel presents a  $[Fe/H] = -2.5$  star. In the fig. 8.17 the stellar parameters in the first three data points, where the  $T_{eff}$  is scaled in 100K units to be presented in the same scale as  $\log(g)$  and  $v_{micro}$ . Following the stellar parameters the elemental abundance precision are presented in  $[X/H]$ .

It is noticeable that the blue-extension has more consistency in the expected precision compared with the baseline. The blue-extension also has access to more elements than the baseline due the extra coverage in the blueward regions.

In fig. 8.18 the two designs are printed, where the first three columns are from the blue-extension and the 4th and 5th columns represents the precision for each element available for the baseline. The same information is shown in the last two column for the full wavelength coverage of both designs considering a constant S/N ratio of 50.

#### 8.2.4 Summary of MOSAIC analysis

MOSAIC associated with the E-ELT has the capability to access a larger sample of faint dwarfs metal-poor stars in our galaxy and the local group. As shown in Figs. 8.14 and 8.15, two simulated observations made using the COMPASS code. Figure 8.14 showing a RGB star and fig. 8.15 showing a main-sequence-turn-off star, both with magnitudes of 24 reach a S/N ratio around 10 in the I band. While in the H band the MOSAIC spectrograph will reach a S/N ratio around 17 for magnitudes of 21 as shown in fig. 8.16.

In terms of specific designs the fig. 8.17 presents the expected precision in the determination of the stellar parameters and element abundances. Considering only the bluewards region, the baseline ( 450 - 592nm; 587-770nm ) and the blue extension ( 390 - 499nm; 486 - 621nm; 608 - 778nm ) display the trade off between the precision when you observe the  $\sim 500$ -600nm region, a well known region for stellar parameters and element abundances determination, and the elements that you can access in the region between  $\sim 390$ -500nm. Showing that the blue extension can reach more elements but it loses precision in their abundance derivation compared with the Baseline.

### 8.3 Observations of bulge globular cluster stars with MOONS

The Multi-Object Optical and Near-IR Spectrograph (MOONS) is a near-infrared spectrograph, which covers the wavelength range of 0.65 to 1.80  $\mu\text{m}$  for a Field of View (FOV) of 25 arcmin of diameter. MOONS will observe in Y and J bands with fixed resolution of R 4,300 while the R, I, and H bands can switch between two resolution modes, medium (  $R_{R,I}$  4,100 and  $R_H$  6,600) and High (  $R_I$  9,200 and  $R_H$  18,300). A crucial and notorious part of this instrument is the Fiber Positioning Unit (FPU). This system uses an input catalogue to allocate each one of the MOONS fibers in a target or in a sky point, depending on the mode.

The combination of Very Large Telescope (VLT) with MOONS large multiplex and the

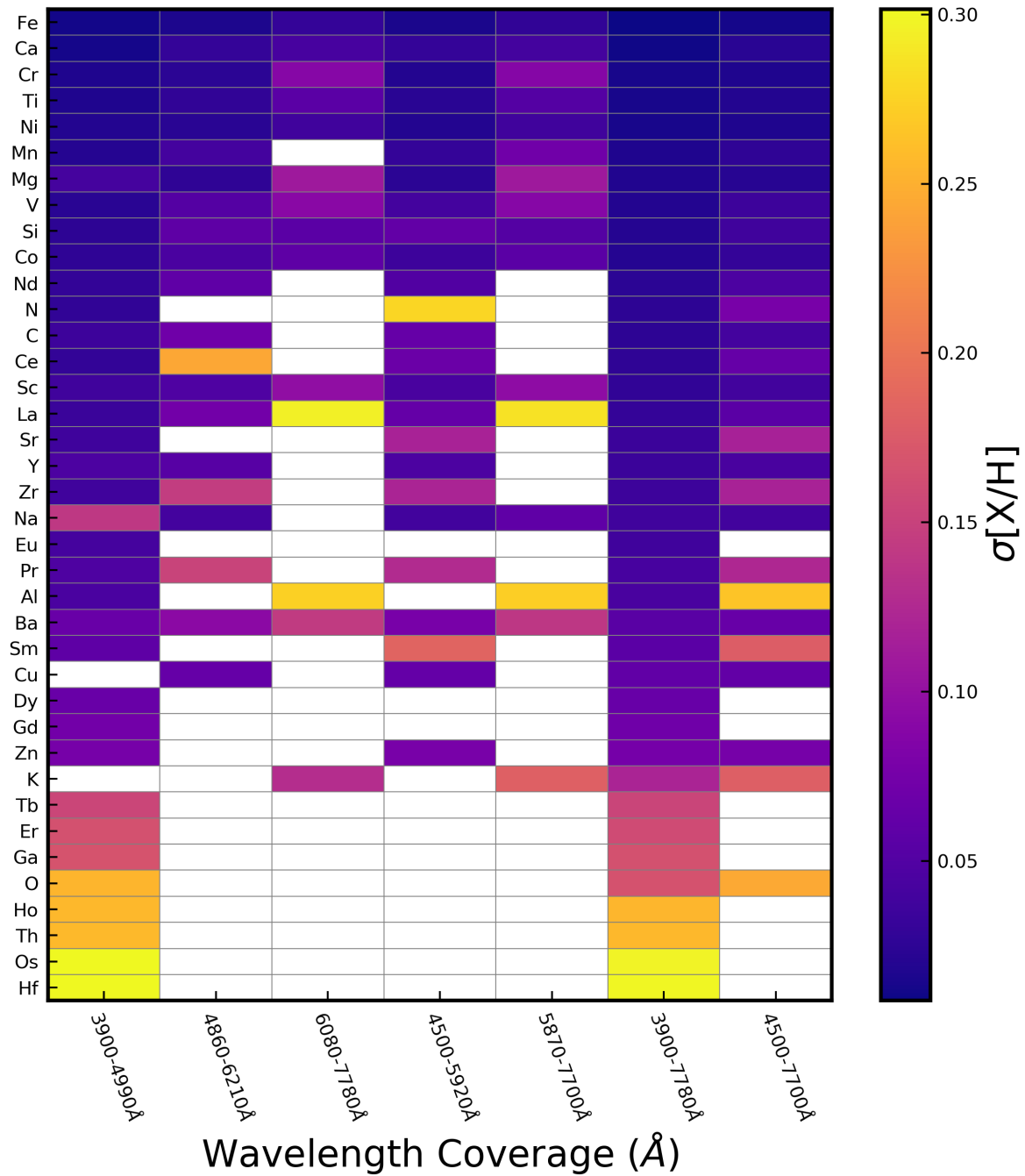


Figure 8.18: The Cramér-Rao Lower Bound for the bands in the blue extension (columns 1-3), the bands in the baseline (columns 4 and 5), and in the columns 6 and 7 the whole wavelength coverage of the two designs. The colour bar represented the spectated precision in elemental abundances for each element found in each band for the same S/N ratio of 50.

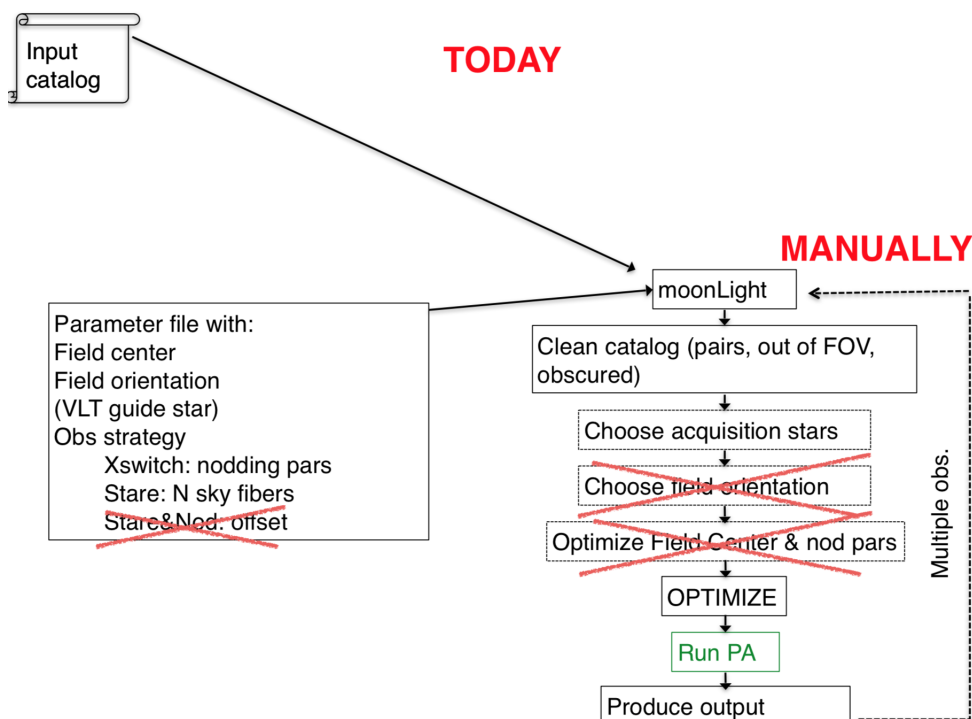


Figure 8.19: MOONlight code diagram.

wavelength coverage will be a very useful tool to study galaxy formation and evolution along the Universe history. Will be possible to see  $z > 8-9$  at the re-ionisation epoch. With this resolution power at this wavelength coverage it is possible to study chemical abundances of stars in Milky Way, in particular the obscured regions in the Galactic bulge.

### 8.3.1 MOONlight code

The MOONlight code, simulate a observation with MOONS. Based in an input catalogue the MOONlight simulate the allocation of each fiber and all the possible paths which the two arms that form the FPU are able to do to reach the final position. The Diagram in figure 8.19 shown two modes, STARE and XSWITCH.

#### 8.3.1.1 STARE

The STARE mode is recommended for the cases that the target are sufficiently bright that sky subtractions is less critical. In this mode a large number of targets can be observed in a single run. In STARE mode less than 10% of the fibers are using to observe 'blank' sky, which those are settled randomly, and avoiding the background sources provided in the

catalogue. The MOONS will be able to create a model of the sky, based on the positions of the fibers.

### 8.3.1.2 XSWITCH

The XSWITCH mode is recommended for faint sources who requires a good sky subtraction. In this template each target has an associated secondary fiber which switch between the sky and the target. The science target is observed with a fiber at both positions, while your secondary observes the sky, see Figure 8.20. Therefore providing excellent sky subtractions both temporary and spacialy.

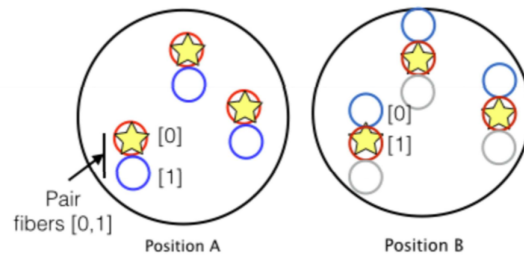


Figure 8.20: XSWITCH Mode.

### 8.3.2 Catalogues

We select 37 GC from Bulge. All those GC were from Bica, Ortolani, and Barbuy, 2016. All catalogues from Aladin software were made using the half light radius and the magnitude of H band from 2MASS for each globular cluster, see table 8.3.2. In this present analysis we do not consider objects in background in our catalogue, even sky points which could be settled in the catalogue we instead choose it to be randomly selected by the MOONS software.

### 8.3.3 Results of the simulations

The MOONS design and wavelength coverage combined show that it could be a useful tool to observe globular cluster. In order to appraise the efficiency of MOONS in observing those objects we defined the fitting factor. The fitting factor was defined to represent which percentage of the fibers in MOONS are allocated in observational targets listed in the input catalogue. For those tests we simulated observations of GCs in the bulge using

Table 8.6 - Bulge globular clusters data from Bica et al. 2016.

ID	l(°)	b(°)	R <sub>sun</sub>	R <sub>gc</sub>	[Fe/H]	V <sub>t</sub>	v <sub>r</sub>	c	r <sub>c</sub>	r <sub>h</sub>
Terzan3	345.08	9.19	8.2	2.5	-0.74	12.00	-136.3	0.70	1.18	1.25
ESO452-SC11	351.91	12.10	8.3	2.1	-1.50	12.00	vr	1.00	0.50	0.50
NGC6256	347.79	3.31	10.3	3.0	-1.02	11.29	-101.4	2.50	0.02	0.86
NGC6266	353.57	7.32	6.8	1.7	-1.18	6.45	-70.1	1.71	0.22	0.92
NGC6304	355.83	5.38	5.9	2.3	-0.45	8.22	-107.3	1.80	0.21	1.42
NGC6316	357.18	5.76	10.4	2.6	-0.45	8.43	71.4	1.65	0.17	0.65
NGC6325	0.97	8.00	7.8	1.1	-1.25	10.33	29.8	2.50	0.03	0.63
NGC6342	4.90	9.72	8.5	1.7	-0.55	9.66	115.7	2.50	0.05	0.73
NGC6355	359.59	5.43	9.2	1.4	-1.37	9.14	-176.9	2.50	0.05	0.88
Terzan2	356.32	2.30	7.5	0.8	-0.69	14.29	109.0	2.50	0.03	1.52
Terzan4	356.02	1.31	7.2	1.0	-1.41	16.00	-50.0	0.90	0.90	1.85
HP1	357.44	2.12	8.2	0.5	-1.00	11.59	45.8	2.50	0.03	3.10
Terzan1	357.57	1.00	6.7	1.3	-1.03	15.90	114.0	2.50	0.04	3.82
Ton2	350.80	-3.42	8.2	1.4	-0.70	12.24	-184.4	1.30	0.54	1.30
NGC6401	3.45	3.98	10.6	2.7	-1.02	9.45	-65.0	1.69	0.25	1.91
Pal6	2.10	1.78	5.8	2.2	-0.91	11.55	181.0	1.10	0.66	1.20
Djorg1	356.69	-2.47	13.7	5.7	-1.51	13.60	-362.4	1.50	0.50	1.59
Terzan5	3.84	1.69	6.9	1.2	-0.23	13.85	-93.0	1.62	0.16	0.72
NGC6440	7.73	3.80	8.5	1.3	-0.36	9.20	-76.6	1.62	0.14	0.48
Terzan6	358.57	-2.16	6.8	1.3	-0.56	13.85	126.0	2.50	0.05	0.44
Terzan9	3.61	-1.99	7.1	1.1	-1.05	16.00	59.0	2.50	0.03	0.78
Djorg2	2.77	-2.50	6.3	1.8	-0.65	9.90	vr	1.50	0.33	1.05
Terzan10	4.49	-1.99	5.8	2.3	-1.00	14.90	vr	0.75	0.90	1.55
NGC6522	1.02	-3.93	7.7	0.6	-1.34	8.27	-21.1	2.50	0.05	1.00
NGC6528	1.14	-4.17	7.9	0.6	-0.11	9.60	206.6	1.50	0.13	0.38
NGC6539	20.80	6.78	7.8	3.0	-0.63	9.33	31.0	1.74	0.38	1.70
NGC6553	5.26	-3.03	6.0	2.2	-0.18	8.06	-3.2	1.16	0.53	1.03
NGC6558	0.20	-6.02	7.4	1.0	-1.32	9.26	-197.2	2.50	0.03	2.15
BH261	3.36	-5.27	6.5	1.7	-1.30	11.00	vr	1.00	0.40	0.55
NGC6624	2.79	-7.91	7.9	1.2	-0.44	7.87	53.9	2.50	0.06	0.82
NGC6626	7.80	-5.58	5.5	2.7	-1.32	6.79	17.0	1.67	0.24	1.97
NGC6638	7.90	-7.15	9.4	2.2	-0.95	9.02	18.1	1.33	0.22	0.51
NGC6637	1.72	-10.27	8.8	1.7	-0.64	7.64	39.9	1.38	0.33	0.84
NGC6642	9.81	-6.44	8.1	1.7	-1.26	9.13	-57.2	1.99	0.10	0.73
NGC6652	1.53	-11.38	10.0	2.7	-0.81	8.62	-111.7	1.80	0.10	0.48
NGC6717	12.88	-10.90	7.1	2.4	-1.26	9.28	22.8	2.07	0.08	0.68
NGC6723	0.07	-17.30	8.7	2.6	-1.10	7.01	-94.5	1.11	0.83	1.53

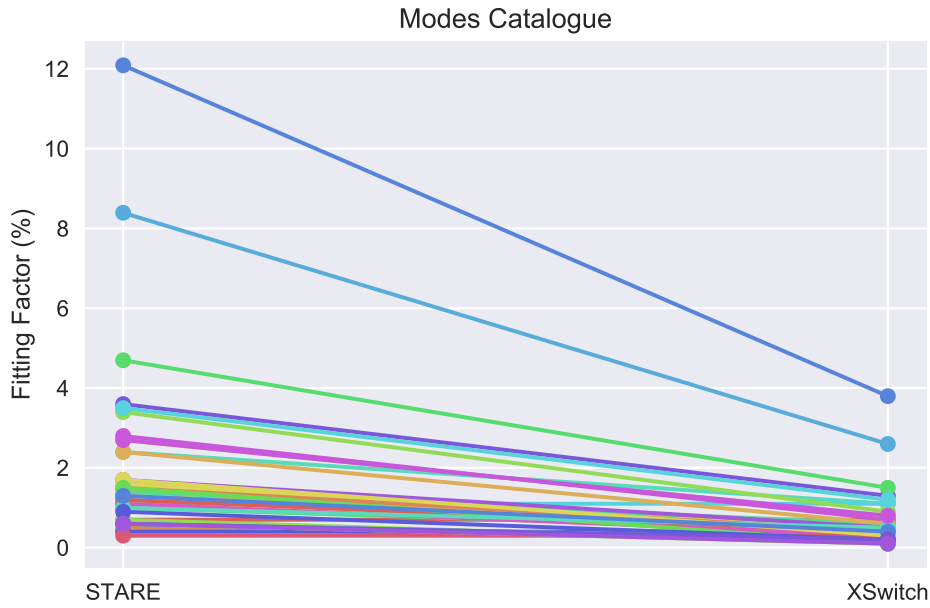


Figure 8.21: Fitting factor of STARE and XSWITCH modes.

the MOONlight code for two modes, STARE and XSWITCH. The STARENod mode was not ready at the time we did the simulations.

Firstly, we evaluated the differences in the fitting factor between the two modes, STARE and XSWITCH. In Fig. 8.21 it is clear that the STARE mode has the ability to allocate more fiber in a single observation than the XSWITCH mode for any cluster in the catalogue. This difference is due the design of the two modes. While the STARE mode uses only one fiber dedicated to the target, the XSWITCH requires a secondary fiber dedicated to the sky associated with the fiber allocated in the science target. For the same region in the FOV we should expect a fitting factor for XSWITCH to be less than half of the fitting factor obtained in the STARE mode.

Secondly, we investigated why the fitting factors appears to be significantly low for globular clusters. In Fig. 8.22 is shown in the left panel the allocations of all the fibers during simulated observation and in the right panel is shown the special distribution of objects in the catalogue. The reason of the lower fitting factor for globular clusters is due to the apparent size of GC in MOONS FOV, reducing the number of fibers that can reach those positions, and the fact that GCs are crowded regions, making impossible to allocate fibers without overlapping them.

To test how these two factors impact an observation, the Figs. 8.23, 8.24, 8.25, and 8.26 shown the fitting factor for all GCs in our sample vs. the  $c$  factor that describes

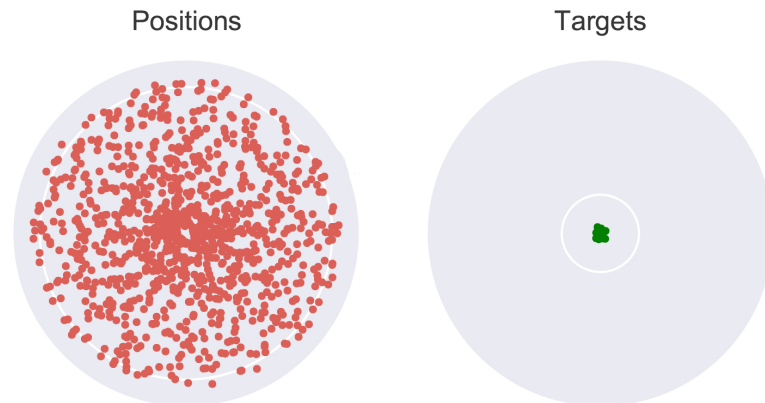


Figure 8.22: Example of a fiber set in a GC case.

how compact is the GC; the number of targets within the input catalogue; the core radii ( $R_c$ ); and the half light radii ( $R_h$ ), respectively. These figures indicate that the  $R_h$  and the number of targets in the catalogue have a linear dependency with the fitting factor. This relation represents the impact of the apparent size in the MOONS FOV and the allocation capability for a large number of targets in a single observation.

MOONS has a clear limitation on how many fiber it can allocate in a single observation of a compact and small source. In order to avoid this limitations it is necessary do multiples observations for the same input catalogue. A possible technique for multiples observations is to remove the previously observed sources and observe the remain targets. In Fig. 8.27 is shown this scenario. It is interesting to notice that there is not a reduction in the fitting factor among the observations when the number of the objects in the catalogue is reduced between the multiples observations. It is possible to observe a globular cluster in its completeness with few observations.

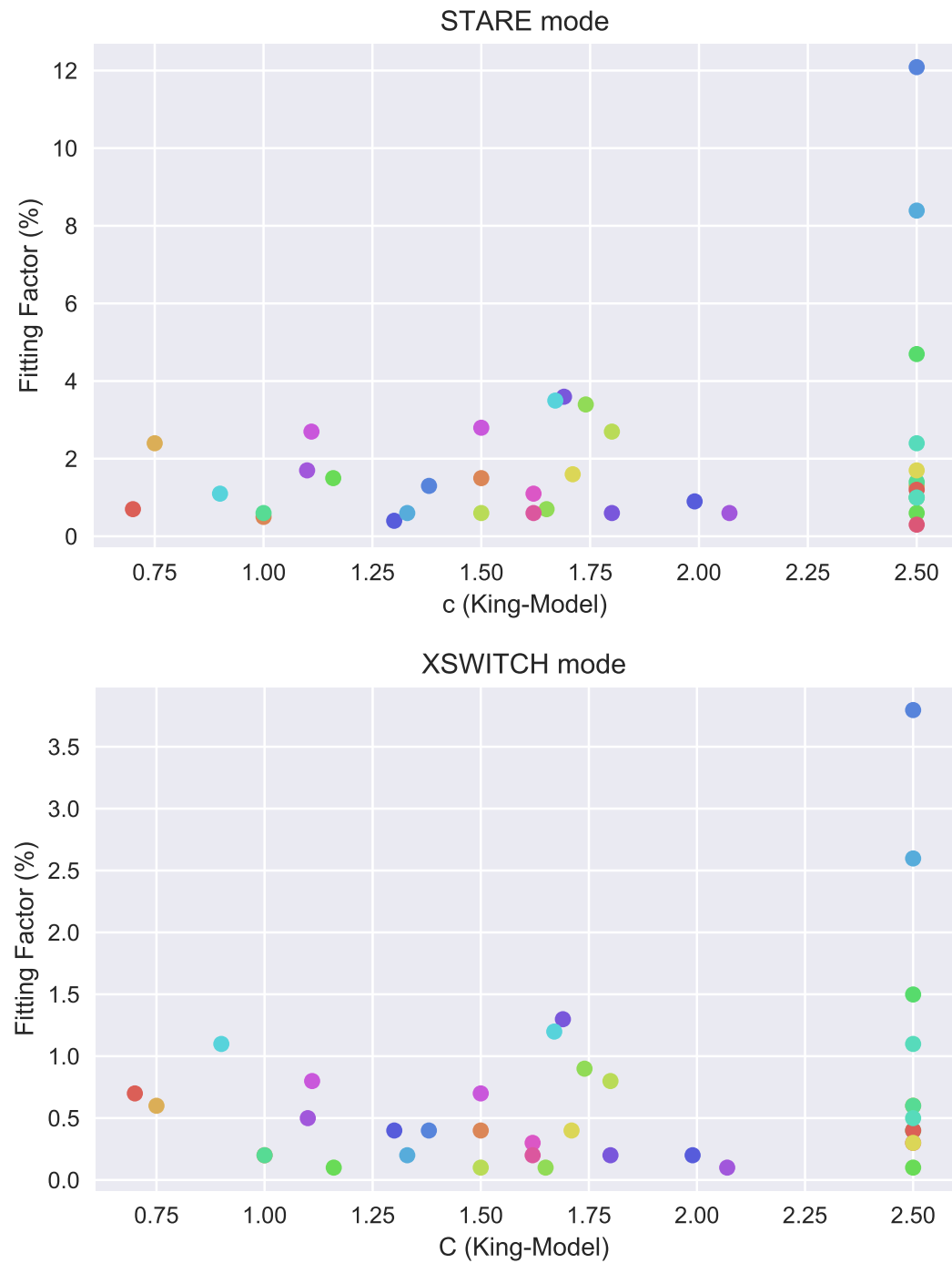


Figure 8.23: Fitting factor over Kingsmodel (c factor).

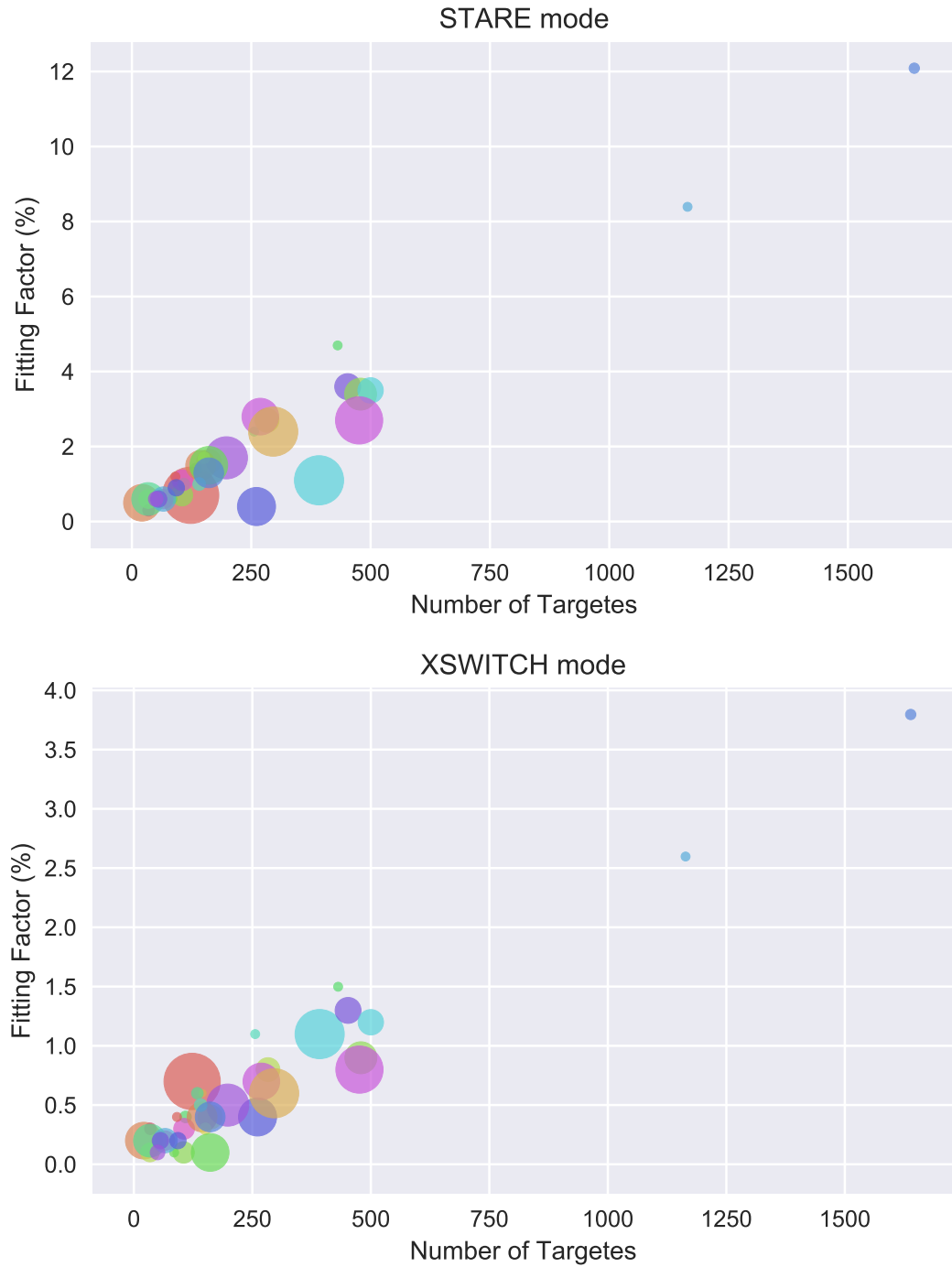


Figure 8.24: Fitting factor over number of targets in the catalogue, the size of the dots is the core radius.

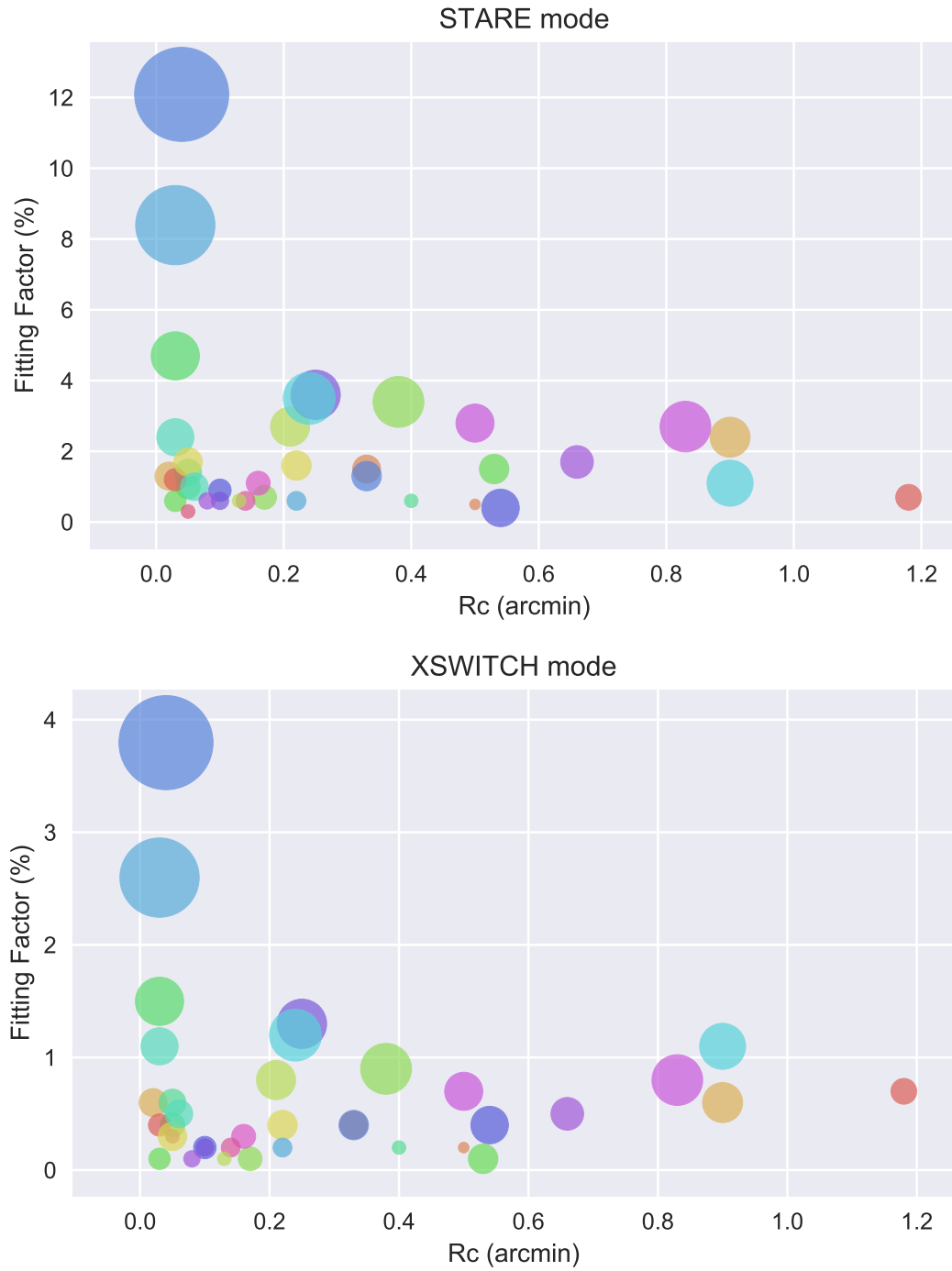


Figure 8.25: Fitting factor over radius of the core, the size of the dots is the number of targets in the catalogue.

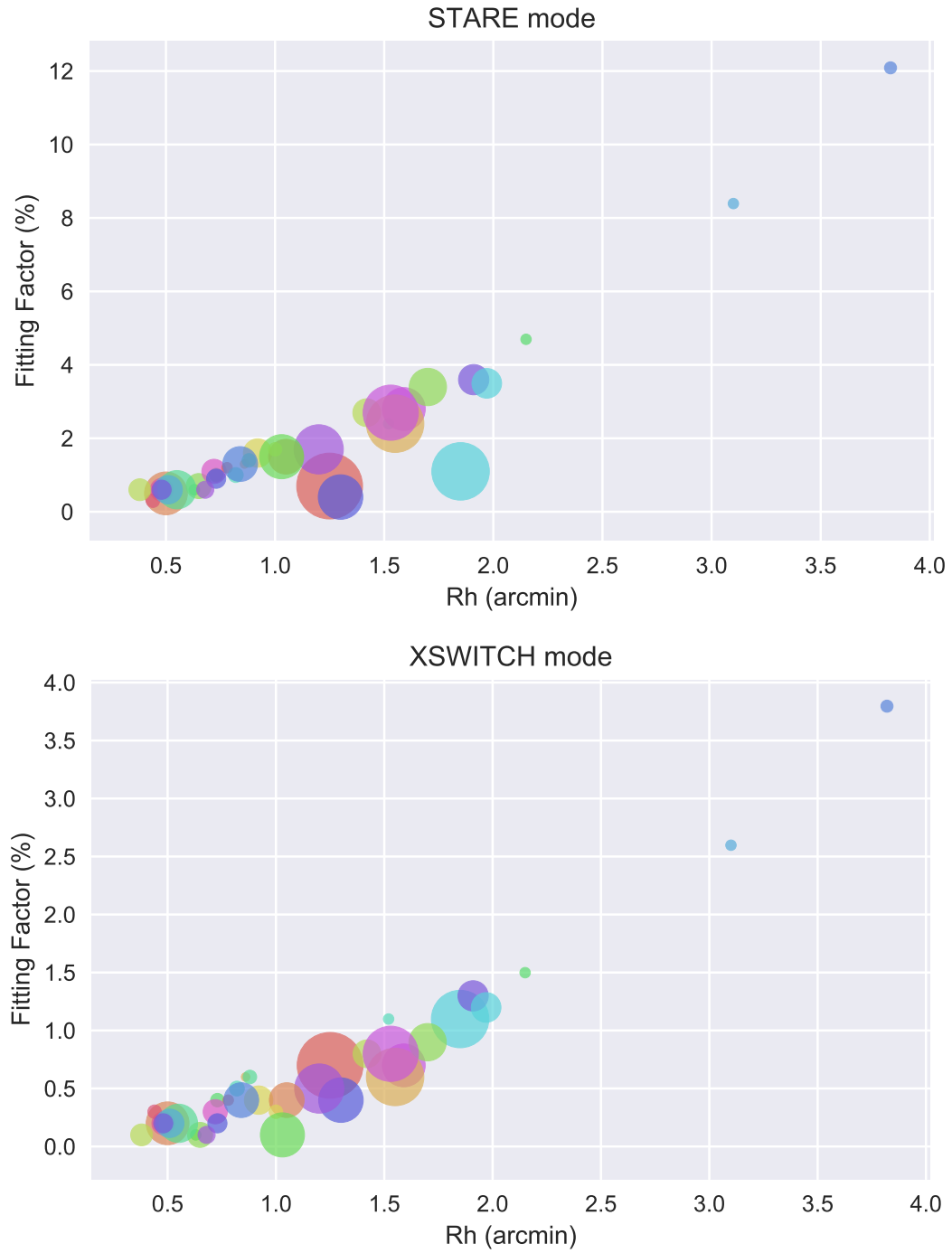


Figure 8.26: Fitting factor over half light radius, the size of the dots is the core radius.

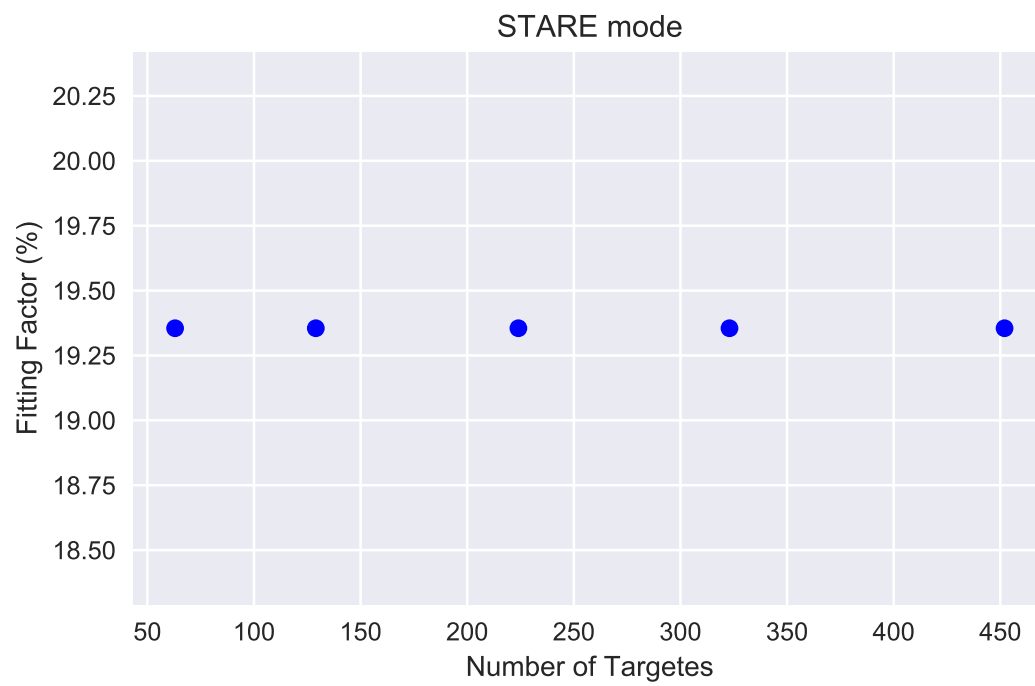


Figure 8.27: Fitting factor over number of targets in the catalogue, running multiples times and removing the targets that have already been obtained for NGC6401.

## Conclusions

In this thesis we analysed the abundances of iron-peak elements in field and globular cluster stars of the Galactic bulge, and in the halo star CS 31082-001. For this we identified best spectra lines, including hyperfine structure for those of odd- $Z$  elements, from the near-UV to the near-IR. The abundances were interpreted in terms of nucleosynthesis processes and chemo-dynamical evolution models computed by Prof. Amâncio Friaça. The comparison with models and literature data allowed to interpret the results.

### *9.1 Galactic bulge and Iron-peak elements*

We concluded so far that the studied moderately metal-poor globular clusters have a typical abundance pattern, with some variation of the heavy element abundances (Barbuy et al. 2018c). The iron-peak elements appear to be more deficient in the moderately metal-poor globular clusters, in particular in terms of V, Mn, Cu, and Zn (Ernandes et al. 2018).

The study on Co and Cu in field bulge stars proved that they can discriminate between the nucleosynthesis processes of alpha-rich freezeout producing them as primary elements (Sukhbold et al. 2016), or the weak-s process in massive stars, and in this case they are secondary elements. It is interesting to note that their abundances can constrain the relative efficiencies of these two contributions (Barbuy et al. 2018b). The data appear to indicate that the weak s-process is dominant for Cu, and alpha-rich freeze-out for Co.

## 9.2 Globular Clusters

We concluded that Terzan 9 is another very old moderately metal-poor and blue horizontal branch globular cluster in the central parts of the Galaxy. We derived a heliocentric radial velocity of  $v_r = 58.1 \text{ km s}^{-1}$  and a metallicity of  $[\text{Fe}/\text{H}] \sim -1.10$ .

The cluster AL 3 appears to be part of the bulge globular clusters that have  $[\text{Fe}/\text{H}] \sim -1.0$  having metallicity of -1.3, joining the family of these old clusters such as globular clusters Terzan 9 (Ernandes et al. 2020), HP 1 (Barbuy et al. 2016), NGC 6522 (Barbuy et al. 2021a), NGC 6558 (Barbuy et al. 2018), Palomar 6 (Souza et al. 2022), and UKS 1 (Fernández-Trincado et al. 2020).

## 9.3 The halo star CS 31082-001

The halo star CS 31082-001 has been the focus of numerous studies that investigated almost all elements with available lines. We conducted our analysis on Be and the iron-peak elements V and Cu. Be displays a lower abundance for this star than the expected for metal-poor stars, because this star is a cool red giant, and Be is depleted in its atmosphere. The Be depletion mechanism is similar to that described in the Spite plateau for Li, which is diffusion along time. The Cu abundance for metal-poor stars not only shows that it is produced in the weak-s process but that hypernovae played an important role in the enrichment of these stars. The V models suggested that neutrino process are necessary to describe the observations.

## 9.4 Upcoming instruments

For further investigations of the Iron-peak elements in the Galactic bulge, bulge globular clusters, and metal-poor stars in the halo the forthcoming instruments can be extraordinary tools.

### 9.4.1 MOSAIC

MOSAIC will allow multi-object spectroscopy in the near-infrared and optical of faint objects, such as dwarf stars in the Galactic bulge. The HMM-VIS mode been capable to observe simultaneously 200 objects with medium and high resolution is a highly desira-

ble feature to observe bulge globular clusters. Beyond this feature the MOSAIC will be capable to observe metal-poor stars of  $I=24$  using HMM-VIS and  $H=21$ , in HMM-NIR ( $S/N/sim20$ ). Pushing the actual observational limits for objects that are invisible for other ground facilities.

#### 9.4.2 CUBES

CUBES will provide spectroscopy at resolutions of  $R= 20,000$  in the near-UV in the range 300-400nm associated with its high efficiency in the UV, allowing to gain 3 magnitudes in the near-ultraviolet. It will allow studies of many more metal-poor stars. With this outstanding instrument it will possible to derive element abundances for stars with  $U=18$ mag, accessing the auspicious ground-UV spectral region for the faintest stars in the Galaxy. In this work we have shown that abundance determination for the elements Bi and U are challenging but feasible in the right circumstances with CUBES.

#### 9.4.3 MOONS

We concluded that MOONS spectrograph can be a helpful tool to observe globular cluster due to its multiplex, observing simultaneously hundreds of objects in the near-infrared. We have shown that observing globular clusters with MOONS can be challenging because the apparent size of the GCs in the MOONS FOV and its fiber allocation system. But feasible and recommended to access multiples objects in a single observation.

### 9.5 Perspectives

The studies of the globular clusters in the bulge then the focused analysis of the Cu and Co for bulge stars have shown that the iron-peak elements plays a distinguished role as key discriminator among the nucleosynthesis process in the massive stars they were synthesised.

The analysis and characterisation of the bulge globular clusters with metallicities  $[Fe/H] \sim -1.0$  have been enlarged with the analysis of AL 3 and Terzan 9.

The study of the nucleosynthesis processes in the very metal-poor halo star unveil the abundance of Be in a cool red giant (not done before), and the necessity of more elaborated chemical evolutionary models for V and Cu, requiring neutrino process and hypernovae

respectively.

Such studies can be the basis to plan for surveys with the MOSAIC spectrograph at the Extremely Large Telescope (ELT) and CUBES spectrograph at the Very Large Telescope (VLT) in particular, in which we are involved, as well with other telescopes and instruments such as GMT, JWST, MOONS@VLT.

# Bibliography

Abate et al. 2015, A&A, 581, A62

Adibekyan, V. Zh., Figueira, P., Santos, N.C. et al. 2013, A&A, 554, A44

Armandroff, T.E., Zinn, R. 1988, AJ, 96, 92 1999, A&AS, 140, 261

Alonso, A., Arribas, S., Martínez-Roger, C. 1999, A&AS, 140, 261

Allende Prieto, C., Lambert, D.L., Asplund, M. 2001, ApJ, 556, L63

Alvarez R. & Plez B., A&A, 330, 1109 (1998)

Alonso, A., Arribas, S., Martínez-Roger, C. 1998, A&AS, 131, 209

Alonso, A., Arribas, S., Martínez-Roger, C. 1999, A&AS, 140, 261 (AAM99)

Alves-Brito, A., Barbuy, B., Ortolani, S., et al. 2005, A&A, 435, 657

Alves-Brito, A., Barbuy, B., Zoccali, M., et al. 2006, A&A, 460, 269.

Anders, F., Chiappini, C., Rodrigues, T.S. et al. 2017, A&A, 597, A30

Andrews, A.D., Lindsay, E.M. 1967, IrAJ, 8, 126

Asplund, M., Grevesse, N., Sauval, A.J., Scott, P. 2009, ARA&A, 47, 481

Baumgardt, H., Hilker, M., Sollima, A., Bellini, A. 2019, MNRAS, 482, 5138

Barbuy, B., Bica, E., Ortolani, S. 1998, A&A, 333, 117

Barbuy, B., Perrin, M.-N., Katz, D., Coelho, P., Cayrel, R., Spite, M., van't Veer-Menneret, C. 2003, A&A, 404, 661

- Barbuy, B., Zoccali, M., Ortolani, S. et al. 2006, A&A, 449, 349
- [Barbuy07] Barbuy, B., Zoccali, M., Ortolani, S. et al. 2007, AJ, 134, 1613
- Barbuy, B., Zoccali, M., Ortolani, S., et al. 2009, A&A, 507, 405
- Barbuy, B., Spite, M., Hill, V. et al. A&A, 534, A60 (2011)
- Barbuy, B., Hill, V., Zoccali, M., et al. 2013, A&A, 559, A5
- Barbuy, B., Chiappini, C., Cantelli, E. 2014, A&A, 570, A76
- Barbuy et al. 2014, Ap&SS, 354, 191
- Barbuy, B., Friaça, A.C.S., da Silveira, C.R. et al. 2015, A&A, 580, A40
- Barbuy, B., Cantelli, E., Vemado, A., et al. 2016, A&A, 591, A53
- Barbuy, B., Chiappini, C., Gerhard, O. 2018a, ARA&A, 56, 223
- Barbuy, B., Trevisan, J., de Almeida, A. 2018b, PASA, 35, 46
- Barbuy, B., Muniz, L.I., Ortolani, S. et al. 2018c, A&A, 619, A178
- Barbuy, B., Cantelli, E., Muniz, L. et al. 2021a, A&A, 654, A29
- Barbuy, B., Ernandes, H., Souza, S.O. et al. 2021b, A&A, 648, A16
- Ballester, P., Modigliani, A., Boitquin, O., Cristiani, S., Hanuschik, R., Kaufer, A., Wolf, S. 2000, in *The Messenger*, 101, 31.
- Battistini, C., Bensby, T., 2015, A&A, 577, A9
- Bergemann, M., Gehren, T. 2008, A&A, 492, 823
- Bergemann, M., Pickering, J.C., Gehren, T. 2010a, MNRAS, 401, 1334B
- Bergemann, M. & Cescutti, G. 2010b, A&A, 522A, 9B
- Beers & Christlieb, 2005, ARA&A, 43, 531
- Bessell, M.S. 1979, PASP, 91, 589
- Bensby, T., Feltzing, S., Lundström, I., 2003, A&A, 410, 527

- 
- Bensby, T., Feltzing, S., Lundström, I., Ilyin, I. 2005, *A&A*, 433, 185
- Bensby, T., Yee, J.C., Feltzing, S. et al. 2013, *A&A*, 549, A147
- Bensby, T., Feltzing, S., Gould, A., et al. 2017, *A&A*, 605, A89
- Bessell, M., *ARA&A*, 43, 293 (2005)
- Bica, E., Bonatto, C., Barbuy, B., Ortolani, S. 2006, *A&A*, 450, 105
- Bica, E., Clariá, J.J., Piatti, A., Bonatto, C. 1998, *A&AS*, 131, 483
- Bica, E., Ortolani, S., Barbuy, B. 2016, *PASA*, 33, 28
- Biehl, D. 1976, PhD thesis, University of Kiel
- Bisterzo, S., Gallino, R., Pignatari, M., Pompéia, L., Cunha, K., Smith, V. 2004, *Mem. S.A.It.*, 75, 741
- Blanco, V.M. 1988, *AJ*, 95, 1400
- Bland-Hawthorn, J., & Gerhard, O. 2016, *ARA&A*, 54, 529
- Boesgaard et al. 1999, *AJ*, 117, 1549
- Boesgaard, A.M., Rich, J.A., Levesque, E.M., Bowler, B.P. 2011, *ApJ*, 743, 140
- Bovard et al. 2017, *PhysRevD*, 96, 124005
- Boissier, S., Prantzos, N., 2000, *MNRAS*, 312, 398
- Bonifacio, P., Caffau, E., Ludwig, H.-G. 2010, *A&A*, 524, A96
- Bressan, A., Marigo, P., Girardi, L. 2012, *MNRAS*, 427, 127
- Buck, T., Ness, M., Macciò, A.V., Obreja, A., Dutton, A.A. 2018, *ApJ*, 861, 88
- Busso, Gallino & Wasserburg, 1999, *ARA&A*, 37, 239
- Carpenter, J.M. 2001, *AJ*, 121, 2851
- Casey, A.R., Schlafman, K.C. 2015, *ApJ*, 809, 110
- Carretta, E., Bragaglia, A., Gratton, R., D’Orazi, V., Lucatello, S. 2009, *A&A*, 508, 695

- Cayrel, R. 1988, in IAU Symposium, Vol. 132, The Impact of Very High S/N Spectroscopy on Stellar Physics, ed. G. Cayrel de Strobel & M. Spite, 345
- Cayrel, R., Perrin, M.-N., Barbuy, B., Buser, R. 1991, *A&A*, 247, 108A&A
- Cayrel et al. 2001, *Nature*, 409, 691
- Cayrel, R., Depagne, E., Spite, M., et al. 2004, *A&A*, 416, 1117
- Cenarro, A. J.; Cardiel, N.; Gorgas, J. et al. 2001, *MNRAS*, 326, 959
- Cescutti, G., Matteucci, F., Lanfranchi, G. 2008, *A&A*, 491, 401
- Cescutti et al. 2015, *A&A*, 577, A139
- Chiappini C., Matteucci F., Romano D., 2001, *ApJ*, 554, 1044
- Chiappini, 2013, *AN*, 334, 595
- Choplan et al. 2016, *A&A*, 593, A36
- Coelho, P., Barbuy, B., Meléndez, J., Schiavon, R.P., Castilho, B.V. 2005, *A&A*, 443, 735
- Cohen, J. G., Christlieb, N., Thompson, I., et al. 2013, *ApJ*, 778, 56
- Cowan, J.J., Sneden, C., Burles, S. et al. 2002, *ApJ*, 572, 861
- da Silveira, C.R. 2017, PhD thesis, Universidade de São Paulo
- da Silveira, C., Barbuy, B., Friça, A. et al. 2018, *A&A*, 614, A149
- Da Costa et al. 2019, *MNRAS* 489, 5900
- Dekker, H., D'Odorico, S., Kaufer, A., Delabre, B., Kotzlowski, H. 2000, *SPIE*, 4008, 534
- Den Hartog, E.A., Lawler, J.E., Sobeck, J.S., Sneden, C., Cowan, J.J. 2011, *ApJS*, 194, 35
- Dias, B., Barbuy, B., Saviane, I., et al. 2015, *A&A*, 573, A13
- Dias, B., Barbuy, B., Saviane, I., et al. 2016, *A&A*, 590, A9
- Dotter, A., Chaboyer, B., Jevremović, D. et al. 2008, *ApJS*, 178, 89
- Dufay, J., Berthier, P., Morignat, B. 1954, *Publ. of the OHP*, 3, No. 17

- Duffau, S., Caffau, E., Sbordone, L. et al. 2017, *A&A*, 605, A128
- Ernandes, H., Barbuy, B., Alves-Brito, A. et al. 2018, *A&A*, 616, A18
- Ernandes, H., Evans, C., Barbuy, B. et al. 2020, *Proceedings of the SPIE*, Volume 11447, id. 1144760
- Ernandes, H., Barbuy, B., Friaça, A. et al. , 2022, *MNRAS*, Volume 510, Issue 4, pp.5362-5375
- Ernandes, H., Barbuy, B., Castilho, B., Evans, C.J., Cescutti, G., 2022, *ExA*, <https://doi.org/10.1007/s10686-021-09829-2>
- Eichler, M., Sayar, W., Arcones, A. & Rauscher, T. *ApJ*, 879, 47 (2019)
- Evans et al. 2016, *Proc. SPIE*, 9908, 9J
- Evans et al. 2018, *Proc. SPIE*, 10702, 2E
- Faber, S.M., Friel, E., Burstein, D., Gaskell, C.M. 1985, *ApJ*, 57, 711
- Farouqi, K., Kratz, K.-L., Pfeiffer, B., et al. 2010, *ApJ*, 712, 1359
- Feltzing, S., Fohlman, M., Bensby, T. 2007, *A&A*, 467, 665
- Fernando, A. M., Bernath, P. F., Hodges, J. N., et al. 2018, *J. Quant. Spec. Radiat. Transf.*, 217, 29. doi:10.1016/j.jqsrt.2018.05.021
- Fishlock, C.K., Yong, D., Karakas, A.I. et al. 2017, *MNRAS*, 466, 4672
- Forsberg, R., Jönsson, H., Ryde, N., Matteucci, F. 2019, *A&A*, 631, A113
- Fragkoudi, F., Di Matteo, P., Haywood, M., et al. 2018, *A&A*, 616, A180
- Freeman K, Bland-Hawthorn J. 2002, *ARA&A*, 40, 487
- Frebel, A., Christlieb, N., Norris, J.E. et al. 2007, *ApJ*, 660, L117
- Friaça, A.C.S., Terlevich R.J., 1998, *MNRAS*, 298, 399
- Friaça, A.C.S., Barbuy, B. 2017, *A&A*, 598, A121
- Frischknecht et al. 2012, *A&A*, 538, 2

- Fulbright, J.P., McWilliam, A., Rich, R.M. 2007, *ApJ*, 661, 1152
- Gaia Collaboration, Brown, A. G. A., Vallenari, A., et al. 2018a, *A&A*, 616, A1
- Genoni, M., Landoni, M., Cupani, G. et al. 2022, *ExA*, <https://doi.org/10.1007/s10686-022-09844-x>
- Girardi, L. 2016, *ARA&A*, 54, 95
- Gratton, R.G. 1989, *A&A*, 208, 171
- Gratton, R.G., Sneden, C. 1990, *A&A*, 234, 366
- Gratton, R.G., Carretta, E., Bragaglia, A. 2012, *A&ARv*, 20, 50
- Gravity Collaboration, Abuter, R., Amorim, A., et al. 2019, *A&A*, 625, L10
- Grevesse, N., Noels, A., Sauval, J. 1996, *ASP Series*, 99, 117 *Astronomical Society of the Pacific Conference Series; volume 99. Proceedings of the sixth (6th) annual October Astrophysics Conference in College Park; Maryland; 9-11 October 1995; San Francisco: Astronomical Society of the Pacific (AS*
- Grevesse, N. & Sauval, J.N. 1998, *SSRev*, 35, 161
- Grevesse, N., Scott, P., Asplund, M., Sauval, A.J. 2015, *A&A*, 573, 25
- Goldman, A., Schoenfeld, W.G., Goorvitch, D. et al. 1998, *JQSRT*, 59, 453
- Goorvitch, D. 1994, *ApJS*, 95, 535
- Gustafsson, B., Edvardsson, B., Eriksson, K. et al. 2008, *A&A*, 486, 951
- Gonzalez, O.A., Rejkuba, M., Zoccali, M. et al. 2011, *A&A*, 530, A54
- Grisoni, V., Spitoni, E., Matteucci, F. et al. 2017, *MNRAS*, 472, 3637
- Grisoni, V., Cescutti, G., Matteucci, F. et al. 2020, *MNRAS*, 492, 2828
- Guarnieri, M.D., Ortolani, S., Montegriffo, P., et al. 1998, *A&A*, 331, 70
- Hansen, B.M.S., Kalirai, J.S., Anderson, J. et al. 2013, *Nature*, 500, 51
- Hansen, C. et al. 2015, *AN*, 336, 665

- 
- Hansen, T. et al. 2015, *ApJ*, 807, 173
- Hansen et al. 2019, *A&A*, 623, 128
- Hasselquist, S., Shetrone, M., Smith, V., et al. 2017, *ApJ*, 845, 162
- Harris W. 1996, *AJ*, 112, 1487 (edition of 2010)
- Heger, A., Kolbe, E., Haxton, W. C., et al., 2005, *Phys. Lett. B*, 606, 258
- Hill, V., Plez, B., Cayrel, R., Beers, T.C. 2001, *ASPC*, 245, 316
- Hill, V., Plez, B., Cayrel, R. et al. 2002, *A&A*, 387, 560
- Hill V, Lecureur A, Gómez A, et al. 2011. *A&A* 534:A80
- Hill, V., Christlieb, N., Beers, T.C. et al. 2017, *A&A*, 607, A91
- Hinkle, K., Wallace, L., Livingston, W. 1995, *PASP*, 107, 1042
- Hinkle, K., Wallace, L., Valenti, J., Harmer, D. 2000, *Visible and Near Infrared Atlas of the Arcturus Spectrum 3727-9300 A*, ed. K. Hinkle, L. Wallace, J. Valenti, and D. Harmer (San Francisco: ASP)
- Houdashelt, M.L., Bell, R.A., Sweigart, A.V. 2000, *AJ*, 119, 1448
- Holmbeck, E.M., Beers, T.C., Roederer, I.U. et al. 2018, *ApJ*, 959, L24
- Holmbeck, E.M., Hansen, T.T., Beers, T.C. et al. 2020, *ApJS*, 249, 30
- Howes, L.M., Asplund, M., Casey, A.R., Keller, S.C., Yong, D., et al. 2014, *MNRAS*, 445, 4241
- Howes, L.M., Casey, A.R., Asplund, M., Keller, S.C., Yong, D., et al. 2015, *Nature*, 527, 484
- Howes, L.M., Asplund, M., Keller, S.C., Casey, A.R., Yong, D., et al. 2016, *MNRAS*, 460, 884
- Huber, K.P., Herzberg, G. 1979, *Constants of diatomic molecules*, Springer, Boston, MA.
- Ishigaki, M.N., Aoki, W., Chiba, M. 2013, *ApJ*, 771, 67

- Iwamoto, K., Brachwitz, F., Nomoto, K. et al. 1999, *ApJS*, 125, 439
- Jofre, O., Heiter, U., Soubiran, C. 2018, arXiv:1811.08041
- Jorgensen, U.G. 1994, *A&A*, 284, 179
- Johnson, C.I., Rich, R.M., Kobayashi, C., Kunder, A., Koch, A. 2014, *AJ*, 148, 67
- Jönsson, H., Ryde, N, Schultheis, M., Zoccali, M. 2017, *A&A*, 600, A101
- Kamann, S., Wisotzki, L., Roth, M. M., 2013, *A&A* 549, A71
- Kamann, S., Husser, T.-O., Dreizler, S. et al. 2018, *MNRAS*, 473, 5591
- Katz, D., Soubiran, C., Cayrel, R., Adda, M., Cautain, R., 1998, *A&A* 338, 151
- Katz, D. 2001, *JAD*, 7, 8
- Katz, D., Soubiran, C. , Cayrel<sup>3</sup>, R., Barbuy, B., Friel<sup>5</sup>, E., Bienaymé, O., Perrin<sup>1</sup>, M. N., 2011, *A&A* 525, A90
- Kerber, L.O., Nardiello, D., Ortolani, S. et al. 2018, *ApJ*, 853, 15
- Kerber, L.O., Libralato, M., Souza, S.O. et al. 2019, *MNRAS*, 484, 5530
- Kirby, E. N., Xie, J. L., Guo, R., Kovalev, M., Bergemann, M., 2018, *ApJS*, 237, 18K
- Kobayashi, C., Umeda, H., Nomoto, K., Tominaga, N., Ohkubo, T., 2006, *ApJ*, 653, 1145
- Kobayashi, C., Izutani, N., Karakas, A. I., et al. 2011a, *ApJL*, 739, L57
- Kobayashi, C., Karakas, I. A., Umeda, H., 2011b, *MNRAS*, 414, 3231
- Kobayashi, C., Karakas, A. I., & Lugaro, M. 2020, *ApJ*, 900(2), 179.
- Koch, A., McWilliam, A., Preston, G.W., Thompson, I.B. 2016, *A&A*, 587, 124
- Kraft, R.P. 1983, in *Highlights of Astronomy*, 6, 129
- Kruijssen, J.M.D. 2015, *MNRAS*, 454, 1658
- Kunder, A., Valenti, E., Dall’Ora, M. et al. 2018, *SSR*, 214, 90
- Kurucz, R. 1993, CD-ROM 23

- 
- Lai, D.K., Bolte, M., Johnson, J.A., Lucatello, S., Heger, A., Woosley, S.E. 2008, *ApJ*, 681, 1524
- Lanfranchi, G. A., Friaça, A. C. S. 2003, *MNRAS*, 343, 481
- Lauberts, A. 1982, *ESO/Uppsala Survey of ESO(B) Atlas*, ESO, Garching
- Lattimer, J. M., Prakash, M. 2001, *ApJ*, 550, 426
- Lawler, J. E., Guzman, A., Wood, M. P., Sneden, C., & Cowan, J. J. 2013, *ApJS*, 205, 11
- Lee Y-W. 1992. *AJ* 104:1780–1789
- Lecureur, A., Hill, V., Zoccali, M., Barbuy, B., Gómez, A., et al. 2007, *A&A*, 465, 799
- Li, Z.-S., Norin, J., Persson, A. et al. 1999, *Phys. Rev. A*, 60, 198
- Limongi & Chieffi, 2003, *ApJ*, 592, 404
- Limongi & Chieffi, 2018, *ApJ*, 237, 13
- Livingston, W., Wallace, L. 1991, *An atlas of the solar spectrum in the infrared from 1850 to 9000 cm<sup>-1</sup> (1.1 to 6.5 micrometer)*, NSO Technical Report, NOAO, Tucson
- Lomaeva, M., Jönsson, H., Ryde, N., Schultheis, M., Thorsbro, B., 2019, *A&A*, 625A, 141L
- Lodders, 2003, *ApJ*, 591, 1220
- Lodders, K., Palme, H., Gail, H.-P. 2009, *Landolt-Börnstein - Group VI Astronomy and Astrophysics Numerical Data and Functional Relationships in Science and Technology Volume 4B: Solar System*. Edited by J.E. Trümper, 2009, 4.4., 44
- Maeda, K., Nomoto, K., 2003, *ApJ*, 598, 1163
- Majewski, S.R., Schiavon, R.P., Frinchaboy, P.M. 2017, *AJ*, 154, 94
- Matteucci, F., Brocato, E. 1990, *ApJ*, 365, 539
- Matteucci et al. 2014, *MNRAS*, 438, 2177
- Martell, S.L., Smolinski, J.P., Beers, T.C., Grebel, E.K. 2011, *A&A*, 534, A136

- Martin, W.C., Fuhr, J.R., Kelleher, D.E., et al. 2002, NIST Atomic Database (version 2.0), <http://physics.nist.gov/asd>. National Institute of Standards and Technology, Gaithersburg, MD.
- McWilliam, A., Preston, G.W., Sneden, C., Searle, L. 1995, *AJ*, 109, 2757
- McWilliam, A., Rich, R. M., Smecker-Hane, T. A. 2003, *ApJ*, 592, L21
- McWilliam, A., Wallerstein, G., Mottini, M. 2013, *ApJ*, 778, 149
- McWilliam, A. 2016. *PASA*, 33, 40
- Meléndez, J., Barbuy, B. 1999, *ApJS*, 124, 527
- Meléndez, J., Barbuy, B., Spite, F. 2001, *ApJ*, 556, 858
- Meléndez, J., Barbuy, B. 2002, *ApJ*, 575, 474
- Meléndez, J., Barbuy, B., Bica, E. et al. 2003, *A&A*, 411, 417
- Minelli, A., Mucciarelli, A., Massari, D. et al. 2021, *ApJ*, 918, L32
- Mishenina, T.V., Kovtyukh, V.V., Soubiran, C., Travaglio, C., Busso, M. 2002, *A&A*, 396, 189
- Navarro, J. F., Frenk, C. S., & White, S. D. M. 1997, *ApJ*, 490, 493
- Ness M, Freeman K, Athanassoula E, et al. 2013a. *MNRAS* 430:836–857
- Nissen, P.E., Chen, Y.Q., Schuster, W.J., Zhao, G. 2000, *A&A*, 353, 722
- Nissen, P.E., Schuster, W.J., 2011, *A&A*, 530, 15
- Nishimura, Takiwaki & Thielemann, 2015, *ApJ*, 810, 109
- Nomoto, K., Tominaga, N., Umeda, H., Kobayashi, C, Maeda, K., 2006, *Nuclear Phys. A*, 777, 424
- Nomoto, K., Kobayashi C., Tominaga N., 2013, *ARAA*, v. 51 p. 457-509
- Ou, X., Roederer, I. U., Sneden, C., et al. 2020, *ApJ* 900, 106
- Oliveira, R.A.P., Souza, S.O., Kerber, L.O. et al. 2020, *ApJ*, 891, 37

- 
- Ortolani, S., Bica, E., Barbuy, B. 1997, MNRAS, 284, 692
- Ortolani, S., Bica, E., Barbuy, B., 1999, A&AS, 138, 267
- Ortolani, S., Bica, E., Barbuy, B. 2006, ApJ, 646, L115
- Origlia, L., Rich, R.M. 2004, AJ, 127, 3422
- Ortolani, S., Barbuy, B., Bica, E., Zoccali, M., Renzini, A. 2007, A&A, 470, 1043
- Ortolani, S., Barbuy, B., Momany, Y., Saviane, I., Bica, E. et al. 2011, ApJ, 737, 31
- Osterbrock, D.E., Fulbright, J.P., Martel, A.R. et al. 1996, PASP, 108, 277
- Pérez-Villegas, A., Rossi, L., Ortolani, S. et al. 2018, PASA, 35, 21
- Pérez-Villegas, A., Barbuy, B., Kerber, L. et al. 2020, MNRAS, 491, 3251
- Peterson, R., Barbuy, B. & Spite, M. A&A, 638, A64 (2020)
- Pian et al. 2017, Nature, 551, 67
- Pickering, J. C. 1996, ApJ, 811, 822
- Pietrinferni, A., Cassisi, S., Salaris, M., Castelli, F. 2006, ApJ, 642, 797
- Pignatari, M., Gallino, R., Heil, M., Wiescher, M., K'appeler, F., Herwig, F., Bisterzo, S. 2010, ApJ, 710, 1557P
- Pietrukowicz P, Udalski A, Soszynski I, et al. 2012. *ApJ* 750:169
- Pignatari, M., Gallino, R., Heil, M. et al. 2010, ApJ, 710, 1557
- Piskunov, N., Kupka, F., Ryabchikova, T., Weiss, W., Jeffery, C., 1995, A&AS, 112, 525
- Placco, V. M., Beers, T. C., Roederer, I. U., et al. 2014, ApJ, 790, 34
- Placco et al. 2015, ApJ, 812, 109
- Placco, V.M., Holmbeck, E.M., Frebel, A., et al. 2017, ApJ, 844, 18
- Plez, B., Hill, V., Cayrel, R. et al. A&A, 428, L9 (2004)

- Plez, B. 2012, Turbospectrum: Code for spectral synthesis, ascl:1205.004, <http://adsabs.harvard.edu/abs/2012ascl.soft05004P>
- Primas et al. 2000a, *A&A*, 362, 666
- Primas et al. 2000b, *A&A*, 364, L4
- Pompéia, L., Hill, V., Spite, M. et al. 2008, *A&A*, 480, 379
- Queiroz, A.B.A., Chiappini, C., Pérez-Villegas, A. et al. 2021, *A&A*, 656, A156
- Ramírez, I., Allende Prieto, C. 2011, *ApJ*, 743, 135
- Recio-Blanco, A. 2014, *IAU Symp.* 298, 366
- Recio-Blanco, A. et al. 2017, *IAU Symposium* 334, in press
- Reeves, H., Fowler, W.A., Hoyle, F. 1970, *Nature*, 226, 727
- Reddy, B.E., Tomkin, J., Lambert, D.L., Allende Prieto, C. 2003, *MNRAS*, 340, 304
- Reddy, B.E., Lambert, D.L., Allende Prieto, C. 2006, *MNRAS*, 367, 1329
- Renzini, A. 2017, *MNRAS*, 469, L63
- Renzini, A., Gennaro, M., Zoccali, M. et al. 2018, *ApJ*, 863, 16
- Rich, R.M., Ortolani, S., Bica, E., Barbuy, B. 1998, *AJ*, 116, 1295
- Roederer, I. U., Preston, G. W., Thompson, I. B., et al., 2014, *AJ*, 147, 136
- Romano, D., Matteucci, F. 2007, 378, L59
- Rossi, L., Ortolani, S., Bica, E., Barbuy, B., Bonfanti, A. 2015, *MNRAS*, 450, 3270
- Rojas-Arriagada A, Recio-Blanco A, Hill V, et al. 2014. *A&A* 569:A103–119
- Rojas-Arriagada A, Recio-Blanco A, et al. 2017. *A&A* 601:A140
- Ryabchikova, T., Piskunov, N., Kurucz, R.L. et al. 2015, *PhyS*, 90, 054005
- Saito, R. et al. (VVV collaboration) 2012, *A&A*, 537, 107
- Sakari, C.M., Placco, V.M., Hansen, T. et al. 2018, *ApJ*, 854, L20

- 
- Sánchez-Blázquez, P., Peletier, R.F., Jiménez-Vicente, J., et al., 2006, MNRAS, 371, 703
- Saviane, I., da Costa, G.S., Held, E.V. et al. 2012, A&A, 540, A27
- Schiavon, R.P., Zamora, O., Carrera, R., et al. 2017, MNRAS, 465, 501
- Scott, P., Grevesse, N., Asplund, M., Sauval, A.J., Lind, K., Takeda, Y., Collet, R., Trampedach, R., Hayek, W. 2015a, A&A, 573, 26
- Schlafly, E., Finkbeiner, D.P. 2011, ApJ, 737, 103
- Schlaufman, Thompson & Casey, 2018, ApJ, 867, 98
- Schiavon, R.P., Barbuy, B. 1999, ApJ, 510, 934
- Schönrich, R., Binney, J., & Dehnen, W. 2010, MNRAS, 403, 1829
- Schultheis, M., Rojas-Arriagada, A., García-Pérez, A.E. et al. 2017, A&A, 600, A1
- Smith & Ruck 2000, A&A, 356, 570S
- Smith, V.V., Cunha, K., Shetrone, M.D. et al. 2013, ApJ, 765, 16
- Smartt et al. 2017, Nature, 551, 75
- Smith, R., Flynn, C., Candlish, G. N., Fellhauer, M., & Gibson, B. K. 2015, MNRAS, 448, 2934
- Smiljanic, R., Pasquini, L., Bonifacio, P., et al. 2009, A&A, 499, 103
- Smiljanic et al. 2014, Ap&SS, 354, 55
- Smiljanic, R., Zych, M. G., Pasquini, L., 2021, A&A, 646A 70S
- Shetrone, M., Bizyaev, D., Lawler, J.E. et al. 2015, ApJS, 221, 24
- Skúladóttir, Á., Tolstoy, E., Salvadori, S., Hill, V., Pettini, M. 2017, A&A, 606, A71
- Skúladóttir, Á., Salvadori, S., Pettini, M., Tolstoy, E., Hill, V. 2018, A&A, in press (ArXiv: 180207325).
- Skrutskie, M.F., Cutri, R.M., Stiening, R. et al. 2006, AJ, 131, 1163

- Smith & Ruck 2000, *A&A*, 356, 570S
- Siegel et al. 2019, *Nature*, 569, 241
- Siqueira-Mello, C., Spite, M., Barbuy, B. et al. *A&A*, 550, A122 (2013)
- Souza, S.O., Kerber, L.O., Barbuy, B. et al. 2020, *ApJ*, 890, 38
- Soto, M., Barbá, R., Gunthardt, G., Minniti, D., Lucas, P. et al. 2013, *A&A*, 552, A101
- Snedden, C., Gratton, R. G., Crocker D. A., 1991, *A&A*, 246, 354
- Snedden, C., Cowan, J.J., Lawler, J.E. et al. 2003, *ApJ*, 591, 936
- Snedden, C., Cowan, J.J., Gallino, R. 2008, *ARA&A*, 46, 241
- Sandford, N. R., Weisz, D. R. & Ting, Y.-S.: Forecasting Chemical Abundance Precision for Extragalactic Stellar Archaeology, *ApJS*, 249, 24 (2020)
- Spite, M. 1967, *Ann. Ap.* 30, 211
- Spite, F., Spite, M. 1982, *A&A*, 115, 357
- Spite, M., Cayrel, R., Plez, B. et al. *A&A*, 430, 655 (2005)
- Spite, M., Caffau, E., Andrievsky, S. et al. 2011, *A&A*, 528, A9
- Spite et al. 2019, *A&A*, 624, A44
- Starkenburger et al. 2017, *MNRAS*, 471, 2587
- Steffen, M., Prakashavicius, D., Caffau, E. et al. 2015, *A&A*, 583, 57
- Stetson, P., Pancino, E. 2008, *PASP*, 120, 1332
- Sukhbold, T., Ertl, T., Woosley, S.E., Brown, J.M., Janka, H.-T., 2016, *ApJ*, 828, 38
- Sobeck, J.S., Ivans, I. I., Simmerer, J. A., Snedden, C., Hoefflich, P., Fulbright, J. P., Kraft, R. P., 2006, *AJ*, 131, 2949
- Tominaga, Iwamoto & Nomoto, 2014, *ApJ*, 785, 98
- Terndrup, D.M. 1988, *AJ*, 96, 884

- 
- Timmes, F.X., Woosley, S.E, Weaver, T.A. 1995, *ApJS*, 98, 617
- Ting, Y.S., Freeman, K.C., Kobayashi, C., de Silva, G.M., Bland-Hawthorn, J. 2012, *MNRAS*, 421, 1231
- Tominaga, N., 2009, *ApJ*, 690, 526
- Valenti, J.A., Piskunov, N. 1996, *A&AS*, 118, 595
- Valenti, E., Ferraro, F.R., Origlia, L. 2007, *AJ*, 133, 1287
- van den Bergh, S., Hagen, G.L. 1975, *AJ*, 80, 11
- van de Hoek L.B., Groenewegen M.A.T., 1997, *A&A*, 123, 305
- van der Swaelmen, M., Barbuy, B., Hill, V., et al. 2016, *A&A*, 586, A1
- Vásquez, S., Zoccali, M., Hill, V. et al. 2015, *A&A*, 580, A121
- Vásquez, S., Saviane, I., Held, E.V. et al. 2018, *A&A*, 619, A13
- Vasiliev, E. 2018, *MNRAS*, 484, 2832
- Viegas, S. M., Friaça, A. C. S., Gruenwald, R., 1999, *MNRAS*, 309, 355
- Villemoes, P., van Leeuwen, R., Arnesen, A. et al. 1992, *PhRvA*, 45, 6241
- Umeda, H., Nomoto, K., 2002, *ApJ*, 565, 385
- Umeda, H., Nomoto, K., 2003, *Nature*, 422, 871
- Umeda, H., Nomoto, K., 2005, *ApJ*, 619, 427
- Wanajo, S. 2007, *ApJ*, 666, L77
- Walker, A.R., Terndeup, D.M. 1991, *ApJ*, 378, 119
- Watson et al. 2019, *Nature*, 574, 497
- Winteler et al. 2012, *ApJ*, 750, L22
- Wolf et al. 2018, *PASA*, 35, 10
- Wood, M.P., Lawler, J.E., Den Hartog, E.A., Sneden, C., Cowan, J.J. 2014, *ApJS*, 214, 18

- Woodgate, G. & Martin, J. Proc. Phys. Soc. A 70 485 1957
- Woosley, S.E., Arnett, W.D., Clayton, D.D. 1973, ApJS, 26, 231
- Woosley, S. E., Weaver, T. A. 1995, ApJS, 101, 181
- Woosley, Heger & Weaver, 2002, RvMP, 74, 1015
- Xu, X.D., Shi, J.R., Yan, H.L. 2019, ApJ, 875, 142
- Yoshida, T., Umeda, H., Nomoto, K., 2008, ApJ, 672, 1043
- Zanutta, A., Cristiani S., Atkinson, D. et al., 2022 ExA, <https://doi.org/10.1007/s10686-022-09837-w>
- Zoccali, M., Renzini, A., Ortolani, S., Bragaglia, A., Bohlin, R. et al. 2001a, ApJ, 553, 733
- Zoccali, M., Renzini, A., Ortolani, S., Bica, E., Barbuy, B. 2001b, AJ, 121, 2638
- Zoccali, M., Barbuy, B., Hill, V., Ortolani, S., Renzini, A., Bica, E., Momany, Y., Pasquini, L., Minniti, D., & Rich, R.M. 2004, A&A, 423, 507
- Zoccali, M., Lecureur, A., Barbuy, B., Hill, V., Renzini, A., et al. 2006, A&A, 457, L1
- Zoccali, M., Hill, V., Lecureur, A. et al. 2008, A&A, 486, 177
- Zoccali, M., Vásquez, S., Gonzalez, O.A. et al. 2017, A&A, 599, A12
- Zoccali, M., Valenti, E., Gonzalez, O.A. 2018, A&A, 618, A147

# Appendix



# Appendix A

## MUSE datacubes and selections

### A.1 Extracted stars from the MUSE datacubes with S/N selection.

Table A.1 - Extracted stars from the MUSE datacubes with S/N selection.

ID	Ra (J2000)	Dec (J2000)	X	Y	V	V-I	$v_r$ (km s <sup>-1</sup> )	$T_{eff}$ (K)	log g	[Fe/H]	[Mg/H]
0056	270.41190087763954	-26.84881101181451	1012.92	707.76	20.33	3.419	45.44	5502 ± 446	3.28 ± 1.12	-1.93 ± 0.40	0.28 ± 0.15
0072	270.41572393678052	-26.83931326833801	1114.09	991.63	17.87	3.812	71.46	4663 ± 424	1.91 ± 0.94	-1.07 ± 0.52	0.29 ± 0.16
0077	270.39844337660554	-26.83810927208998	653.68	1027.14	18.80	3.242	-73.29	4356 ± 214	1.97 ± 0.58	0.10 ± 0.23	0.10 ± 0.14
0081	270.40878978697526	-26.83563435071913	929.55	1101.25	18.42	3.841	43.78	5103 ± 790	2.48 ± 1.11	-0.55 ± 0.66	0.28 ± 0.17
0084	270.41628613193024	-26.83376140131479	1129.81	1157.05	18.74	3.937	40.57	5216 ± 764	2.65 ± 1.08	-0.49 ± 0.60	0.28 ± 0.17
0089	270.39971802548109	-26.83175463546964	687.86	1217.57	18.58	3.717	74.50	4834 ± 320	3.57 ± 0.95	-1.15 ± 0.43	0.23 ± 0.17
0092	270.40890223869229	-26.83148706400694	932.48	1225.10	18.88	4.252	57.60	4872 ± 514	2.21 ± 0.97	-1.04 ± 0.55	0.27 ± 0.17
0411	270.40878978697526	-26.84934607221381	929.19	691.60	19.44	3.342	55.90	5568 ± 506	2.97 ± 1.13	-1.79 ± 0.45	0.23 ± 0.17
0427	270.40594094367941	-26.84737302443697	853.42	750.13	19.99	3.357	29.74	5494 ± 468	3.10 ± 1.29	-2.04 ± 0.30	0.27 ± 0.15
0437	270.40357930558883	-26.84713893173680	790.31	757.66	17.94	3.820	65.87	4672 ± 429	2.12 ± 0.92	-1.00 ± 0.52	0.29 ± 0.17
0439	270.41193835972967	-26.84670418686454	1013.23	770.62	19.11	2.968	-10.02	4279 ± 214	1.95 ± 0.55	0.06 ± 0.25	0.11 ± 0.14
0440	270.40391668783866	-26.84630288242150	799.67	782.35	21.20	3.466	33.94	5423 ± 464	2.90 ± 1.16	-1.98 ± 0.37	0.28 ± 0.15
0444	270.40058027344475	-26.84647009277922	710.04	777.99	18.90	2.681	24.56	6187 ± 382	3.69 ± 0.80	0.22 ± 0.18	0.13 ± 0.15
0473	270.414824414117821	-26.84392846865514	1090.16	853.74	19.68	3.417	67.41	5130 ± 594	2.03 ± 0.93	-1.81 ± 0.48	0.31 ± 0.15
0476	270.41291288630140	-26.84386158303839	1039.90	855.81	18.96	2.186	38.52	5356 ± 350	4.08 ± 0.63	0.09 ± 0.27	0.14 ± 0.15
0486	270.40204231931438	-26.84319272469550	749.29	875.62	20.68	3.995	63.04	5392 ± 426	3.00 ± 1.05	-1.79 ± 0.43	0.28 ± 0.16
0508	270.40740286608144	-26.84118612594116	892.29	935.38	20.61	3.368	55.55	5549 ± 466	3.04 ± 1.04	-1.88 ± 0.43	0.26 ± 0.16
0512	270.41920946639590	-26.84038347647692	1207.38	953.44	20.32	3.504	6.37	5506 ± 550	3.26 ± 0.95	-1.05 ± 0.55	0.23 ± 0.17
0513	270.40084269441360	-26.84045036414967	717.94	957.50	18.12	3.950	52.90	4634 ± 370	1.97 ± 0.91	-1.16 ± 0.47	0.30 ± 0.16
0517	270.39859333662503	-26.84038347647692	657.66	959.92	20.77	3.642	74.68	5394 ± 450	3.04 ± 1.35	-2.03 ± 0.34	0.28 ± 0.15
0519	270.40522871287448	-26.84014936931105	834.70	966.68	18.82	4.022	89.65	5251 ± 420	2.77 ± 1.19	-0.53 ± 0.69	0.27 ± 0.17
0520	270.41220073374063	-26.83994870564067	1020.38	972.22	17.97	3.688	66.53	4510 ± 450	1.38 ± 0.88	-1.29 ± 0.49	0.30 ± 0.14
0527	270.40282956083570	-26.83874471614948	770.35	1008.17	21.09	3.716	38.01	5517 ± 428	3.13 ± 1.15	-1.85 ± 0.43	0.27 ± 0.16
0531	270.40133004476354	-26.83797549393892	730.15	1031.03	20.45	2.744	-29.51	5856 ± 464	3.57 ± 0.67	0.11 ± 0.23	0.14 ± 0.14
0533	270.41920946639590	-26.83790860480411	1207.26	1033.13	20.79	3.176	77.19	4707 ± 310	2.44 ± 0.69	-0.17 ± 0.40	0.12 ± 0.16
0538	270.4004303181837	-26.83700559761804	706.96	1060.15	19.55	3.686	58.47	5374 ± 490	2.77 ± 1.31	-2.20 ± 0.21	0.29 ± 0.14
0544	270.40402914819009	-26.83693870791048	802.09	1062.45	18.22	2.341	-24.86	7272 ± 180	3.78 ± 0.52	0.22 ± 0.15	0.06 ± 0.17
0549	270.41917198860142	-26.83626980866259	1206.10	1082.43	18.34	3.984	62.58	4625 ± 401	1.66 ± 0.96	-1.34 ± 0.51	0.33 ± 0.14
0554	270.39728117444548	-26.83586846721821	622.57	1094.94	18.25	3.849	64.49	5093 ± 538	2.73 ± 1.13	-1.04 ± 0.53	0.26 ± 0.17
0556	270.41673588446287	-26.83536678841363	1141.40	1109.26	20.24	3.541	7.81	5311 ± 484	3.61 ± 0.91	-0.72 ± 0.49	0.22 ± 0.16
0568	270.39904321455822	-26.83479821641681	669.99	1126.52	19.96	3.248	-104.96	4465 ± 307	2.34 ± 0.85	0.00 ± 0.30	0.13 ± 0.16
0569	270.39863082657450	-26.83453065213716	658.29	1134.33	21.30	3.664	22.11	5447 ± 447	3.07 ± 1.34	-2.01 ± 0.32	0.28 ± 0.15
0571	270.41534913724621	-26.83476477091640	1104.23	1127.62	17.69	4.144	68.77	4480 ± 345	1.73 ± 0.88	-1.14 ± 0.42	0.29 ± 0.16
0573	270.40125506803014	-26.83469787988597	728.67	1129.96	18.09	4.245	-111.04	3982 ± 244	1.41 ± 0.66	-0.68 ± 0.36	0.20 ± 0.16
0574	270.40016789544495	-26.83449720655778	699.74	1135.72	17.50	3.996	56.12	4912 ± 404	2.45 ± 1.03	-1.51 ± 0.43	0.28 ± 0.16
0578	270.41864729715377	-26.83419619589934	1192.40	1144.92	18.47	4.122	70.39	4529 ± 386	1.51 ± 0.94	-1.35 ± 0.45	0.30 ± 0.14
0582	270.40155497443243	-26.83379484711128	736.12	1156.14	17.82	3.900	64.45	4505 ± 376	1.76 ± 0.89	-1.16 ± 0.47	0.32 ± 0.16
0584	270.41310029354156	-26.83366106386613	1044.23	1160.69	19.74	4.040	73.12	4925 ± 631	2.09 ± 1.19	-1.31 ± 0.60	0.33 ± 0.13
0593	270.40346684444040	-26.83282491500708	787.65	1185.26	18.18	2.277	-16.91	6024 ± 358	3.80 ± 0.75	0.27 ± 0.15	0.12 ± 0.15
0595	270.41197584179770	-26.83265768449528	1014.50	1190.66	20.21	3.861	47.95	5556 ± 470	3.07 ± 1.11	-1.90 ± 0.43	0.28 ± 0.15
0596	270.42059612922424	-26.83262423836331	1244.70	1191.40	21.21	3.834	53.65	5380 ± 448	3.04 ± 1.17	-2.12 ± 0.27	0.29 ± 0.15
0597	270.41632361142973	-26.83252389990823	1130.98	1194.59	20.71	5.679	-31.57	5318 ± 432	3.08 ± 1.33	-1.96 ± 0.34	0.28 ± 0.15
0606	270.41977163065576	-26.83175463546964	1222.62	1217.03	18.38	2.237	-4.29	6283 ± 364	4.13 ± 0.41	-0.05 ± 0.28	0.16 ± 0.15
0610	270.40635328417665	-26.83135327803886	864.91	1229.44	18.27	3.985	61.81	4884 ± 595	2.47 ± 0.99	-0.54 ± 0.56	0.28 ± 0.16
0611	270.40365427957710	-26.83118604535684	792.25	1234.08	19.50	3.688	69.07	5226 ± 678	2.37 ± 1.16	-1.47 ± 0.59	0.28 ± 0.17
0615	270.41692328041040	-26.83078468591398	1146.62	1246.95	18.63	4.089	64.79	5372 ± 874	2.83 ± 1.08	-0.40 ± 0.64	0.26 ± 0.17
0626	270.40627831337639	-26.82964749311400	862.07	1280.35	20.96	4.045	59.56	5472 ± 467	3.11 ± 1.28	-2.00 ± 0.33	0.28 ± 0.15
0631	270.42070856001681	-26.82911233961694	1247.46	1296.56	18.68	3.530	78.43	5433 ± 454	2.75 ± 0.98	-1.95 ± 0.39	0.29 ± 0.15
0639	270.41426220607519	-26.82830960463914	1075.54	1320.77	20.82	4.687	31.80	5194 ± 412	2.95 ± 1.25	-1.88 ± 0.40	0.28 ± 0.15
0644	270.41887216544848	-26.82767410208828	1198.96	1339.58	20.25	3.580	-33.13	5080 ± 406	3.05 ± 0.79	-0.21 ± 0.41	0.19 ± 0.17
0645	270.41343762517886	-26.82717238703481	1053.09	1354.89	19.53	3.807	62.45	6465 ± 459	3.84 ± 0.66	-0.18 ± 0.40	0.15 ± 0.17
0649	270.40942701073709	-26.82713893928574	946.51	1355.98	20.10	3.966	18.10	5561 ± 476	3.21 ± 1.18	-2.06 ± 0.28	0.28 ± 0.15
0656	270.41830999321689	-26.82650343018094	1183.90	1374.20	19.85	2.326	81.44	6208 ± 393	3.95 ± 0.48	-0.14 ± 0.31	0.17 ± 0.14
0660	270.40286704828367	-26.82586791751890	771.56	1393.63	21.03	3.596	89.21	5597 ± 448	3.32 ± 1.10	-2.04 ± 0.32	0.29 ± 0.14
0919	270.40372925347680	-26.84810874119522	794.03	728.94	19.68	2.602	-29.32	5817 ± 470	3.52 ± 0.84	0.18 ± 0.21	0.15 ± 0.15
0931	270.41789773041393	-26.83994870564067	1172.17	972.00	19.77	4.151	22.12	3950 ± 208	1.48 ± 0.58	-0.45 ± 0.40	0.17 ± 0.16
0936	270.40346684444040	-26.83446376096855	787.64	1136.18	17.35	4.109	73.77	4406 ± 286	1.89 ± 0.79	-0.96 ± 0.41	0.26 ± 0.17
0944	270.41066395624409	-26.82984817502465	979.89	1274.78	21.86	4.179	87.53	5372 ± 448	3.04 ± 1.30	-2.21 ± 0.21	0.28 ± 0.14
1255	270.40732789652100	-26.84887789450299	890.81	705.01	20.41	3.328	31.16	5743 ± 486	3.36 ± 0.86	-1.34 ± 0.56	0.27 ± 0.16
1263	270.40893972255373	-26.84834283188660	933.62	721.41	20.71	3.557	119.81	5429 ± 474	3.46 ± 0.77	-0.68 ± 0.53	0.26 ± 0.16
1266	270.40676562199502	-26.84700516426188	875.96	761.52	20.13	3.448	-74.53	4743 ± 370	2.43 ± 0.67	-0.59 ± 0.52	0.17 ± 0.18
1279	270.41047654180801	-26.84713893173680	974.17	757.19	20.88	3.505	-23.44	5430 ± 482	2.97 ± 1.02	-1.52 ± 0.50	0.24 ± 0.17
1285	270.40522871287448	-26.84620255608814	834.61	785.31	20.79	3.514	24.70	5508 ± 488	3.43 ± 1.18	-1.55 ± 0.52	0.30 ± 0.14
1288	270.40875230302527	-26.84650353482109	928.55	776.54	21.28	3.396	-4.80	5350 ± 440	3.03 ± 1.31	-1.98 ± 0.36	0.28 ± 0.15
1291	270.41958424312276	-26.84633632451283	1217.26	781.37	19.82	2.547	-30.21	5256 ± 477	2.75 ± 0.99	-1.24 ± 0.55	0.21 ± 0.16

Table A.1 - continued.

ID	Ra (J2000)	Dec (J2000)	X	Y	V	V-I	$v_r$ (km s $^{-1}$ )	$T_{eff}$ (K)	log g	[Fe/H]	[Mg/H]
1293	270.41681084290832	-26.84620255608814	1143.36	785.14	19.43	3.339	35.35	5512 $\pm$ 474	2.97 $\pm$ 0.99	-1.81 $\pm$ 0.44	0.27 $\pm$ 0.16
1302	270.41594881543824	-26.84560059621841	1120.91	803.82	20.84	3.348	19.40	5573 $\pm$ 438	3.30 $\pm$ 1.15	-1.95 $\pm$ 0.40	0.27 $\pm$ 0.15
1307	270.41864729715377	-26.84493174816004	1192.44	823.73	20.62	3.407	38.03	5559 $\pm$ 454	3.20 $\pm$ 1.20	-1.99 $\pm$ 0.36	0.28 $\pm$ 0.15
1317	270.40845243062859	-26.84456388004165	920.72	834.08	20.93	2.948	17.51	5965 $\pm$ 428	3.73 $\pm$ 0.79	-0.64 $\pm$ 0.40	0.20 $\pm$ 0.17
1321	270.40350433151201	-26.84422945344111	788.45	844.79	20.53	2.384	12.47	5446 $\pm$ 447	3.29 $\pm$ 1.00	-1.38 $\pm$ 0.51	0.26 $\pm$ 0.16
1322	270.40650322551147	-26.8438322419999	868.55	840.65	21.70	3.594	75.88	5688 $\pm$ 470	3.34 $\pm$ 1.08	-2.00 $\pm$ 0.38	0.28 $\pm$ 0.15
1324	270.42070856001681	-26.84426289614565	1247.52	843.99	19.08	3.031	-61.92	4825 $\pm$ 270	2.02 $\pm$ 1.00	-2.07 $\pm$ 0.32	0.30 $\pm$ 0.14
1326	270.42044622119079	-26.84372781168620	1240.75	859.02	19.42	2.225	34.96	5220 $\pm$ 373	3.51 $\pm$ 0.74	0.15 $\pm$ 0.21	0.12 $\pm$ 0.13
1330	270.40069273970704	-26.84402879700613	713.35	850.24	20.85	5.001	-196.25	5439 $\pm$ 428	3.20 $\pm$ 1.34	-1.97 $\pm$ 0.35	0.28 $\pm$ 0.15
1333	270.40211729511799	-26.84389502585170	751.14	854.84	20.81	3.905	-150.60	5091 $\pm$ 484	2.89 $\pm$ 0.95	-1.20 $\pm$ 0.56	0.26 $\pm$ 0.17
1337	270.40436652804897	-26.84272452150244	811.48	889.54	21.24	3.682	-56.14	4962 $\pm$ 460	2.58 $\pm$ 0.99	-1.19 $\pm$ 0.56	0.25 $\pm$ 0.17
1338	270.41722311277505	-26.84366092595078	1154.03	861.08	20.84	3.550	48.13	5497 $\pm$ 448	3.03 $\pm$ 1.06	-1.79 $\pm$ 0.45	0.29 $\pm$ 0.15
1339	270.41684832209785	-26.84359404017581	1144.64	863.17	20.71	3.839	79.63	4355 $\pm$ 294	2.05 $\pm$ 0.64	-0.07 $\pm$ 0.34	0.14 $\pm$ 0.15
1342	270.41332518149903	-26.84332649668046	1050.16	871.39	19.54	3.358	66.38	4589 $\pm$ 355	1.33 $\pm$ 0.75	-1.75 $\pm$ 0.44	0.33 $\pm$ 0.12
1343	270.41748546493153	-26.84172122242159	1161.95	919.27	20.30	2.773	-0.70	6088 $\pm$ 208	3.44 $\pm$ 1.05	-2.05 $\pm$ 0.36	0.27 $\pm$ 0.17
1345	270.40714047223253	-26.84315928167454	885.10	876.72	18.85	2.266	-8.63	5936 $\pm$ 378	3.82 $\pm$ 0.75	0.26 $\pm$ 0.16	0.12 $\pm$ 0.15
1346	270.41092633552461	-26.84312583864370	986.21	877.12	19.17	3.423	50.91	4578 $\pm$ 363	1.31 $\pm$ 0.81	-1.54 $\pm$ 0.50	0.32 $\pm$ 0.12
1353	270.40620334248763	-26.84269107834307	860.67	890.05	19.27	3.669	46.19	4610 $\pm$ 405	1.52 $\pm$ 0.84	-1.64 $\pm$ 0.44	0.28 $\pm$ 0.12
1367	270.42123323441365	-26.84115268232712	1261.10	936.40	20.00	3.398	27.30	5528 $\pm$ 592	2.82 $\pm$ 1.02	-1.65 $\pm$ 0.55	0.28 $\pm$ 0.17
1368	270.40965191171358	-26.84152056153792	952.73	925.10	17.73	3.714	46.31	4572 $\pm$ 364	1.51 $\pm$ 0.88	-1.36 $\pm$ 0.45	0.29 $\pm$ 0.14
1378	270.41579889642168	-26.84081824564326	1116.35	946.41	20.76	3.584	60.84	5782 $\pm$ 590	2.96 $\pm$ 0.96	-1.57 $\pm$ 0.55	0.24 $\pm$ 0.17
1379	270.40297951049473	-26.84071791444541	774.97	949.56	20.29	4.597	4.63	3817 $\pm$ 185	1.19 $\pm$ 0.84	-0.38 $\pm$ 0.35	0.17 $\pm$ 0.12
1380	270.40871481905322	-26.84061758315861	927.83	952.88	18.55	3.358	42.78	5715 $\pm$ 180	2.38 $\pm$ 0.89	-0.65 $\pm$ 0.54	0.20 $\pm$ 0.18
1389	270.42067108310812	-26.83998214961044	1246.36	971.64	19.86	3.370	51.73	5800 $\pm$ 740	3.03 $\pm$ 1.16	-1.06 $\pm$ 0.66	0.21 $\pm$ 0.17
1394	270.40237970973322	-26.83988181767150	758.73	974.79	20.51	3.991	26.87	4306 $\pm$ 324	1.93 $\pm$ 0.78	-0.68 $\pm$ 0.48	0.18 $\pm$ 0.17
1395	270.42235752207716	-26.83948048902660	1291.20	986.08	20.02	3.381	48.92	5489 $\pm$ 518	2.81 $\pm$ 0.93	-1.82 $\pm$ 0.46	0.28 $\pm$ 0.16
1399	270.40399166142845	-26.83934671249548	801.46	990.74	19.76	3.821	63.09	4726 $\pm$ 461	1.68 $\pm$ 1.02	-1.73 $\pm$ 0.48	0.30 $\pm$ 0.13
1400	270.40361679259399	-26.83917949160931	791.40	995.22	21.27	4.438	63.08	4764 $\pm$ 367	2.59 $\pm$ 0.71	-0.52 $\pm$ 0.47	0.19 $\pm$ 0.17
1402	270.39855584665332	-26.83927982417065	656.25	992.25	20.55	2.800	-28.95	5547 $\pm$ 453	3.41 $\pm$ 0.73	0.07 $\pm$ 0.26	0.15 $\pm$ 0.16
1406	270.41171346685678	-26.83907915895905	1007.24	998.86	17.34	3.912	60.66	4552 $\pm$ 330	1.76 $\pm$ 0.76	-1.12 $\pm$ 0.36	0.33 $\pm$ 0.14
1411	270.40219227083304	-26.83864438311399	753.70	1011.15	20.99	3.582	79.36	5398 $\pm$ 452	3.04 $\pm$ 1.31	-1.98 $\pm$ 0.32	0.28 $\pm$ 0.15
1412	270.41935937735241	-26.83867782746903	1211.30	1010.98	20.43	2.630	59.85	5652 $\pm$ 414	3.48 $\pm$ 0.85	-1.09 $\pm$ 0.49	0.23 $\pm$ 0.17
1413	270.40451647407730	-26.83857749437426	815.57	1013.86	20.19	3.636	64.42	5166 $\pm$ 543	2.36 $\pm$ 1.05	-1.65 $\pm$ 0.51	0.27 $\pm$ 0.16
1414	270.417897370041393	-26.83851060559504	1172.89	1015.09	19.36	3.793	62.28	4771 $\pm$ 576	1.60 $\pm$ 0.92	-1.26 $\pm$ 0.55	0.32 $\pm$ 0.11
1424	270.40605340404431	-26.83750726916576	856.06	1045.16	20.68	3.193	12.71	7535 $\pm$ 139	3.46 $\pm$ 0.84	-1.72 $\pm$ 0.59	0.22 $\pm$ 0.18
1425	270.39896823512407	-26.83687181816342	667.54	1064.16	19.66	3.550	47.61	5527 $\pm$ 541	2.89 $\pm$ 0.97	-1.70 $\pm$ 0.48	0.26 $\pm$ 0.17
1426	270.40852739886060	-26.83764104786989	922.82	1041.32	19.62	3.630	47.58	4520 $\pm$ 296	1.32 $\pm$ 0.73	-1.93 $\pm$ 0.39	0.30 $\pm$ 0.12
1428	270.41977163065576	-26.83764104786989	1222.77	1041.69	19.49	2.953	157.45	5584 $\pm$ 581	3.29 $\pm$ 1.06	-1.12 $\pm$ 0.57	0.28 $\pm$ 0.15
1431	270.40747783555332	-26.83707248728611	894.83	1058.69	20.73	3.746	69.00	5974 $\pm$ 564	3.48 $\pm$ 1.00	-0.91 $\pm$ 0.52	0.28 $\pm$ 0.15
1433	270.41804764447045	-26.83723971128347	1176.21	1053.57	19.48	3.204	50.22	6622 $\pm$ 139	3.50 $\pm$ 0.83	-1.37 $\pm$ 0.48	0.24 $\pm$ 0.18
1436	270.40331689593256	-26.83690526304189	783.33	1063.18	21.33	3.117	55.79	5096 $\pm$ 420	3.08 $\pm$ 1.22	-1.52 $\pm$ 0.47	0.27 $\pm$ 0.15
1441	270.41197584179770	-26.836663770373768	1014.86	1071.40	17.49	3.923	50.43	5438 $\pm$ 280	1.66 $\pm$ 0.69	-1.08 $\pm$ 0.37	0.34 $\pm$ 0.13
1443	270.40207980722721	-26.83590191239287	750.86	1093.99	20.31	3.432	36.55	4257 $\pm$ 484	2.97 $\pm$ 0.79	-0.22 $\pm$ 0.42	0.21 $\pm$ 0.17
1444	270.41699823863445	-26.83643703384482	1148.03	1077.47	20.79	3.428	51.21	5442 $\pm$ 447	2.97 $\pm$ 1.17	-1.95 $\pm$ 0.35	0.28 $\pm$ 0.15
1445	270.40848991475565	-26.83640358882812	921.63	1078.11	21.51	3.577	78.78	5503 $\pm$ 462	3.13 $\pm$ 1.28	-2.05 $\pm$ 0.28	0.28 $\pm$ 0.15
1446	270.41519921681248	-26.83626980866259	1100.71	1082.30	21.34	3.426	48.87	5617 $\pm$ 462	3.23 $\pm$ 1.22	-2.02 $\pm$ 0.29	0.28 $\pm$ 0.15
1447	270.42093342100407	-26.83616947343477	1253.94	1085.56	19.00	3.681	60.67	5444 $\pm$ 578	2.62 $\pm$ 1.06	-1.86 $\pm$ 0.47	0.27 $\pm$ 0.16
1448	270.41201332384355	-26.83543367904923	1015.41	1107.86	20.09	3.801	38.76	4649 $\pm$ 258	1.50 $\pm$ 0.78	-2.00 $\pm$ 0.36	0.29 $\pm$ 0.14
1449	270.40729041170761	-26.83576813163499	889.55	1097.08	20.42	2.777	-23.21	5735 $\pm$ 479	3.93 $\pm$ 0.67	-0.29 $\pm$ 0.41	0.18 $\pm$ 0.16
1452	270.39971802548109	-26.83543367904923	687.37	1107.17	19.81	3.289	114.83	5036 $\pm$ 428	2.91 $\pm$ 0.83	-0.86 $\pm$ 0.47	0.21 $\pm$ 0.17
1455	270.40582848671522	-26.83536678841363	850.21	1109.77	19.74	2.408	-37.07	6394 $\pm$ 413	3.87 $\pm$ 0.61	0.20 $\pm$ 0.18	0.12 $\pm$ 0.16
1457	270.42059612922424	-26.83489855285882	1244.78	1123.98	21.24	3.693	58.68	5398 $\pm$ 438	3.10 $\pm$ 1.17	-2.17 $\pm$ 0.24	0.29 $\pm$ 0.14
1458	270.40976436190294	-26.83516611626990	955.51	1115.55	20.84	6.019	-238.23	3612 $\pm$ 74	1.22 $\pm$ 0.71	0.10 $\pm$ 0.17	0.17 $\pm$ 0.14
1464	270.42333188859749	-26.83463098881604	1317.18	1131.98	18.98	2.253	13.55	5357 $\pm$ 473	3.11 $\pm$ 0.79	0.07 $\pm$ 0.26	0.17 $\pm$ 0.17
1465	270.39780604257140	-26.83422964156754	636.25	1143.81	21.11	3.709	63.27	5532 $\pm$ 466	3.06 $\pm$ 1.17	-1.95 $\pm$ 0.36	0.27 $\pm$ 0.16
1470	270.42108332788604	-26.83376140131479	1257.76	1157.47	18.94	2.226	9.61	5880 $\pm$ 400	3.59 $\pm$ 0.78	-0.94 $\pm$ 0.44	0.21 $\pm$ 0.17
1476	270.39840588654533	-26.83346038870239	652.50	1166.94	19.80	3.155	-1.17	5550 $\pm$ 485	3.04 $\pm$ 0.99	-1.81 $\pm$ 0.46	0.26 $\pm$ 0.16
1478	270.41748546493153	-26.83292525319577	1161.51	1182.79	21.38	3.854	-72.09	5226 $\pm$ 408	3.02 $\pm$ 1.28	-1.70 $\pm$ 0.48	0.26 $\pm$ 0.16
1482	270.40234222199746	-26.83299214527224	757.69	1180.27	20.26	3.583	56.99	5426 $\pm$ 505	2.76 $\pm$ 1.06	-1.85 $\pm$ 0.45	0.28 $\pm$ 0.16
1483	270.40267961082242	-26.83272457672959	766.17	1188.28	21.10	3.775	-23.77	4833 $\pm$ 361	2.52 $\pm$ 0.64	-0.52 $\pm$ 0.46	0.18 $\pm$ 0.17
1485	270.41336266274777	-26.83295869923892	1051.06	1181.79	18.66	2.235	-12.52	5383 $\pm$ 303	4.21 $\pm$ 0.55	0.20 $\pm$ 0.20	0.12 $\pm$ 0.12
1489	270.40597842928986	-26.83255734606978	854.06	1193.07	21.17	3.940	164.16	4840 $\pm$ 472	2.51 $\pm$ 0.88	-0.90 $\pm$ 0.53	0.22 $\pm$ 0.17
1493											

Table A.1 - continued.

ID	Ra (J2000)	Dec (J2000)	X	Y	V	V-I	$v_r$ (km s $^{-1}$ )	$T_{eff}$ (K)	log g	[Fe/H]	[Mg/H]
2047	270.41058899053604	-26.83590191239287	977.29	1093.88	20.81	3.056	31.32	5646 ± 435	3.37 ± 1.06	-1.95 ± 0.41	0.26 ± 0.15
2051	270.40335438309268	-26.83563435071913	784.68	1101.81	19.18	3.838	-63.93	4724 ± 412	2.17 ± 0.78	-0.62 ± 0.44	0.29 ± 0.15
2055	270.40136753309707	-26.83533334308101	731.65	1110.99	18.01	3.885	61.27	4648 ± 400	1.94 ± 0.93	-1.13 ± 0.50	0.29 ± 0.16
2057	270.39724368369906	-26.83506578006477	621.25	1118.70	20.25	3.872	52.29	4639 ± 390	2.27 ± 0.81	-0.91 ± 0.56	0.21 ± 0.18
2059	270.41321273761992	-26.83489855285882	1047.41	1123.13	21.58	4.099	-54.03	4697 ± 346	2.45 ± 0.64	-0.21 ± 0.41	0.16 ± 0.17
2062	270.40886475480875	-26.83419619589934	931.93	1144.49	20.25	4.076	45.12	5545 ± 631	3.08 ± 1.10	-1.02 ± 0.57	0.23 ± 0.17
2069	270.40582848671522	-26.83386173867463	850.92	1154.26	20.64	3.245	55.75	6489 ± 156	3.43 ± 0.97	-1.93 ± 0.52	0.25 ± 0.17
2072	270.40747783555332	-26.83362761803018	894.61	1161.70	20.12	3.221	-103.85	4649 ± 355	2.70 ± 0.86	-0.09 ± 0.36	0.15 ± 0.15
2077	270.41546157733899	-26.83322626722906	1107.45	1173.62	21.75	3.734	73.49	5514 ± 462	3.22 ± 1.17	-2.06 ± 0.28	0.29 ± 0.15
2082	270.40080520577015	-26.83205565261057	716.65	1208.71	19.25	2.193	-45.91	6214 ± 406	4.19 ± 0.34	-0.32 ± 0.37	0.20 ± 0.16
2102	270.42209519007167	-26.82964749311400	1284.65	1280.37	20.65	3.232	-72.18	5313 ± 466	3.46 ± 1.06	-1.05 ± 0.50	0.23 ± 0.16
2107	270.41999649496461	-26.82904544525234	1228.16	1298.77	19.34	2.142	48.31	5657 ± 404	3.86 ± 0.63	0.12 ± 0.23	0.14 ± 0.14
2129	270.417373202842591	-26.82670411765099	1158.46	1368.99	20.71	3.577	96.77	5460 ± 436	3.19 ± 1.23	-1.94 ± 0.39	0.27 ± 0.15
2139	270.41797268748644	-26.82598626185992	1174.61	1390.36	19.07	2.279	-16.74	6571 ± 342	3.93 ± 0.56	-0.61 ± 0.40	0.17 ± 0.17
2352	270.41103878345558	-26.84539994221631	989.78	809.38	19.38	3.284	45.49	5131 ± 816	1.68 ± 0.98	-1.47 ± 0.52	0.33 ± 0.13
2354	270.41392487882194	-26.84506551808822	1066.26	819.62	20.34	3.541	38.87	5533 ± 446	3.12 ± 1.10	-1.80 ± 0.47	0.28 ± 0.16
2355	270.41429968677039	-26.84473109297108	1076.29	829.32	19.03	3.459	67.11	4710 ± 251	1.65 ± 0.68	-1.91 ± 0.38	0.25 ± 0.12
2356	270.41160102012145	-26.84466420782898	1004.81	831.79	21.49	3.334	44.70	5495 ± 450	3.09 ± 1.33	-2.01 ± 0.29	0.28 ± 0.15
2374	270.41564897705081	-26.83570124119681	1112.35	1099.31	20.57	2.971	-21.89	6810 ± 154	3.50 ± 0.92	-1.88 ± 0.50	0.25 ± 0.17
2379	270.41587385597427	-26.83222288401026	1118.52	1203.20	21.38	4.150	48.64	5465 ± 402	3.12 ± 1.12	-1.90 ± 0.41	0.27 ± 0.15
2381	270.40144250969763	-26.83041677184377	733.52	1257.98	19.75	3.384	52.14	6118 ± 644	3.27 ± 0.94	-0.90 ± 0.55	0.23 ± 0.19
2482	270.41010171127533	-26.84640320866580	964.95	779.80	20.60	3.351	34.54	5615 ± 452	3.37 ± 1.10	-1.88 ± 0.43	0.27 ± 0.15
2485	270.40560357218914	-26.84623599820915	844.45	784.37	20.40	3.227	-0.22	4973 ± 446	3.33 ± 1.22	-1.62 ± 0.36	0.30 ± 0.15
2493	270.40867733505900	-26.84366092595078	926.84	861.78	19.91	3.497	51.99	5001 ± 500	2.09 ± 1.02	-1.77 ± 0.45	0.29 ± 0.16
2494	270.41482441417821	-26.84259074880568	1090.80	893.86	21.06	2.171	19.19	5203 ± 344	3.58 ± 0.71	0.08 ± 0.25	0.14 ± 0.14
2496	270.40065525097509	-26.84329305369905	712.98	872.37	21.33	3.792	27.89	5591 ± 423	3.19 ± 1.34	-2.05 ± 0.28	0.29 ± 0.15
2497	270.41546157733899	-26.84315928167454	1107.43	876.11	20.68	2.730	-24.30	7337 ± 134	3.66 ± 0.83	-1.71 ± 0.63	0.22 ± 0.17
2499	270.41707319676988	-26.84252386239799	1150.21	895.89	21.92	3.542	26.24	5649 ± 510	3.22 ± 1.10	-2.06 ± 0.28	0.27 ± 0.15
2500	270.41726059172095	-26.84295862334118	1155.22	882.88	20.78	3.622	44.04	5694 ± 446	3.10 ± 0.95	-1.71 ± 0.48	0.26 ± 0.17
2505	270.40575351592909	-26.84168777896568	848.28	920.43	19.20	3.204	128.40	4299 ± 220	1.92 ± 0.59	0.03 ± 0.28	0.11 ± 0.15
2506	270.40545362872894	-26.84192188294944	840.91	913.68	20.39	3.716	48.97	5279 ± 643	2.42 ± 1.10	-1.65 ± 0.54	0.31 ± 0.15
2507	270.41542409733017	-26.84142023096267	1106.02	928.68	19.72	2.203	2.12	5087 ± 362	3.59 ± 0.80	0.16 ± 0.19	0.11 ± 0.12
2509	270.39690626598491	-26.84182155272999	612.08	916.87	19.90	2.606	13.31	5318 ± 391	3.48 ± 0.80	0.12 ± 0.24	0.13 ± 0.14
2511	270.41801016598953	-26.84165433549990	1175.63	921.54	20.59	3.487	42.20	5465 ± 462	3.01 ± 1.10	-1.86 ± 0.46	0.28 ± 0.16
2515	270.399834049327088	-26.84111923870320	690.11	937.87	20.68	3.547	71.01	5352 ± 433	3.08 ± 1.29	-2.05 ± 0.33	0.29 ± 0.15
2517	270.41883468745471	-26.84108579506941	1197.23	938.52	21.14	3.441	44.25	5548 ± 462	3.23 ± 1.14	-2.04 ± 0.34	0.28 ± 0.15
2518	270.41639857036233	-26.84024970101285	1132.82	963.10	20.05	3.554	48.25	5370 ± 551	2.81 ± 1.10	-1.78 ± 0.51	0.28 ± 0.16
2521	270.41879720943882	-26.83998214961044	1196.64	971.60	21.68	3.438	107.95	5497 ± 470	3.22 ± 1.21	-2.02 ± 0.33	0.28 ± 0.15
2523	270.40455396052903	-26.83981492966281	816.13	976.28	19.84	3.724	53.43	4627 ± 304	1.42 ± 0.72	-1.90 ± 0.35	0.30 ± 0.12
2525	270.40852739886060	-26.83964770946819	922.68	981.08	18.97	3.557	42.29	4631 ± 464	1.60 ± 0.90	-1.56 ± 0.49	0.27 ± 0.12
2526	270.41853486270742	-26.83911260318569	1189.45	997.87	21.39	3.533	59.48	5540 ± 434	3.15 ± 1.28	-1.97 ± 0.39	0.28 ± 0.15
2528	270.41100130083407	-26.83901227047617	988.86	1000.97	17.76	3.646	67.21	4603 ± 362	1.76 ± 0.94	-1.28 ± 0.47	0.31 ± 0.15
2531	270.41662344662865	-26.83864438311399	1138.03	1011.05	20.82	3.092	105.68	6102 ± 192	3.49 ± 1.01	-2.01 ± 0.41	0.27 ± 0.16
2532	270.41759790123791	-26.83824305008303	1164.84	1023.05	20.97	3.747	53.52	5484 ± 477	3.04 ± 1.02	-1.48 ± 0.52	0.26 ± 0.16
2534	270.41242562488651	-26.83754071385660	1026.74	1044.32	19.56	3.575	55.39	4806 ± 354	1.82 ± 0.97	-1.98 ± 0.33	0.31 ± 0.14
2537	270.40350433151201	-26.83790860480411	788.65	1033.32	19.60	2.893	16.65	7824 ± 132	3.13 ± 0.83	-1.54 ± 0.58	0.19 ± 0.21
2538	270.40564105799882	-26.83774138179427	845.04	1038.54	20.81	3.630	-119.00	4694 ± 334	2.52 ± 0.71	-0.01 ± 0.32	0.15 ± 0.15
2540	270.419022017720210	-26.83740693503398	1202.32	1048.31	20.26	2.779	-180.89	4860 ± 362	3.07 ± 0.84	-0.21 ± 0.40	0.20 ± 0.17
2543	270.40586597239206	-26.83697215276922	851.10	1061.65	19.93	2.494	-38.10	5390 ± 428	3.27 ± 0.85	0.21 ± 0.18	0.14 ± 0.15
2545	270.41842242806183	-26.83620291852058	1186.45	1084.14	20.34	3.140	-79.02	5531 ± 452	3.45 ± 0.63	-0.07 ± 0.32	0.17 ± 0.16
2546	270.40256714808004	-26.83657081381289	763.51	1073.61	19.30	2.277	-22.30	5760 ± 390	3.85 ± 0.66	0.18 ± 0.20	0.13 ± 0.14
2547	270.40222975865737	-26.83630325371879	754.38	1081.57	21.30	3.833	67.58	5498 ± 484	3.04 ± 1.24	-2.01 ± 0.33	0.27 ± 0.15
2548	270.41763537996241	-26.83657081381289	1165.23	1073.99	21.04	3.684	-61.24	4883 ± 357	2.69 ± 0.70	-0.14 ± 0.37	0.15 ± 0.17
2549	270.41643604979544	-26.83650392384860	1133.56	1075.53	20.79	3.162	19.28	5468 ± 472	3.13 ± 1.23	-2.02 ± 0.35	0.27 ± 0.15
2551	270.42033378993318	-26.83610258323353	1237.05	1087.50	19.92	4.580	-117.44	4944 ± 429	2.74 ± 1.08	-1.39 ± 0.49	0.27 ± 0.17
2552	270.400631579878760	-26.83586846721821	863.74	1094.38	21.60	3.533	32.71	5358 ± 462	3.00 ± 1.23	-2.21 ± 0.24	0.28 ± 0.14
2556	270.41699823863445	-26.83486510738803	1148.26	1124.29	21.27	3.910	65.11	5478 ± 450	3.10 ± 1.25	-2.10 ± 0.30	0.28 ± 0.15
2561	270.41246310666668	-26.83439686976047	1027.36	1138.66	20.40	3.656	58.40	5912 ± 624	3.06 ± 1.02	-1.85 ± 0.50	0.27 ± 0.17
2562	270.40207980722721	-26.83432997851290	750.53	1140.22	19.18	3.456	44.89	4760 ± 448	1.89 ± 0.93	-1.35 ± 0.52	0.28 ± 0.11
2563	270.419846585513294	-26.83399552168295	1224.68	1150.46	20.29	2.593	50.08	5447 ± 434	3.08 ± 1.34	-2.00 ± 0.34	0.28 ± 0.15
2566	270.40953946139498	-26.83312592930676	949.58	1176.23	20.28	4.189	77.73	5503 ± 593	2.90 ± 1.09	-1.50 ± 0.53	0.28 ± 0.17
2570	270.41624865240857	-26.83312592930676	1128.59	1176.58	21.42	3.828	30.92	5442 ± 480	3.08 ± 1.11	-1.69 ± 0.52	0.28 ± 0.15
2571	270.41681084290832	-26.83302559129567	1143.73	1179.18	21.03	3.857	42.02	5526 ± 465	3.23 ± 1.15	-2.04 ± 0.34	0.28 ± 0.15
2572	270.40710298730841	-26.83305903730923	884.72	1178.76	21.45	3.985	-20.11	5371 ± 440	2.89 ± 1.14	-1.91 ± 0.40	0.26 ± 0.15
2573	270.41283792325038	-26.83289180714274	1037.44	1183.96	20.57	4.048	49.09	5513 ± 545	3.02 ± 1.06	-1.63 ± 0.54	0.27 ± 0.16
2574	270.40601591487814	-26.83215599147999	855.66	1205.50	21.25	3.085	5.67	5381 ± 520	3.03 ± 0.98	-0.82 ± 0.53	0.19 ± 0.17
2575	270.41021416066764	-26.83205565261057	967.65	1208.54	19.98	4.012	41.64	5573 ± 543	2.88 ± 0.95	-1.61 ± 0.49	0.26 ± 0.17
2580	270.40241719744688	-26.83101881242823	759.21	1239.77	20.89	3.455	45.91	5607 ± 456	3.29 ± 1.07	-1.96 ± 0.40	0.28 ± 0.15
2581	270.40080520577015	-26.83145361752971	716.72	1226.51	20.81	3.558	163.33	5507 ± 441	3.22 ± 1.15	-1.88 ± 0.42	0.28 ± 0.15
2582	270.40792765052475	-26.83075123922963	906.16	1247.98	20.55	3.218	-7.15	6424 ± 218	3.44 ± 1.09	-2.04 ± 0.41	0.25 ± 0.17
2585	270.41055180764885	-26.83051711216310	976.85	1254.28	20.90	3.855					

Table A.1 - continued.

ID	Ra (J2000)	Dec (J2000)	X	Y	V	V-I	$v_r$ (km s $^{-1}$ )	$T_{eff}$ (K)	log g	[Fe/H]	[Mg/H]
2845	270.40177990330437	-26.83974804161461	742.28	978.78	19.91	2.632	-54.03	4863 $\pm$ 328	3.66 $\pm$ 0.85	0.12 $\pm$ 0.24	0.12 $\pm$ 0.12
2846	270.40702801739371	-26.83727315605332	882.52	1052.78	19.92	3.370	23.22	6995 $\pm$ 125	3.66 $\pm$ 0.84	-1.23 $\pm$ 0.55	0.22 $\pm$ 0.18
2848	270.40931455994996	-26.83650392384860	943.93	1075.06	20.03	3.633	47.92	5647 $\pm$ 640	3.10 $\pm$ 1.13	-1.18 $\pm$ 0.62	0.24 $\pm$ 0.17
2851	270.41040157587861	-26.83289180714274	972.15	1183.44	18.23	4.281	64.02	4737 $\pm$ 405	2.18 $\pm$ 0.88	-0.85 $\pm$ 0.47	0.26 $\pm$ 0.17
2889	270.40286704828367	-26.84777432508066	771.54	738.24	20.56	3.617	57.56	5402 $\pm$ 446	3.02 $\pm$ 1.27	-1.98 $\pm$ 0.35	0.28 $\pm$ 0.15
2892	270.40796513496178	-26.84657041887514	907.94	774.52	20.57	2.602	-37.44	5428 $\pm$ 468	3.12 $\pm$ 1.06	-1.44 $\pm$ 0.53	0.25 $\pm$ 0.16
2893	270.40661568128013	-26.84647009277922	871.18	777.10	20.32	3.071	-5.94	6540 $\pm$ 148	3.64 $\pm$ 0.85	-1.89 $\pm$ 0.49	0.25 $\pm$ 0.17
2895	270.41643604979544	-26.84536649984802	1133.45	810.45	21.30	3.285	43.69	5531 $\pm$ 430	3.26 $\pm$ 1.23	-2.00 $\pm$ 0.35	0.27 $\pm$ 0.15
2897	270.40447898760340	-26.84389502585170	814.91	854.88	21.21	3.179	-24.84	5314 $\pm$ 440	3.33 $\pm$ 1.15	-1.90 $\pm$ 0.40	0.29 $\pm$ 0.14
2898	270.41396235971644	-26.84349371143920	1067.92	866.66	20.86	3.521	79.27	5660 $\pm$ 498	3.18 $\pm$ 1.14	-1.77 $\pm$ 0.48	0.28 $\pm$ 0.15
2903	270.41171346685678	-26.84192188294944	1007.51	913.48	19.93	3.361	50.68	4568 $\pm$ 268	1.25 $\pm$ 0.61	-2.01 $\pm$ 0.30	0.32 $\pm$ 0.12
2906	270.42138314058695	-26.83981492966281	1265.39	976.54	20.71	3.471	78.88	4838 $\pm$ 340	2.63 $\pm$ 0.65	-0.11 $\pm$ 0.36	0.15 $\pm$ 0.17
2907	270.42179538073668	-26.83968115352688	1276.47	980.78	20.25	3.283	62.91	5930 $\pm$ 536	3.48 $\pm$ 0.98	-1.25 $\pm$ 0.52	0.24 $\pm$ 0.16
2909	270.41688580126521	-26.83851060559504	1145.41	1015.09	21.39	3.588	52.05	5396 $\pm$ 475	3.01 $\pm$ 1.31	-2.02 $\pm$ 0.33	0.28 $\pm$ 0.15
2911	270.40234222199746	-26.83814271660306	757.65	1026.02	20.49	2.619	20.60	4868 $\pm$ 296	4.29 $\pm$ 0.61	0.07 $\pm$ 0.29	0.12 $\pm$ 0.13
2912	270.41336266274777	-26.83787516022189	1051.14	1034.01	19.03	2.369	-21.33	4928 $\pm$ 245	4.48 $\pm$ 0.39	0.13 $\pm$ 0.21	0.09 $\pm$ 0.12
2913	270.40485385134588	-26.83797549393892	824.02	1031.60	21.11	3.853	127.91	4698 $\pm$ 374	2.42 $\pm$ 0.78	-0.67 $\pm$ 0.52	0.21 $\pm$ 0.17
2915	270.41639857036233	-26.83703904245702	1132.55	1059.18	20.30	3.055	-27.32	6765 $\pm$ 150	3.64 $\pm$ 0.93	-1.93 $\pm$ 0.46	0.24 $\pm$ 0.17
2916	270.40863985104261	-26.83707248728611	925.95	1058.88	20.10	3.453	63.66	4694 $\pm$ 370	1.64 $\pm$ 0.89	-1.92 $\pm$ 0.35	0.35 $\pm$ 0.12
2920	270.41096381819040	-26.83446376096855	987.02	1136.55	21.93	3.537	3.28	5338 $\pm$ 452	3.07 $\pm$ 1.12	-1.65 $\pm$ 0.49	0.27 $\pm$ 0.15
2923	270.40781519708077	-26.83292525319577	903.23	1182.02	20.92	3.862	30.78	5510 $\pm$ 460	3.04 $\pm$ 1.23	-1.99 $\pm$ 0.35	0.27 $\pm$ 0.15
2925	270.41373747401747	-26.83152051047430	1061.32	1224.71	21.66	4.026	37.24	5486 $\pm$ 464	3.24 $\pm$ 1.35	-1.98 $\pm$ 0.33	0.27 $\pm$ 0.15
2927	270.41778529463897	-26.82740652100239	1169.10	1347.16	20.88	3.751	36.70	5313 $\pm$ 440	3.45 $\pm$ 0.80	-0.30 $\pm$ 0.38	0.21 $\pm$ 0.17
2958	270.40841494647935	-26.83827649455660	919.59	1022.07	20.24	3.683	61.61	4998 $\pm$ 476	1.97 $\pm$ 0.98	-1.92 $\pm$ 0.34	0.30 $\pm$ 0.14
2959	270.41163850238871	-26.83754071385660	1005.29	1044.83	19.58	3.104	140.86	6775 $\pm$ 120	3.55 $\pm$ 0.96	-1.09 $\pm$ 0.62	0.21 $\pm$ 0.18
2962	270.41231317941322	-26.83506578006477	1023.68	1118.13	20.65	2.680	18.26	5178 $\pm$ 394	3.18 $\pm$ 0.81	0.14 $\pm$ 0.23	0.14 $\pm$ 0.15
2963	270.41197584179770	-26.83469787988597	1014.40	1129.59	19.16	3.956	61.84	4656 $\pm$ 514	1.62 $\pm$ 0.91	-1.43 $\pm$ 0.58	0.29 $\pm$ 0.12
2968	270.40252966045495	-26.83152051047430	762.65	1224.71	19.53	3.612	71.38	5514 $\pm$ 612	3.13 $\pm$ 1.14	-1.18 $\pm$ 0.49	0.24 $\pm$ 0.17
2991	270.41223821565364	-26.84523273027590	1021.01	814.65	18.61	3.567	13.24	4551 $\pm$ 321	1.41 $\pm$ 0.76	-1.77 $\pm$ 0.51	0.32 $\pm$ 0.12
3011	270.40957694480994	-26.83719272469550	950.36	875.07	20.14	3.129	-35.79	5546 $\pm$ 510	3.02 $\pm$ 1.32	-1.96 $\pm$ 0.33	0.27 $\pm$ 0.16
3012	270.42108332788604	-26.84269107834307	1257.94	890.67	20.81	3.071	13.23	5109 $\pm$ 398	3.30 $\pm$ 0.73	-0.45 $\pm$ 0.45	0.21 $\pm$ 0.17
3013	270.41163850238871	-26.84041692031824	1005.29	958.48	20.05	3.216	58.95	5448 $\pm$ 472	2.92 $\pm$ 1.06	-1.83 $\pm$ 0.45	0.28 $\pm$ 0.16
3014	270.40755280493659	-26.84038347647692	896.18	959.62	21.12	4.032	50.43	5570 $\pm$ 476	3.07 $\pm$ 1.09	-1.91 $\pm$ 0.42	0.27 $\pm$ 0.16
3015	270.40867733505900	-26.83924637999342	926.09	993.76	20.05	3.366	61.64	5022 $\pm$ 626	2.14 $\pm$ 1.24	-1.31 $\pm$ 0.55	0.30 $\pm$ 0.11
3016	270.41396235971644	-26.83841027235212	1067.35	1018.58	20.60	2.986	53.74	5591 $\pm$ 454	3.28 $\pm$ 1.11	-2.02 $\pm$ 0.36	0.27 $\pm$ 0.15
3017	270.40590345804679	-26.83827649455660	852.44	1022.76	22.27	3.610	31.15	5527 $\pm$ 444	3.24 $\pm$ 1.10	-1.94 $\pm$ 0.41	0.27 $\pm$ 0.15
3018	270.41291288630140	-26.83757415853756	1039.63	1043.40	19.16	3.302	11.43	4336 $\pm$ 224	1.93 $\pm$ 0.54	0.00 $\pm$ 0.29	0.12 $\pm$ 0.14
3019	270.39919317316088	-26.83730660081330	673.51	1051.49	21.04	3.452	41.66	5479 $\pm$ 464	3.20 $\pm$ 1.26	-1.96 $\pm$ 0.37	0.27 $\pm$ 0.15
3020	270.40729041170761	-26.83747382446505	889.83	1046.55	20.59	3.644	49.81	5658 $\pm$ 588	2.79 $\pm$ 0.91	-1.59 $\pm$ 0.54	0.27 $\pm$ 0.17
3023	270.41924694416826	-26.83399552168295	1208.44	1150.86	19.00	2.294	21.85	5274 $\pm$ 354	3.77 $\pm$ 0.78	0.19 $\pm$ 0.18	0.12 $\pm$ 0.12
3025	270.41340014397434	-26.83121949191296	1052.14	1233.74	21.59	3.914	48.54	5501 $\pm$ 429	3.05 $\pm$ 1.00	-1.79 $\pm$ 0.45	0.26 $\pm$ 0.16
3026	270.40219227083304	-26.830784688591398	753.07	1246.36	21.04	3.513	81.43	5393 $\pm$ 447	2.99 $\pm$ 1.25	-1.96 $\pm$ 0.38	0.27 $\pm$ 0.15
3042	270.40912714152859	-26.84182155272999	938.05	916.28	20.07	3.516	37.95	4724 $\pm$ 292	1.74 $\pm$ 0.80	-1.79 $\pm$ 0.44	0.26 $\pm$ 0.15
3043	270.41328770022812	-26.84111923870320	1049.60	937.49	20.25	3.714	48.69	5444 $\pm$ 468	2.92 $\pm$ 1.05	-1.88 $\pm$ 0.43	0.27 $\pm$ 0.16
3057	270.41032660986065	-26.83951393313467	970.33	985.97	20.42	3.564	63.66	5927 $\pm$ 462	3.55 $\pm$ 0.93	-1.67 $\pm$ 0.47	0.28 $\pm$ 0.16
3059	270.40968939513215	-26.83623636359634	953.56	1083.19	19.65	3.190	39.44	5729 $\pm$ 489	3.60 $\pm$ 0.73	0.05 $\pm$ 0.27	0.15 $\pm$ 0.17
3060	270.41246310666668	-26.83576813163499	1027.24	1097.22	21.08	3.879	55.96	5382 $\pm$ 442	3.02 $\pm$ 1.27	-2.16 $\pm$ 0.25	0.28 $\pm$ 0.14
3062	270.40256714808004	-26.83399552168295	763.53	1150.28	21.28	3.472	77.31	5497 $\pm$ 412	3.17 $\pm$ 1.24	-1.95 $\pm$ 0.34	0.27 $\pm$ 0.15
3067	270.41257555187428	-26.83951393313467	1030.46	985.23	19.27	3.114	28.30	7102 $\pm$ 132	3.20 $\pm$ 0.82	-1.55 $\pm$ 0.57	0.21 $\pm$ 0.21
3068	270.40987681189301	-26.83332660506254	958.32	1170.29	18.39	4.245	52.44	4678 $\pm$ 395	2.10 $\pm$ 0.89	-0.98 $\pm$ 0.47	0.28 $\pm$ 0.17
3087	270.41396235971644	-26.83881160479041	1067.01	1006.80	20.38	3.448	26.60	5616 $\pm$ 496	3.16 $\pm$ 1.04	-1.82 $\pm$ 0.48	0.26 $\pm$ 0.16
3088	270.41512425646278	-26.83723971128347	1098.60	1053.20	19.63	3.565	49.04	4729 $\pm$ 286	1.66 $\pm$ 0.70	-1.86 $\pm$ 0.40	0.26 $\pm$ 0.12
3089	270.42276975589351	-26.82877786739959	1302.02	1306.29	20.52	3.690	80.10	5448 $\pm$ 443	3.04 $\pm$ 1.25	-1.96 $\pm$ 0.38	0.28 $\pm$ 0.15
3095	270.41977163065576	-26.84125301313957	1222.53	933.62	19.64	3.184	20.45	5453 $\pm$ 492	2.98 $\pm$ 1.13	-1.76 $\pm$ 0.46	0.27 $\pm$ 0.17
3096	270.39956806811807	-26.83770793716270	683.56	1039.10	20.21	3.604	34.48	5388 $\pm$ 506	2.98 $\pm$ 1.06	-1.44 $\pm$ 0.52	0.24 $\pm$ 0.16
3100	270.41257555187428	-26.84503207562101	1030.47	820.78	20.16	3.470	32.83	5564 $\pm$ 484	3.09 $\pm$ 1.05	-1.84 $\pm$ 0.43	0.27 $\pm$ 0.16
3102	270.41253807016051	-26.83794204937645	1029.20	1032.22	19.86	3.474	69.93	5557 $\pm$ 522	2.86 $\pm$ 0.86	-1.81 $\pm$ 0.45	0.28 $\pm$ 0.16
3104	270.41396235971644	-26.83744037975444	1067.02	1047.56	19.44	3.429	52.31	4688 $\pm$ 301	1.42 $\pm$ 0.65	-1.96 $\pm$ 0.38	0.29 $\pm$ 0.13
3113	270.41767285866479	-26.84630288242150	1166.03	782.38	19.06	2.426	-25.69	5811 $\pm$ 518	3.54 $\pm$ 0.78	0.21 $\pm$ 0.20	0.14 $\pm$ 0.15
3114	270.42108332788604	-26.84305895255234	1257.33	879.10	21.06	3.351	49.21	5870 $\pm$ 576	3.27 $\pm$ 1.04	-1.96 $\pm$ 0.43	0.27 $\pm$ 0.16
3116	270.41122619623110	-26.83713937691468	994.14	1056.88	19.02	3.580	64.22	4690 $\pm$ 488	1.59 $\pm$ 0.91	-1.48 $\pm$ 0.46	0.28 $\pm$ 0.12
3125	270.41171346685678	-26.84085168935612	1007.98	945.95	20.35	3.353	56.54	5607 $\pm$ 494	3.10 $\pm$ 1.10	-1.85 $\pm$ 0.45	0.27 $\pm$ 0.15

Table A.2 - Identified member stars from MUSE datacubes selected with  $S/N > 85$ . Columns correspond to: ID from NTT 2012 data, coordinates (RA, DEC-J2000), proper motions from Gaia, NTT pixels  $x$ ,  $y$ , NTT  $V$ , NTT  $V-I$ , and  $S/N$ .

ID	RA (J2000)	DEC (J2000)	pmRA	pmDEC	X	Y	V	V-I	S/N
0072	270.41522393678054	-26.83960326833801	-1.6470	-7.1760	1114.09	991.63	17.87	3.812	129.80
0081	270.40828978697527	-26.83592435071913	-1.8160	-7.1100	929.55	1101.25	18.42	3.841	125.00
0084	270.41578613193025	-26.83405140131479	-2.5750	-7.6500	1129.81	1157.05	18.74	3.937	114.13
0089	270.39921802548110	-26.83204463546964	-2.1770	-7.3860	687.86	1217.57	18.58	3.717	114.03
0092	270.40840223869230	-26.83177706400694	-2.0010	-7.4560	932.48	1225.10	18.88	4.252	121.02
0437	270.40307930558885	-26.84742893173680	-1.8330	-7.4950	790.31	757.66	17.94	3.820	106.96
0473	270.41432441417822	-26.84421846865514	-3.0010	-7.9650	1090.16	853.74	19.68	3.417	99.41
0513	270.40034269441361	-26.84074036414967	-2.2920	-7.4720	717.94	957.50	18.12	3.950	117.32
0520	270.41170073374064	-26.84023870564067	-2.4930	-7.5020	1020.38	972.22	17.97	3.688	129.40
0549	270.41867198860143	-26.83655980866259	-2.0500	-7.5950	1206.10	1082.43	18.34	3.984	122.03
0554	270.39678117444549	-26.83615846721820	-2.1590	-7.5650	622.57	1094.94	18.25	3.849	113.81
0571	270.41484913724622	-26.83505477091640	-1.7740	-7.5350	1104.23	1127.62	17.69	4.144	116.83
0578	270.41814729715378	-26.83448619589934	-2.6740	-7.1830	1192.40	1144.92	18.47	4.122	124.17
0582	270.40105497443244	-26.83408484711128	-2.0170	-8.0870	736.12	1156.14	17.82	3.900	104.30
0584	270.41260029354157	-26.83395106386613	-1.4360	-6.8510	1044.23	1160.69	19.74	4.040	122.81
0595	270.41147584179771	-26.83294768449528	-3.1640	-8.3520	1014.50	1190.66	20.21	3.861	101.16
0610	270.40585328417666	-26.83164327803886	-2.6140	-7.7440	864.91	1229.44	18.27	3.985	116.47
0611	270.40315427957711	-26.83147604535684	-2.6990	-7.5050	792.25	1234.08	19.50	3.688	108.72
0615	270.41642328041041	-26.83107468591398	-2.2590	-7.1160	1146.62	1246.95	18.63	4.089	120.39
0631	270.42020856001682	-26.82940233961694	-1.4360	-6.7630	1247.46	1296.56	18.68	3.530	88.71
0645	270.41293762517887	-26.82746238703481	-2.4270	-7.2970	1053.09	1354.89	19.53	3.807	85.38
0936	270.40296684444041	-26.83475376096855	-2.1910	-7.6940	787.64	1136.18	17.35	4.109	108.45
1342	270.41282518149904	-26.84361649668046	-3.1550	-7.4820	1050.16	871.39	19.54	3.358	112.85
1353	270.40570334248764	-26.84298107834307	-2.0320	-7.2650	860.67	890.05	19.27	3.669	125.42
1368	270.40915191171359	-26.84181056153792	-2.0550	-7.3130	952.73	925.10	17.73	3.714	140.45
1380	270.40821481905323	-26.84090758315861	-2.3690	-7.6940	927.83	952.88	18.55	3.358	122.89
1399	270.40349166142846	-26.83963671249548	-2.4830	-7.9150	801.46	990.74	19.76	3.821	109.47
1406	270.41121346685679	-26.83936915895905	-2.6190	-6.5930	1007.24	998.86	17.34	3.912	100.73
1413	270.40401647407731	-26.83886749437426	-1.6550	-7.3100	815.57	1013.86	20.19	3.636	97.36
1414	270.41739773041394	-26.83880060559504	-1.8270	-7.2750	1172.89	1015.09	19.36	3.793	127.92
1426	270.40802739886061	-26.83793104786989	-1.6750	-7.0070	922.82	1041.32	19.62	3.630	110.36
1433	270.41754764447046	-26.83752971128347	-3.0530	-6.8120	1176.21	1053.57	19.48	3.204	112.48
1441	270.41147584179771	-26.83692770373768	-1.8900	-7.1330	1014.86	1071.40	17.49	3.923	117.52
1447	270.42043342100408	-26.83645947343477	-2.1240	-7.1800	1253.94	1085.56	19.00	3.681	95.24
1448	270.41151332384356	-26.83572367904923	-4.4920	-5.4910	1015.41	1107.86	20.09	3.801	101.22
1514	270.40776500966109	-26.83184395693179	-1.6220	-7.7590	915.49	1223.40	19.15	4.193	120.53
1545	270.40735268158420	-26.83003783411370	-2.7280	-7.4070	904.67	1277.56	19.82	4.459	97.37
2009	270.40877707631000	-26.84067347647692	-3.6420	-8.4780	942.11	959.88	20.09	3.377	85.56
2011	270.41027640464006	-26.84037248146045	-2.5990	-6.7240	982.66	968.88	18.39	3.704	134.41
2013	270.40559088598837	-26.84033903752032	-0.5410	-6.5740	857.80	969.23	18.46	3.706	131.43
2032	270.41080116118627	-26.83816516022189	-2.3340	-7.1630	996.01	1034.08	17.77	3.760	129.99
2034	270.41559873410057	-26.83803138179427	-1.8210	-7.2890	1124.13	1038.38	18.78	3.591	130.93
2038	270.40971416066765	-26.83689425878022	-2.7190	-7.7350	967.22	1072.12	19.62	3.568	110.74
2055	270.40086753309708	-26.83562334308101	-1.8830	-7.3890	731.65	1110.99	18.01	3.885	117.00
2062	270.40836475480876	-26.83448619589934	-3.1760	-6.6610	931.93	1144.49	20.25	4.076	97.77
2352	270.41053878345559	-26.84568994221631	-3.3940	-8.8530	989.78	809.38	19.38	3.284	109.77
2355	270.41379968677040	-26.84502109297108	-2.1480	-8.0110	1076.29	829.32	19.03	3.459	136.97
2518	270.41589857036234	-26.84053970101285	-1.4380	-6.7830	1132.82	963.10	20.05	3.554	89.15
2523	270.40405396052904	-26.84010492966281	-2.7670	-7.9990	816.13	976.28	19.84	3.724	113.03
2525	270.40802739886061	-26.83993770946819	-3.5260	-8.1130	922.68	981.08	18.97	3.557	130.86
2561	270.41196310666669	-26.83468686976047	-3.7640	-6.1900	1027.36	1138.66	20.40	3.656	90.63
2562	270.40157980722722	-26.83461997851290	-1.9920	-7.2260	750.53	1140.22	19.18	3.456	106.00
2573	270.41233792325039	-26.83318180714274	-1.7830	-6.5100	1037.44	1183.96	20.57	4.048	86.81
2575	270.40971416066765	-26.83234565261057	-3.1110	-7.9170	967.65	1208.54	19.98	4.012	109.40
2748	270.41245036779372	-26.83956982417065	-3.8680	-6.1480	1040.01	992.71	18.99	3.412	121.33
2848	270.40881455994997	-26.83679392384860	-1.3960	-6.2670	943.93	1075.06	20.03	3.633	92.35
2851	270.40990157587862	-26.83318180714274	-2.1280	-7.6950	972.15	1183.44	18.23	4.281	112.67
2903	270.41121346685679	-26.84221188294944	-3.6720	-7.2970	1007.51	913.48	19.93	3.361	92.13
2963	270.41147584179771	-26.83498787988597	-2.0390	-7.2200	1014.40	1129.59	19.16	3.956	133.76
2968	270.40202966045496	-26.83181051047429	-2.1270	-7.6880	762.65	1224.70	19.53	3.612	108.05
3042	270.40862714152860	-26.84211155272999	-2.4570	-6.7110	938.05	916.28	20.07	3.516	94.47
3068	270.40937681189303	-26.83361660506254	-1.1350	-5.7000	958.32	1170.29	18.39	4.245	129.01
3088	270.41462425646279	-26.83752971128347	-1.9910	-7.4270	1098.60	1053.20	19.63	3.565	115.52
3104	270.41346235971645	-26.83773037975444	-1.1950	-7.6990	1067.02	1047.56	19.44	3.429	104.55
3162	270.40746513496180	-26.84254631637180	-2.5720	-7.5880	907.93	903.03	16.76	3.917	99.54
3187	270.41020143906485	-26.83769693503397	-1.9390	-7.7700	980.88	1048.00	17.63	3.717	110.81
3194	270.41275021893512	-26.84047281322153	-1.7490	-7.7720	1048.33	965.88	16.95	4.072	102.53

Table A.3 - Identified members stars from MUSE datacubes selected with S/N>85. Columns correspond to: ID and results from the present work:  $v_r^h$  (km s<sup>-1</sup>),  $T_{\text{eff}}$  (K), log g, [Fe/H], [Mg/Fe], and [Fe/H]<sub>CaT</sub>.

ID	$v_r$ (km s <sup>-1</sup> )	$T_{\text{eff}}$ (K)	log g	[Fe/H]	[Mg/Fe]	EWa	EWb	EW'	[Fe/H] <sub>CaT</sub>
0072	63.06	4660 ± 42	1.99 ± 0.15	-0.85 ± 0.07	0.27 ± 0.03	3.095 ± 0.114	2.365 ± 0.102	5.460 ± 0.153	-1.20 ± 0.09
0081	35.38	4893 ± 49	2.21 ± 0.13	-0.80 ± 0.06	0.24 ± 0.02	2.994 ± 0.161	2.383 ± 0.141	5.377 ± 0.214	-1.07 ± 0.12
0084	32.17	4885 ± 52	2.33 ± 0.13	-0.81 ± 0.07	0.24 ± 0.02	2.963 ± 0.138	2.240 ± 0.121	5.203 ± 0.183	-1.06 ± 0.11
0089	66.10	4988 ± 28	2.72 ± 0.10	-0.68 ± 0.05	0.21 ± 0.02	3.626 ± 0.138	3.135 ± 0.161	6.761 ± 0.212	-0.08 ± 0.16
0092	49.20	4788 ± 46	2.15 ± 0.12	-0.81 ± 0.07	0.26 ± 0.02	3.128 ± 0.143	2.410 ± 0.126	5.539 ± 0.190	-0.81 ± 0.12
0437	57.47	4628 ± 36	2.12 ± 0.12	-0.79 ± 0.06	0.27 ± 0.03	3.198 ± 0.112	2.411 ± 0.096	5.610 ± 0.148	-1.09 ± 0.09
0473	59.01	5220 ± 90	2.19 ± 0.17	-1.42 ± 0.10	0.30 ± 0.03	2.489 ± 0.143	2.040 ± 0.118	4.529 ± 0.185	-1.14 ± 0.10
0513	44.50	4630 ± 37	2.06 ± 0.12	-0.86 ± 0.06	0.29 ± 0.03	3.144 ± 0.139	2.293 ± 0.117	5.437 ± 0.182	-1.13 ± 0.10
0520	58.13	4670 ± 66	1.69 ± 0.20	-1.02 ± 0.10	0.29 ± 0.03	3.121 ± 0.140	2.389 ± 0.125	5.510 ± 0.188	-1.14 ± 0.11
0549	54.18	4728 ± 49	1.88 ± 0.18	-1.02 ± 0.08	0.30 ± 0.03	3.081 ± 0.118	2.390 ± 0.106	5.471 ± 0.159	-1.04 ± 0.10
0554	56.09	4934 ± 39	2.45 ± 0.12	-0.81 ± 0.06	0.24 ± 0.02	3.154 ± 0.132	2.647 ± 0.119	5.801 ± 0.178	-0.87 ± 0.11
0571	60.37	4524 ± 49	1.88 ± 0.17	-0.77 ± 0.08	0.29 ± 0.03	3.213 ± 0.132	2.499 ± 0.121	5.712 ± 0.179	-1.11 ± 0.10
0578	61.99	4554 ± 62	1.75 ± 0.21	-1.08 ± 0.09	0.30 ± 0.03	3.071 ± 0.150	2.361 ± 0.143	5.432 ± 0.207	-1.02 ± 0.12
0582	56.05	4632 ± 44	1.94 ± 0.14	-0.76 ± 0.07	0.30 ± 0.03	3.252 ± 0.147	2.509 ± 0.138	5.761 ± 0.201	-1.04 ± 0.12
0584	64.72	4972 ± 87	2.09 ± 0.22	-1.12 ± 0.10	0.28 ± 0.03	2.797 ± 0.155	2.199 ± 0.136	4.996 ± 0.206	-0.84 ± 0.13
0595	39.55	5286 ± 39	2.74 ± 0.12	-1.46 ± 0.06	0.28 ± 0.01	— ± —	— ± —	— ± —	— ± —
0610	53.41	4767 ± 36	2.26 ± 0.12	-0.68 ± 0.06	0.24 ± 0.02	3.185 ± 0.144	2.404 ± 0.127	5.589 ± 0.192	-0.99 ± 0.11
0611	60.67	5134 ± 78	2.27 ± 0.16	-1.27 ± 0.08	0.27 ± 0.03	2.698 ± 0.124	2.021 ± 0.097	4.719 ± 0.158	-1.09 ± 0.10
0615	56.39	5056 ± 46	2.42 ± 0.12	-0.67 ± 0.06	0.24 ± 0.02	3.080 ± 0.106	2.377 ± 0.094	5.457 ± 0.141	-0.95 ± 0.09
0631	70.03	5348 ± 43	2.78 ± 0.13	-1.66 ± 0.06	0.29 ± 0.01	2.523 ± 0.098	2.209 ± 0.230	4.732 ± 0.250	-1.35 ± 0.12
0645	54.05	5684 ± 42	2.97 ± 0.09	-0.72 ± 0.05	0.15 ± 0.02	2.890 ± 0.127	2.281 ± 0.125	5.171 ± 0.178	-0.81 ± 0.11
0936	65.37	4264 ± 33	1.83 ± 0.14	-0.77 ± 0.07	0.24 ± 0.03	3.325 ± 0.103	2.633 ± 0.087	5.958 ± 0.135	-1.08 ± 0.09
1342	57.98	4821 ± 64	1.71 ± 0.19	-1.50 ± 0.10	0.30 ± 0.04	2.483 ± 0.117	1.919 ± 0.099	4.403 ± 0.153	-1.26 ± 0.09
1353	37.79	4714 ± 134	1.81 ± 0.34	-1.36 ± 0.15	0.26 ± 0.05	2.740 ± 0.160	2.098 ± 0.161	4.837 ± 0.227	-1.10 ± 0.12
1368	37.91	4589 ± 70	1.85 ± 0.21	-1.05 ± 0.10	0.28 ± 0.04	2.859 ± 0.146	2.154 ± 0.117	5.013 ± 0.188	-1.48 ± 0.09
1380	34.38	5498 ± 410	2.17 ± 0.38	-1.08 ± 0.25	0.20 ± 0.07	2.628 ± 0.152	2.368 ± 0.161	4.996 ± 0.222	-1.24 ± 0.12
1399	54.69	4796 ± 104	1.90 ± 0.27	-1.45 ± 0.12	0.29 ± 0.03	2.688 ± 0.134	2.092 ± 0.119	4.781 ± 0.179	-0.97 ± 0.11
1406	52.26	4582 ± 62	1.87 ± 0.17	-0.74 ± 0.07	0.32 ± 0.04	3.298 ± 0.123	2.660 ± 0.127	5.958 ± 0.176	-1.08 ± 0.10
1413	56.02	5110 ± 78	2.33 ± 0.18	-1.35 ± 0.09	0.27 ± 0.03	2.430 ± 0.165	1.879 ± 0.161	4.309 ± 0.231	-1.10 ± 0.13
1414	53.88	4788 ± 96	1.72 ± 0.27	-1.44 ± 0.14	0.27 ± 0.04	2.774 ± 0.129	2.200 ± 0.116	4.974 ± 0.173	-0.99 ± 0.11
1426	39.18	4753 ± 76	1.70 ± 0.22	-1.57 ± 0.12	0.29 ± 0.04	2.650 ± 0.193	2.095 ± 0.213	4.745 ± 0.287	-1.04 ± 0.16
1433	41.82	6586 ± 96	3.12 ± 0.11	-1.48 ± 0.08	0.24 ± 0.03	— ± —	— ± —	— ± —	— ± —
1441	42.03	4622 ± 44	1.86 ± 0.12	-0.69 ± 0.07	0.33 ± 0.03	3.430 ± 0.162	2.703 ± 0.136	6.134 ± 0.212	-0.93 ± 0.13
1447	52.27	5217 ± 49	2.50 ± 0.12	-1.28 ± 0.06	0.27 ± 0.02	2.828 ± 0.129	2.288 ± 0.162	5.116 ± 0.207	-1.02 ± 0.12
1448	30.36	4865 ± 76	1.85 ± 0.24	-1.65 ± 0.15	0.29 ± 0.05	— ± —	— ± —	— ± —	— ± —
1514	41.44	5244 ± 106	2.48 ± 0.18	-0.79 ± 0.10	0.20 ± 0.04	3.005 ± 0.183	2.317 ± 0.180	5.322 ± 0.256	-0.85 ± 0.15
1545	46.67	5072 ± 42	2.52 ± 0.12	-1.01 ± 0.07	0.25 ± 0.02	3.139 ± 0.115	2.511 ± 0.111	5.650 ± 0.160	-0.37 ± 0.12
2009	50.38	5277 ± 54	2.44 ± 0.14	-1.35 ± 0.07	0.28 ± 0.02	2.466 ± 0.142	1.906 ± 0.149	4.371 ± 0.206	-1.10 ± 0.12
2011	44.21	4776 ± 78	1.73 ± 0.22	-1.25 ± 0.15	0.29 ± 0.04	2.972 ± 0.135	2.457 ± 0.122	5.429 ± 0.182	-1.04 ± 0.11
2013	53.35	4859 ± 96	1.75 ± 0.25	-1.12 ± 0.15	0.28 ± 0.04	2.861 ± 0.147	2.269 ± 0.148	5.130 ± 0.209	-1.20 ± 0.11
2032	50.53	4774 ± 45	2.11 ± 0.12	-0.80 ± 0.07	0.26 ± 0.02	3.166 ± 0.147	2.525 ± 0.135	5.692 ± 0.199	-1.10 ± 0.11
2034	35.99	4848 ± 96	1.79 ± 0.25	-1.25 ± 0.15	0.29 ± 0.04	2.781 ± 0.183	2.256 ± 0.167	5.037 ± 0.248	-1.14 ± 0.13
2038	55.53	5277 ± 57	2.56 ± 0.14	-1.36 ± 0.07	0.27 ± 0.02	2.278 ± 0.152	1.607 ± 0.138	3.885 ± 0.205	-1.51 ± 0.10
2055	52.87	4690 ± 40	1.98 ± 0.14	-0.83 ± 0.07	0.28 ± 0.03	3.165 ± 0.132	2.521 ± 0.121	5.687 ± 0.179	-1.02 ± 0.11
2062	36.72	5252 ± 42	2.69 ± 0.12	-0.95 ± 0.06	0.22 ± 0.02	2.671 ± 0.156	2.060 ± 0.139	4.731 ± 0.209	-0.83 ± 0.13
2352	37.09	5190 ± 136	1.92 ± 0.17	-1.52 ± 0.10	0.32 ± 0.03	2.542 ± 0.145	2.512 ± 0.165	5.054 ± 0.220	-0.93 ± 0.13
2355	58.71	4854 ± 86	1.92 ± 0.28	-1.50 ± 0.18	0.24 ± 0.04	2.329 ± 0.145	1.886 ± 0.130	4.215 ± 0.195	-1.51 ± 0.09
2518	39.85	5290 ± 56	2.55 ± 0.14	-1.41 ± 0.07	0.27 ± 0.02	— ± —	— ± —	— ± —	— ± —
2523	45.03	4810 ± 56	1.75 ± 0.17	-1.53 ± 0.09	0.30 ± 0.03	2.585 ± 0.172	2.110 ± 0.172	4.695 ± 0.244	-0.99 ± 0.14
2525	33.89	4820 ± 134	1.79 ± 0.35	-1.37 ± 0.14	0.26 ± 0.05	2.644 ± 0.143	1.959 ± 0.120	4.603 ± 0.186	-1.33 ± 0.10
2561	50.00	5950 ± 56	2.91 ± 0.11	-1.48 ± 0.07	0.27 ± 0.02	2.508 ± 0.149	2.516 ± 0.179	5.024 ± 0.233	-0.58 ± 0.15
2562	36.49	4922 ± 108	1.95 ± 0.29	-1.22 ± 0.15	0.25 ± 0.04	2.827 ± 0.137	2.258 ± 0.127	5.085 ± 0.186	-0.98 ± 0.11
2573	40.69	5317 ± 38	2.67 ± 0.11	-1.32 ± 0.06	0.26 ± 0.02	— ± —	— ± —	— ± —	— ± —
2575	33.24	5331 ± 42	2.74 ± 0.12	-1.27 ± 0.06	0.26 ± 0.02	2.451 ± 0.214	1.962 ± 0.261	4.413 ± 0.337	-1.11 ± 0.17
2748	46.19	4775 ± 134	1.83 ± 0.34	-1.36 ± 0.15	0.26 ± 0.05	2.800 ± 0.170	2.240 ± 0.201	5.040 ± 0.264	-1.07 ± 0.14
2848	39.52	5335 ± 40	2.78 ± 0.12	-1.12 ± 0.06	0.22 ± 0.02	— ± —	— ± —	— ± —	— ± —
2851	55.62	4632 ± 38	2.10 ± 0.12	-0.73 ± 0.07	0.25 ± 0.02	3.299 ± 0.129	2.523 ± 0.107	5.821 ± 0.168	-0.86 ± 0.11
2903	42.28	4760 ± 55	1.73 ± 0.18	-1.63 ± 0.10	0.30 ± 0.03	2.335 ± 0.132	1.933 ± 0.123	4.267 ± 0.180	-1.21 ± 0.10
2963	53.44	4802 ± 135	1.78 ± 0.35	-1.23 ± 0.15	0.26 ± 0.05	2.850 ± 0.113	2.142 ± 0.102	4.992 ± 0.152	-1.04 ± 0.09
2968	62.98	5318 ± 40	2.70 ± 0.12	-1.00 ± 0.05	0.24 ± 0.02	2.539 ± 0.114	2.052 ± 0.103	4.590 ± 0.154	-1.16 ± 0.09
3042	29.55	4926 ± 86	1.96 ± 0.27	-1.50 ± 0.19	0.25 ± 0.04	2.584 ± 0.174	2.113 ± 0.177	4.697 ± 0.248	-0.91 ± 0.14
3068	44.04	4716 ± 38	2.10 ± 0.12	-0.73 ± 0.06	0.27 ± 0.03	3.216 ± 0.143	2.584 ± 0.132	5.800 ± 0.194	-0.82 ± 0.12
3088	40.64	4887 ± 86	1.93 ± 0.28	-1.50 ± 0.19	0.25 ± 0.04	2.437 ± 0.172	1.977 ± 0.161	4.414 ± 0.235	-1.23 ± 0.12
3104	43.91	4927 ± 75	1.91 ± 0.24	-1.64 ± 0.15	0.29 ± 0.05	2.212 ± 0.150	1.802 ± 0.148	4.014 ± 0.211	-1.50 ± 0.10
3162	73.13	4016 ± 34	1.47 ± 0.17	-0.99 ± 0.12	0.28 ± 0.04	3.385 ± 0.099	2.663 ± 0.085	6.048 ± 0.131	-1.22 ± 0.08
3187	42.36	4646 ± 44	1.95 ± 0.14	-0.79 ± 0.07	0.29 ± 0.03	3.203 ± 0.132	2.506 ± 0.109	5.709 ± 0.172	-1.13 ± 0.10
3194	51.23	4040 ± 34	1.61 ± 0.18	-0.92 ± 0.12	0.29 ± 0.04	3.356 ± 0.101	2.582 ± 0.088	5.938 ± 0.134	-1.22 ± 0.08

## Abundances

### *B.1 NLTE corrections to cobalt abundances*

The NLTE corrections to the derived LTE abundances of Co, derived from calculations made available online by Bergemann et al. (2010) (see text), are given in Table B.1.

### *B.2 Fits of studied lines to the spectra of the Sun, Arcturus, and $\mu$ Leo*

The lines of Cu I and Co I employed to derive abundances in the present work were first fitted to the spectra of the Sun, Arcturus, and  $\mu$  Leo, as shown in Figs. B.4 and B.5. Details on the adopted parameters are given in Sect. 3.

### *B.3 Abundances of C, N, O, Na, Mg, Al, Mn, Co, and Cu for the 56 sampled red giants*

In Table B.2, the metallicity from Zoccali et al. (2006), Lecureur et al. (2007), and Hill et al. (2011) for the 56 sample red giants is reported in column 2. The abundances of C, N, O, Na, Mg, Al, Mn, Co, Cu, and Zn from the following sources are reported: CNO abundances revised in Friaça & Barbuy (2017); Na, Mg, and Al from Lecureur et al. (2007); Mn from Barbuy et al. (2013); Zn from Barbuy et al. (2015) and da Silveira et al. (2018); and the present results on Co (LTE and NLTE-corrected) and Cu.

Table B.1 - NLTE corrections to the derived LTE abundances of Co.

Star	[Co/Fe] 5212.691 Å	[Co/Fe] 5280.629 Å	[Co/Fe] 5301.047 Å	[Co/Fe] 5342.708 Å	[Co/Fe] 5454.572 Å	[Co/Fe] 5647.234 Å	[Co/Fe] 6117.000 Å	[Co/Fe] 6188.996 Å
B6-b1	0.117	0.169	0.341	0.000	0.000	0.219	0.088	0.081
B6-b2	0.097	0.146	0.312	0.000	0.000	0.186	0.074	0.066
B6-b3	0.124	0.185	0.320	0.000	0.000	0.216	0.094	0.106
B6-b4	0.105	0.119	0.274	0.000	0.000	0.138	0.038	0.036
B6-b5	0.123	0.158	0.255	0.000	0.000	0.169	0.072	0.074
B6-b6	0.122	0.181	0.333	0.000	0.000	0.220	0.088	0.097
B6-b8	0.088	0.129	0.266	0.000	0.000	0.157	0.052	0.047
B6-f1	0.095	0.137	0.302	0.000	0.000	0.182	0.068	0.061
B6-f2	0.158	0.199	0.245	0.000	0.000	0.192	0.123	0.115
B6-f3	0.147	0.202	0.255	0.000	0.000	0.204	0.126	0.128
B6-f5	0.116	0.145	0.285	0.000	0.000	0.165	0.060	0.059
B6-f7	0.101	0.116	0.302	0.000	0.000	0.139	0.036	0.031
B6-f8	0.139	0.216	0.283	0.000	0.000	0.224	0.145	0.163
BW-b2	0.111	0.167	0.287	0.000	0.000	0.191	0.075	0.067
BW-b4	0.111	0.186	0.342	0.000	0.000	0.214	0.102	0.091
BW-b5	0.078	0.123	0.210	0.000	0.000	0.121	0.012	0.030
BW-b6	0.101	0.122	0.320	0.000	0.000	0.164	0.052	0.039
BW-b7	0.105	0.177	0.322	0.000	0.000	0.196	0.087	0.077
BW-f1	0.131	0.212	0.314	0.000	0.000	0.213	0.098	0.091
BW-f4	0.305	0.270	0.343	0.000	0.000	0.305	0.285	0.244
BW-f5	0.188	0.220	0.243	0.000	0.000	0.212	0.155	0.140
BW-f6	0.091	0.116	0.268	0.000	0.000	0.135	0.035	0.028
BW-f7	0.118	0.165	0.329	0.000	0.000	0.216	0.088	0.079
BW-f8	0.407	0.347	0.468	0.000	0.000	0.412	0.415	0.363
BL-1	0.105	0.132	0.301	0.000	0.000	0.173	0.051	0.052
BL-3	0.106	0.133	0.307	0.000	0.000	0.190	0.057	0.049
BL-4	0.128	0.194	0.329	0.000	0.000	0.227	0.100	0.109
BL-5	0.122	0.174	0.327	0.000	0.000	0.222	0.092	0.081
BL-7	0.131	0.160	0.197	0.000	0.000	0.154	0.074	0.070
B3-b1	0.122	0.119	0.216	0.000	0.000	0.113	0.039	0.022
B3-b2	0.131	0.193	0.348	0.000	0.000	0.233	0.106	0.092
B3-b3	0.124	0.177	0.329	0.000	0.000	0.218	0.097	0.080
B3-b4	0.122	0.171	0.322	0.000	0.000	0.219	0.090	0.081
B3-b5	0.125	0.185	0.340	0.000	0.000	0.229	0.091	0.092
B3-b7	0.131	0.200	0.348	0.000	0.000	0.226	0.105	0.087
B3-b8	0.120	0.130	0.244	0.000	0.000	0.135	0.046	0.034
B3-f1	0.115	0.168	0.339	0.000	0.000	0.216	0.080	0.079
B3-f2	0.112	0.149	0.260	0.000	0.000	0.162	0.065	0.075
B3-f3	0.112	0.154	0.324	0.000	0.000	0.207	0.076	0.071
B3-f4	0.108	0.148	0.304	0.000	0.000	0.200	0.074	0.063
B3-f5	0.089	0.120	0.235	0.000	0.000	0.155	0.045	0.045
B3-f7	0.124	0.189	0.301	0.000	0.000	0.213	0.102	0.118
B3-f8	0.141	0.222	0.342	0.000	0.000	0.248	0.130	0.141
BWc-1	0.112	0.158	0.317	0.000	0.000	0.211	0.077	0.069
BWc-2	0.132	0.191	0.340	0.000	0.000	0.232	0.107	0.087
BWc-3	0.146	0.221	0.355	0.000	0.000	0.239	0.117	0.095
BWc-4	0.124	0.186	0.270	0.000	0.000	0.202	0.106	0.120
BWc-5	0.155	0.247	0.328	0.000	0.000	0.231	0.114	0.099
BWc-6	0.125	0.174	0.231	0.000	0.000	0.178	0.090	0.095
BWc-7	0.114	0.145	0.282	0.000	0.000	0.173	0.062	0.060
BWc-8	0.159	0.244	0.347	0.000	0.000	0.243	0.125	0.104
BWc-9	0.125	0.178	0.331	0.000	0.000	0.226	0.093	0.084
BWc-10	0.122	0.182	0.290	0.000	0.000	0.206	0.097	0.107
BWc-11	0.139	0.207	0.365	0.000	0.000	0.244	0.117	0.097
BWc-12	0.141	0.209	0.353	0.000	0.000	0.240	0.116	0.097
BWc-13	0.162	0.262	0.373	0.000	0.000	0.252	0.129	0.108

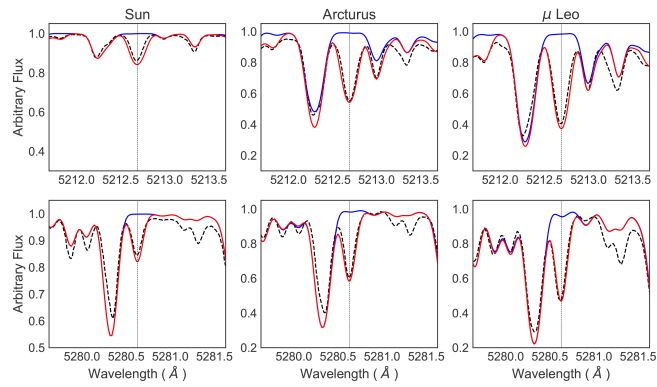


Figure B.1: Co I 5212.537, 5280.629 Å fitted to the Sun, Arcturus, and  $\mu$  Leo.

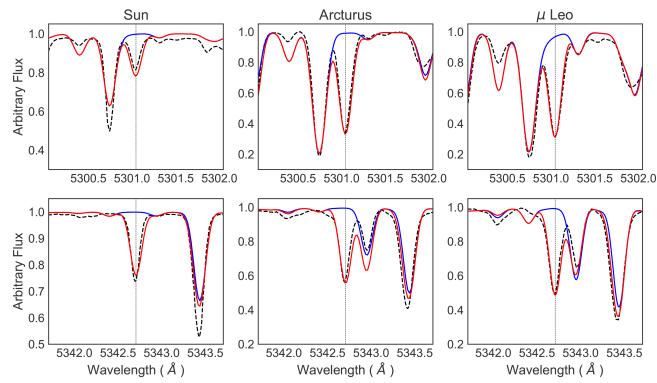


Figure B.2: Co I 5301.039, 5342.695 Å fitted to the Sun, Arcturus, and  $\mu$  Leo.

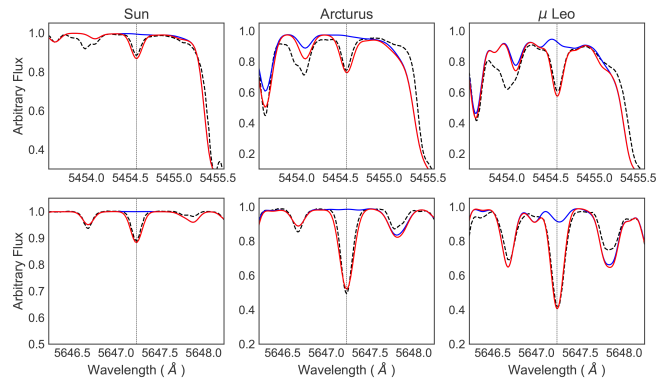


Figure B.3: Co I 5454.572, 5647.234 Å fitted to the Sun, Arcturus, and  $\mu$  Leo.

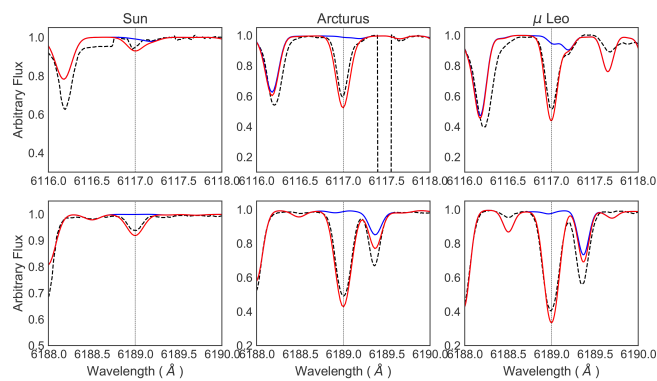


Figure B.4: Co I 6117.0, 6188.996 Å fitted to the Sun, Arcturus, and  $\mu$  Leo.

Table B.2 - Metallicity [Fe/H] and abundances of C, N, O, Na, Mg, Al, Mn, Co, Cu for the 56 sample red giants.

Star	[Fe/H]	[C/Fe]	[N/Fe]	[O/Fe]	[Na/Fe]	[Mg/Fe]	[Al/Fe]	[Mn/Fe]	[Cu/Fe]	[Co/Fe] <sub>LTE</sub>	[Co/Fe] <sub>NLTE</sub>	[Zn/Fe]
B6-b1	0.07	-0.15	0.50	0.00	0.57	0.21	0.59	0.06	-0.20	-0.20	-0.07	-0.20
B6-b2	-0.01	-0.05	0.35	0.00	—	—	—	-0.03	0.03	-0.15	-0.04	-0.15
B6-b3	0.10	-0.25	0.50	-0.12	0.45	0.21	0.43	0.00	0.03	-0.05	0.08	-0.27
B6-b4	-0.41	-0.15	0.15	0.30	0.15	0.41	0.31	-0.20	-0.08	-0.06	0.03	0.00
B6-b5	-0.37	-0.10	0.30	0.15	0.32	0.42	0.58	-0.04	0.13	-0.05	0.06	0.10
B6-b6	0.11	-0.15	0.50	-0.10	0.68	0.32	0.67	0.00	-0.03	-0.08	0.05	-0.40
B6-b8	0.03	0.00	0.10	-0.03	0.46	0.31	0.50	-0.03	-0.15	-0.20	-0.11	-0.08
B6-f1	-0.01	0.05	0.20	0.03	0.20	0.24	0.41	0.02	-0.20	-0.14	-0.03	-0.30
B6-f2	-0.51	0.00	0.20	0.20	0.22	0.44	0.57	-0.08	-0.20	-0.08	0.05	0.05
B6-f3	-0.29	-0.05	0.30	0.15	0.31	0.43	0.53	0.00	0.05	0.01	0.14	0.10
B6-f5	-0.37	0.05	0.00	0.10	0.23	0.41	0.74	-0.08	-0.08	-0.04	0.06	0.10
B6-f7	-0.42	0.00	0.30	—	0.22	0.54	0.68	0.00	-0.18	0.00	0.09	-0.15
B6-f8	0.04	-0.10	0.30	-0.20	0.50	0.27	0.72	0.00	0.10	-0.01	0.14	-0.60
BW-b2	0.22	-0.10	0.20	-0.10	0.01	0.40	0.26	0.00	-0.15	-0.11	0.00	-0.15
BW-b4	0.07	-0.10	0.00	-0.10	—	—	—	0.00	-0.30	-0.13	0.00	0.00
BW-b5	0.17	0.00	0.05	-0.10	0.37	0.19	0.49	0.00	-0.35	-0.02	0.05	-0.30
BW-b6	-0.25	0.00	0.65	0.15	0.22	0.59	0.55	0.00	-0.30	-0.06	0.04	0.00
BW-b7	0.10	-0.25	0.10	-0.20	—	—	—	0.00	-0.25	-0.18	-0.06	-0.30
BW-f1	0.32	-0.20	0.45	-0.18	0.93	0.46	0.49	0.00	-0.40	-0.04	0.09	-0.35
BW-f4	-1.21	0.30	0.30	0.30	-0.06	0.42	0.86	-0.72	-0.80	0.00	0.22	0.30
BW-f5	-0.59	0.10	0.40	0.25	0.23	0.45	0.50	0.00	-0.15	-0.06	0.08	0.15
BW-f6	-0.21	0.08	0.40	0.20	-0.08	0.61	0.25	0.00	-0.50	0.00	0.08	0.15
BW-f7	0.11	-0.20	0.70	-0.25	0.36	0.29	0.26	0.00	—	-0.17	-0.05	-0.20
BW-f8	-1.27	0.00	0.20	0.35	9.99	0.56	9.99	-0.60	-0.65	0.05	0.35	0.30
BL-1	-0.16	0.15	0.40	0.30	0.17	0.32	0.44	-0.01	0.05	0.12	0.22	0.05
BL-3	-0.03	0.07	0.00	0.05	0.03	0.35	0.40	-0.02	-0.10	-0.02	0.09	0.10
BL-4	0.13	-0.10	0.20	-0.20	0.70	0.39	0.78	0.00	0.23	0.00	0.14	-0.30
BL-5	0.16	0.00	0.40	-0.05	0.51	0.32	0.58	0.00	0.00	-0.08	0.05	-0.27
BL-7	-0.47	0.00	0.30	0.30	0.06	0.46	0.36	-0.30	0.08	0.06	0.16	0.30
B3-b1	-0.78	0.00	0.60	0.35	0.04	0.53	0.40	-0.35	—	-0.01	0.07	0.30
B3-b2	0.18	—	0.20	-0.10	0.27	0.35	0.19	0.00	-0.15	-0.11	0.03	-0.10
B3-b3	0.18	-0.10	0.00	-0.20	0.46	0.37	0.37	0.00	—	0.00	0.13	—
B3-b4	0.17	-0.15	0.40	-0.05	0.49	0.50	0.27	0.00	-0.13	-0.03	0.10	0.00
B3-b5	0.11	-0.20	0.00	-0.30	0.56	0.32	0.59	0.00	0.05	-0.06	0.07	0.00
B3-b7	0.20	-0.15	0.25	-0.20	0.34	0.12	0.39	0.00	0.13	0.00	0.14	-0.50
B3-b8	-0.62	-0.15	0.15	0.30	-0.02	0.47	0.34	-0.10	0.10	0.00	0.09	0.30
B3-f1	0.04	0.00	0.40	0.10	0.45	0.35	0.52	0.00	-0.13	-0.06	0.06	0.00
B3-f2	-0.25	—	—	—	0.53	0.55	0.66	0.00	0.30	0.01	0.11	0.00
B3-f3	0.06	0.00	0.00	-0.10	0.34	0.54	0.25	0.00	0.00	-0.09	0.03	0.00
B3-f4	0.09	0.00	0.10	0.10	9.99	0.20	9.99	0.00	-0.20	-0.03	0.08	0.03
B3-f5	0.16	-0.05	0.50	-0.05	—	—	—	0.00	-0.40	-0.09	-0.00	0.15
B3-f7	0.16	0.00	0.20	-0.25	—	—	—	0.00	0.00	-0.08	0.05	—
B3-f8	0.20	-0.20	0.30	-0.30	—	—	—	0.20	0.40	0.00	0.15	-0.60
BWc-1	0.09	0.05	0.30	0.10	0.24	0.29	0.41	0.05	0.00	0.00	0.12	-0.45
BWc-2	0.18	-0.20	0.15	-0.20	0.13	0.21	0.35	-0.16	-0.60	-0.15	-0.01	-0.20
BWc-3	0.28	-0.10	0.40	-0.05	0.54	0.12	0.56	0.06	0.18	-0.07	0.08	—
BWc-4	0.06	-0.10	0.05	-0.05	0.10	0.44	0.52	0.03	-0.20	-0.03	0.10	-0.30
BWc-5	0.42	-0.05	0.30	-0.10	0.72	0.01	0.60	0.20	-0.10	-0.01	0.14	-0.35
BWc-6	-0.25	-0.20	0.70	0.05	0.22	0.52	0.47	-0.04	0.00	0.00	0.11	0.00
BWc-7	-0.25	-0.20	0.30	0.05	0.21	0.39	0.26	-0.30	-0.15	-0.05	0.05	0.00
BWc-8	0.37	-0.30	0.10	-0.35	0.23	0.21	0.17	-0.06	-0.05	-0.10	0.05	0.00
BWc-9	0.15	-0.10	0.20	-0.05	0.14	0.08	0.32	0.05	0.30	-0.02	0.11	-0.05
BWc-10	0.07	-0.20	0.30	0.00	0.11	0.31	0.41	-0.06	-0.30	-0.09	0.04	0.00
BWc-11	0.17	-0.20	0.00	-0.20	0.29	0.18	0.31	-0.10	-0.15	-0.06	0.09	-0.05
BWc-12	0.23	-0.15	0.05	-0.10	0.49	0.30	0.59	0.10	-0.18	-0.07	0.07	-0.45
BWc-13	0.36	0.00	-0.15	-0.10	-0.03	0.27	0.35	-0.05	-0.25	-0.06	0.10	-0.20

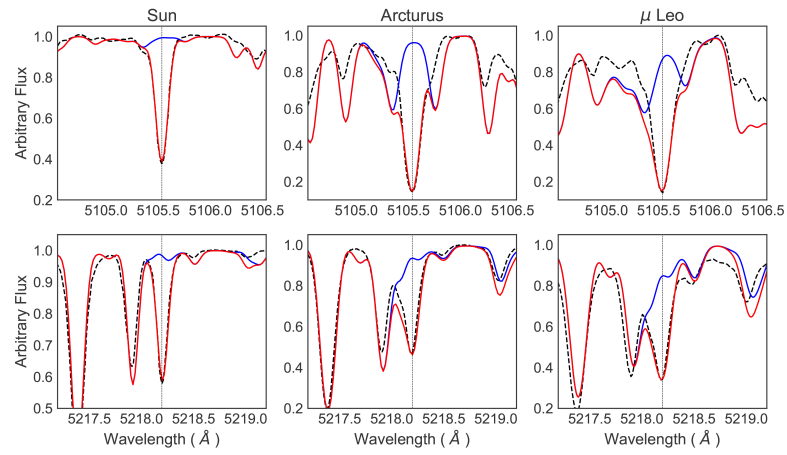


Figure B.5: Copper lines CuI 5105.537 and 5218.197 Å, as fitted to the Sun, Arcturus, and  $\mu$  Leo.



# Appendix C

---

## Line lists

### C.0.1 Near-UV line list

### C.0.2 Near-Infrared line list

Table C.2 - Line list of prominent lines in the wavelength region 15520-16000 Å, with species, their wavelengths, excitation potential (eV), and oscillator strengths from Meléndez & Barbuy (1999, MB99), APOGEE, and VALD.

species	$\lambda$ (Å)	$\chi_{\text{ex}}$ (eV)	log gf			
			MB99	APO	VALD	Adopt
Fe I	15518.891	6.278	-1.38	-1.207	-0.817	-1.38
Fe I	15519.096	6.287	-1.19	-1.098	-1.615	-1.19
Fe I	15519.361	6.287	-0.57	-0.431	-2.915	-0.57
Si I	15520.115	7.108	—	-2.279	-2.279	-2.279
Ti I	15520.508	5.202	-4.363	-4.363	-4.363	-4.363
Fe I	15521.681	6.323	-1.44	-1.217	-1.252	0.0
Y I	15521.684	4.244	-1.539	-1.539	-1.539	-1.539
Fe I	15522.607	6.321	-1.07	-0.886	-1.118	-1.07
Fe I	15524.309	5.793	-1.51	-1.441	-0.881	-1.51
Mn I	15525.664	4.885	—	-0.105	—	-1.0
Fe I	15527.207	6.324	-1.01	-1.108	-1.806	-0.60
Si I	15527.535	7.140	—	-3.220	—	-3.220
Ca I	15527.803	3.488	-3.478	-3.478	—	-3.478
Ca I	15527.827	3.488	-3.324	-3.488	—	-3.488
Fe I	15528.063	5.948	-4.894	-4.894	-3.338	-5.2
Ni I	15528.811	6.297	-6.996	-6.162	-6.886	-6.162
Ni I	15528.820	6.297	-4.503	-4.503	-4.503	-4.503
Fe I	15530.811	6.566	-1.115	-1.115	-1.863	-1.863
Ti I	15531.298	4.655	—	0.545	-0.161	+0.545

Table C.2 - continued.

Fe I	15531.752	5.643	-0.73	-0.564	-0.243	-0.73
Fe I	15531.802	6.242	-1.016	-1.016	—	-1.016
Si I	15532.263	7.140	—	-2.450	—	-2.450
Si I	15532.449	6.719	—	-1.990	-1.397	-1.990
Si I	15533.977	7.140	—	-3.660	—	-3.660
Fe I	15534.245	5.642	-0.47	-0.384	-0.382	-0.47
Mg I	15534.409	6.784	—	-1.890	—	-1.890
Mn I	15536.350	4.143	—	-1.369	—	-1.1
Fe I	15536.589	6.667	—	-6.012	-6.032	-6.512
Ca I	15536.826	5.575	—	-2.165	-2.193	-2.165
Fe I	15536.912	6.592	—	-3.256	-3.033	-3.256
Fe I	15537.453	5.793	-1.71	-1.599	-1.084	-1.084
Fe I	15537.695	6.324	-0.38	-0.261	-0.033	-0.70
Fe I	15538.093	6.334	—	-2.648	-2.693	-2.648
Si I	15538.463	6.761	—	-2.614	-2.208	-2.614
Fe I	15538.772	6.454	-2.750	-2.750	—	-2.750
Al I	15539.074	6.780	—	-2.020	—	-2.020
Fe I	15539.347	5.794	—	-4.850	-4.884	-4.884
Al I	15539.731	6.780	—	-2.540	—	-2.540
Si I	15539.992	6.804	—	-1.866	-2.431	-1.866
Fe I	15540.228	6.667	—	-6.776	-6.792	-6.776
Fe I	15540.231	6.667	—	-6.719	-6.724	-6.719
Fe I	15541.405	5.845	—	-2.801	-2.765	-2.801
Fe I	15541.424	6.394	—	-5.544	-6.589	-5.544
Fe I	15541.833	5.967	—	-2.767	-2.449	-2.767
Fe I	15541.845	6.371	—	-2.488	-2.432	-2.488
Fe I	15541.878	6.324	—	-2.425	-0.958	-2.425
Fe I	15542.079	5.642	-0.70	-0.577	-0.337	-0.70
Si I	15542.016	7.009	-1.38	-2.507	-1.617	-1.38
Ti I	15542.195	4.690	—	-0.815	-0.815	-0.815
Fe I	15542.615	5.931	—	-3.871	-3.870	-3.870
Fe I	15542.951	6.620	—	-5.324	-5.056	-5.324
Fe I	15543.662	6.658	—	-5.597	-5.615	-5.10
Ti I	15543.758	1.879	-1.48	-1.160	-1.080	0.0
Y I	15543.845	4.013	—	-2.423	-2.423	-2.423
Fe I	15545.450	6.743	—	-3.430	-4.572	-3.430
Fe I	15547.711	6.781	—	-2.824	-0.650	-2.824
Fe I	15548.685	6.348	—	-3.839	-1.834	-3.839
Fe I	15550.436	6.324	—	-0.492	-0.102	-0.492
Fe I	15550.480	6.366	—	-0.752	-3.080	-0.752
Fe I	15550.548	6.113	—	-3.119	-3.096	-3.096

Table C.2 - continued.

Fe I	15550.635	6.665	—	-3.835	-4.035	-4.035
Fe I	15551.433	6.348	-0.31	-0.258	-0.371	-0.31
Fe I	15552.098	5.524	—	-4.264	-2.231	-4.264
Fe I	15552.202	5.621	—	-3.744	-3.323	-3.744
Fe I	15552.381	6.543	—	-3.979	-4.024	-4.024
Fe I	15553.192	6.324	—	-3.485	-1.615	-3.485
Fe I	15553.577	5.479	—	-4.453	-2.471	-4.453
Fe I	15554.416	6.743	—	-3.942	-3.583	-3.942
Fe I	15554.518	6.278	—	-1.081	-1.962	-1.081
Fe I	15554.540	6.411	—	-3.308	-3.400	-3.308
Ti I	15554.547	4.434	—	-1.453	-1.453	-1.453
Fe I	15555.435	6.410	—	-3.872	-1.859	-3.872
Ni I	15555.12	5.28	-0.61		-0.512	-0.61
Ni I	15555.21	5.28	-1.03		—	-1.03
Ni I	15555.375	5.489	0.007	0.007	0.218	0.007
Fe I	15556.684	5.931	—	-2.660	-2.671	-2.660
Fe I	15557.091	6.654	—	-3.475	-4.153	-3.475
Si I	15557.779	5.965	-0.90	-0.820	-0.810	-0.90
Fe I	15558.503	6.369	—	-3.431	-3.894	-3.431
Fe I	15559.382	6.591	—	-5.186	—	-5.186
Ni I	15559.471	5.869	—	-2.816	-2.816	-2.816
Fe I	15559.721	5.929	—	-3.865	-3.871	-3.871
Fe I	15560.038	6.665	—	-2.656	-2.654	-2.654
Mn I	15560.418	5.424	—	0.705	—	0.20
Fe I	15560.784	6.350	-0.55	-0.536	-0.475	-0.55
Si I	15561.251	7.041	—	-1.397	-1.456	-1.397
Fe I	15561.343	6.654	—	-5.198	-5.852	-5.198
Fe I	15561.472	6.711	—	-3.917	-5.126	-3.917
Fe I	15562.491	6.716	—	-3.828	-3.663	-3.828
Ni I	15562.567	6.367	—	-2.095	-2.095	-2.095
Fe I	15562.920	6.412	—	-4.372	-3.952	-4.372
Fe I	15563.180	6.238	—	-4.085	-2.085	-4.085
Fe I	15563.184	6.342	—	-4.596	-4.312	-4.596
Fe I	15563.223	6.548	—	-3.217	—	-3.217
Fe I	15563.335	6.342	—	-2.442	—	-2.442
Fe I	15563.904	6.351	—	-3.900	-1.918	-3.900
Fe I	15564.115	5.931	—	-5.908	-5.818	-5.818
Fe I	15564.357	5.615	—	-4.377	-2.409	-4.377
Fe I	15564.871	6.616	—	-5.602	-5.362	-5.602
Fe I	15565.150	5.427	—	-4.058	-4.147	-4.058
Fe I	15565.222	6.324	-0.95	-0.925	-0.557	-0.95

Table C.2 - continued.

Fe I	15565.688	6.835	—	-4.456	—	-4.456
Fe I	15566.243	6.039	—	-3.525	-3.345	-3.525
Fe I	15566.725	6.351	-0.50	-0.413	-0.681	-0.50
Fe I	15567.253	6.351	—	-4.033	-5.054	-4.033
Fe I	15567.501	6.441	—	-3.982	-1.995	-3.982
Fe I	15567.571	6.616	—	-1.989	—	-1.989
Fe I	15568.335	5.884	—	-4.390	-2.550	-4.390
Fe I	15569.236	5.513	-2.36	-2.248	-2.709	-2.36
Fe I	15569.928	6.710	—	-3.792	-3.384	-3.792
Fe I	15570.446	6.803	—	-2.435	—	-2.435
Al I	15570.752	6.780	—	-3.634	—	-3.634
Fe I	15571.118	5.880	-1.69	-1.582	-1.421	-1.69
Fe I	15571.749	6.322	-0.90	-0.769	-0.857	-0.50
Fe I	15572.586	6.592	—	-4.151	—	-4.151
Ni I	15573.937	6.117	—	-2.485	-2.485	-2.485
Fe I	15574.070	6.312	-1.44	-2.355	-2.323	-1.44
Fe I	15575.368	6.441	.....	-6.028	-5.669	
Fe I	15576.038	5.507	-2.27	-2.158	-2.234	-2.5
Fe I	15576.448	6.683	—	-6.193	-6.178	-6.193
Fe I	15576.463	6.683	—	-4.803	-4.816	-4.803
Fe I	15576.490	6.683	—	-4.843	-4.833	-4.843
Fe I	15576.533	6.282	—	-2.747	-2.844	-2.747
Fe I	15577.526	6.654	—	-1.975	—	-1.975
Ca I	15577.861	5.251	—	-3.983	—	-3.983
Fe I	15577.876	6.441	—	-2.489	-2.389	-2.489
Fe I	15579.077	6.324	-0.99	-1.148	-2.123	-0.99
Fe I	15579.582	6.266	—	-5.461	-5.439	-5.461
Ca I	15580.434	5.251	—	-1.210	—	-1.210
Fe I	15580.667	6.342	—	-3.963	-3.589	-3.963
Fe I	15580.818	6.342	—	-4.761	-4.808	-4.761
Fe I	15581.508	6.456	—	-3.465	—	-3.465
Fe I	15581.867	5.386	—	-3.727	-3.829	-3.727
Fe I	15582.508	6.276	—	-4.408	-4.574	-4.408
Fe I	15582.749	5.796	—	-3.855	-3.899	-3.855
Fe I	15583.477	6.687	—	-4.551	—	-4.551
Fe I	15584.583	6.654	—	-2.913	-2.961	-2.913
Fe I	15584.602	6.645	—	-6.231	-6.235	-6.235
Fe I	15584.617	6.645	—	-4.823	-4.824	-4.824
Fe I	15585.059	6.640	—	-5.257	-4.500	-5.257
Fe I	15585.370	6.360	—	-2.742	-2.827	-2.742
Fe I	15585.727	6.242	—	-3.645	-1.677	-3.645

Table C.2 - continued.

Fe I	15586.138	6.645	—	-6.213	-5.123	-6.213
Fe I	15586.182	4.594	—	-6.078	-6.072	-6.072
Fe I	15586.692	6.543	—	-4.474	-4.563	-4.574
Fe I	15586.928	6.365	—	-2.665	-0.659	-2.664
Fe I	15587.513	6.351	—	-6.062	-6.774	-6.062
Fe I	15588.089	6.837	—	-2.738	—	-2.738
Fe I	15588.259	6.367	0.22	0.267	0.419	0.10
Fe I	15588.26	5.49	-2.76	—	—	-2.76
Fe I	15588.663	5.491	—	-6.294	-4.420	-6.294
Fe I	15588.738	6.259	—	-3.385	-3.227	-3.385
Fe I	15588.758	6.485	—	-3.265	-3.284	-3.265
Ni I	15589.020	5.448	—	-2.750	-2.750	-2.750
Fe I	15589.555	5.948	—	-3.317	-3.920	-3.317
Fe I	15589.796	6.645	—	-3.800	-3.801	-3.800
Fe I	15590.046	6.242	-0.55	-0.379	-0.829	-0.55
Fe I	15590.365	6.611	—	-4.451	-4.336	-4.451
Fe I	15590.724	6.365	—	-1.059	-1.544	-1.059
Fe I	15591.298	6.580	—	-3.631	—	-3.361
Fe I	15591.490	6.242	0.36	0.702	0.874	0.36
Fe I	15591.498	6.365	0.36	-0.297	-0.687	0.36
Si I	15591.841	6.270	—	-3.319	-3.319	-3.319
Ca I	15592.166	5.575	—	-2.412	-2.443	-2.412
Fe I	15592.222	6.730	—	-4.460	-4.451	-4.460
Fe I	15592.232	6.730	—	-4.731	-4.723	-4.731
Fe I	15592.266	6.669	—	-7.741	-7.710	-7.741
Fe I	15592.269	6.669	—	-7.520	-7.318	-7.520
Fe I	15592.536	5.934	—	-3.513	-3.502	-3.502
Fe I	15592.665	6.772	—	-6.210	—	-6.210
Fe I	15592.835	6.254	—	-2.166	-1.493	-2.166
Fe I	15592.993	2.223	—	-13.332	—	-13.33
Ca I	15593.718	5.027	—	-1.717	-1.626	-1.717
Fe I	15593.229	5.880	—	-3.451	-3.352	-3.451
Fe I	15593.750	5.034	-1.98	-1.801	-1.922	-1.98
Fe I	15593.886	6.730	—	-4.334	-4.325	-4.334
Fe I	15594.027	6.687	—	-5.477	-6.108	-5.477
Fe I	15594.253	6.621	—	-6.068	-5.166	-6.068
Fe I	15594.397	6.350	—	-2.091	-0.091	-2.091
Fe I	15595.341	6.365	—	-4.146	-3.984	-4.146
Fe I	15595.869	6.548	—	-2.905	—	-2.905
Fe I	15595.993	5.796	—	-4.738	-2.810	-4.738
Fe I	15596.085	6.986	—	-4.758	—	-4.758

Table C.2 - continued.

Fe I	15596.311	6.366	—	-5.125	-5.190	-5.125
Fe I	15596.392	6.730	—	-4.731	-4.705	-4.731
Fe I	15596.538	2.845	—	-10.073	—	-10.073
Fe I	15596.586	6.885	—	-3.690	-1.697	-3.690
Fe I	15596.883	6.254	—	-2.364	-3.062	-2.364
Fe I	15597.141	5.411	—	-4.454	-7.139	-4.454
Fe I	15597.564	6.512	—	-4.055	-4.421	-4.055
Fe I	15598.572	5.948	—	-3.772	-3.820	-3.772
Fe I	15598.769	6.350	—	-2.281	-0.282	-2.281
Fe I	15598.869	6.242	-0.92	-0.739	-0.236	-0.92
Ti I	15599.134	4.690	-0.03	—	-0.501	-0.03
Fe I	15599.195	5.633	—	-5.640	-5.711	-5.640
Fe I	15600.295	2.223	—	-8.765	-8.765	-8.765
Fe I	15600.295	2.223	—	-11.691	—	-11.691
Fe I	15600.524	6.645	—	-5.060	—	-5.060
Fe I	15600.690	6.366	—	-5.151	-4.267	-5.151
Fe I	15600.887	6.366	—	-3.479	-3.475	-3.479

### C.1 Molecular line lists: CO, OH and CN

Table C.1 - List of near-UV absorption lines considered.

Ion	Wavelength (Å)	Ion	Wavelength (Å)	Ion	Wavelength (Å)
BeII	3130.42	ZrII	3357.26	NdII	3826.41
BeII	3131.07	ZrII	3404.83	NdII	3838.98
ScII	3576.34	ZrII	3408.08	SmII	3568.27
ScII	3590.47	ZrII	3410.24	SmII	3796.75
TiI	3998.64	ZrII	3430.53	SmII	3896.97
TiII	3321.70	ZrII	3438.23	EuII	3724.93
TiII	3343.76	ZrII	3457.56	EuII	3819.67
TiII	3491.05	ZrII	3458.93	EuII	3907.11
VII	3951.96	ZrII	3479.02	EuII	3930.40
CrI	3578.68	ZrII	3479.39	GdII	3549.36
MnII	3441.99	ZrII	3481.15	GdII	3557.06
MnII	3460.32	ZrII	3496.20	GdII	3712.70
MnII	3482.90	ZrII	3505.67	GdII	3768.40
MnII	3488.68	ZrII	3506.05	TbII	3600.41
MnII	3495.83	ZrII	3525.81	TbII	3702.85
MnII	3497.53	ZrII	3549.51	DyII	3531.71
CoI	3412.34	ZrII	3551.95	DyII	3536.02
CoI	3412.63	ZrII	3556.59	DyII	3550.22
CoI	3449.16	ZrII	3576.85	DyII	3563.15
CoI	3529.03	ZrII	3588.31	DyII	3694.81
CoI	3842.05	ZrII	3607.37	DyII	3757.37
CoI	3845.47	ZrII	3614.76	DyII	3944.68
NiI	3437.28	ZrII	3751.59	DyII	3996.69
NiI	3483.77	ZrII	3766.82	HoII	3466.01
NiI	3500.85	ZrII	3836.76	HoII	3796.80
NiI	3597.71	ZrII	3998.96	HoII	3890.65
NiI	3807.14	NbII	3028.44	ErII	3692.65
CuI	3247.53	NbII	3215.59	ErII	3729.52
CuI	3273.95	NbII	3225.47	ErII	3786.84
ZnI	3075.90	MoI	3864.10	ErII	3830.48
ZnI	3302.58	RuI	3436.74	ErII	3896.23
ZnI	3345.01	RuI	3498.94	ErII	3906.31
GeI	3039.07	RuI	3742.28	TmII	3701.36
YII	3549.01	RuI	3798.90	TmII	3795.76
YII	3584.52	RuI	3799.35	TmII	3848.02
YII	3600.74	RhI	3396.82	YbII	3694.20
YII	3601.91	RhI	3434.89	HfII	3276.85
YII	3611.04	RhI	3692.36	HfII	3399.79
YII	3774.33	RhI	3700.91	HfII	3719.28
YII	3788.69	PdI	3242.70	OsI	3058.66
YII	3818.34	PdI	3404.58	IrI	3220.78
YII	3950.35	PdI	3516.94	IrI	3800.12
ZrII	3054.84	AgI	3280.68	PbI	3683.46
ZrII	3095.07	AgI	3382.90	BiI	3024.64
ZrII	3125.92	SnI	3801.01	ThII	3351.23
ZrII	3129.76	BaII	3891.78	ThII	3433.99
ZrII	3273.05	LaII	3794.77	ThII	3435.98
ZrII	3279.26	LaII	3949.10	ThII	3469.92
ZrII	3284.71	LaII	3988.51	ThII	3539.59
ZrII	3305.15	LaII	3995.74	ThII	3675.57
ZrII	3334.62	CeII	3999.24	UII	3859.57
ZrII	3344.79	NdII	3784.24		
ZrII	3356.09	NdII	3810.48		

Table C.3 - Molecular lines: CO and OH

Molecule	Wavelength( $\text{\AA}$ )	( $v',v''$ )	branch	J
CO	15577.4	3-0	R	35
CO	15577.4	3-0	R	34
CO	15577.6	3-0	R	33
CO	15577.8	3-0	R	36
CO	15578.0	3-0	R	32
CO	15578.4	3-0	R	37
CO	15578.8	3-0	R	31
CO	15579.3	3-0	R	38
CO	15579.8	3-0	R	30
CO	15580.4	3-0	R	39
CO	15581.0	3-0	R	29
CO	15581.8	3-0	R	40
CO	15582.6	3-0	R	28
CO	15583.5	3-0	R	41
CO	15584.4	3-0	R	27
CO	15585.4	3-0	R	42
CO	15586.4	3-0	R	26
CO	15587.7	3-0	R	43
CO	15588.8	3-0	R	25
CO	15590.1	3-0	R	44
CO	15591.4	3-0	R	24
CO	15592.9	3-0	R	45
CO	15594.2	3-0	R	23
CO	15595.9	3-0	R	46
CO	15597.3	3-0	R	22
CO	15599.3	3-0	R	47
OH	15535.46	3-1	P1e5.5	
OH	15536.71	3-1	P1f5.5	
OH	15542.10			
OH	15560.24	2-0	P2e10.5	
OH	15565.91	4-2	R2ef2.5	
OH	15568.78	2-0	P1e11.5	

Table C.4 - Molecular lines: CN

Molecule	Wavelength(Å)	(v',v'')	branch	J
CN	15522.7	0-1	R1	73
CN	15528.2	2-3	Q2	33
CN	15528.8	2-3	P21	34
CN	15529.9	0-1	Q12	52
CN	15530.8	0-1	P1	53
CN	15534.1	2-3	R12	32
CN	15534.6	2-3	Q1	33
CN	15535.8	2-3	P2	25
CN	15536.6	1-2	Q1	50
CN	15538.1	1-2	P12	33
CN	15539.7	1-2	Q12	40
CN	15540.4	1-2	P1	41
CN	15542.2	2-3	P12	18
CN	15544.5	0-1	Q2	62
CN	15542.9	2-3	R1	45
CN	15545.7	2-3	R2	45
CN	15550.5	2-3	Q12	24
CN	15550.9	2-3	P1	25
CN	15552.7	1-2	P2	41
CN	15553.6	1-2	Q2	5
CN	15554.5	1-2	P21	51
CN	15555.6	0-1	R2	73
CN	15555.8	2-3	Q2	34
CN	15556.4	2-3	P21	35
CN	15557.9	0-1	P2	53
CN	15558.7	0-1	P12	45
CN	15560.6	2-3	Q1	34
CN	15561.4	3-4	R2	4
CN	15561.4	3-4	R2	9
CN	15561.5	3-4	Q21	10
CN	15562.2	0-1	R12	62
CN	15563.4	0-1	Q1	63
CN	15563.4	3-4	Q21	11
CN	15565.3	2-3	P2	26
CN	15565.9	3-4	R2	11
CN	15566.0	3-4	Q21	12
CN	15569.1	3-4	R2	12
CN	15569.3	3-4	Q21	13
CN	15571.0	2-3	R1	46
CN	15572.4	2-3	P12	19
CN	15573.2	0-1	R1	74
CN	15573.3	3-4	Q21	14
CN	15575.0	1-2	R2	46
CN	15576.3	1-2	Q1	51
CN	15577.7	3-4	R2	14
CN	15577.9	3-4	Q21	15
CN	15577.9	2-3	Q12	25
CN	15578.4	2-3	P1	26
CN	15579.8	0-1	Q12	53
CN	15580.2	1-2	Q12	41
CN	15580.8	0-1	P1	54
CN	15580.9	1-2	P1	42
CN	15583.1	3-4	R2	15
CN	15583.3	3-4	Q21	16
CN	15584.2	2-3	Q2	35
CN	15584.8	2-3	P21	36
CN	15586.4	3-4	Q2	2
CN	15586.9	2-3	R12	34
CN	15587.5	2-3	Q1	35
CN	15589.1	3-4	R2	16
CN	15589.4	3-4	Q21	17
CN	15592.3	3-4	Q2	3
CN	15594.6	1-2	Q2	51
CN	15594.8	0-1	Q2	63
CN	15595.7	2-3	P2	27
CN	15595.9	0-1	P21	64
CN	15596.0	3-4	R2	17
CN	15596.3	3-4	Q21	18
CN	15598.7	3-4	Q2	4
CN	15598.8	3-4	P2	2
CN	15598.8	3-4	P21	5



## Atomic data

### *D.1 Hyperfine structure constants*

The hyperfine structure (HFS) constants A-factor and B-factor for magnetic dipole and electronic quadrupole, respectively are summarised in Tables D.1, D.2, and D.3. In Table D.1 we present the HFS constants for Sc, V and Cu lines; In Table D.2 the constants for Co I and Cu I lines employed; And in Table D.3 are listed the HFS for ground-UV lines of Sc II, V II, Mn II, Co I, Cu I.

In Tables D.4, D.5, D.6, , D.7, and D.8 are listed the lines of Co I in terms of their HFS components, and corresponding oscillator strengths. In Tables D.9 and D.10 are presented the HFS components and their corresponding oscillator strengths for the Cu I 3247.53Å, 3273.95Å, 5105.50Å, and 5218.20Å lines.

Table D.1 - Atomic constants for ScI and ScII used to compute hyperfine structure: A and B constants from Mansour, N. B., Dinneen, T. P., Young, L. 1989, NIMPB, 40-252M, Villemoes et al. 1992, PhRvA, 45-6241V for ScII and Biehl (1976) for ScI. For VI the A and B constants are from 1 UBDE Unkel, P., Buch, P., Dembczynski, J., Ertmer, W., and Johan, U. 1989, Z. Phys. D 11, 259-271. 2 CPGC Childs, W.J., Poulsen, O., Goodman, L.S., and Crosswhite, H. 1979, Phys. Rev. A 19, 168-176. 3 PBAG Palmeri, P., Biemont, E., Aboussaid, A., and Godefroid, M. 1995, J.Phys.B 28, 3741-3752. 4 CBFV Cochrane, E.C.A., Benton, D.M., Foreset, D.H., and Griffith, J.A.R. 1998, J.Phys.B 31, 2203-2213. 5 LGB Lefebvre, P-H, Garnir, H-P, Biemont, E 2002, Physica Scripta 66, 363-366. B constants not available in the literature are assumed as null.

Species	$\lambda$ (Å)	Lower level	J	A(mK)	A(MHz)	B(mK)	B(MHz)	Upper level	J	A(mK)	A(MHz)	B(mK)	B(MHz)
<sup>45</sup> ScI	5671.805	3d <sup>2</sup> ( <sup>3</sup> F)4s 4F	9/2	+9.5	284.8029	-0.4	-11.9917	3d <sup>2</sup> ( <sup>3</sup> F)4p 4G	11/2	+1.5	44.9689	—	—
<sup>45</sup> ScI	5686.826	3d <sup>2</sup> ( <sup>3</sup> F)4s 4F	7/2	+8.3	248.8278	-0.3	-8.9938	3d <sup>2</sup> ( <sup>3</sup> F)4p 4G	7/2	+4.9	146.8983	—	—
<sup>45</sup> ScI	6210.676	3d4s <sup>2</sup> 2D	3/2	+8.98	269.2137	-0.88	-26.3817	3d4s(1D)4p 2D	3/2	-11.5	-344.7614	—	—
<sup>45</sup> ScII	5526.790	3p <sup>6</sup> 3d <sup>2</sup> 1G	4.0	—	M 135.232	—	M -63.44	3p <sup>6</sup> 3d4p 1F <sup>o</sup>	3.0	—	193.1	—	-65
<sup>45</sup> ScII	5552.224	3p <sup>6</sup> 4s <sup>2</sup> 1S	0.0	—	—	—	—	3p <sup>6</sup> 3d4p 3P <sup>o</sup>	1.0	—	258.0	—	12.0
<sup>45</sup> ScII	5657.896	3p <sup>6</sup> 3d <sup>2</sup> 3P	2.0	—	M -27.732	—	M 22.13	3p <sup>6</sup> 3d4p 3P <sup>o</sup>	2.0	—	105.6	—	-21
<sup>45</sup> ScII	5684.202	3p <sup>6</sup> 3d <sup>2</sup> 3P	2.0	—	-27.2	—	26.0	3p <sup>6</sup> 3d4p 3P <sup>o</sup>	1.0	—	258.0	—	12.0
<sup>45</sup> ScII	6245.637	3p <sup>6</sup> 3d <sup>2</sup> 3P	2.0	—	M -27.732	—	22.13	3p <sup>6</sup> 3d4p 3D <sup>o</sup>	3.0	—	101.8	—	24
<sup>45</sup> ScII	6300.698	3p <sup>6</sup> 3d <sup>2</sup> 3P	2.0	—	-27.2	—	26.0	3p <sup>6</sup> 3d4p 3D <sup>o</sup>	2.0	—	125.7	—	6.0
<sup>45</sup> ScII	6320.84	3p <sup>6</sup> 3d <sup>2</sup> 3P	1.0	—	-108.1	—	-13.0	3p <sup>6</sup> 3d4p 3D <sup>o</sup>	1.0	—	307.0	—	1.0
<sup>45</sup> ScII	6604.601	3p <sup>6</sup> 3d <sup>2</sup> 1D	2.0	—	149.361	—	7.818	3p <sup>6</sup> 3d4p 1D <sup>o</sup>	2.0	—	215.7	—	18
<sup>51</sup> VI	5703.5603d <sup>4</sup> ( <sup>5</sup> D)4s a <sup>4</sup> D3/2	7.558 <sup>1</sup>	—	2.075 <sup>1</sup>	—	3d <sup>4</sup> ( <sup>5</sup> D)4p y <sup>4</sup> F <sup>0</sup>	5/2	—	216.0 <sup>5</sup>	—	0.0 <sup>5</sup>	—	—
<sup>51</sup> VI	6081.4403d <sup>4</sup> ( <sup>5</sup> D)4s a <sup>4</sup> D3/2	7.558 <sup>1</sup>	—	2.075 <sup>1</sup>	—	3d <sup>4</sup> ( <sup>5</sup> D)4p z <sup>4</sup> F <sup>0</sup>	3/2	—	-286.4 <sup>2</sup>	—	-6.0 <sup>2</sup>	—	—
<sup>51</sup> VI	6090.2203d <sup>4</sup> ( <sup>5</sup> D)4s a <sup>4</sup> D7/2-160.172 <sup>1</sup>	—	—	15.256 <sup>1</sup>	—	3d <sup>4</sup> ( <sup>5</sup> D)4p z <sup>4</sup> F <sup>0</sup>	5/2	—	-89.8 <sup>2</sup>	—	8.0 <sup>2</sup>	—	—
<sup>51</sup> VI	6119.5203d <sup>4</sup> ( <sup>5</sup> D)4s a <sup>4</sup> D5/2-143.367 <sup>1</sup>	—	—	1.067 <sup>1</sup>	—	3d <sup>4</sup> ( <sup>5</sup> D)4p z <sup>4</sup> F <sup>0</sup>	3/2	—	-286.4 <sup>2</sup>	—	-6.0 <sup>2</sup>	—	—
<sup>51</sup> VI	6199.1903d <sup>4</sup> ( <sup>5</sup> D)4s a <sup>6</sup> D7/2 382.368 <sup>1</sup>	—	—	2.220 <sup>1</sup>	—	3d <sup>3</sup> ( <sup>4</sup> F)4s4p( <sup>3</sup> P <sup>0</sup> ) z <sup>6</sup> D <sup>0</sup>	9/2	—	503.46 <sup>4</sup>	—	3.3 <sup>4</sup>	—	—
<sup>51</sup> VI	6243.1003d <sup>4</sup> ( <sup>5</sup> D)4s a <sup>6</sup> D9/2 406.854 <sup>1</sup>	—	—	14.721 <sup>1</sup>	—	3d <sup>3</sup> ( <sup>4</sup> F)4s4p( <sup>3</sup> P <sup>0</sup> ) z <sup>6</sup> D <sup>0</sup>	9/2	—	503.46 <sup>4</sup>	—	3.3 <sup>4</sup>	—	—
<sup>51</sup> VI	6251.8203d <sup>4</sup> ( <sup>5</sup> D)4s a <sup>6</sup> D7/2 382.368 <sup>1</sup>	—	—	2.220 <sup>1</sup>	—	3d <sup>3</sup> ( <sup>4</sup> F)4s4p( <sup>3</sup> P <sup>0</sup> ) z <sup>6</sup> D <sup>0</sup>	7/2	—	514.35 <sup>4</sup>	—	-1.2 <sup>4</sup>	—	—
<sup>51</sup> VI	6274.6503d <sup>4</sup> ( <sup>5</sup> D)4s a <sup>6</sup> D3/2 405.605 <sup>1</sup>	—	—	-8.060 <sup>1</sup>	—	3d <sup>3</sup> ( <sup>4</sup> F)4s4p( <sup>3</sup> P <sup>0</sup> ) z <sup>6</sup> D <sup>0</sup>	1/2	—	939.94 <sup>4</sup>	—	0.0 <sup>4</sup>	—	—
<sup>51</sup> VI	6285.1603d <sup>4</sup> ( <sup>5</sup> D)4s a <sup>6</sup> D5/2 373.595 <sup>1</sup>	—	—	-2.575 <sup>1</sup>	—	3d <sup>3</sup> ( <sup>4</sup> F)4s4p( <sup>3</sup> P <sup>0</sup> ) z <sup>6</sup> D <sup>0</sup>	3/2	—	594.69 <sup>4</sup>	—	-4.4 <sup>4</sup>	—	—
<sup>63</sup> CuI	5105.537	4p 2P [case e]	1.5	6.5	194.865	-0.96	-28.78	4s2 2D [case b]	2.5	24.97	748.582	6.20	185.871
<sup>63</sup> CuI	5218.197	4p 2P [case e]	1.5	6.5	194.865	-0.96	-28.78	4d 2D [—]	2.5	0.0*	0.0*	0.0*	0.0*
<sup>65</sup> CuI	5105.537	4p 2P [case e]	1.5	6.96	208.66	-0.86	-25.78	4s2 2D [case b]	2.5	26.79	803.14	5.81	174.18
<sup>65</sup> CuI	5218.197	4p 2P [case e]	1.5	6.96	208.66	-0.86	-25.78	4d 2D [—]	2.5	0.0*	0.0*	0.0*	0.0*

Table D.2 - Atomic constants for CoI and CuI used to compute hyperfine structure: A and B constants from Pickering (1996) for CoI. For CuI, the A and B constants are from Kurucz (1993) and Biehl (1976), and they are reported in Ernandes et al. (2018).

Species	$\lambda$ (Å)	Lower level	J	A(mK)	A(MHz)	B(mK)	B(MHz)	Upper level	J	A(mK)	A(MHz)	B(mK)	B(MHz)
<sup>59</sup> CoI	4749.612	( <sup>4</sup> F)4sp z <sup>6</sup> D	9/2	28.05	840.9180	0.08	2.3983	( <sup>5</sup> F)s5s e <sup>6</sup> F	11/2	31.45	942.8475	0.07	2.0985
<sup>59</sup> CoI	5212.691	( <sup>4</sup> F)4sp z <sup>4</sup> F	9/2	27.02	810.0394	0.08	2.3983	( <sup>5</sup> F)s5s f <sup>4</sup> F	11/2	35.92	1076.8546	0.07	2.0985
<sup>59</sup> CoI	5280.629	( <sup>4</sup> F)4sp z <sup>4</sup> G	9/2	17.25	517.1420	0.09	2.6981	( <sup>5</sup> F)s5s f <sup>4</sup> F	7/2	28.25	846.9138	0.07	2.0985
<sup>59</sup> CoI	5301.047	d <sup>7</sup> s <sup>4</sup> a <sup>4</sup> P	5/2	5.90	176.8776	0.20	5.9959	( <sup>3</sup> F)4p y <sup>4</sup> D	5/2	15.50	464.6784	0.20	5.9959
<sup>59</sup> CoI	5342.708	( <sup>3</sup> F)4p y <sup>4</sup> G	11/2	10.0	299.7925	0.20	5.9959	( <sup>3</sup> F)4d e <sup>4</sup> H	13/2	7.60	227.8423	0.20	5.9959
<sup>59</sup> CoI	5454.572	( <sup>3</sup> F)4p y <sup>4</sup> F	9/2	9.90	296.7946	0.10	2.9979	( <sup>3</sup> F)4d g <sup>4</sup> F	9/2	9.18	275.2095	0.08	2.3983
<sup>59</sup> CoI	5647.234	( <sup>3</sup> P)4s a <sup>2</sup> P	3/2	11.20	335.7676	0.20	5.9959	( <sup>3</sup> F)4p y <sup>3</sup> D	5/2	16.40	491.6597	0.10	2.9979
<sup>59</sup> CoI	6117.000	d <sup>4</sup> s <sup>2</sup> a <sup>4</sup> P	1/2	-23.60	-707.5103	0.20	5.9959	3( <sup>4</sup> F)4sp z <sup>4</sup> D	1/2	27.50	824.4294	0.10	2.9979
<sup>59</sup> CoI	6188.996	d <sup>7</sup> s <sup>2</sup> a <sup>4</sup> P	5/2	5.90	176.8776	0.08	2.3983	( <sup>5</sup> F)4sp z <sup>4</sup> D	5/2	23.22	696.1182	0.09	2.6981
<sup>63</sup> CuI	5105.5374p 2P [case e]	1.5	6.5	194.865	-0.96	-28.78	4s2 2D [case b]	2.5	24.97	748.582	6.20	185.871	
<sup>63</sup> CuI	5218.1974p 2P [case e]	1.5	6.5	194.865	-0.96	-28.78	4d 2D [—]	2.5	0.0*	0.0*	0.0*	0.0*	
<sup>65</sup> CuI	5105.5374p 2P [case e]	1.5	6.96	208.66	-0.86	-25.78	4s2 2D [case b]	2.5	26.79	803.14	5.81	174.18	
<sup>65</sup> CuI	5218.1974p 2P [case e]	1.5	6.96	208.66	-0.86	-25.78	4d 2D [—]	2.5	0.0*	0.0*	0.0*	0.0*	

Table D.3 - Hyperfine constants A and B for Sc II (Villemoes et al. 1992; Kurucz, 1993); V II (Wood et al. 2014); Mn II (Den Hartog et al. 2011); Co I (Pickering 1996); Cu I (Biehl, 1976; Kurucz, 1993). For transitions where the electric quadrupole constants were not available we adopted the B-factor as zero.

Species	$\lambda$ (Å)	Config.	J	Lower level				Config.	J	Upper level			
				A (mK)	A (MHz)	B (mK)	B (MHz)			A (mK)	A (MHz)	B (mK)	B (MHz)
<sup>45</sup> Sc II	3576.34	3d4s 3D	2.0	507.67	15219.5665	-34.7	-1040.28	3d4p 3D	2.0	125.3	758.475	10.0	299.7925
<sup>45</sup> Sc II	3590.47	3d4s 3D	3.0	654.8	19630.4141	-63.0	-1888.6929	3d4p 3D	2.0	125.3	758.475	10.0	299.7592
<sup>51</sup> V II	3517.299	(4F)4s a3F	4.0	-2.9	-86.9398	...	...	(4F)4p z5D	3.0	...	...	...	...
<sup>51</sup> V II	3545.196	(4F)4s a3F	3.0	6.0	179.8755	...	...	(4F)4p z3D	2.0	...	...	...	...
<sup>51</sup> V II	3715.464	d4 a3H	6.0	—	—	...	...	(4F)4p z3G	5.0	...	...	...	...
<sup>51</sup> V II	3951.96	d4 a3P	2.0	0.0	0.0	...	...	(4F)4p z3D	3.0	...	...	...	...
<sup>55</sup> Mn II	3441.99	d6 a5D	4.0	74.0	2218.4646	...	...	(6S)4p z5P	3.0	-150.3	-4505.8818	85.0	2548.2363
<sup>55</sup> Mn II	3460.32	d6 a5D	3.0	5.8	173.8797	-71.0	-2129.5269	(6S)4p z5P	2.0	-310.7	-9314.5527	-87.0	-2608.1948
<sup>55</sup> Mn II	3482.90	d6 a5D	2.0	-35.0	-1049.2738	-40.0	-1199.1700	(6S)4p z5P	2.0	-310.7	-9314.5527	-87.0	-2608.1948
<sup>55</sup> Mn II	3488.68	d6 a5D	1.0	-59.0	-1768.7758	-53.0	-1588.9004	(6S)4p z5P	1.0	-737.0	22094.7090	9.0	269.8133
<sup>55</sup> Mn II	3495.83	d6 a5D	0.0	0.0	0.0	...	...	(6S)4p z5P	1.0	-737.0	22094.7090	9.0	269.8133
<sup>55</sup> Mn II	3497.53	d6 a5D	1.0	-59.0	-1768.7758	-53.0	-1588.9004	(6S)4p z5P	2.0	-310.7	-9314.5527	-87.0	-2608.1948
<sup>59</sup> Co I	3412.34	(3F)4s b4F	3.5	22.3127	668.9181	-2.643	-79.2352	(3F)4p y2G	4.5	14.73	441.5943	0.0	0.0
<sup>59</sup> Co I	3412.63	d7s2	4.5	15.01984	450.2835	4.644	139.2236	4F)4sp z4D	3.5	25.05	750.9802	3.0	89.9378
<sup>59</sup> Co I	3449.16	(3F)4s b4F	2.5	18.7524	562.1829	-1.828	-54.8021	(3F)4p y4G	2.5	26.85	804.9429	-4.0	-119.9170
<sup>59</sup> Co I	3529.03	d7s2 a4F	2.5	20.4591	613.3486	2.253	67.5433	4F)4sp z4G	3.5	14.95	448.1898	5.0	149.8963
<sup>59</sup> Co I	3842.05	(3F)4s a2F	3.5	13.01	390.0301	-5	-149.8963	4F)4sp z2D	2.5	15.4	461.6805	...	...
<sup>59</sup> Co I	3845.47	(3F)4s a2F	3.5	13.01	390.0301	-5	-149.8963	(3F)4p y2G	4.5	14.73	441.5943	0.0	0.0
<sup>63</sup> Cu I	3247.53	4s 2S	0.5	194	5815.9746	0.0	0.0	4p 2P	1.5	6.5	194.685	-0.96	-28.78
<sup>63</sup> Cu I	3273.95	4s 2S	0.5	194	5815.9746	0.0	0.0	4p 2P	0.5	6.5	194.685	-0.96	-28.78
<sup>65</sup> Cu I	3247.53	4s 2S	0.5	208	6235.6841	0.0	0.0	4p 2P	1.5	6.96	208.66	-0.86	-25.78
<sup>65</sup> Cu I	3273.95	4s 2S	0.5	208	6235.6841	0.0	0.0	4p 2P	0.5	6.96	208.66	-0.86	-25.78

Table D.4 - Calculated hyperfine structure for the Co I 3412.34, 3412.63, and 3449.16 Å lines.

3412.34Å; $\chi = 0.5136$ eV log gf(total) = 0.030			3412.63Å; $\chi = 0.00$ eV log gf(total) = -0.780			3449.16Å; $\chi = 0.5815$ eV log gf(total) = -0.090		
$\lambda$ (Å)	log gf	iso	$\lambda$ (Å)	log gf	iso	$\lambda$ (Å)	log gf	iso
3412.332	-1.776	59	3412.643	-2.5861	59	3449.171	-1.741	59
3412.334	-1.709	59	3412.640	-2.519	59	3449.164	-1.486	59
3412.331	-1.513	59	3412.634	-3.218	59	3449.176	-1.486	59
3412.340	-2.408	59	3412.643	-2.323	59	3449.169	-3.395	59
3412.336	-1.513	59	3412.637	-2.323	59	3449.159	-1.287	59
3412.331	-1.309	59	3412.629	-3.063		3449.176	-1.287	59
3412.344	-2.25	59	3412.642	-2.119		3449.166	-2.152	59
3412.339	-1.40	59	3412.634	-2.218		3449.153	-1.223	59
3412.332	-1.13	59	3412.622	-3.063		3449.175	-1.223	59
3412.350	-2.25	59	3412.640	-1.949		3449.162	-1.434	59
3412.343	-1.36	59	3412.629	-2.171		3449.146	-1.254	59
3412.334	-0.99	59	3412.614	-3.160		3449.173	-1.254	59
3412.356	-2.35	59	3412.637	-1.803		3449.157	-1.028	59
3412.347	-1.36	59	3412.623	-2.177		3449.139	-1.435	59
3412.363	-2.55	59	3412.633	-1.674		3449.152	-0.737	59
3412.353	-1.44	59	3412.615	-2.250				
3412.341	-0.74	59	3412.594	-3.762				
3412.370	-2.95	59	3412.628	-1.558				
3412.358	-1.65	59	3412.607	-2.461				
3412.345	-0.64	59	3412.622	-1.453				

Table D.5 - Calculated hyperfine structure for the Co I 3529.03, 3842.05, and 3845.47 Å lines.

3529.03Å; $\chi = 0.1744$ eV log gf(total) = -0.880			3842.05Å; $\chi = 0.9227$ eV log gf(total) = -0.770			3845.47Å; $\chi = 0.9227$ eV log gf(total) = 0.010		
$\lambda$ (Å)	log gf	iso	$\lambda$ (Å)	log gf	iso	$\lambda$ (Å)	log gf	iso
3529.030	-2.686	59	33842.044	-2.566	59	3845.480	-1.796	59
3529.028	-2.401	59	33842.046	-2.281	59	3845.482	-1.729	59
3529.025	-2.656	59	33842.042	-2.536	59	3845.478	-1.533	59
3529.033	-2.656	59	33842.051	-2.536	59	3845.487	-2.428	59
3529.030	-2.213	59	33842.046	-2.093	59	3845.482	-1.533	59
3529.025	-2.268	59	33842.039	-2.587		3845.476	-1.329	59
3529.037	-2.707	59	33842.052	-2.148		3845.489	-2.273	59
3529.032	-2.122	59	33842.045	-2.002		3845.482	-1.428	59
3529.025	-2.013	59	33842.036	-2.712		3845.473	-1.159	59
3529.042	-2.832	59	33842.054	-1.893		3845.490	-2.273	59
3529.035	-2.100	59	33842.045	-1.980		3845.482	-1.381	59
3529.026	-1.815	59	33842.033	-2.934		3845.471	-1.013	59
3529.048	-3.054	59	33842.054	-1.695		3845.491	-2.370	59
3529.039	-2.154	59	33842.043	-2.034		3845.481	-1.387	59
3529.028	-1.651	59	33842.030	-3.344		3845.468	-0.884	59
3529.054	-3.464	59	33842.054	-1.531		3845.492	-2.574	59
3529.043	-2.350	59	33842.041	-2.230		3845.479	-1.460	
3529.029	-1.510	59	33842.053	-1.390		3845.464	-0.768	
						3845.491	-2.972	
						3845.476	-1.671	
						3845.458	-0.663	

Table D.6 - Hyperfine structure for Co I lines.

4749.612Å; $\chi = 3.053$ eV log gf(total) = -0.321			5212.691Å; $\chi = 3.514$ eV log gf(total) = -0.110			5280.629Å; $\chi = 3.629$ eV log gf(total) = -0.030		
$\lambda$ (Å)	log gf	iso	$\lambda$ (Å)	log gf	iso	$\lambda$ (Å)	log gf	iso
4746.669	-1.7470	59	5212.691	-1.5360	59	5280.629	-1.8362	59
4749.651	-1.7470	59	5212.771	-1.5360	59	5280.660	-1.8362	59
4749.664	-2.1985	59	5212.786	-1.9875	59	5280.652	-1.7692	59
4749.643	-1.6287	59	5212.757	-1.4177	59	5280.637	-2.4682	59
4749.683	-3.1985	59	5212.808	-2.9875	59	5280.662	-1.5729	59
4749.662	-1.9877	59	5212.779	-1.7767	59	5280.646	-1.5729	59
4749.633	-1.5106	59	5212.740	-1.2996	59	5280.623	-2.3133	59
4749.687	-2.9925	59	5212.808	-2.7815	59	5280.661	-1.3688	59
4749.659	-1.8921	59	5212.770	-1.6811	59	5280.637	-1.4682	59
4749.623	-1.3992	59	5212.721	-1.1882	59	5280.605	-2.3133	59
4749.690	-2.9645	59	5212.806	-2.7535	59	5280.656	-1.1994	59
4749.655	-1.8561	59	5212.757	-1.6451	59	5280.625	-1.4212	59
4749.612	-1.2954	59	5212.699	-1.0844	59	5280.585	-2.4102	59
4749.693	-3.0436	59	5212.801	-2.8326	59	5280.649	-1.0532	59
4749.650	-1.8717	59	5212.743	-1.6607	59	5280.609	-1.4268	59
4749.601	-1.1989	59	5212.674	-0.9879	59	5280.563	-2.6143	59
4749.694	-3.2355	59	5212.794	-3.0245	59	5280.638	-0.9241	59
4749.645	-1.9539	59	5212.726	-1.7429	59	5280.591	-1.5004	59
4749.588	-1.1088	59	5212.648	-0.8978	59	5280.536	-3.0123	59
4749.695	-3.6245	59	5212.785	-3.4135	59	5280.625	-0.8082	59
4749.639	-2.1722	59	5212.707	-1.9612	59	5280.570	-1.7112	59
4749.575	-1.0245	59	5212.619	-0.8135	59	5280.608	-0.7026	59

Table D.7 - Hyperfine structure for Co I lines.

5301.047Å; $\chi= 1.710$ eV log gf(total) = -2.000			5342.708Å; $\chi= 4.021$ eV log gf(total) = 0.690			5454.572Å; $\chi= 4.072$ eV log gf(total) = +0.238		
$\lambda$ (Å)	log gf	iso	$\lambda$ (Å)	log gf	iso	$\lambda$ (Å)	log gf	iso
5301.077	-3.6513	59	5342.700	-0.5933	59	5454.568	-1.4018	59
5301.068	-3.3960	59	5342.708	-1.3181	59	5454.562	-1.5981	59
5301.081	-3.3960	59	5342.700	-0.5100	59	5454.574	-1.5981	59
5301.072	-5.3045	59	5342.720	-2.5312	59	5454.568	-1.3877	59
5301.059	-3.1973	59	5342.711	-1.0998	59	5454.560	-1.3774	59
5301.077	-3.1973	59	5342.701	-0.4239	59	5454.577	-1.3774	59
5301.064	-4.0615	59	5342.726	-2.2971	59	5454.569	-1.2504	59
5301.046	-3.1328	59	5342.715	-1.0058	59	5454.558	-1.2738	59
5301.070	-3.1328	59	5342.702	-0.3396	59	5454.581	-1.2738	59
5301.053	-3.3442	59	5342.732	-2.2513	59	5454.570	-1.0827	59
5301.031	-3.1639	59	5342.719	-0.9739	59	5454.556	-1.2313	59
5301.061	-3.1639	59	5342.704	-0.2585	59	5454.584	-1.2313	59
5301.040	-2.9376	59	5342.739	-2.3183	59	5454.571	-0.9143	59
5301.013	-3.3454	59	5342.724	-0.9941	59	5454.554	-1.2416	59
5301.049	-3.3454	59	5342.707	-0.1810	59	5454.588	-1.2416	59
5301.023	-2.6465	59	5342.747	-2.5012	59	5454.572	-0.7549	59
			5342.729	-1.0809	59	5454.553	-1.3194	59
			5342.709	-0.1073	59	5454.593	-1.3194	59
			5342.755	-2.8833	59	5454.573	-0.6070	59
			5342.735	-1.3036	59	5454.552	-1.5340	59
			5342.713	-0.0370	59	5454.597	-1.5340	59
						5454.575	-0.4706	59

Table D.8 - Hyperfine structure for Co I lines.

5647.234Å; $\chi= 2.280$ eV log gf(total) = -1.560			6117.000Å; $\chi= 1.785$ eV log gf(total) = -2.490			6188.996Å; $\chi= 1.710$ eV log gf(total) = -2.450		
$\lambda$ (Å)	log gf	iso	$\lambda$ (Å)	log gf	iso	$\lambda$ (Å)	log gf	iso
5105.562	-2.8856	59	5218.195	-1.2041	63	5218.195	-1.2041	59
5647.269	-2.7641	59	6117.043	-3.4511	59	6189.071	-4.1013	59
5647.258	-2.7641	59	6117.002	-2.9740	59	6189.053	-3.8460	59
5647.243	-3.0652	59	6117.008	-2.9740	59	6189.075	-3.8460	59
5647.269	-2.9402	59	6116.967	-3.1201	59	6189.058	-5.7545	59
5647.253	-2.6003	59				6189.031	-3.6473	59
5647.232	-2.6258	59				6189.064	-3.6473	59
5647.268	-3.1901	59				6189.038	-4.5115	59
5647.247	-2.5924	59				6189.002	-3.5828	59
5647.220	-2.3425	59				6189.046	-3.5828	59
5647.265	-3.6180	59				6189.011	-3.7942	59
5647.238	-2.7527	59				6188.967	-3.6139	59
5647.207	-2.1273	59				6189.022	-3.6139	59
						6188.978	-3.3876	59
						6188.924	-3.7954	59
						6188.991	-3.7954	59
						6188.938	-3.0965	59

Table D.9 - Calculated hyperfine structure for the Cu I 3247.53 and 3273.95 Å lines.

3247.53Å; $\chi = 0.00$ eV log gf(total) = -0.062			3273.95Å; $\chi = 0.00$ eV log gf(total) = -0.359		
$\lambda$ (Å)	log gf	iso	$\lambda$ (Å)	log gf	iso
3247.507	-1.420	63	3273.925	-1.720	63
3247.506	-1.022	63	3273.923	-1.021	63
3247.505	-1.022	63	3273.966	-1.021	63
3247.547	-1.721	63	3273.965	-1.021	63
3247.546	-1.022	63	3273.923	-2.066	65
3247.544	-0.575	63	3273.922	-1.367	65
3247.506	-1.766	65	3273.968	-1.367	65
3247.505	-1.368	65	3273.966	-1.367	65
3247.503	-1.368	65			
3247.549	-2.067	65			
3247.547	-1.368	65			
3247.545	-0.921	65			

Table D.10 - Hyperfine structure for Cu I lines.

5105.50Å; $\chi = 1.39$ eV log gf(total) = -1.520			5218.20Å; $\chi = 3.82$ eV log gf(total) = +0.0		
$\lambda$ (Å)	log gf	iso	$\lambda$ (Å)	log gf	iso
5105.562	-2.8856	63	5218.195	-1.2041	63
5105.563	-2.9314	63	5218.197	-1.2499	63
5105.554	-2.5634	63	5218.197	-0.8819	63
5105.567	-3.8856	63	5218.201	-2.2041	63
5105.558	-2.8187	63	5218.201	-1.1372	63
5105.540	-2.3135	63	5218.203	-0.6320	63
5105.562	-4.0617	63	5218.206	-2.3802	63
5105.544	-2.9156	63	5218.206	-1.2341	63
5105.516	-2.1075	63	5218.206	0.0	63
5105.565	-3.3619	65	5218.194	-1.2041	65
5105.566	-3.4077	65	5218.196	-1.2499	65
5105.555	-3.0397	65	5218.196	-0.8819	65
5105.570	-4.3619	65	5218.201	-2.2041	65
5105.559	-3.2950	65	5218.201	-1.1372	65
5105.540	-2.7898	65	5218.201	-0.6320	65
5105.564	-4.5380	65	5218.206	-2.3802	65
5105.545	-3.3919	65	5218.206	-1.2341	65
5105.514	-2.5838	65	5218.206	-0.4260	65

## Line fits to Arcturus and CS 31082-001

In support of the analysis in Section 7, here we show the model fits to the reference star Arcturus for Co and Cu in figs. E.1 and E.2, and our fits to Sc, Ti, Mn, Co, Ni and Zn for CS 31082-001 in figs. E.3, E.4, E.5, E.6, E.7, E.8, and E.9.

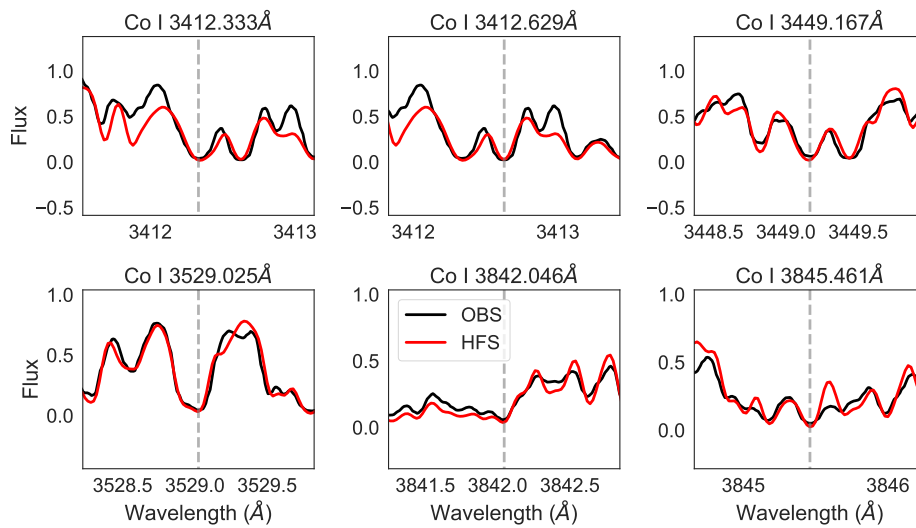


Figure E.1: Arcturus: Fits to the six selected lines of Co I.

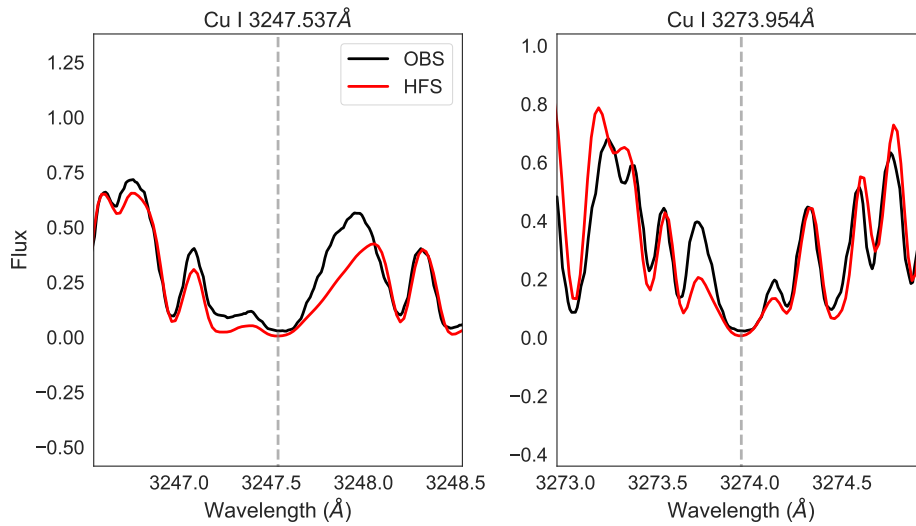


Figure E.2: Arcturus: Fits to Cu I 3247.537 and 3273.954 Å lines.

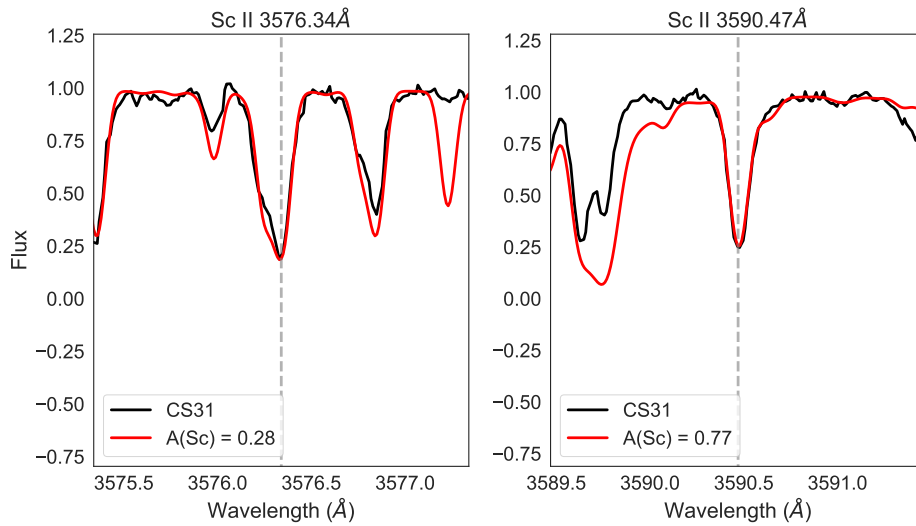


Figure E.3: Best-fit abundances for the Sc II lines computed with  $[\text{Sc}/\text{Fe}] = +0.03$  for the Sc II 3576.34 Å line and  $[\text{Sc}/\text{Fe}] = +0.52$  for the Sc II 3590.47 Å line (without hyperfine structure).

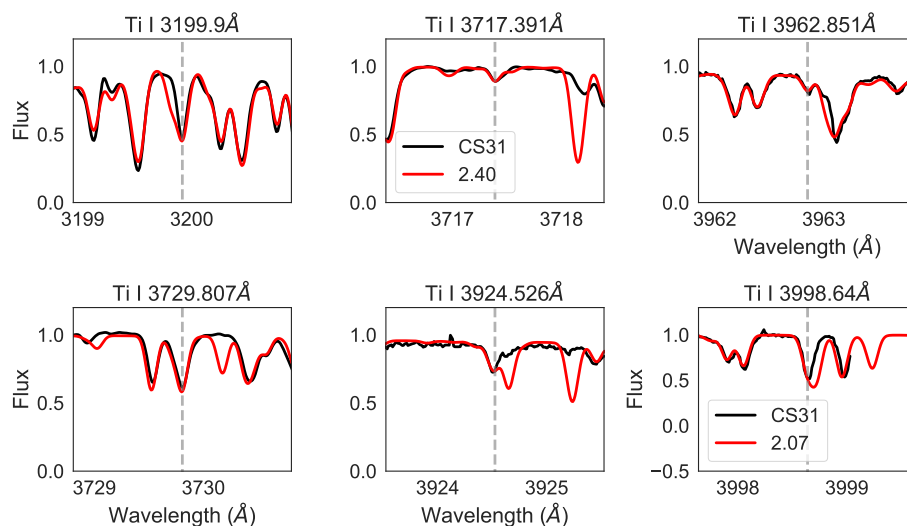


Figure E.4: Best-fit abundances for the Ti I lines, computed with  $[\text{Ti}/\text{Fe}] = +0.35$ , whereas for the Ti I 3998.64 Å line a best fit is found for  $[\text{Ti}/\text{Fe}] = +0.02$ .

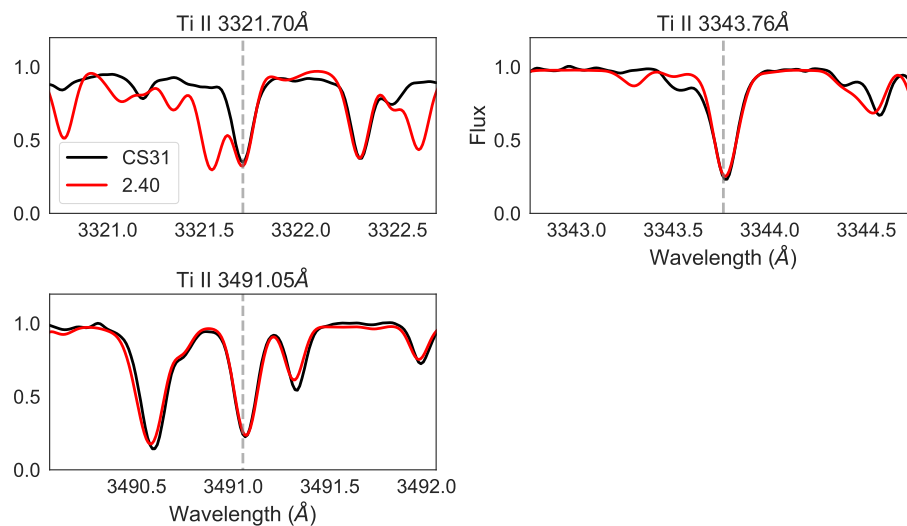


Figure E.5: Best-fit abundance for the Ti II lines, computed with  $[\text{Ti}/\text{Fe}] = +0.35$ .

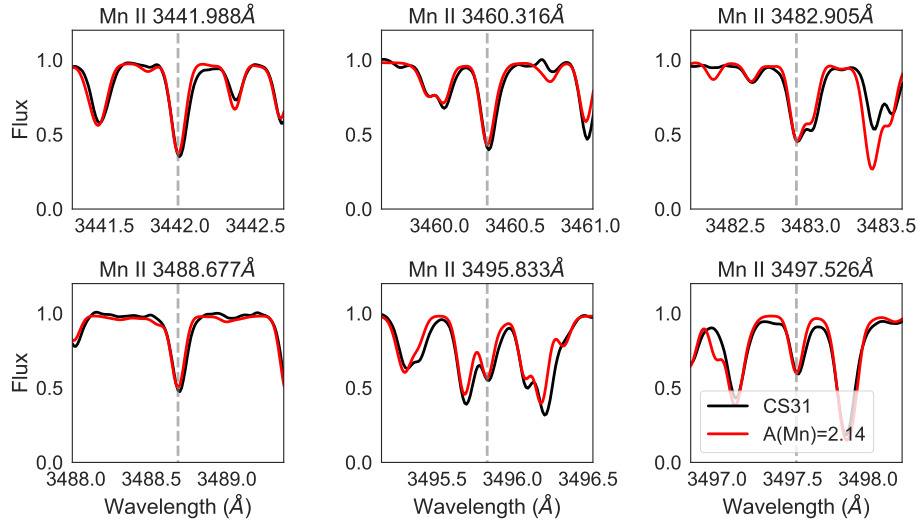


Figure E.6: Best-fit abundance for the Mn II lines, computed with  $[\text{Mn}/\text{Fe}] = -0.39$  (without hyperfine structure).

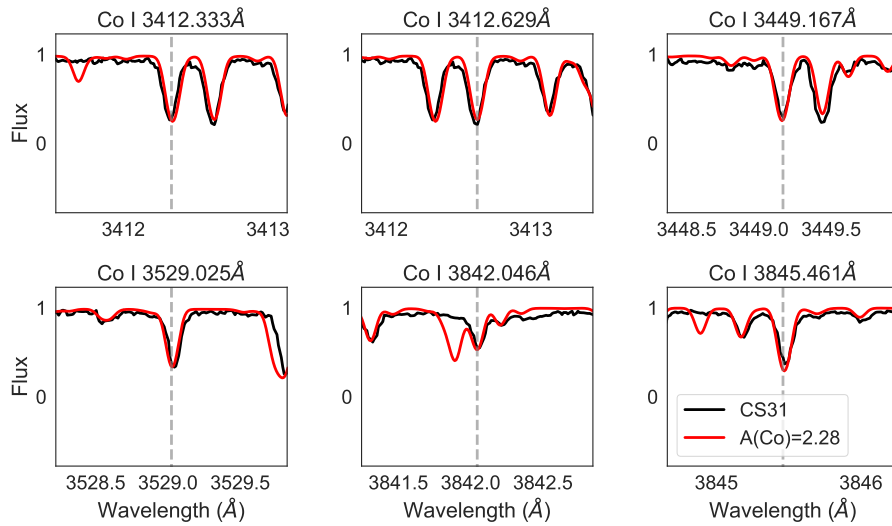


Figure E.7: Best-fit abundance for the Co I lines, computed with  $[\text{Co}/\text{Fe}] = +0.19$  (including hyperfine structure).

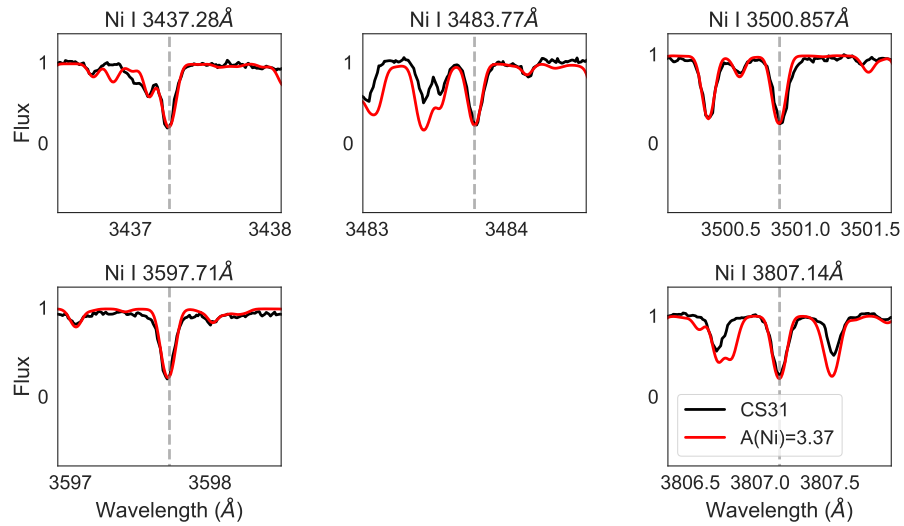


Figure E.8: Best-fit abundance for the Ni I lines, computed with  $[\text{Ni}/\text{Fe}] = +0.05$ .

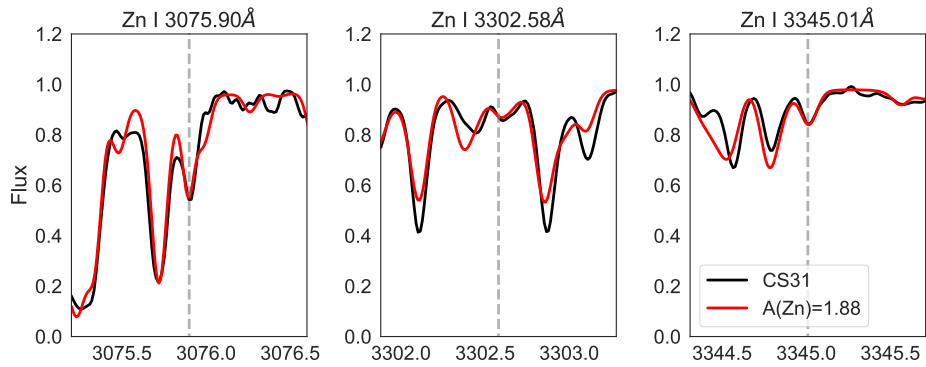


Figure E.9: Best-fit abundance for the Zn I lines, computed with  $[\text{Zn}/\text{Fe}] = +0.22$ .